Universitá degli Studi dell'Insubria

Doctoral Thesis

MYSCE, a new Monte Carlo code for star cluster simulations

Axion-like particles and very-high energy astrophysics

Author:
Giorgio Galanti

Supervisor:
Prof. Monica Colpi
Co-Supervisors:
Dr. Emanuele Ripamonti
Prof. Marco Roncadelli

A thesis submitted in fulfilment of the requirements for the degree of Doctor of Philosophy

in

Astronomy and Astrophysics
Dipartimento di Fisica e Matematica

November 2013

UNIVERSITÁ DEGLI STUDI DELL'INSUBRIA

Abstract

Facoltá di Scienze MM. FF. NN.
Dipartimento di Fisica e Matematica

Doctor of Philosophy

`MYSCE`, a new Monte Carlo code for star cluster simulations

Axion-like particles and very-high energy astrophysics

by Giorgio Galanti

This thesis focuses on two different topics: (i) star clusters, as favourite environments for the formation of black holes of very high mass, and (ii) the implications of axion-like particles for very-high energy astrophysics by considering γ-ray observations from blazars.

In the first part of this thesis we develop a new Monte Carlo code `MYSCE` (Montecarlo Young Star Cluster Evolution) which improves and solves some problems of the original scheme presented by Hénon. We use our code to simulate star clusters and to inquire if an episode of gas infall during the cluster lifetime can lead to the formation of an intermediate mass black hole and/or a super massive black hole seed.

In the second part of this thesis we explore axion-like particles in an astrophysical context. We describe their origin and properties within extensions of the Standard Model of elementary particle physics. We show how axion-like particles can in principle solve the cosmic opacity problem for distant blazars and naturally explain the emission of very-high energy photons from flat spectrum radio quasars.

Acknowledgements

I am deeply grateful to Prof. Monica Colpi, Dr. Emanuele Ripamonti, and Prof. Marco Roncadelli for their encouragement, support and cooperation to this work.

I want to thank also Prof. Alessandro De Angelis, Dr. Massimo Dotti, Dr. Michela Mapelli, Dr. Fabrizio Tavecchio for useful and stimulating discussions.

Lastly, I want to thank people in Milano-Bicocca and everyone who contributed to this thesis.

Contents

Abstract iii

Acknowledgements v

List of Figures xi

List of Tables xvii

I MYSCE, a new Monte Carlo code for star cluster simulations 1

Introduction 3

1 Star clusters 7
- 1.1 Self-gravitating systems . . . 9
- 1.2 Star cluster models . . . 12
- 1.3 Star cluster dynamics . . . 17
  - 1.3.1 Two-body interactions . . . 18
  - 1.3.2 Core collapse . . . 20
  - 1.3.3 Three-body interactions . . . 23
  - 1.3.4 Effects of stellar evolution . . . 26
  - 1.3.5 A summary of star cluster dynamical evolution . . . 26

2 MYSCE code description 29
- 2.1 Numerical methods to simulate Star Clusters . . . 29
- 2.2 Outline of the MYSCE algorithm . . . 31
  - 2.2.1 Overview . . . 31
  - 2.2.2 Time step . . . 34
  - 2.2.3 Gravitational potential . . . 34
  - 2.2.4 Two-body interactions . . . 34
  - 2.2.5 Three-body interactions . . . 36
  - 2.2.6 Possible mergers . . . 39
  - 2.2.7 Removal of unbound stars . . . 41
  - 2.2.8 Star position and velocity recalculation . . . 42
  - 2.2.9 Stellar evolution . . . 43
  - 2.2.10 Spurious relaxation . . . 43

3 Initial conditions **45**
3.1 Star position and velocity distribution 45
3.2 Initial mass function 47
3.3 Primordial binary initial conditions 48

4 Gas infall into star clusters **51**
4.1 State of the art 51
4.2 Gas infall in the absence of physical interactions 54
4.3 Gas infall in the presence of physical interactions 58
4.3.1 Young star clusters 60
4.3.2 Massive star clusters 64
4.3.3 An extreme case 69

Conclusions **71**

A Spurious relaxation **75**
A.1 Overview 75
A.2 Spurious relaxation correction 76
A.2.1 Previous approaches 76
A.2.2 A possible effective correction 77
A.2.3 Tests 79
A.3 Discussion 80

Bibliography **83**

II Axion-like particles and very-high energy astrophysics **89**

Introduction **91**

1 Axion-like particles (ALPs) **101**
1.1 Motivation 101
1.2 Axion as a prototype 103
1.3 Beyond the axion: ALPs 104
1.4 Photon-ALP mixing 105
1.5 Photon/ALP beam propagation 106
1.6 Astrophysical and cosmological constraints 112

2 Transparency of the Universe to γ rays **115**
2.1 Evaluation of the pair-production cross-section 116
2.2 Evaluation of the optical depth 117
2.3 Soft photon background 118
2.4 Results 120
2.5 Discussion 122

3 Very-high energy blazar spectra **123**
3.1 Blazars 123

3.2 Conventional photon propagation . . . 126
3.3 Understanding observed VHE blazar spectra . . . 127
3.4 The cosmic opacity problem . . . 130

4 DARMA scenario 133
4.1 An intuitive insight . . . 133
4.2 General strategy . . . 134
4.3 Photon absorption . . . 136
4.4 Intergalactic medium (IGM) . . . 139
4.5 Propagation over a single domain . . . 141
4.6 Propagation over many domains . . . 143

5 ALP consequences on blazar spectra 147
5.1 Predictions for future observations . . . 149
5.2 A new interpretation of observed VHE blazars . . . 153
5.2.1 Solution of the cosmic opacity problem . . . 156
5.2.2 Fitting individual sources . . . 156

6 A model for the FSRQ PKS 1222+216 165
6.1 Observations and setup . . . 165
6.2 Oscillations in the inhomogeneous magnetic field . . . 168
6.3 Photon-ALP oscillations before the BLR . . . 170
6.4 Photon-ALP oscillations in the large scale jet . . . 172
6.5 Photon-ALP oscillations in the host galaxy . . . 173
6.6 Photon-ALP oscillations in extragalactic space . . . 174

7 Spectral energy distribution of PKS 1222+216 177
7.1 No oscillations in extragalactic space . . . 177
7.2 Oscillations in extragalactic space . . . 181
7.3 Spectral energy distribution (SED) . . . 183

8 ALPs from irregularities in γ ray source spectra? 187
8.1 Setting the stage . . . 188
8.2 Probabilities for polarized and unpolarized beams . . . 189
8.3 A particular case . . . 191
8.4 Photon survival probability . . . 191
8.5 Observed flux . . . 192
8.6 Discussion . . . 194

Conclusions 197

A Schödinger-like equation with constant coefficients 201

B Approximate EBL behaviour 205

Bibliography 209

List of Figures

1.1 The GC Messier 92 in the Hercules constellation. 8
1.2 The Pleiades, an example of OC. 8
1.3 The YSC R136 in the 30 Doradus region of the Large Magellanic Cloud. . 9
1.4 Picture of a two-body encounter. A test star approaches the field star at velocity v and impact parameter b. The velocity is perturbed only by the component of the gravitational force $F_\perp$ perpendicular to v. 18
1.5 Typical behaviour of the Lagrangian radii when the SC approaches to the core collapse [91]. The inner Lagrangian radii shrink, while the outer Lagrangian radii widen. 21
1.6 Typical behaviour of the core radius $r_{\rm c}$, binary half-mass radius $r_{\rm h,b}$ and single star half-mass radius $r_{\rm h,s}$ when the SC experiences gravothermal oscillations [29]. 27

2.1 Block diagram of the modified Monte Carlo method used in the code `MYSCE`. 33
2.2 Scheme of a three-body interaction between a binary and a single star (figure by [53]). Here, V is the relative velocity, m_3 is the mass of the single star and ρ is the impact parameter. In the text we called these quantities: $v_{\rm rel}$, m', and b, respectively. 39

3.1 Probability distribution associated to the distribution function of the Plummer model for a SC of $N = 10^4$ stars and with a scale radius $a = 1\,{\rm pc}$. 46
3.2 Spatial distribution of stars according to the Plummer model for a SC of $N = 10^4$ stars and with a scale radius $a = 1\,{\rm pc}$. 46
3.3 Radius probability density according to the Plummer model for a SC of $N = 10^4$ stars and with a scale radius $a = 1\,{\rm pc}$. 47
3.4 Velocity probability density at different radii (at 0.25, 0.5 times the scale radius, at scale radius and at two times the scale radius, from left to right, respectively) according to the Plummer model for a SC of $N = 10^4$ stars and with a scale radius $a = 1\,{\rm pc}$. 47
3.5 Mass probability density according to the Salpeter IMF for a SC of $N = 10^4$ stars and with a scale radius $a = 1\,{\rm pc}$. 48

4.1 Theoretical estimate (left panel) and simulation results (right panel) of the final stellar scale radius $a_{*,f}$ after gas infall for different choices of the gas scale radius $a_{\rm G}$. $a_{*,f}$ and $a_{\rm G}$ are in units of the initial stellar scale radius $a_{*,i}$. From top to bottom curves refer to $M_{\rm G,0} = 1, 2, 5, 10\,M_*$. . . . 57

4.2 Final stellar velocity dispersion $\sigma_{*,f}$ after gas infall for different choices of the gas scale radius $a_{\rm G}$, as obtained from the numerical simulations. $\sigma_{*,f}$ is in units of the initial stellar velocity dispersion $\sigma_{*,i}$ and $a_{\rm G}$ is in units of the initial stellar scale radius $a_{*,i}$. From bottom to top curves refer to $M_{\rm G,0} = 1, 2, 5, 10\, M_*$. 58
4.3 Contraction parameter ξ after gas infall for different choices of the gas scale radius $a_{\rm G}$, as obtained from the numerical simulations. $a_{\rm G}$ is in units of the initial stellar scale radius $a_{*,i}$. From top to bottom curves refer to $M_{\rm G,0} = 1, 2, 5, 10\, M_*$. 58
4.4 Velocity gain parameter η after gas infall for different choices of the gas scale radius $a_{\rm G}$, as obtained from the numerical simulations. $a_{\rm G}$ is in units of the initial stellar scale radius $a_{*,i}$. From top to bottom curves refer to $M_{\rm G,0} = 1, 2, 5, 10\, M_*$. 59
4.5 Core-collapse time (calculated in the absence of three-body interactions) after gas infall as a function of the mass $M_{\rm G,0}$ of the gas and of the gas scale radius $a_{\rm G}$. The final core-collapse time $t_{{\rm cc},f}$ is in units of the initial core-collapse time $t_{{\rm cc},i}$. Lower curve refers to the case $\alpha_{\rm G} = 0.1$, upper curve to the case $\alpha_{\rm G} = 1$ 60
4.6 Interaction time as a function of different relative velocities ($\sim$ velocity dispersion) for the semi major axes lower ($a = 0.5\,{\rm AU}$) and upper ($a = 1000\,{\rm AU}$) limits and for the fixed hardness ratio $x = 1$, for the SC with $N = 10^4$ stars and for $m_1 = 10\,{\rm M}_\odot$, $m_2 = m_3 = 1\,{\rm M}_\odot$. Open circle represents the core-collapse time (calculated in the absence of three-body interactions) before gas infall. Filled circle represents the core-collapse time (calculated in the absence of three-body interactions) after gas infall. 62
4.7 Evolution of the binary semi major axes a in a YSC of $N = 10^4$ stars, with $a_{*,i} = 1\,{\rm pc}$ without gas infall. a is in units of $a_0 = 1\,{\rm AU}$. Left panel represents the initial semi major axis distribution, right panel represents the semi major axis distribution at core-collapse time ($\sim 8\,{\rm Myr}$, see Fig. 4.9). The vertical dashed line represents the boundary ($x = 1$) between hard ($x > 1$, on the left) and soft ($x < 1$, on the right) binaries. 64
4.8 Same as Fig. 4.7 but now in the presence of a gas infall with $M_{\rm G,0} = 10\, M_*$ and $a_{\rm G} = 0.1\,{\rm pc}$. In the right panel we plot semi major axis distribution at core-collapse time ($\sim 30\,{\rm Myr}$, see Fig. 4.10). 65
4.9 Evolution of the Lagrangian radii of a YSC of $N = 10^4$ stars, with $a_{*,i} = 1\,{\rm pc}$ without gas infall. From bottom to top, lines represent the Lagrangian radii corresponding to 0.5%, 5%, 10%, 20%, 30%, 50%, 70%, 90%, 95% of the mass of the system, respectively. 65
4.10 Same as Fig. 4.9 but now in the presence of a gas infall with $M_{\rm G,0} = 10\, M_*$ and $a_{\rm G} = 0.1\,{\rm pc}$. 66
4.11 Interaction time (broken black line and light grey area) and gravitational radiation inspiral time (solid black line and dark grey area) as a function of different relative velocities ($\sim$ velocity dispersion) for the semi major axes lower ($a = 0.1\,{\rm AU}$) and upper ($a = 100\,{\rm AU}$) limits and for the fixed hardness ratio $x = 1$, for a SC of $N = 10^6$ stars and for $m_1 = m_2 = m_3 = 10\,{\rm M}_\odot$. 68
4.12 Same as Fig. 4.11 for a SC of $N = 10^7$ stars. 70

A.1 Evolution of the Lagrangian radii within a 5000 particles system, as a function of the number of time steps. The simulations were performed with `MYSCE` in the absence of non-radial forces (e.g. few-body interactions), and in the absence of the proposed SR correction. From bottom to top, lines represent the Lagrangian radii corresponding to 0.5%, 5%, 10%, 20%, 30%, 50%, 70%, 90%, 95% of the mass of the system, respectively. 81

A.2 Same as Fig. A.1, but in this case the simulations included the proposed SR correction. For clarity of visualization, data are binned: each point is the average of ten real steps. Note that the scales are different from Fig. A.1, as we plot a much larger number of time steps, over a smaller vertical range. 81

3 The pair-production mean free path λ_γ of a VHE photon is plotted versus its energy E within the EBL model of FRV. Only conventional physics is assumed and in particular the possibility of photon-ALP oscillations is ignored. 93

2.1 Source redshifts z_s at which the optical depth takes fixed values as a function of the observed hard photon energy E_0; the y-scale on the right side shows the distance in Mpc for nearby sources. The curves from bottom to top correspond to a photon survival probability of $e^{-1} \simeq 0.37$ (the horizon), $e^{-2} \simeq 0.14$, $e^{-3} \simeq 0.05$ and $e^{-4.6} \simeq 0.01$. For $D \simeq 8$ kpc the photon survival probability is larger than 0.37 for any value of E_0. . . 121

2.2 Comparison of the mean free path λ_γ for $\gamma\gamma \to e^+e^-$ as derived in the text using a low-frequency cutoff at 2 MHz (red dot-dashed line) with the one obtained by CA in the local Universe ($z_s = 0$) as a function of the observed energy E. The CA black lines labelled by a, b, c represent three different EBL models, the black solid line corresponds to the CMB, the black lines labelled by 1, 2, 3 represent a model of the RB with low-frequency cutoff at 5, 2 and 1 MHz, respectively, and the black triangles correspond to the RB under the assumption that it is completely extragalactic. 121

3.1 Schematic structure of an AGN. 125

3.2 The observed values of the observed spectral index $\Gamma_{\rm obs}$ versus the source redshift for all blazars detected so far in the VHE band are represented by dots and corresponding error bars. 128

5.1 Behaviour of $P^{\rm DARMA}_{\gamma\to\gamma}$ versus the observed energy E_0 for: $z = 0.031$ (top row), $z = 0.188$ (second row), $z = 0.444$ (third row), $z = 0.536$ (bottom row). The solid black line corresponds to $\xi = 5.0$, the dotted-dashed line to $\xi = 1.0$, the dashed line to $\xi = 0.5$, the dotted line to $\xi = 0.1$ and the solid grey line to conventional physics. We have taken $L_{\rm dom} = 4\,$Mpc (left column) and $L_{\rm dom} = 10\,$Mpc (right column). 150

5.2 Behaviour of $P^{\rm DARMA}_{\gamma\to\gamma}$ versus the observed energy E_0 for: $z = 0.031$ (top row left), $z = 0.188$ (top row right), $z = 0.444$ (bottom row left), $z = 0.536$ (bottom row right) for $L_{\rm dom} = 0.05\,$Mpc. The solid black line corresponds to $\xi = 5.0$, the dotted-dashed line to $\xi = 1.0$, the dashed line to $\xi = 0.5$, the dotted line to $\xi = 0.1$ and the solid grey line to conventional physics. . 152

5.3 Behaviour of $\Gamma_{\rm obs}^{\rm DARMA}$ for the blazars 3C 66B, Mrk 421, Mrk 501 (with the two measurements of $\Gamma_{\rm obs}$ in the literature), 1ES 2344+514 and Mrk 180. The solid black line corresponds to $\Gamma_{\rm em}^{\rm DARMA} = 2.51$ and the grey strip represents the range $2.31 < \Gamma_{\rm em}^{\rm DARMA} < 2.71$. 159
5.4 Behaviour of $\Gamma_{\rm obs}^{\rm DARMA}$ for the blazars 1ES 1959+650, BL Lacertae, PKS 0548-322, PKS 2005-489, RGB J0152+017 and W Comae. The solid black line corresponds to $\Gamma_{\rm em}^{\rm DARMA} = 2.51$ and the grey strip represents the range $2.31 < \Gamma_{\rm em}^{\rm DARMA} < 2.71$. 160
5.5 Behaviour of $\Gamma_{\rm obs}^{\rm DARMA}$ for the blazars PKS 2155-304, H 1426+428, 1ES 0806+524, 1ES 0229+200, H 2356-309 and 1ES 1218+304. The solid black line corresponds to $\Gamma_{\rm em}^{\rm DARMA} = 2.51$ and the grey strip represents the range $2.31 < \Gamma_{\rm em}^{\rm DARMA} < 2.71$. 161
5.6 Behaviour of $\Gamma_{\rm obs}^{\rm DARMA}$ for the blazars 1ES 1101-232, 1ES 0347-121, 1ES 1011+496, S5 0716+714, PG 1553+113 and PKS 1222+216. The solid black line corresponds to $\Gamma_{\rm em}^{\rm DARMA} = 2.51$ and the grey strip represents the range $2.31 < \Gamma_{\rm em}^{\rm DARMA} < 2.71$. 162
5.7 Behaviour of $\Gamma_{\rm obs}^{\rm DARMA}$ for the blazars 3C 66A, PKS 1424+240 and 3C 279. The solid black line corresponds to $\Gamma_{\rm em}^{\rm DARMA} = 2.51$ and the grey strip represents the range $2.31 < \Gamma_{\rm em}^{\rm DARMA} < 2.71$. 163

6.1 Effective optical depth plotted as a function of rest-frame energy for VHE photons propagating in the BLR of PKS 1222+216. The blue long-dashed line corresponds to the process $\gamma\gamma \to e^+e^-$. The other three lines pertain to our model containing ALPs. Specifically, the violet dashed-dotted line corresponds to $(B = 2\,{\rm G}, M = 4{\cdot}10^{11}\,{\rm GeV})$, the green short-dashed line to $(B = 0.4\,{\rm G}, M = 1.5{\cdot}10^{11}\,{\rm GeV})$ and the red solid line to $(B = 0.2\,{\rm G}, M = 7 \cdot 10^{10}\,{\rm GeV})$ (more about this, later and in Chapter 7 Sec. 7.1). 166

7.1 Red points at high and VHE are the spectrum of PKS 1222+216 recorded by *Fermi*/LAT and the one detected by MAGIC but EBL-deabsorbed according to conventional physics using Eq. (7.1). 178
7.2 The quantity Π as a function of B and M. The three white blobs correspond to our benchmark cases. 180
7.3 Red points at high energy and VHE are the spectrum of PKS 1222+216 recorded by *Fermi*/LAT and the one detected by MAGIC but EBL-deabsorbed according to conventional physics using Eq. (7.1). The black points represent the same data once further corrected for the photon-ALP oscillation effect employing Eq. (7.5) in the case $(B = 0.2\,{\rm G}, M = 7 \cdot 10^{10}\,{\rm GeV})$. The gray data points below $10^{20}\,{\rm Hz}$ are irrelevant for the present discussion (details can be found in [142]. 181
7.4 Red points at high energy and VHE are the spectrum of PKS 1222+216 recorded by *Fermi*/LAT and the one detected by MAGIC but EBL-deabsorbed according to conventional physics using Eq. (7.1). The black points represent the same data once further corrected for the photon-ALP oscillation effect employing Eq. (7.5) in the case $(B = 0.4\,{\rm G}, M = 1.5 \cdot 10^{11}\,{\rm GeV})$. The gray data points below $10^{20}\,{\rm Hz}$ are irrelevant for the present discussion (details can be found in [142]. 182

7.5 Red points at high energy and open red squares at VHE are the spectrum of PKS 1222+216 recorded by *Fermi*/LAT and the one *observed* by MAGIC and not EBL-deabsorbed. The black points represent the same data once further corrected for the photon-ALP oscillation effect in the case ($B = 0.2\,\mathrm{G}, M = 7{\cdot}10^{10}\,\mathrm{GeV}$) including also photon-ALP oscillations in extragalactic space, where a magnetic field with strength $B = 0.7$ nG is supposed to exist. So, they are obtained from the red points and the open red squares by means of Eq. (7.10). The gray data points below $10^{20}\,\mathrm{Hz}$ are irrelevant for the present discussion (details can be found in [142]). . . 183
7.6 Same as Fig. 7.3 for the case ($B = 0.2\,\mathrm{G}, M = 7 \cdot 10^{10}\,\mathrm{GeV}$) without photon-ALP oscillations in extragalactic space, but in addition the dashed and solid curves show the SED resulting from the considered two blobs which account for the γ-ray emission at high energy and VHE, respectively. 185
7.7 Same as Fig. 7.4 for the case ($B = 0.4\,\mathrm{G}, M = 1.5 \cdot 10^{11}\,\mathrm{GeV}$) without photon-ALP oscillations in extragalactic space, but in addition the dashed and solid curves show the SED resulting from the considered two blobs which account for the γ-ray emission at high energy and VHE, respectively. 186
7.8 Same as Fig. 7.5 for the case ($B = 0.2\,\mathrm{G}, M = 7 \cdot 10^{10}\,\mathrm{GeV}$) with photon-ALP oscillations in extragalactic space, but in addition the dashed and solid curves show the SED resulting from the considered two blobs which account for the γ-ray emission at high energy and VHE, respectively. . . . 186

8.1 The upper panel corresponds to the case of an initially *polarized* beam, while the lower panel corresponds to the case of an initially *unpolarized* beam. The solid black line represents the photon survival probability along a single randomly chosen trajectory followed by the beam in the presence of ALPs for a source at $z_s = 0.1$, using $B = 1\,\mathrm{nG}$, the size of a magnetic domain equal to $1\,\mathrm{Mpc}$, $g = 8 \cdot 10^{-11}\,\mathrm{GeV}^{-1}$ and $m_a = 2\,\mathrm{neV}$. The dashed red line represents the same quantity with ALPs discarded (conventional physics). 192
8.2 The upper panel corresponds to the case of a *polarized* beam, while the lower panel corresponds to the case of an *unpolarized* beam. The solid black line represents the unbinned spectrum and the broken red line the binned spectrum, both in the case of photon-ALP oscillations. The dashed black line corresponds to the best fit to the bins (regardless of the underlying physics). 193
8.3 Distribution of the residuals in three cases. Polarized beam with ALP effects: red blobs. Unpolarized beam with ALP effects: green stars. Conventional physics: blue triangles. 194

B.1 The spectral photon number density in the present Universe $n_\gamma(\cdot, 0)$ is plotted versus the energy ϵ_0 in the energy range $0.25 - 2.5\,\mathrm{eV}$. The solid line represents the result of the FRV model. The dotted and dashed lines correspond to the lower ($\alpha = 0.9$) and upper ($\alpha = 3.6$) limit, respectively, of our power-law approximation defined in Eq. (B.4). 206
B.2 Plot of the behaviour of $I(z)$. 208

B.3 The approximate pair-production mean free path $\lambda_\gamma^{\rm app}$ of a VHE photon is plotted versus its energy E and it is represented by the shadowed area as the parameter α varies in the range 0.9 – 3.6. The dotted and dashed lines correspond to $\alpha = 0.9$ and $\alpha = 3.6$, respectively. Superimposed is the exact result obtained within the FRV model and shown in Fig. 3. . . 208

List of Tables

4.1 Calculation of the relaxation time $t_{\rm rel}$, core-collapse time $t_{\rm cc}$ and single star-binary interaction time t_{2+1} ($m_1 = 10\,{\rm M}_\odot, m_2 = m_3 = 1\,{\rm M}_\odot$) for the two cases of a YSCs of $N = 10^4$ and 10^5 stars in the presence/absence of gas infall ($M_{\rm G,0} = 10\,M_*$, $a_{\rm G} = 0.1\,a_{*,i}$). a_* and σ_* are the initial scale radius (gas, no) and after gas infall (gas, yes). We consider the two cases: (i) we calculate the hardness ratio x starting from the semi major axis lower limit $a = 0.5\,{\rm AU}$ (initial condition) and (ii) we calculate which is a for the case $x = 1$. 61

4.2 Same as Table 4.1 but with a gas infall of $M_{\rm G,0} = 5\,M_*$ and $a_{\rm G} = a_{*,i}$. . . 63

4.3 Same as Table 4.1 but with a gas infall of $M_{\rm G,0} = 10\,M_*$ and $a_{\rm G} = 0.2\,a_{*,i}$). In this case the SC is an evolved system, more massive stars have already gone out of the main-sequence. As a result, several BHs formed: we consider typical BH binaries ($m_1 = m_2 = 10\,{\rm M}_\odot$) in the centre ($a$, x, t_{2+1} are referred to them). We calculate also the BH binary coalescence time for gravitational radiation inspiral $t_{\rm gr}$. In addition, we calculate the segregation time $t_{\rm seg}$ instead of the core-collapse time. 67

4.4 Same as Table 4.3 but for a SC of $N = 10^7$ stars and with a gas infall of $M_{\rm G,0} = 10\,M_*$ and $a_{\rm G} = 0.1\,a_{*,i}$. 70

A.1 Ratio between final and initial Lagrangian radii at 0.5%, 5%, 10%, 20%, 30%, 50%, 70%, 90%, 95% of the total mass of the system when SR correction is neglected after a number of time steps equal to the number of stars. 79

A.2 Ratio between final and initial Lagrangian radii at 0.5%, 5%, 10%, 20%, 30%, 50%, 70%, 90%, 95% of the total mass of the system when SR correction is considered after a number of time steps equal to the number of stars and equal to ten times the number of stars. 80

3.1 Blazars observed so far with the IACTs with known redshift z, measured energy range, measured spectral index $\Gamma_{\rm obs}$, and unfolded spectral index at emission $\Gamma_{\rm em}$ using the FRV model of the EBL. Statistical and systematic errors are added in quadrature to produce the total error reported on the measured spectral index. When only statistical errors are quoted, systematic errors are taken to be 0.1 for H.E.S.S. and 0.2 for MAGIC. The last two rows show the spread $\Delta\Gamma_{\rm em}$ of the values of $\Gamma_{\rm em}$ discarding errors and the average value $\langle\Gamma_{\rm em}\rangle$ including errors, respectively. 124

5.1 Allowed values of M and B_0 in the considered cases. 148

5.2 Upper bounds on the ALP mass in the considered cases. 148

5.3 We have inferred the emitted spectral index $\Gamma_{\rm em}$ by de-absorbing within the DARMA scenario the observed value of $\Gamma_{\rm obs}$ for every source neglecting errors. This procedure has been carried out for the choice of parameters $\xi = 0.1$, $\xi = 0.5$, $\xi = 1.0$ and $\xi = 5.0$. In all cases, we have taken $L_{\rm dom} = 4\,{\rm Mpc}$. The similar values obtained in Chapter 3 Sec. 3.3 within conventional physics have been quoted for comparison and are denoted by $\Gamma_{\rm em}^{\rm CP}$. The last two lines report the spread $\Delta\Gamma_{\rm em}$ of the value of $\Gamma_{\rm em}$ discarding errors and the average value $\langle\Gamma_{\rm em}\rangle$ including errors, respectively, for the various cases. 155

5.4 Same as Table 5.3 but with $L_{\rm dom} = 10\,{\rm Mpc}$. 156

8.1 Values of the variance to the fit residuals for the various cases considered in the text. 194

To my parents and to my grandparents

Part I

MYSCE, a new Monte Carlo code for star cluster simulations

Introduction

Star clusters (hereafter SCs) are dense aggregates of stars that can include $10^3 - 10^7$ elements. The study of SCs is of paramount importance to understand the dynamics of stellar systems. In fact, SCs are exquisite laboratories to analyze several key processes such as two- and three-body encounters among stars and stellar evolution, and to test their consequences on the SC macroscopic evolution driving the SC to relaxation, core collapse, etc.

SCs are proposed as favoured environments for the formation of black holes (hereafter BHs) more massive than $\sim 10^2\,\mathrm{M}_\odot$. While BHs with mass lower than $\sim 10^2\,\mathrm{M}_\odot$ are the result of the evolution of massive stars, the formation of BHs with a higher mass still represents a challenge.

Intermediate mass black holes (IMBHs) with a mass in the range $10^3 - 10^5\,\mathrm{M}_\odot$ are proposed as an explanation of several observations. However, there is no compelling evidence that IMBHs are present inside galaxies and SCs. The very high central velocity dispersion of the globular clusters M15 and G1 hints to the existence of a central IMBH [35, 36, 108]. Moreover, the high core rotation observed in the clusters M15, ω Cen, 47 Tuc, and G1 [35, 108, 109] might be explained by the existence of a core angular momentum source, such as an IMBH binary [71], and observations of a millisecond pulsar in the halo of NGC 6752 might suggest the presence of an IMBH binary in the core [19]. But these phenomena can be explained without resorting to a central IMBH: for example also a collection of compact stellar remnants in the core may explain the observations of these clusters [9].

Super Massive Black Holes (SMBHs) with a mass in the range $10^5 - 10^9\,\mathrm{M}_\odot$ are present in the centre of many galaxies. SMBHs with mass $M_{\mathrm{smbh}} \sim 10^9\,\mathrm{M}_\odot$ have been observed at redshifts $z > 6$ [8, 113]. It is very unlikely that such massive objects formed directly from primordial gas; instead, it is quite possible that they formed as much smaller BH "seeds", and then got most of their mass through accretion. However, if the accretion was Eddington-limited, the seed mass must be much more massive ($M_{\mathrm{seed}} > 1000\,\mathrm{M}_\odot$) than a stellar-mass BH ($M_{\mathrm{sbh}} < 100\,\mathrm{M}_\odot$).

Several different channels have been proposed in order to explain the formation of SMBH seeds ($\sim 10^5\,M_\odot$) (see Chapter 4 Sec. 4.1). One of them is the possibility that a massive and dense SC undergoes core collapse, producing a massive central BH through mergers of compact objects thanks to the aid of a large gas infall [21]. This process could lead to the formation of seeds as massive as $10^5\,M_\odot$ in a short time scale.

In the first part of this thesis we investigate in a quantitative fashion the SMBH seed formation channel proposed by [21] (see Chapter 4): by means of the `MYSCE` (Montecarlo Young Star Cluster Evolution) code – a new Monte Carlo code developed by us (see Chapter 2) – we estimate gas infall consequences: SC Lagrangian radii contraction, cluster star velocity dispersion evolution, and fate of the primordial binaries, in order to understand if conditions for star/stellar BH runaway merger can be reached in a realistic environment.

We study also if a gas infall can help the formation of an IMBH in a young star cluster via the collapse of a very massive star produced by the runaway merger of main-sequence stars [26, 43, 44, 83, 85]. Other ways to produce IMBHs are discussed in the literature and they are sketched in Chapter 4 Sec. 4.1.

Among the numerical methods (see Chapter 2 Sec. 2.1) used to simulate SCs we select a Monte Carlo method since it is faster than a N-body method and allows therefore to study a higher number of stars. Furthermore, the Monte Carlo method guaranties a high accuracy when treating energy exchanges by two- and three-body interactions which is similar to the one of a N-body method and better than the one of a pure statistical method. In addition, the MC scheme can be easily modified in order to introduce other physical processes such as stellar evolution and its metallicity dependence. In particular, the code `MYSCE` (see Chapter 2) is a modified version of the Hénon Monte Carlo scheme [49, 50]. We choose this scheme since it drastically reduces the computational burden not requiring orbit integration and because it uses time steps which are fractions of the relaxation time instead of fractions of the crossing time. The algorithms used in `MYSCE` differ from the original ones by Hénon in four main aspects: the code treats each particle in the simulation as a real star, reduces the duration of the time step, describes in more details three-body interactions, and solves the spurious relaxation problem.

Plan of the first part of the thesis

The plan of the first part of the thesis is as follows: in Chapter 1 we describe the SCs, their mathematical model and the physical processes driving their evolution; in Chapter 2 we present an overview of numerical methods used to simulate SCs and we describe the

modified version of the Hénon MC method used in the code `MYSCE`, which we developed as part of this thesis; in Chapter 3 we account for SC initial conditions; in Chapter 4 we first sketch different mechanisms to produce IMBHs and SMBH seeds present in the literature, then we describe the consequences of gas infall on a SC when all other physical interactions are turned off and we finally add two- and three-body interactions to study binary evolution and the fate of the SC; in Appendix A we present our solution to the spurious relaxation problem.

The material discussed in the first part of this thesis is reported also in the following publications:

- [dyn1] Galanti, G., & Ripamonti, E., *"An improved treatment of spurious relaxation in the Monte Carlo method"*, paper submitted to New Astronomy (2013)
- [dyn2] Galanti, G., Colpi, M., Lupi, A., Ripamonti, E., & Mapelli, M., *"Consequences of gas infall inside star clusters"*, paper in preparation (2013)
- [dyn3] Lupi, A., Colpi, M., Devecchi, B., Galanti, G., & Volonteri, M., *"Constraining the high redshift formation of black hole seeds in nuclear star clusters with gas inflows"*, paper in preparation (2013)

In particular, [dyn1] deals with the topic of Appendix A, [dyn2] treats the matter developed in Chapters 2, 3 and 4, and [dyn3] discusses part of the subject of Chapter 4.

Chapter 1

Star clusters

A star cluster (SC) is a self-gravitating system (see Sec. 1.1) of stars of coeval formation. It is formed by a number of stars that can vary from tens to millions and it is often roughly spherical. SCs are commonly classified into three types: globular clusters, open clusters and young star clusters.

- *Globular clusters* (GCs) – GCs are spherical collections of $10^4 - 10^6$ stars (Fig. 1.1 shows an example); they are gas poor and have very high central densities ($10^5 - 10^6\,\mathrm{stars}\cdot\mathrm{pc}^{-3}$). They are old evolved systems (often $\sim 10\,\mathrm{Gyr}$) constituted by Population II stars with masses lower than $1 - 2\,\mathrm{M}_\odot$ and have low metallicities [46]. Such stars predominate because hotter and more massive stars have evolved, becoming white dwarfs, neutron stars or black holes. GCs are highly gravitationally bound systems so that GCs can survive for many billions of years: their self-gravity dominates on tidal effects due to their host galaxies. GCs are found in the galactic haloes with a roughly spherical distribution. The Milky Way counts about 150 GCs [46] but other galaxies can contain over a thousand [7]. GCs orbit the Milky Way mainly around $\sim 2 - 20\,\mathrm{kpc}$ from the centre [46].

- *Open clusters* (OCs) – OCs are formed by less than 10^4 stars, are less dense ($< 10^4\,\mathrm{stars}\cdot\mathrm{pc}^{-3}$), present a more irregular shape, and may be gas rich (Fig. 1.2 shows an example of OCs). OCs are only weakly bound and generally survive for a few hundred million years (because of the tidal field of their host galaxy) and can be disrupted by encounters with other clusters. They are generally quite young objects ($\sim 10^8\,\mathrm{yr}$) and are constituted by Population I stars with a rather broad range of masses and metallicities. In the Milky Way, OCs are located in the galactic plane; in general, they are mainly found within the arms of spiral galaxies.

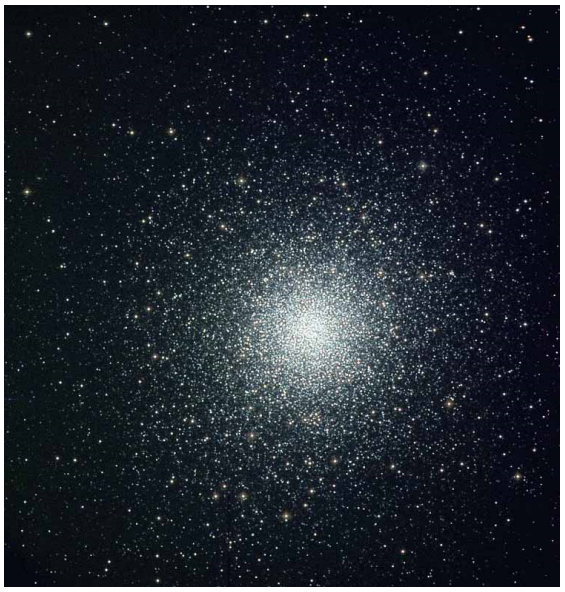

FIGURE 1.1: The GC Messier 92 in the Hercules constellation.

FIGURE 1.2: The Pleiades, an example of OC.

- *Young star clusters* (YSCs) – The observations of YSCs are quite recent [18, 20, 32]. They are very young ($\sim 10^7$ yr) systems constituted by $10^3 - 10^5$ stars (Fig. 1.3 shows an example). They are formed by Population I young stars with a very broad mass range ($0.2 - 120\,M_\odot$). They have very high central densities similar to GCs; but in contrast with GCs they may be gas rich, and are a disk population in galaxies – like OCs. Like GCs, YSCs are rather gravitationally bound systems. Some speculations suggest YSCs to be similar to the progenitors of GCs even if they are not massive enough to become the GCs observable today. Because of their young age, broad mass range, and high densities YSCs are extremely important laboratories to study early stages of SC dynamics, and to observe processes such as two- and three-body relaxation, mass segregation, and core collapse.

FIGURE 1.3: The YSC R136 in the 30 Doradus region of the Large Magellanic Cloud.

1.1 Self-gravitating systems

SCs (mainly GCs and YSCs, because OCs are only weakly bound) can be described with a good approximation as self-gravitating systems. A self-gravitating system $\mathcal{S}$ of N elements is defined as an isolated system whose elements interact gravitationally (for a full description see for example [92]).

By calling m_α $(1 \leq \alpha \leq N)$ the mass of the α-th element of $\mathcal{S}$, with M its total mass and with $m \equiv M/N$ the average mass of the elements of $\mathcal{S}$ the potential energy U of $\mathcal{S}$ reads

$$U = -\frac{G}{2} \sum_{\alpha=1}^{N} \sum_{\beta \neq \alpha}^{N} \frac{m_\alpha m_\beta}{|\mathbf{x}_\alpha - \mathbf{x}_\beta|} \ , \tag{1.1}$$

while the escape velocity $v_{\mathrm{f},\alpha}$ of the α-th element is

$$v_{\mathrm{f},\alpha}^2 = 2G \sum_{\beta \neq \alpha}^{N} \frac{m_\beta}{|\mathbf{x}_\alpha - \mathbf{x}_\beta|} \ , \tag{1.2}$$

where G is the gravitational constant, and $\mathbf{x}_\alpha$ and $\mathbf{x}_\beta$ are the positions of the α-th and β-th element, respectively.

The dynamics of $\mathcal{S}$ is ruled by two time scales.

- *Crossing time* t_{cross} – The crossing time (also called dynamical time) is defined as the time that a generic element of $\mathcal{S}$ needs to cross the system. By calling d the

linear size of $\mathcal{S}$, and v the typical velocity of an element of $\mathcal{S}$ $t_{\rm cross}$ reads

$$t_{\rm cross} \simeq \frac{d}{v} \ . \tag{1.3}$$

Starting from a particular initial condition $\mathcal{S}$ usually gets a stationary condition after a few $t_{\rm cross}$.

- *Relaxation time* $t_{\rm rel}$ – It is defined as the time that a generic element of $\mathcal{S}$ needs to lose memory of its own initial condition. $t_{\rm rel}$ is linked to $t_{\rm cross}$ by (more about this in Sec. 1.3.1)

$$t_{\rm rel} \simeq 0.1 \left(\frac{N}{\ln N} \right) t_{\rm cross} \ , \tag{1.4}$$

and when $N \gtrsim 100$ (i.e. for all but the smallest SCs) we get

$$t_{\rm rel} \gg t_{\rm cross} \ . \tag{1.5}$$

System relaxation is driven by gravitational encounters (two-body interactions) among the elements of $\mathcal{S}$ (see Sec. 1.3 for more details). The physical meaning of $t_{\rm rel}$ can be understood also by considering that a system is *relaxed* when the velocity variation experienced by each element of $\mathcal{S}$ during the whole history of the SC is, on average, of the order of the velocity of an element of $\mathcal{S}$.

When $\mathcal{S}$ is in a stationary condition the *virial theorem* subsists

$$2K + U = 0 \ , \tag{1.6}$$

where $K = M\langle v^2 \rangle / 2 = \frac{3}{2} k_{\rm B} T$ is the kinetic energy of $\mathcal{S}$ [1], $\langle v^2 \rangle$ is the mean square velocity of an element of $\mathcal{S}$, T is the average kinetic temperature of $\mathcal{S}$, and $k_{\rm B}$ is the Boltzmann constant.

If $\mathcal{S}$ is in *virial equilibrium* its energy

$$E \equiv K + U \ , \tag{1.7}$$

can be written by using Eq. (1.6) as

$$E = -K = \frac{U}{2} \ . \tag{1.8}$$

Eq. (1.8) shows that the formation of a bound system from a condition in which all the elements of $\mathcal{S}$ were initially at rest at infinity, implies a release of kinetic energy by an

[1] If $\mathcal{S}$ is in motion with respect to the observer – as usually happens – $\langle v^2 \rangle$ must be substituted by the tridimensional dispersion velocity $\sigma^2 \equiv \langle v^2 \rangle - \langle v \rangle^2$

amount equal to half of the gravitational energy of the new equilibrium configuration. This implies that some of the elements evaporate at the time of system formation.

By remembering the meaning of K and using Eqs. (1.1) and (1.8) the mean square velocity $\langle v^2 \rangle$ reads

$$\langle v^2 \rangle = \frac{G}{2M} \sum_{\alpha=1}^{N} \sum_{\beta \neq \alpha}^{N} \frac{m_\alpha m_\beta}{|\mathbf{x}_\alpha - \mathbf{x}_\beta|} \ . \tag{1.9}$$

By defining the mean square escape velocity $\langle v_{\rm f}^2 \rangle$ as

$$\langle v_{\rm f}^2 \rangle = \frac{1}{M} \sum_{\alpha=1}^{N} m_\alpha v_{{\rm f},\alpha}^2 \ , \tag{1.10}$$

Eq. (1.2) implies

$$\langle v_{\rm f}^2 \rangle = \frac{2G}{M} \sum_{\alpha=1}^{N} \sum_{\beta \neq \alpha}^{N} \frac{m_\alpha m_\beta}{|\mathbf{x}_\alpha - \mathbf{x}_\beta|} \ . \tag{1.11}$$

So, in the presence of the virial equilibrium we get

$$\langle v_{\rm f}^2 \rangle = 4 \langle v^2 \rangle \ . \tag{1.12}$$

The physical meaning of this relation is quite clear: at the virial equilibrium $\langle v_{\rm f}^2 \rangle = 4\langle v^2 \rangle$. If $\langle v_{\rm f}^2 \rangle \ll \langle v^2 \rangle$, $\mathcal{S}$ would evaporate, while in the opposite case, if $\langle v_{\rm f}^2 \rangle \gg \langle v^2 \rangle$, $\mathcal{S}$ would collapse – and both these processes would happen in about $t_{\rm cross}$, hence the virial equilibrium would be impossible over this time scale.

From the virial theorem we can also infer the termodynamic behaviour of $\mathcal{S}$. By using Eq. (1.8) and remembering the thermodynamic meaning of K we get

$$E = -\frac{3}{2} N k_{\rm B} T \ . \tag{1.13}$$

The sign of Eq. (1.13) implies that $\mathcal{S}$ has a *negative thermal capacity*: a decrease of the total energy ($\Delta E < 0$) warms the system ($\Delta T > 0$), while an increase of the total energy ($\Delta E > 0$) cools $\mathcal{S}$ ($\Delta T < 0$).

Eq. (1.13) predicts the *evaporation* of $\mathcal{S}$ in a finite time. In fact, Eq. (1.12) implies that the quickest elements of $\mathcal{S}$ have velocities higher than the escape velocity so that they can leave the system. As a consequence, the total energy of $\mathcal{S}$ decreases. Because of the negative thermal capacity the average velocity of the survived elements of $\mathcal{S}$ increases. This fact amplifies the evaporation process. It is possible to get that the *evaporation time* of $\mathcal{S}$ is of the order of

$$t_{\rm ev} \simeq 10^2 \, t_{\rm rel} \ . \tag{1.14}$$

In the usual case where $N \gg 1$, we can use Eq. (1.5) to infer that $t_{\rm ev} \gg t_{\rm cross}$. Therefore, the virial equilibrium exists over multiples of $t_{\rm cross}$ but cannot persist for an infinite time.

When $t_{\rm rel} \gg t_{\rm ev}$ $\mathcal{S}$ is called *collisionless* system: in this case, the interaction rate among the elements of $\mathcal{S}$ is so low that the system cannot relax before its evaporation. When $t_{\rm rel} \ll t_{\rm ev}$ $\mathcal{S}$ is called *collisional* system: in this case, two-body interactions drive the system to relaxation before its evaporation. Collisional systems experience several dynamical processes such as mass segregation, core collapse, etc. (see Sec. 1.3 for more details). Among the collisional systems important examples are given by SCs, while galaxies are examples of collisionless systems.

1.2 Star cluster models

It is a matter of fact that it is impossible to follow the evolution of all the elements inside a system composed by many body: a statistical approach is necessary – discrete distribution functions are substituted with their smooth counterparts. In this fashion, the kinetic description of a self-gravitating system $\mathcal{S}$ is based on the distribution function of single particle (star) $f(\mathbf{x}, \mathbf{v}, t)$ which satisfies the Boltzmann equation

$$\frac{\partial f}{\partial t} + v_i \frac{\partial f}{\partial x_i} + a_i \frac{\partial f}{\partial v_i} = \Gamma[f] \ , \tag{1.15}$$

where $\mathbf{x}$, $\mathbf{v}$, and $\mathbf{a}$ are the position, velocity, and acceleration of an element of $\mathcal{S}$ and $\Gamma[f]$ is the *collisional term*, which represents the variation of f due to elastic collisions among elements of $\mathcal{S}$.

A particle (star) of $\mathcal{S}$ moves in a conservative force field and it is also subject to impulsive forces due to the *granularity* of matter which give birth to collisions. Both these categories of forces have a gravitational origin so that we must divide the gravitational field exerted on an element of $\mathcal{S}$ into two components.

- A *mean*, *smooth* field (with a potential $\Phi(\mathbf{x}, t)$) generated by a continuous distribution of matter $\rho(\mathbf{x}, t)$ which represents the average effect of all other elements of $\mathcal{S}$.
- A rapidly *fluctuating* field (both in space and time) that takes into account the gravitational (two- and three-body) encounters among the elements of $\mathcal{S}$.

$\Phi(\mathbf{x}, t)$ satisfies the Poisson equation

$$\Delta\Phi = 4\pi G\rho \ . \tag{1.16}$$

As a result, Eq. (1.15) becomes

$$\frac{\partial f}{\partial t} + v_i \frac{\partial f}{\partial x_i} - \frac{\partial \Phi}{\partial x_i}\frac{\partial f}{\partial v_i} = \Gamma[f] \ , \tag{1.17}$$

where $\Gamma[f]$ results from the fluctuating field. The source of the main field is given by the constituents of $\mathcal{S}$ such that the density in the Poisson equation reads

$$\rho(\mathbf{x}, t) = m \int d^3\mathbf{v}\, f(\mathbf{x}, \mathbf{v}, t) \ , \tag{1.18}$$

where m is is the average mass of an element of $\mathcal{S}$. As a result, the Boltzmann equation is non linear and coupled with the Poisson equation. The ultimate goal is to find the solutions f of the system of equations

$$\frac{\partial f}{\partial t} + v_i \frac{\partial f}{\partial x_i} - \frac{\partial \Phi}{\partial x_i}\frac{\partial f}{\partial v_i} = \Gamma[f] \ , \tag{1.19}$$

$$\Delta\Phi = 4\pi m G \int d^3\mathbf{v}\, f \ . \tag{1.20}$$

In order to simulate SCs we want to get its initial configuration. In order to get this goal we neglect the collisional term in the Bolzmann equation (1.19) and since we want to study *stationary* SC models where the distribution function f and the mean potential Φ are time-independent the system of Eqs. (1.19) and (1.20) becomes

$$v_i \frac{\partial f}{\partial x_i} - \frac{\partial \Phi}{\partial x_i}\frac{\partial f}{\partial v_i} = 0 \ , \tag{1.21}$$

$$\Delta\Phi = 4\pi m G \int d^3\mathbf{v}\, f \ , \tag{1.22}$$

where Eq. (1.21) is called stationary Vlasov equation.

We can build *stationary* distribution functions by means of the *Jeans theorem* according to which *each stationary distribution function is an integral of motion in the potential* Φ *and vice versa*. As a consequence,

- each stationary solution of the Vlasov equation depends on $\mathbf{x}$, $\mathbf{v}$ *only* through the independent integrals of motion in the potential Φ
- each function of the independent integrals of motion is a stationary solution of the Vlasov equation

Now, with the results of the Jeans theorem in mind in order to build a stationary SC model we can proceed as follows: first we formally solve Eq. (1.21) by expressing $f(\mathbf{x}, \mathbf{v})$ as functions of the independent integrals of motion. In this way it is possible to decouple

Eqs. (1.21) and (1.22) and then we can solve Eq. (1.22) and get the distribution function f.

We restrict ourselves to the case of complete spherical symmetry (spherical symmetry in the phase space). In this case, the potential is function only of the radial distance. Since the spherical symmetry is complete f is function only of the energy E of a test star and of the norm of its angular momentum L (i.e. $f = f(E, L^2)$).

A particularly important case is when the distribution function depends only on the energy (i.e. $f = f(E)$). In this case, we have

$$E = \frac{1}{2}v^2 + \Phi(r) \ , \tag{1.23}$$

where we remind that we take the mass of a generic star m to be unity. By considering Eq. (1.23), Eq. (1.21) is identically satisfied, and by expressing the laplacian in spherical coordinates and using Eq. (1.23) we can rewrite Eq. (1.22) as

$$\frac{1}{r^2}\frac{d}{dr}\left(r^2\frac{d\Phi}{dr}\right) = 16\pi^2 G\int_0^\infty dv\, v^2 f\left(\frac{1}{2}v^2 + \Phi\right) \ . \tag{1.24}$$

It is useful to introduce the *relative potential*

$$\Psi(r) \equiv \Phi_0 - \Phi(r) \ , \tag{1.25}$$

and the *relative energy*

$$\mathcal{E} \equiv \Phi_0 - E \tag{1.26}$$

of a test star. As a result, from Eqs. (1.25) and (1.26)

$$\mathcal{E} = \Psi(r) - \frac{1}{2}v^2 \ . \tag{1.27}$$

We choose Φ_0 such that $f > 0$ for $\mathcal{E} > 0$ and $f = 0$ for $\mathcal{E} \leq 0$: correspondingly, the Poisson equation (1.24) results

$$\frac{1}{r^2}\frac{d}{dr}\left(r^2\frac{d\Psi}{dr}\right) = -16\pi^2 G\int_0^{\sqrt{2\Psi}} dv\, v^2 f\left(\Psi - \frac{1}{2}v^2\right) \ , \tag{1.28}$$

where $f = f(\mathcal{E})$ and $\mathcal{E} = \Psi - \frac{1}{2}v^2$, as in Eq. (1.27).

We consider three models

- *Polytropic models* – They are defined by the distribution function

$$f(\mathcal{E}) = \begin{cases} F\mathcal{E}^{n-3/2}, & \mathcal{E} > 0 \\ 0, & \mathcal{E} \leq 0 \end{cases} , \tag{1.29}$$

where F is an arbitrary constant and n is called polytropic index. Polytropes are self-gravitating gaseous spheres that are a useful approximation to realistic stellar models or star distributions in SCs or galaxies. There is a polytropic relation between pressure P and density ρ

$$P = F\rho^{1+\frac{1}{n}} , \tag{1.30}$$

where F is a positive constant. The case $n = 5$ corresponds to the Plummer model [88] which is often used to model SCs. In the case $n \to \infty$, the polytrope tends to the isothermal sphere. We can observe that as the polytropic index increases, the central density becomes higher and higher.

As mentioned above, the polytrope with $n = 5$ is called Plummer model. It is characterized by the potential

$$\Phi(r) = -\frac{GM}{\sqrt{r^2 + a^2}} , \tag{1.31}$$

where a is the Plummer scale radius that defines the extension of the core and which approximately contains the 35% of the total mass M of the SC. The corresponding density distribution is

$$\rho(r) = \frac{3M}{4\pi a^3}\left(1 + \frac{r^2}{a^2}\right)^{-5/2} , \tag{1.32}$$

and its velocity dispersion reads

$$\sigma^2(r) = \frac{63\pi}{256}\frac{GM}{\sqrt{r^2 + a^2}} . \tag{1.33}$$

Plummer represents one of the most widely used models to describe SCs both for its accuracy, and for its simplicity, since potential, density profile, and velocity dispersion have an analytical form.

- *Isothermal sphere* – This model is defined by the distribution function

$$f(\mathcal{E}) = \frac{\rho_0}{(2\pi\sigma^2)^{3/2}} e^{\mathcal{E}/\sigma^2} , \tag{1.34}$$

where ρ_0 is an arbitrary constant and σ is the velocity dispersion. We can understand why this model is called isothermal sphere by comparing it with an

isothermal gas. By combining the condition of hydrostatic equilibrium for a self-gravitating sphere and the equation of state for an ideal gas applied to an isothermal sphere of gas we obtain an equation that is structurally identical to Eq. (1.28) in which f is given by Eq. (1.34). The two equations overlap if

$$\sigma^2 \equiv \frac{k_{\rm B}T}{m_{\rm g}} \ , \tag{1.35}$$

where $m_{\rm g}$ is the mass of a gas particle and T is the gas temperature. This shows that a self-gravitating isothermal sphere of gas is identical to a collisionless system of stars described by the distribution function (1.34). As a result, the star velocity distribution overlaps the maxwellian velocity distribution of a gas at the constant temperature T.

The density distribution of the isothermal sphere is

$$\rho(r) = \frac{\sigma^2}{2\pi G r^2} \ , \tag{1.36}$$

while its corresponding potential reads

$$\Phi(r) = 2\sigma^2 \ln(Fr) \ , \tag{1.37}$$

where F is an arbitrary constant.

Without invoking particular boundary conditions (more about this further) the isothermal sphere however presents two physical inconsistencies: from Eq. (1.36) we observe that the central density ($\rho(r = 0)$) diverges to infinity and if we integrate Eq. (1.36) the corresponding mass profile diverges at infinity ($r \to \infty$). These issues are solved in the King model.

- *King model* – The King model [59] is defined by the distribution function

$$f(\mathcal{E}) = \begin{cases} \frac{\rho_0}{(2\pi\sigma^2)^{3/2}}(e^{\mathcal{E}/\sigma^2} - 1), & \mathcal{E} > 0 \\ 0, & \mathcal{E} \leq 0 \end{cases} \ , \tag{1.38}$$

where ρ_0 is an arbitrary constant and σ is the dispersion velocity. The King model eliminates the unphysical properties of the isothermal sphere. The King radius or core radius

$$r_{\rm c} = \sqrt{\frac{3\sigma^2}{4\pi G \rho_0}} \ , \tag{1.39}$$

is used to get a finite density for $r \to 0$, while the tidal radius $r_{\rm t}$ is introduced to avoid the mass divergence at infinity. $r_{\rm t}$ can be considered as the distance (from the centre of the SC) where tidal effects due to the host galaxy are comparable to

the SC self gravity. Therefore, r_t defines the boundary of the SC. The region within r_c is called core, it is approximately isothermal and has a rather constant density, while the region between r_c and r_t is called halo, it has a lower density than the core and is not isothermal as the velocity dispersion decreases to zero at r_t. Different King models exist in dependence of the value of the concentration parameter $c \equiv \log_{10}(r_\mathrm{t}/r_\mathrm{c})$. c is usually in the range $0.3 - 3.3$, the case $c \to \infty$ corresponds to the isothermal sphere. The King model is a very good approximation of the star distribution in SCs.

What we called isothermal sphere is also known as *singular* isothermal sphere since its density diverges for $r \to 0$. As we have seen, a way to overcome this issue is to consider the King model. For completeness, another solution has been proposed: the *soft* isothermal sphere whose density profile is

$$\rho(r) = \frac{\sigma^2}{2\pi G}\frac{1}{a^2 + r^2} \ , \tag{1.40}$$

where a is called nuclear radius. It is evident that in the case $r \gg a$ the soft isothermal sphere reduces to the singular isothermal sphere. The importance of the isothermal sphere is not confined to the description of the star distribution inside SCs or inside galaxies: in fact observations show that dark matter haloes surrounding both singular galaxies and galaxy clusters are well described by a singular isothermal sphere, at least at high distances from the centre. Dark matter haloes are however commonly described by the profile [79].

1.3 Star cluster dynamics

As we mentioned in Sec. 1.1 SCs are self-gravitating collisional systems. In fact their relaxation time is shorter than their life time. As a result two-body interactions between elements of the SC are efficient to erase the memory of the initial conditions of the system – i.e. they are efficient to relax it. Two-body interactions (see Sec. 1.3.1) are long-range exchanges of energy between distant particles that interact gravitationally. The result of this process is a redistribution of the energy inside the SC. As a consequence, the SC experiments two phases: the core-collapse phase (see Sec. 1.3.2) and the post core-collapse phase (see Sec. 1.3.5). In this scenario also impulsive three-body encounters (between binaries and single stars) (see Sec. 1.3.3) play an important role: they may slow down or even revert the core collapse depending on their strength.

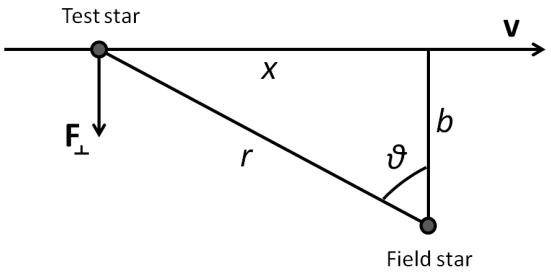

FIGURE 1.4: Picture of a two-body encounter. A test star approaches the field star at velocity v and impact parameter b. The velocity is perturbed only by the component of the gravitational force $F_\perp$ perpendicular to v.

1.3.1 Two-body interactions

We consider a SC with homogeneous density, a characteristic radius R and composed of N identical stars with mass m. We study the evolution of the velocity of a test star during one system crossing [13].

We suppose that the test star passes with a velocity $\mathbf{v}$ at the minimal distance b (impact parameter) (see Fig. 1.4) from a field star. $\mathbf{v}$ is deflected by $\delta\mathbf{v}$ because of the encounter and the amount of the deflection depends on b, and on the masses of the stars, and on their velocities. Without loss of generality, we assume that the field star is stationary during the encounter and that the encounter produces a small perturbation on the velocity of the test star: that is, $||\delta\mathbf{v}||/v \ll 1$, where $v \equiv ||\mathbf{v}||$. We assume that the test star passes the field star on a straight-line trajectory. $\mathbf{v}$ is perturbed only by $\delta\mathbf{v}_\perp$, the component of $\delta\mathbf{v}$, perpendicular to $\mathbf{v}$.

If we define the istant $t = 0$ to be coincident with the closest approach of the two stars, the perpendicular force $\mathbf{F}_\perp$ – origin of $\delta\mathbf{v}_\perp$ – reads

$$F_\perp = \frac{Gm^2}{b^2+x^2}\cos\theta = \frac{Gm^2 b}{(b^2+x^2)^{3/2}} \simeq \frac{Gm^2}{b^2}\left[1+\left(\frac{vt}{b}\right)^2\right]^{-3/2} , \tag{1.41}$$

where x is the (signed) distance of the test star from its position at closest approach with the field star (see Fig. 1.4). By substituting the Newton's laws $d/dt(m\mathbf{v}_\perp) = \mathbf{F}_\perp$ into Eq. (1.41) and integrating with respect to time we get

$$\delta v_\perp \equiv ||\delta\mathbf{v}_\perp|| \simeq \frac{Gm}{b^2}\int_{-\infty}^{\infty}\left[1+\left(\frac{vt}{b}\right)^2\right]^{-3/2} dt = \frac{2Gm}{bv} . \tag{1.42}$$

Remembering that the surface density of stars in the SC is of the order $N/\pi R^2$, we can estimate the number δn of encounters with impact parameter between b and $b+db$ that

a test star suffers in one SC crossing as

$$\delta n = \frac{2N}{R^2} b\, db \ . \tag{1.43}$$

Since perturbations $\mathbf{v}_\perp$ to test star velocity are randomly distributed around $\mathbf{v}$, the mean value $\langle \mathbf{v}_\perp \rangle = 0$. We can instead calculate the variation $\delta v^2_{\perp,\mathrm{b}}$ in one crossing on the square of the perpendicular component of $\mathbf{v}$ (caused by encounters with impact parameters between b and $b + db$) by approximating it using Eqs. (1.42) and (1.43) as

$$\delta v^2_{\perp,\mathrm{b}} \simeq \delta v^2_\perp \, \delta n = \left(\frac{2Gm}{bv} \right)^2 \frac{2N}{R^2} b\, db \ . \tag{1.44}$$

By integrating Eq. (1.44) over all impact parameters in the range $b_{\min} - b_{\max}$ we get the total variation $\Delta v^2_\perp$

$$\Delta v^2_\perp \equiv \int_{b_{\min}}^{b_{\max}} \delta v^2_{\perp,\mathrm{b}} \simeq 8N \left(\frac{Gm}{Rv} \right)^2 \ln \Lambda \ , \tag{1.45}$$

where

$$\ln \Lambda \equiv \ln \left(\frac{b_{\max}}{b_{\min}} \right) \tag{1.46}$$

is called Coulomb logarithm. We can estimate $b_{\min}$ as the impact parameter at which the perturbation approach is not valid anymore, i.e. when $\delta v \sim v$: correspondingly $b_{\min} = 2Gm/v^2$, while $b_{\max}$ can be assumed of the order of R. If we assume that the system is in virial equilibrium we can use Eq. (1.8) so that we can write

$$v^2 \simeq \langle v^2 \rangle = \frac{GNm}{R} \ , \tag{1.47}$$

where $v^2 \simeq \langle v^2 \rangle$ is justified since the typical velocity of a star in a SC is similar to the mean square velocity. Now, by combining Eq. (1.45) with Eq. (1.47) we get

$$\frac{\Delta v^2_\perp}{v^2} = \frac{8 \ln \Lambda}{N} \simeq \frac{8 \ln N}{N} \ , \tag{1.48}$$

where the second relation derives from the definition of the Coulomb logarithm and from Eq. (1.47). We remember that the relaxation time is the time in which an (average) element of the system undergoes a total velocity variation of the order of its velocity. In each SC crossing $v^2_\perp$ changes of $\sim \Delta v^2_\perp$; so, in order to have $\Delta v^2_\perp / v^2 \simeq 1$ we need a number of crossing

$$n_{\mathrm{rel}} = \frac{N}{8 \ln N} \ . \tag{1.49}$$

We can now justify the expression of the relaxation time of Eq. (1.4). In fact, by remembering that t_{cross} is the time necessary for a star to cross the system (see Eq.

(1.3)) the relaxation time reads

$$t_{\rm rel} = n_{\rm rel}\, t_{\rm cross} = \left(\frac{N}{8\ln N}\right) t_{\rm cross} \ , \tag{1.50}$$

where we have used Eq. (1.49). In conclusion, we infer that a star is significantly perturbed only after many crossing times. If we consider time scales of the order of the crossing time, the system can be considered in a quasi-stationary state. Furthermore, on such time scales it is perfectly legitimate to consider that the system is ruled by the mean potential, with (two-body) interactions playing a negligible role. Only after many crossing times interactions become important and as a consequence, the system changes its initial configuration, suffers an energy redistribution and loses memory of its initial condition. Obviously, only systems with a life time (evaporation time) higher than $t_{\rm rel}$ (for example SCs) may relax: in fact, in the opposite case (for example in galaxies, where $t_{\rm rel}$ is higher than the age of the Universe), the system evolves so slowly that evaporates before interactions may perturb it and may change its initial condition. Eq. (1.50) gives a general idea about the order of magnitude of the global relaxation time of a system; but the different parts of the system – we can think to the SC core with respect to the halo – evolve with different rates (in particular the SC core evolves faster than the rest of the SC). In order to account for this fact it is useful to introduce a local relaxation time [103]

$$t_{\rm rel} \sim 0.3 \frac{\sigma^3}{G^2 \langle m \rangle \rho \ln \Lambda} \ , \tag{1.51}$$

where σ is the local velocity dispersion, $\langle m \rangle$ is the local average stellar mass, ρ is the local density, while the Coulomb logarithm reads

$$\ln \Lambda = \ln(\gamma N) \ , \tag{1.52}$$

where γ is a parameter whose value is either inferred by theoretical considerations or calculated numerically. For equal-mass systems $\gamma \sim 0.11$ [37] is generally higher – as argued in [51] – than for unequal mass systems where $\gamma \sim 0.021$ [39].

1.3.2 Core collapse

The core collapse is a phase in the life time of SCs when energy is redistributed. In particular, some stars fall down towards the centre losing kinetic energy, while some others leave the centre. The core becomes denser and denser, while the halo widens to such an extent that core and halo become two almost separate systems (see Fig. 1.5). These processes are due to the two-body interaction: in a heuristic vision what happens can be sketched as follows. During two-body interactions the stars that lose velocity

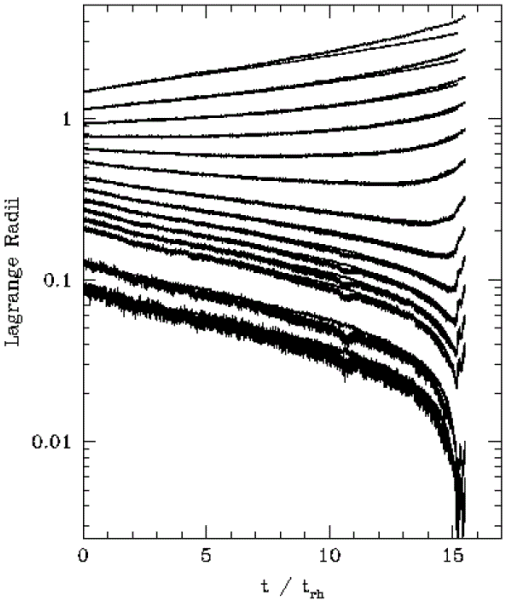

FIGURE 1.5: Typical behaviour of the Lagrangian radii when the SC approaches to the core collapse [91]. The inner Lagrangian radii shrink, while the outer Lagrangian radii widen.

tend to go towards the centre of the SC while stars that increase their velocity tend to depart from it. As the two-body interaction goes on, two different systems develop: one, the core, made by slower stars tend to become more bound, the other, the halo, made by faster stars becomes less bound and less dense. During this phase the core loses a great amount of stars which enrich the halo or even leave the SC if they have enough velocity to overcome the escape velocity. The system tends to develop an infinite central density, but, since SCs with infinite density have not been observed so far there should exist a process that inverts, stops or at least slows down the core collapse: three-body interactions (see Sec. 1.3.3) are a good candidate. After this qualitative description of the core collapse we want to be more precise and quantitative in describing which is the physical process responsible for the core collapse: the *gravothermal catastrophe*.

A SC is a self-gravitating system which reaches virial equilibrium soon after its birth. As a consequence Eqs. (1.6), (1.8) and (1.13) describe the system. The gravothermal instability is due to the negative heat capacity expressed by Eq. (1.13). In more details, two-body relaxation is responsible for a redistribution of energy among the stars of the SC. In this way, some stars get enough energy to escape from the core (or even the SC). This fact breaks the virial equilibrium and we get

$$2K + U < 0 \ , \tag{1.53}$$

since kinetic energy decreases more than the potential energy. In fact, escaped stars

are the fastest in the core and and take with them an amount of kinetic energy that is much larger than their potential energy. As a result, since potential energy is dominant over kinetic energy in the core, the immediate consequence of Eq. (1.53) is that the core contracts in order to get a new equilibrium state. But, as the core contracts it becomes hotter because of the negative heat capacity, therefore the dispersion velocity increases. In this way, other stars will get enough velocity to leave the core starting a runaway process. This runaway process is called gravothermal catastrophe. The asymptotic conclusion would be a core with infinite density and infinitesimal size and a scattered halo with almost unbound stars which separates its evolution from the rest of the SC. We will see in Sec. 1.3.3 that three-body interactions prevent the system from this extreme fate.

So far we have not imposed any condition on the mass spectrum of the SC: in fact, the process described is valid both for equal-mass and multi-mass systems. If the SC has a broad mass distribution, the result is an accelerated core collapse with respect to the case of a equal-mass system. The reason lies in the *equipartition theorem* of statistical mechanics that states that every system tends to a condition of equipartition of energy: stars tend to have the same kinetic energy. If we have a system with two populations of mass and velocity $(m_1, \langle v_1 \rangle)$ and $(m_2, \langle v_2 \rangle)$, the equipartition theorem assures that the system tends to condition

$$\frac{1}{2} m_1 \langle v_1^2 \rangle = \frac{1}{2} m_2 \langle v_2^2 \rangle \ . \tag{1.54}$$

If $m_1 > m_2$ then $\langle v_1 \rangle < \langle v_2 \rangle$, i.e. population 1 will be on average slower than population 2. In general, at energy equipartition more massive stars have lower average velocities than lighter ones.

It is quite possible that high and low-mass stars are born with similar velocities within a SC; but this implies that the average kinetic energy of high-mass stars is larger than that of low-mass stars, and equipartition will drive the system to a status where the two populations have the same average kinetic energy, so that high-mass stars will become slower than low-mass stars: the result is a *mass segregation*.

More massive stars becoming slower and slower tend to sink to the centre, while lighter stars becoming faster and faster tend to leave it. As a result, more massive stars in the core separate from the lighter ones in the halo. So the effect of the two-body encounters on the SC is magnified by the tendency of the system to get kinetic energy equipartition. In fact, the resulting mass segregation makes the loss of kinetic energy and increase of potential energy of the core more efficient. While for many SCs mass segregation forms dynamically through the above-mentioned process [3], some SCs with primordial mass segregation exist [14, 41, 98]. The segregation time (i.e. the characteristic time for the

mass segregation process) for a star of mass m_* reads [28]

$$t_{\rm seg}(m_*) = \frac{\langle m \rangle}{m_*} t_{\rm rel} \ , \tag{1.55}$$

with $\langle m \rangle$ the average stellar mass in the SC and $t_{\rm rel}$ the SC relaxation time.

We conclude this section giving an estimation of the core-collapse time $t_{\rm cc}$. It is related to the relaxation time $t_{\rm rel}$ – which is not surprising since core collapse is driven by two-body interactions responsible for SC relaxation. Several numerical simulations estimate $t_{\rm cc} \sim 15\, t_{\rm rel}$ for equal-mass systems (e.g. [100]). In the case of multi-mass systems, simulations have demonstrated that $t_{\rm cc}$ is lower than in the case of equal-mass SCs but they are not in complete agreement about the amount: anyway, typical estimates are in the range $t_{\rm cc} \sim\ 0.15 - 0.20\, t_{\rm rel}$ [2] [43, 85].

1.3.3 Three-body interactions

Binaries are of crucial importance for the evolution of a SC: in fact, the encounters between single and binary stars can tap the internal energy reservoir of the binaries, so that binaries act as a sort of source of energy, and might prevent the complete core collapse of the system, or at least slow down the process.

Binaries can originate from three mechanisms:

- *Gravitational collapse of a gas cloud* – This is the origin of the *primordial binaries*. These stars are already bound at the birth of the SC.
- *Three-body interactions between stars* – During a gravitational encounter among three stars with positive energy, one of them may increase its own kinetic energy to an extent that the final energy of the system constituted by the two others is negative. As a result, those two stars are bound in a binary.
- *Tidal capture between couples of stars* – This process happens when two stars pass very close to each other. The tidal interaction dissipates part of the relative kinetic energy of the two stars, and can lead to the formation of a binary.

From a dynamical point of view we can distinguish between *hard* and *soft* binaries. A hard binary is a binary whose binding energy $E_{\rm b}$ is greater than the average kinetic energy of a SC star $\langle E_{\rm k} \rangle$, i.e.

$$\frac{G m_1 m_2}{2a} \geq \frac{1}{2} \langle m \rangle \sigma^2 \ , \tag{1.56}$$

[2] It is discussed if $t_{\rm rel}$ must be calculated at the half-mass radius or at the core radius.

where m_1 and m_2 are the masses of the two stars forming the binary, a is their semi-major axis, $\langle m \rangle$ is the average star mass in the SC, and σ star velocity dispersion. A soft binary is instead a binary whose binding energy is less than the average star kinetic energy in the SC. It is useful to introduce also the ratio x between the binary binding energy E_b and the average star kinetic energy $\langle E_\mathrm{k} \rangle$

$$x = \frac{E_\mathrm{b}}{\langle E_\mathrm{k} \rangle} = \frac{G m_1 m_2}{a \langle m \rangle \sigma^2}. \tag{1.57}$$

As a result, a binary is considered hard if $x > 1$ and soft in the opposite case.

During three-body encounters there may be an energy exchange between the binary internal energy and the kinetic energy of the single star: part of the binary internal energy may be transformed into single star kinetic energy or vice versa [75]. In the former case the binary becomes more bound (harder) and the single star becomes faster, in the latter case the binary becomes less bound (softer) and the single star decreases its velocity.

The behaviour of binaries in three-body interaction can be effectively described by the Heggie's law [47]: *"hard binaries get harder, soft binaries get softer"*. The meaning of this sentence is quite clear: hard binaries tend to become more and more bound, they increase their bounding energy and decrease their semi-major axis, while soft binaries tend to become less and less bound, they decrease their bounding energy and increase their semi-major axis, until they become totally unbound. This behaviour must be considered in a statistical fashion: in any particular encounter a hard binary might widen and a soft binary might shrink.

The binary-single star cross section σ_coll can be defined as the area of the circle centred on the centre of mass of the binary, and with radius equal to the maximum impact parameter b_max for which the energy exchange is high enough [97]

$$\sigma_\mathrm{coll} = \pi b_\mathrm{max}^2 \ . \tag{1.58}$$

In the case where the gravitational focusing (the deflection of the trajectory of the single star as an effect of the gravitational attraction due to the binary) is important Eq. (1.58) becomes

$$\sigma_\mathrm{coll} = \pi a^2 \left(1 + \frac{2 G m_\mathrm{T}}{v_\mathrm{rel}^2 a} \right) , \tag{1.59}$$

where $m_\mathrm{T} = m_1 + m_2$ is the total mass of the binary and v_rel is the relative velocity between the single star and the binary. By calling n the stellar density we can define

the interaction time t_{2+1} between binary and single star as

$$t_{2+1} = \frac{1}{n\sigma_{\rm coll} v_{\rm rel}} \ . \tag{1.60}$$

After some mathematical manipulations and by using the virial theorem and Eq. (1.57) t_{2+1} reads

$$t_{2+1} \simeq 0.02 \frac{G M_c^2 m_3}{m_{\rm T}^2 v_{\rm rel}^3} \frac{x^2}{1+2x} \ , \tag{1.61}$$

where $M_{\rm c}$ is the mass of the SC and m_3 is the mass of the single star interacting with the binary.

The results of single star-binary interaction can be classified as [97]:

- *Flyby* – The final state is similar to the initial state but with energy exchange.
- *Exchange* – The single star becomes part of the binary, while one of the initial components of the binary becomes a single star.
- *Ionization* – The binary is destroyed and the final state is made up of three single stars.
- *Merger* – Two of the three stars merge in a new star and the third star may remain bound into a binary or not.
- *Triple system* – In the final state all the three stars are bound in a triple system. Anyway this kind of system is unstable [16]: one of the stars leaves the system within a few crossing times.

The average energy exchange in a single scattering is proportional to the mass of the single star and inversely proportional to the total mass of the binary [52, 90]

$$\frac{\Delta E_{\rm b}}{E_{\rm b}} \propto \frac{m_3}{m_1 + m_2} \ , \tag{1.62}$$

where $E_{\rm b}$ is the binary binding energy and m_3 is the mass of the single star.

If a SC has a significant fraction of hard binaries, these latter represent a energy reservoir to support the cluster from a complete core collapse. In particular, when the core shrinks, its density grows and the rate of three-body encounters increases. As a result, the total energy due to three-body encounters can overcome the potential energy of the core: in this case, the collapse stops and the core re-expands. This phase is called *core bounce* [33].

1.3.4 Effects of stellar evolution

Stellar evolution produces a mass loss in the SC. In fact, massive stars ($> 20\,M_\odot$) suffer strong stellar winds which gradually decrease their mass. Furthermore, supernova explosions are impulsive processes: they partially or totally destroy massive stars as nuclear reactions are unable to prevent their collapse. This mass loss influences SC evolution since it decreases the gravitational energy of the core, where for the segregation process more massive stars are more frequently located (see Sec. 1.3.2). This fact breaks the virial equilibrium and we get

$$2K + U > 0 \; . \tag{1.63}$$

As an effect, the core widens and the velocity dispersion decreases. In this way, the relaxation time increases and the core collapse is slowed down [4, 5, 58]. The result of star evolution on the SC is therefore qualitatively similar to the three-body interactions even if the causes are different. In three-body interactions the total energy due to interactions can overcome the potential energy of the core which tends to expand in order to get a new equilibrium, while stellar evolution depletes the core of mass and hence the potential energy decreases and the result is again an expansion of the core.

While three-body interactions are important during all the life of the SC, stellar evolution influences SC fate only in the first $\sim 50\,\mathrm{Myr}$ since the birth of a SC. In fact, supernovae explosions occur less than $\sim 50\,\mathrm{Myr}$ from the birth of a star, and most stars which can produce strong winds already evolved, too. The remaining stars are slowly evolving. By calling t_{se} the time at which most of the massive stars has already evolved, we can observe that if $t_{\mathrm{rel}} \lesssim t_{\mathrm{se}}$ stellar evolution can only delay core collapse [6, 86] but if $t_{\mathrm{rel}} \gg t_{\mathrm{se}}$ stellar evolution can expand the SC before the gravothermal instability begins. In the second case the SC can become so sparse that it can evaporate without evolving towards core collapse [17]. Initially segregated systems [110] and high stellar metallicity (e.g. [65, 87]) can even increase this effect.

1.3.5 A summary of star cluster dynamical evolution

In the previous sections we described the physical processes that rule the evolution of a SC: two-body interactions are responsible for the SC relaxation and drive the SC to the core collapse. In this scenario binaries represent an internal energy source for the SC and through three-body interactions can stop and also invert the core-collapse making the core re-expand. Another feedback effect against core collapse is the stellar evolution

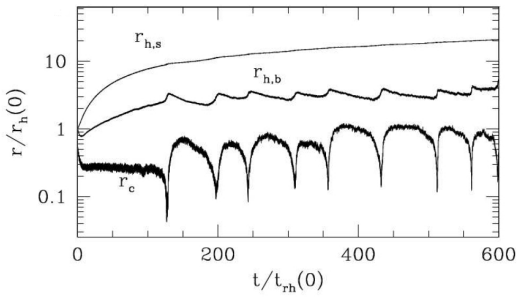

FIGURE 1.6: Typical behaviour of the core radius $r_{\rm c}$, binary half-mass radius $r_{\rm h,b}$ and single star half-mass radius $r_{\rm h,s}$ when the SC experiences gravothermal oscillations [29].

(see Sec. 1.3.4). In this section we want to put together all these processes in order to understand the fate of a SC.

Putting all physical processes (two-body encounters, three-body interactions, and stellar evolution) together, we can describe the fate of a SC. The evolution of a SC is primarily ruled by two-body interactions which drive the system to the gravothermal catastrophe and to core collapse – the process is faster with an initial broad mass distribution. But, stellar evolution can slow down this process in the first 50 Myr or even prevent it in the case the SC has a very high relaxation time. So, after a phase of collapse, the SC re-expands. In this first phase, if primordial binaries are present [3], they greatly contribute to slow down the core collapse [54]. After the SC gets a new condition of virial equilibrium, two-body interactions are still in action. As a consequence, the SC suffers again a contraction phase. The effect of stellar evolution is now negligible since supernova explosions have already occurred as more massive stars have already evolved and no significant stellar winds are in action. So, the only remaining feedback effect against collapse is the three-body interaction. In conclusion, after the first core collapse the SC experiences several phases of expansion and contraction (see Fig. 1.6) called *gravothermal oscillations* since gravothermal instability is considered as the cause of both the phases [4] [70].

[3] If there are no primordial binaries, it is anyway possible to demonstrate that they will surely form during the approach to core collapse [78].

[4] It is actually debated whether also the re-expansion phase is of gravothermal nature. A competitive explanation is that binaries or massive stars may be ejected from the core by strong three-body interactions [56, 73].

Chapter 2

MYSCE code description

In this Chapter we first describe the different numerical methods used to simulate SCs, then, we present our modified Hénon Monte Carlo approach on which our code `MYSCE` is based.

2.1 Numerical methods to simulate Star Clusters

As far as the methods to simulate SCs are concerned, four main approaches have been adopted in the literature: (i) the N-body method, (ii) a fluid dynamic approach, (iii) a statistical description of the system based on a distribution function, and (iv) the Monte Carlo method (for a review of the methods see i.e. [30, 49]).

The N-body method is basically the numerical integration of the equations of motion of N bodies, starting from assigned initial conditions. This approach allows to follow the evolution of each star in the SC and its interaction (two- and three-body encounters) with each other star in the system. As a consequence, it is the most accurate and allows to have control over both the global and microscopic characteristics of the SC. The disadvantage is its computational burden: the time required for the computation of the mutual forces is proportional to N^2, and as N increases, close interactions become more frequent and the time step must be accordingly reduced. The number of steps per crossing time is proportional to N and by remembering that the relaxation time is proportional N times the crossing time (see Eq. (1.4)), as a result, the total computational time is proportional to N^4 [112]. It is possible to improve the situation by using individual time steps for the stars in the different regions of the system [1], or by introducing a binary three in order to reduce the burden of calculations of the far interactions [55]. Anyway, the time step remains a fraction of the crossing time (for

reasons of accuracy) and the computational burden still remains very high: as a result, it is currently difficult to simulate systems of $N > 10^5$ stars with this method. An alternative solution would be to use results obtained from systems of a limited number of stars and extrapolate them to a large value of N. However, the different processes in a SC (relaxation, evaporation, stellar evolution) depend in different ways on N so that this extrapolation may be at least risky [2, 48, 74].

In the second approach SCs containing an extremely large number of stars are considered as a fluid [38, 63, 64, 67, 68]. This approach is based on the treatment of the collisional Boltzmann equation (Eq. (1.15)). The main disadvantage of this approach is that a precise model and integration of collisions is very difficult because of the continuous nature of the method.

The third approach uses a distribution function $f(\mathbf{r}, \mathbf{v}, m, t)$ to describe the system in a statistical fashion, where $\mathbf{r}$ is the position,$\mathbf{v}$ the velocity, m the mass of a star and t is the time. f satisfies the Fokker-Planck equation [93], which is numerically integrated [12]. Again, the main problem is the treatment of collisions which cause an increase of the complexity of the method since they would require a modification of the distribution function f.

The forth approach to study SCs is the so-called Monte Carlo (hereafter MC) method. The underlining hypothesis in the MC scheme is similar to the method that solves the Fokker-Planck equation: in fact, we start by considering a distribution function $f(\mathbf{r}, \mathbf{v}, m, t)$. However, the MC method is based on particles, and in this sense it is similar to the N-body method. Actually, two different MC schemes exist: the so-called Princeton method [99–102] that numerically integrates the orbit of each star and allows the simulation of fast physical processes, and the Hénon method developed in [49, 50] which does not follow the orbit of any star and recalculates the radial position of stars at the end of each time step with a sample procedure (for more details see Sec. 2.2.8). While the first method can be used also for violent and fast processes (the time step is a fraction of the dynamical time), the second one is less time consuming and allows to include several physical processes such as stellar collisions, and a stellar mass distribution – which would instead slow down too much the first approach. The MC method is an intermediate approach between N-body and statistical methods and tries to combine their advantages. N-body method gives an amount of information about the motion of single stars that is not necessary since we are interested in the global properties of the SC (such as the Lagrangian radii evolution or the variation of the stellar velocity dispersion). Moreover, the N-body method does not make any theoretical hypothesis or simplifications, while the MC scheme can reduce the computational burden by considering the symmetry of the problem and by making appropriate theoretical

assumptions. In the Hénon scheme a SC is a spherical system that evolves on the scale of the relaxation time [1], so that the time step should be a small fraction of that time scale instead of a small fraction of the crossing time, as happens in the N-body simulations. By using such information we can simplify the problem and decrease the computational burden without losing accuracy in the results about SC global properties. The evolution of the spherical SC is computed by following a sample of test-stars representing spherical star shells. The gravitational field is divided in two parts: a main smooth field, and a small fluctuating field. The smooth potential is calculated by using the assumption of spherical symmetry. During a time step the motion of a star is ruled only by the smooth potential. The fluctuating field is important on larger time scales ($\sim$ relaxation time) and allows us to simulate relaxation. Its origin is the perturbation due to two-body interactions: we should consider for each star its interaction with all the others. This would drive us back to the N-body approach. So we apply the MC tactics: first, we randomly consider only a particular point in the test star orbit where we calculate the perturbation instead of integrating it along all its orbit, second, we take a single field star as representative of all interactions with the test star and we multiply this perturbation by a factor that takes into account all perturbations and their duration. In this way, we do not get the correct perturbation of the test star but we can maintain the correctness of its statistical properties. The computational time of a MC method is roughly proportional to $N - N^2$ compared to $N^3 - N^4$ of a N-body method: a first factor N is saved since perturbations are calculated in only a point of the orbit, and a second one since the interaction is calculated with only a single field star, rather than N. As a result, we can consider the evolution of the system without integrating stellar orbits (as in a statistical method); but, we can describe collisional interactions with some accuracy (since the MC scheme is a particle method like the N-body method). In fact, despite the much lower computational burden, the accuracy about the global properties of the SC is comparable to the one obtained with a N-body integration (and much better than what can be obtained with statistical methods).

2.2 Outline of the MYSCE algorithm

2.2.1 Overview

The MYSCE code is based on a MC method since our aim is to simulate SCs composed by a number of stars in a broad range ($10^4 - 10^7$) – which would be impossible with a

[1] This approach cannot be applied to the initial phases of the life of the cluster, where it evolves on the crossing time scale; instead, the Princeton scheme is well suited for followig these rapidly evolving phases.

N-body method (limited to $N \lesssim 10^5$ particles), and because we want to include a good description of two- and three-body interactions – which would be impossible with a pure statistical method. Moreover, we choose a MC method since it allows to include stellar evolution, and metallicity dependence in a easier and more accurate way than a pure statistical method. Among the different MC methods [49, 95, 99], we choose the one developed by Hénon [49, 50] because it allows to reduce drastically the computational burden not requiring orbit integration and since it allows the use of time steps which are fractions of the relaxation time instead of fractions of the dynamical time. This method is widely used to simulate SCs [30, 57]. `MYSCE` is indeed based on a modified version of the Monte Carlo method developed by Hénon [49, 50] and successively used and improved by [40, 104, 105].

Four main aspects differ our method from the original one described by [50]:

1. In the original implementation, each particle is a superstar representing some stars with similar properties, whereas in our version each particle is a single star – which allows us to represent in a more realistic way star initial mass distribution, interaction, and evolution.

2. `MYSCE` generally uses a time step which is a smaller fraction of the relaxation time than what was originally suggested by [49, 50], because we wish to follow in deeper detail SC evolution (in particular the SC core, where processes are faster).

3. We use a few-body integrator to treat three-body interactions in order to have an higher accuracy than statistical or semi-analytical approaches. Obviously, the exact integration of the three-body encounters increases the whole computational time of a simulation but the reason for this choice is that such interactions are crucial for the SC evolution (see Chapter 1 Sec. 1.3.5).

4. Monte Carlo methods suffer a known numerical problem, the *spurious relaxation*: even in the absence of physical interactions (two- and three-body interactions) the system tends to a "numerical relaxation" (inner Lagrangian radii tend to shrink, the outer ones to widen). We include in `MYSCE` a spurious relaxation correction that, in principle, completely removes the problem. For a deeper discussion of the spurious relaxation and for the method adopted for its solution, see Sec. 2.2.10 and Appendix A.

The scheme of our algorithm is represented in the block diagram of Fig. 2.1. For a system with spherical symmetry and containing N particles (stars) the method can be summarized as follows. Each star is generated with an appropriate value of mass m, distance from the centre r, radial velocity v_r, and tangential velocity v_t according to

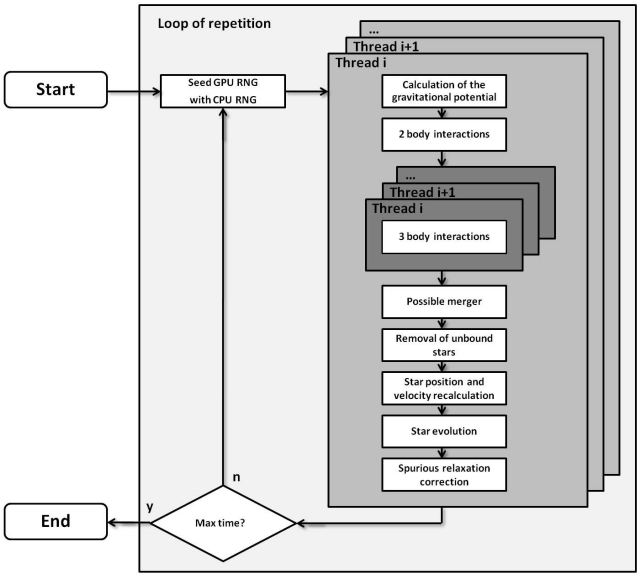

FIGURE 2.1: Block diagram of the modified Monte Carlo method used in the code MYSCE.

appropriate distributions (for more details see Chapter 3). Before entering into the loop of repetition and performing all the calculations pertaining to each time step, energy and angular momentum of each star are evaluated. At the beginning of the time step the gravitational potential is calculated; then, the effects of two-body interactions among stars are calculated using an "on average" (Monte Carlo) procedure which perturbates energy and angular momentum of each star. Next, three-body interactions are calculated by means of a few-body integrator. Afterwards, possible single star-single star and/or single star-binary mergers are treated. Stars having positive total energy after interactions and are therefore unbound (by the SC) are removed from the system. Once new energy and angular momentum are assigned to each star, the entire system is updated by giving to each star a new position and velocity consistent with the constants of motion. The new position is chosen randomly but weighted by the time spent by the star along its orbit. Star evolution (stellar winds, red giant, white dwarf, neutron star, BH formation, etc.) is then considered. At the end of the step we add the spurious relaxation correction mechanism.

As far as the code implementation is concerned, we decided to parallelize both the entire time step and, inside each time step, three-body interactions since these latter are the most computationally burdensome operations in our code.

2.2.2 Time step

The time step Δt must be short enough to simulate the two-body relaxation in the core, otherwise, for too large time steps the system is under-relaxed. In order to obtain this goal we take for all the SC a small fraction of the relaxation time in the core $t_{\rm rel,core}$ [103] (see Eq. (1.51)) that reads

$$t_{\rm rel,core} \sim \frac{0.3}{\ln\Lambda}\frac{\sigma^3_{\rm core}}{G^2\nu_{\rm core}\langle m\rangle}, \tag{2.1}$$

where $\ln\Lambda$ is the Coulomb logarithm, $\sigma_{\rm core}$ is the core dispersion velocity, G is the gravitational constant, $\nu_{\rm core}$ is the star number density in the core, and $\langle m\rangle$ is the average mass for a star in the core.

2.2.3 Gravitational potential

Thanks to spherical symmetry, the angular positions of stars do not matter for the calculation of the gravitational potential which depends only on radial position of stars. After sorting all the N stars according to their distance from the SC centre, and calling r_k and r_{k+1} the position of two consecutive stars the potential Φ at r with $r_k < r < r_{k+1}$ reads

$$\Phi(r) = G\left(-\frac{1}{r}\sum_{i=1}^{k} m_i - \sum_{i=k+1}^{N}\frac{m_i}{r_i}\right), \tag{2.2}$$

where m_i is the mass of the i-th star.

The gravitational potential is normally calculated only once at the beginning of the time step and few times after the spurious relaxation correction (see Sec. 2.2.10 and Appendix A for more details): in fact the most frequent physical interaction is the two-body relaxation which is however supposed to perturb only the star velocity but not the star position. The only cases when potential is updated during the time step is in the case of mergers and in the case of star exchange in three-body encounters.

2.2.4 Two-body interactions

In order to treat two-body relaxation in a Monte Carlo fashion we should first select at random the position of each star along its orbit. Anyway, this is not necessary neither in the first step (since positions are chosen randomly according to an initial distribution function) nor in successive steps (since positions are again selected in a random way but weighted by the time spent by the stars along their orbit, see Sec. 2.2.8 for more details). Therefore, each star is considered as a test star which interacts with only another star

representative of the field stars. Since the greatest part of the two-body perturbation on a star is given by the closest stars, it is safe and convenient to choose the closest one (according to the radial distance) as representative of the field stars. The role of the test star and of the star representing the field stars can be inverted so that star perturbations are calculated in couple.

Following the notation introduced by Hénon, the properties of the test stars are described by (r, v_r, v_t, m) while the star representative of the field stars by (r', v'_r, v'_t, m'). We define $\mathbf{v}$ the total velocity of the test star and $\mathbf{v}'$ the total velocity of the field star. By considering a reference frame where the centre of mass of the test star and the field star are at rest, the norm of the velocity of the test star remains unchanged after the encounter, and only its direction is deflected by an angle β defined by

$$\tan\frac{\beta}{2} = \frac{G(m+m')}{w^2 l}, \tag{2.3}$$

where $w \equiv ||\mathbf{w}|| \equiv ||\mathbf{v}' - \mathbf{v}||$ is the relative velocity and l is the impact parameter that reads

$$l = \frac{1}{\sqrt{2\pi w \Delta t \nu \ln N}}, \tag{2.4}$$

where ν is the local (around the test star) number density of field stars (for more details, see [50][2] and references therein). In addition to the impact parameter we must know also the angle ψ which the plane of relative motion $(\mathbf{r}' - \mathbf{r}, \mathbf{v}' - \mathbf{v})$ forms with some reference plane. To obtain this goal we can take ψ randomly in the interval $[0, 2\pi)$ with an uniform distribution. Then, we consider an orthogonal reference frame such that $\mathbf{r}$ is parallel to the z-axis and $\mathbf{v}$ is parallel to the (x, z) plane. Since the two stars are supposed to be as close as possible each to the other, we can impose, without any loss of generality, that $\mathbf{r}' \parallel \mathbf{r}$. Consequently, v'_r and v_r are aligned but v'_t and v_t can be directed randomly in the plane (x, z): we define the x-axis to be parallel to v_t, while v'_t lies in a random direction in the (x, z) plane. So we can write the total velocities of the two stars $\mathbf{v}$ and $\mathbf{v}'$ as

$$\mathbf{v} = (v_t, 0, v_r), \qquad \mathbf{v}' = (v'_t \cos\phi, v'_t \sin\phi, v'_r), \tag{2.5}$$

where ϕ is randomly chosen in the interval $[0, 2\pi)$ with an uniform distribution. The relative velocity $\mathbf{w} = (w_x, w_y, w_z)$ reads

$$\mathbf{w} = (v'_t \cos\phi - v_t, v'_t \sin\phi, v'_r - v_r). \tag{2.6}$$

[2] In our method ν is not estimated, it is actually calculated since the number N of stars in the SC is high enough to perform a suitable evaluation.

Then we build an orthogonal reference frame $(\mathbf{w}, \mathbf{w_1}, \mathbf{w_2})$. $\mathbf{w_1}$ and $\mathbf{w_2}$ are defined

$$\mathbf{w_1} = (w_y w/w_p, -w_x w/w_p, 0), \tag{2.7}$$

$$\mathbf{w_2} = (-w_x w_z/w_p, -w_y w_z/w_p, w_p), \tag{2.8}$$

where w is the norm of the vector $\mathbf{w}$ and $w_p = (w_x^2 + w_y^2)^{1/2}$. By assuming that ψ is measured in the plane $(\mathbf{w_1}, \mathbf{w_2})$ the relative velocity $\mathbf{w}^*$ after the encounter is

$$\mathbf{w}^* = \mathbf{w}\cos\beta + \mathbf{w_1}\sin\beta\cos\psi + \mathbf{w_2}\sin\beta\cos\psi. \tag{2.9}$$

The new velocities $\mathbf{v}^*$ and $\mathbf{v'}^*$ of the two stars after the encounter can be written as

$$\mathbf{v}^* = \mathbf{v} - \frac{m'}{m+m'}(\mathbf{w}^* - \mathbf{w}), \tag{2.10}$$

$$\mathbf{v'}^* = \mathbf{v'} + \frac{m}{m+m'}(\mathbf{w}^* - \mathbf{w}). \tag{2.11}$$

Since we assume that the two stars do not change position during the interaction, also the direction of the radial velocity does not change (only its norm does change): hence, by using Eq. (2.10) for the first star we get

$$v_r^* = v_z^*, \quad v_t^* = \sqrt{v_x^{*2} + v_y^{*2}}; \tag{2.12}$$

its energy E^* and angular momentum J^* are therefore

$$E^* = \Phi(r) + \frac{1}{2}(v_r^{*2} + v_t^{*2}), \quad J^* = r v_t^*. \tag{2.13}$$

Similar equations can be written for the second star.

2.2.5 Three-body interactions

In MYSCE, a binary is completely described by the mass m_1 of the more massive star, the mass m_2 of the less massive star, the semi-major axis a and its eccentricity e. These properties are used only for the three-body interactions, while, throughout the rest of the code, a binary is considered as a single star with mass $m = m_1 + m_2$, and with position and velocity equal to those of the binary centre of mass.

At each time step we must select which single stars interact with a particular binary. The only condition which a single star should satisfy is that its impact parameter with the binary is less than a threshold value (more details further). Anyway, such a calculation for all the single stars would be extremely inefficient and computationally onerous. This is the reason why we introduce preliminary conditions to be met. We follow the same

convention of Sec. 2.2.4. Here, not-primed quantities are related to the binary and defined with respect to its centre of mass ($m = m_1 + m_2$ is the total mass of the binary), while primed quantities refer to the single star. We evaluate two conditions

$$||\mathbf{r}' - \mathbf{r}|| < \sqrt[3]{\frac{1}{\nu_{\rm loc}(\mathbf{r})}}, \tag{2.14}$$

$$\frac{||\mathbf{r}' - \mathbf{r}||}{\sqrt{v_r'^2 + v_t'^2}} < 0.1\, T_{\rm bin}, \tag{2.15}$$

where $\nu_{\rm loc}$ is the local (around the binary) star number density, and $T_{\rm bin}$ is the binary orbital period. Condition (2.14) ensures that the single star is close enough to the binary. Condition (2.15) ensures that the single star is fast enough when approaching to the binary, so that this latter does not move too much within the SC. As a first step, stars which do not satisfy condition (2.14) or condition (2.15) where $\mathbf{r}$ and $\mathbf{r}'$ are substituted with the radial distances r and r' are not considered anymore. If a single star overcomes this first selection, by assuming binary position along the x-axis, we evaluate the position of the single star by generating two random angles: δ such that $\cos\delta$ is uniformly distributed in the interval $[-1, 1)$ and ϵ in the interval $[0, 2\pi)$. Consequently, $\mathbf{r}$ and $\mathbf{r}'$ read

$$\mathbf{r} = (r, 0, 0), \qquad \mathbf{r}' = (r'\sin\delta\cos\epsilon, r'\sin\delta\sin\epsilon, r'\cos\delta). \tag{2.16}$$

Then, we check if the single star satisfies, with the calculation of the real distance, *both* condition (2.14) *and* condition (2.15): if this is the case we proceed further. Then, we consider also the direction of motion of the centre of mass of the binary and of the single star: we suppose that the tangential velocity of the centre of mass of the binary is along the y-axis. So its total velocity reads

$$\mathbf{v} = (v_r, v_t, 0). \tag{2.17}$$

The calculation of the total velocity of the single star is more complicated. Its radial velocity $\mathbf{v}'_\mathbf{r}$ reads

$$\mathbf{v}'_\mathbf{r} = (v'_r\sin\delta\cos\epsilon, v'_r\sin\delta\sin\epsilon, v'_r\cos\delta). \tag{2.18}$$

The tangential velocity $\mathbf{v}'_\mathbf{t}$ must be orthogonal to $\mathbf{v}'_\mathbf{r}$, so we can define the subsidiary vector $\mathbf{v}'_{\mathbf{t,aux}}$ (orthogonal to $\mathbf{v}'_\mathbf{r}$)

$$\mathbf{v}'_{\mathbf{t,aux}} = \frac{(0, v'_t, v'_t\tan\delta\sin\epsilon)}{\sqrt{1 + (\tan\delta\sin\epsilon)^2}}. \tag{2.19}$$

$\mathbf{v}'_{\mathbf{t,aux}}$ cannot be the correct tangential velocity since we chose a particular direction: we do not know the direction of $\mathbf{v}'_\mathbf{t}$. In order to calculate the correct $\mathbf{v}'_\mathbf{t}$ we must generate a

random angle ζ uniformly distributed in the interval $[0, 2\pi)$ and make a rotation $\mathcal{R}(\mathbf{v'_r}, \zeta)$ of $\mathbf{v'_{t,aux}}$ around the axis of direction $\mathbf{v'_r}$ such that

$$\mathbf{v'_t} = \mathcal{R}(\mathbf{v'_r}, \zeta)\mathbf{v'_{t,aux}}, \tag{2.20}$$

where

$$\mathcal{R}(\mathbf{v'_r}, \zeta) \equiv \begin{pmatrix} c_z + \frac{v'^2_{r,x}}{v'^2_r}(1-c_z) & \frac{v'_{r,x}v'_{r,y}}{v'^2_r}(1-c_z) - \frac{v'_{r,z}}{v'_r}s_z & \frac{v'_{r,x}v'_{r,z}}{v'^2_r}(1-c_z) + \frac{v'_{r,x}}{v'_r}s_z \\ \frac{v'_{r,x}v'_{r,y}}{v'^2_r}(1-c_z) + \frac{v'_{r,z}}{v'_r}s_z & c_z + \frac{v'^2_{r,y}}{v'^2_r}(1-c_z) & \frac{v'_{r,y}v'_{r,z}}{v'^2_r}(1+c_z) - \frac{v_{r,x}}{v'^2_r}s_z \\ \frac{v'_{r,x}v'_{r,z}}{v'^2_r}(1-c_z) - \frac{v_{r,x}}{v'^2_r}s_z & \frac{v'_{r,y}v'_{r,z}}{v'^2_r}(1+c_z) + \frac{v'_{r,x}}{v'^2_r}s_z & c_z + \frac{v'^2_{r,z}}{v'^2_r}(1-c_z) \end{pmatrix}, \tag{2.21}$$

where $c_z = \cos\zeta$ and $s_z = \sin\zeta$. Finally, we can write the total velocity of the single star $\mathbf{v'}$ as

$$\mathbf{v'} = \mathbf{v'_r} + \mathbf{v'_t}. \tag{2.22}$$

Afterwards, we calculate the maximum impact parameter $b_{\max}$ [53]

$$b_{\max} = \left(\frac{Cv_c}{||\mathbf{v'} - \mathbf{v}||} + D\right)a, \tag{2.23}$$

where a is the binary semi major axis and

$$v_c^2 = G\frac{m_1 m_2(m_1 + m_2 + m')}{m'(m_1 + m_2)a}, \tag{2.24}$$

is the critical velocity for which the total energy of the three-body system vanishes, and C and D are suitable parameters. A good choice to explore all possible outcomes of three-body interactions (flyby, exchange, and ionization) is $C = 4$ and $D = 0.6(1 + e)$, where e is the eccentricity of the binary [53]. Then, we calculate the impact parameter b defined as the perpendicular distance between the path of a projectile star and the centre of mass of the binary.

In order to completely define the three-body system we must know the three masses of the stars m_1, m_2, and m', the initial eccentricity of the binary e, the relative velocity $v_{\rm rel} = ||\mathbf{v'} - \mathbf{v}||$, the impact parameter b, the two impact direction angles θ and ϕ, the impact orientation ψ, and the binary initial phase f (see Fig. 2.2). Among the previous quantities θ and ϕ are easily calculated by writing $v_{\rm rel}$ in spherical coordinates, ψ is randomly generated in the interval $[0, 2\pi)$ with an uniform distribution. f is randomly generated in the interval $[0, 2\pi)$ but with a distribution taking into account the time fraction which the system spends at each particular orbital phase (for a description of a good method to obtain f see [53]).

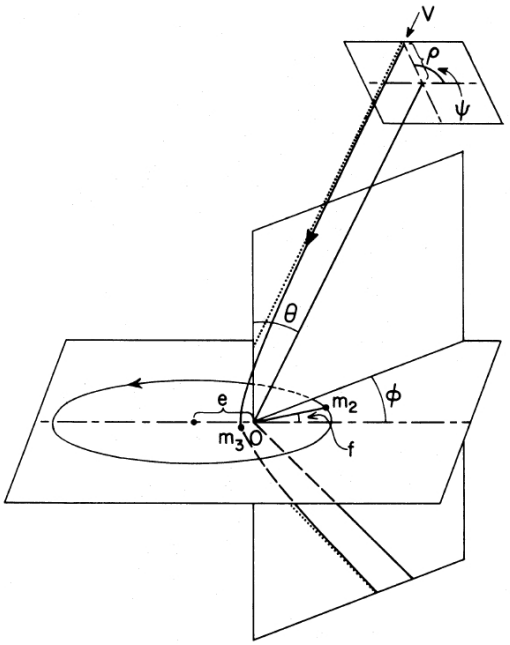

FIGURE 2.2: Scheme of a three-body interaction between a binary and a single star (figure by [53]). Here, V is the relative velocity, m_3 is the mass of the single star and ρ is the impact parameter. In the text we called these quantities: $v_{\rm rel}$, m', and b, respectively.

If $b < b_{\rm max}$, the three-body interaction does happen, and we proceed with the integration of the system by using the few-body code developed by [71]. After the integration of the three-body system we obtain new values for the velocities $\mathbf{v}$ and $\mathbf{v}'$ and consequently for the radial and tangential velocities v_r, v_t, v'_r, and v'_t, for the semi major axis a and the eccentricity e. We assume that the positions are conserved: in the case of ionization nothing changes as regard position (for a complete ionization we take for both the stars once forming the binary the position of the centre of mass of the old binary), instead in the case of exchange we put the star exiting out of the binary in the position belonging to the intruder star before the interaction.

For more details about the initial setting of the three-body system and for the solution method in a N-body fashion see [71].

2.2.6 Possible mergers

Two- and three-body interactions and stellar evolution [3] can give rise to conditions suitable for stellar mergers. While single star-single star merger is more and more probable as SC density grows in later stages of its evolution, merger in three-body encounters can happen also in the first phases.

[3] A star can increase its radius during its evolution phases (red giant). As a result, in a binary, such star can become at contact with the other star.

The basic idea is that two stars coalesce if they touch i.e. if during their motion the distance between their centres become less than the sum of their radii. We start by considering single star-single star merger. We know only the radial distance of stars which are sorted according to their distance from the SC centre. In order to be as efficient as possible we start from the star closest to the centre and we investigate (following the sorting) which stars have a difference of radial distance less than the sum of their radii. For the stars surviving the last condition we calculate the real distance by generating two random angles: δ such that $\cos\delta$ is equally chosen in the interval $[-1, 1)$ and ϵ in the interval $[0, 2\pi)$. We use the same convention of Sec. 2.2.4. Therefore the position $\mathbf{r}$ of the current star and the position $\mathbf{r}'$ of the star candidate to merge read

$$\mathbf{r} = (0, 0, r), \qquad \mathbf{r}' = (r'\sin\delta\cos\epsilon, r'\sin\delta\sin\epsilon, r'\cos\delta). \tag{2.25}$$

By calling R and R' the stellar radii of the two stars, these latter merge if

$$||\mathbf{r}' - \mathbf{r}|| < R' + R. \tag{2.26}$$

Since condition (2.26) can be met only if the distance of the two stars is much smaller than the size of the cluster (and, usually, than $||\mathbf{r}||$), we can suppose (without loss of generality) that $\mathbf{r}' \parallel \mathbf{r}$, i.e. only stars with $\delta \sim 0$ are good candidate to merge. With this in mind we infer that Eq. (2.5) represents the velocities of the two stars with, again, ϕ randomly chosen in the interval $[0, 2\pi)$ since we do not know relative direction of the tangential velocities. Position, radial velocity, tangential velocity, and mass $(r_{\rm M}, v_{r,{\rm M}}, v_{t,{\rm M}}, m_{\rm M})$ of the new star after the merger read

$$r_{\rm M} = \frac{mr + m'r'}{m + m'}, \tag{2.27}$$

$$v_{r,{\rm M}} = \frac{mv_r + m'v_r'}{m + m'}, \tag{2.28}$$

$$v_{t,{\rm M}} = \frac{\sqrt{(mv_t + m'v_t'\cos\phi)^2 + (m'v_t'\sin\phi)^2}}{m + m'}, \tag{2.29}$$

$$m_{\rm M} = \alpha(m + m'), \tag{2.30}$$

where α is a parameter measuring the efficiency of the merger. In the simulations performed in this thesis, we always take $\alpha = 1$ but we plan to modify it in the near future in order to describe the merger process with greater accuracy.

Merger during three-body interaction can happen between the single star (intruder) and one of the star forming the binary or between the two stars of the binary which become so tight to coalesce. In order to inquire these possibilities, during the integration of the three-body system (see Sec. 2.2.5) mutual distances among the three stars are

monitored and if condition (2.26) between two of the three stars is satisfied their merger is considered.

In the case of merger between the single star and a star of the binary the merger procedure is only slightly different with respect to the one described above (single star-single star merger). If now, not-primed quantities are referred to the binary and primed quantities to the single star, $\mathbf{r}$ is the position of the centre of mass of the binary, v_r and v_t are the radial and tangential velocities of the centre of mass of the binary and m is its total mass. We obtain $r_{\rm M} = r$ since the single star is close to the binary during three-body interaction. As soon as radial and tangential velocity are concerned, Eq. (2.28) and Eq. (2.29) are still in use with the new meaning of the not-primed quantities. As regard the mass of the new star resulting from the merger, Eq. (2.30) is still valid but in this particular case m represent the mass of the binary component which suffers the merger with the single star.

Also the initial semi major axis a_i of the binary is modified by the merger. By calling $E_{{\rm k},i} = 0.5m(v_r^2 + v_t^2) + 0.5m'(v_r'^2 + v_t'^2)$ the initial kinetic energy, $E_{{\rm b},i} = -Gm_1m_2/2a_i$ the initial binary binding energy (m_1 and m_2 are the masses of the two binary stars), and $E_{{\rm k},f} = 0.5m_{\rm M}(v_{r,{\rm M}}^2 + v_{t,{\rm M}}^2)$ the final kinetic energy, the final binding energy $E_{{\rm b},f}$ arises from the energy conservation so that $E_{{\rm b},f} = E_{{\rm k},i} + E_{{\rm b},i} - E_{{\rm k},f}$. Hence, the final semi major axis a_f reads

$$a_f = -\frac{G(m_1 + m')m_2}{2E_{{\rm b},f}} \quad \text{or} \quad a_f = -\frac{Gm_1(m_2 + m')}{2E_{{\rm b},f}}, \tag{2.31}$$

in the case the single star merges with the first star of the binary or with the second one, respectively.

When the two stars forming the binary merge, the calculation is even simpler: in fact the new star has the position, radial and tangential velocity of the binary centre of mass and mass equal to the total binary mass (with eventual mass loss), i.e. $r_{\rm M} = r$, $v_{r,{\rm M}} = v_r$, $v_{t,{\rm M}} = v_t$, and $m_{\rm M} = \alpha(m_1 + m_2)$.

2.2.7 Removal of unbound stars

Once energy and angular momentum perturbations due to two- and three-body interactions are calculated stars may have a positive total energy. If this is the case they are unbound and are assumed to leave the SC within a crossing time. As a consequence we immediately remove them from the simulation since our time step is a fraction of the relaxation time which is always orders of magnitude greater than the crossing time.

2.2.8 Star position and velocity recalculation

The perturbations induced by two- and three-body interactions give a new energy E and angular momentum J to each particle, so that a new realization of the entire system must be calculated: new position r, radial velocity v_r, and tangential velocity v_t are randomly assigned to each star according to the new constants of motion. The position and corresponding velocity are chosen such that the position is weighted by the amount of time spent by the star at that location. Each star describes a rosette orbit with r oscillating between the periapsis $r_{\min}$ and the apoapsis $r_{\max}$. $r_{\min}$ and $r_{\max}$ are the loci of points where $v_r = 0$ and are therefore solution of

$$Q(r) = 2E - 2\Phi(r) - \frac{J^2}{r^2} = 0. \tag{2.32}$$

A general discussion is present in [12], while for details about a method of solution of Eq. (2.32), see [50].

The new position r of the star is randomly chosen between the two extremes $r_{\min}$ and $r_{\max}$ with a distribution dictated by the time spent by the star at each radial distance dr from the centre of the cluster

$$\frac{dt}{T} = \frac{dr/|v_r|}{\int_{r_{\min}}^{r_{\max}} dr/|v_r|}. \tag{2.33}$$

where T is the orbital period and the radial velocity v_r is given by

$$|v_r| = \sqrt{2E - 2\Phi(r) - \frac{J^2}{r^2}} = \sqrt{Q(r)}. \tag{2.34}$$

The classical von Neumann rejection technique [45] could in principle determine a suitable value for r according to a distribution function proportional to $f(r) = 1/|v_r|$. However $f(r)$ diverges in the two extremes $r_{\min}$ and $r_{\max}$ where $v_r = 0$. A solution for this problem in to apply a change of variable by introducing the new variable s linked to r by an appropriate relation $r = r(s)$. The new distribution function is proportional to

$$g(s) = \frac{1}{|v_r|}\frac{dr}{ds}. \tag{2.35}$$

By applying now the von Neumann rejection technique to Eq. (2.35) an appropriate value for the star position r can be obtained (for a deeper discussion see [50]). The new radial velocity v_r is calculated by means of Eq. (2.34), while the tangential velocity v_t is obtained by $v_t = J/r$.

2.2.9 Stellar evolution

In the future we plan to make evolve stars in function of initial metallicity by using results obtained by [15]. We will be able to follow the initial mass loss of massive stars ($M > 10\,\mathrm{M}_{\odot}$) due to stellar winds, their path through the main sequence until they become red giants, white dwarfs, neutron stars, or BHs. Suitable changes in the value of stellar mass and radius will be taken into account in each time step.

2.2.10 Spurious relaxation

Spurious relaxation is a numerical artefact first discovered by [50] which tends to relax the SC even in the absence of physical interactions (two- and three-body interactions): inner Lagrangian radii shrink while outer ones widen. The reason for this behaviour lies in the random nature of the MC algorithm: even in the absence of any interaction at each time step a new random realization of the system is generated and this latter differs from any previous one. Each new realization generates small random fluctuations in the new gravitational potential and consequently in the energy of each star (see Eq. (2.13)). By using the potential calculated at the beginning throughout the time step a mismatch between total energy, gravitational potential, and kinetic energy forms – which provokes the spurious relaxation. In order to eliminate spurious relaxation effects, after generating the set of new stellar position r we calculate the new potential and we estimate the radial velocity v_r with Eq. (2.34) but by inserting the new potential instead of the one calculated at the beginning of the time step. This procedure is performed for each star and totally removes the spurious relaxation problem. For a deeper discussion about spurious relaxation and for more details about our solution of the problem, see Appendix A.

Chapter 3

Initial conditions

In this Chapter we describe the initial conditions that we use to describe the SCs simulated with our Monte Carlo code `MYSCE` (see Chapter 2). We use a Plummer model [88] to describe the stellar position and velocity distribution, a Salpeter initial mass function (hereafter IMF) [94], and the initial condition reported in [82] to describe primordial binaries.

3.1 Star position and velocity distribution

To describe the distribution of the stellar positions and velocities in the SC we use a Plummer model with $n = 5$ (see Chapter 1 Sec. 1.2) [88]. The corresponding distribution function reads

$$f(\mathcal{E}) = \begin{cases} F_1 \mathcal{E}^{7/2}, & \mathcal{E} > 0 \\ 0, & \mathcal{E} \leq 0 \end{cases} , \tag{3.1}$$

where F_1 is a normalization constant. $\mathcal{E}$ reads

$$\mathcal{E} = \Psi(r) - \frac{1}{2} v^2 , \tag{3.2}$$

where $\Psi(r)$ is the relative potential (see Eq. (1.25)) for the Plummer model (see Eq. (1.31)) calculated for a star at the position r and with a velocity v. Fig. 3.1 represents the probability distribution associated to the distribution function of the Plummer model of Eq. (3.1). Once the probability distribution is calculated, it is possible to generate N stars with positions and velocities distributed according to Eq. (3.1) by generating random numbers – i.e. in a Monte Carlo fashion. The stellar spatial distribution for a SC of $N = 10^4$ stars and scale radius $a = 1\,\mathrm{pc}$ is plotted in Fig. 3.2. Fig. 3.3 shows the star radius probability density, while Fig. 3.4 the star velocity probability density

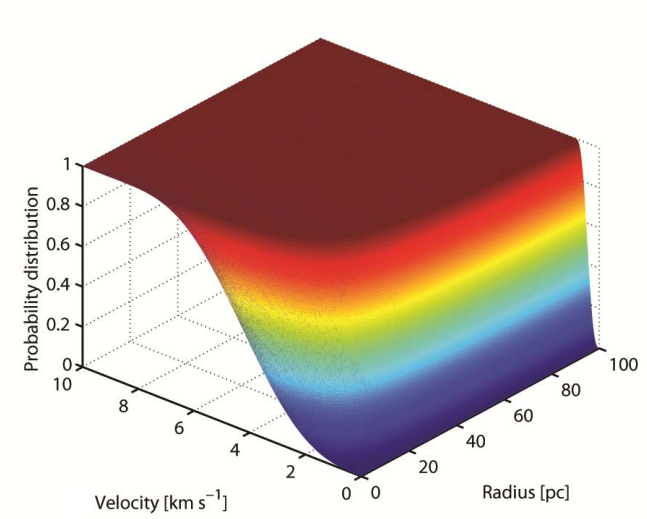

FIGURE 3.1: Probability distribution associated to the distribution function of the Plummer model for a SC of $N = 10^4$ stars and with a scale radius $a = 1\,\mathrm{pc}$.

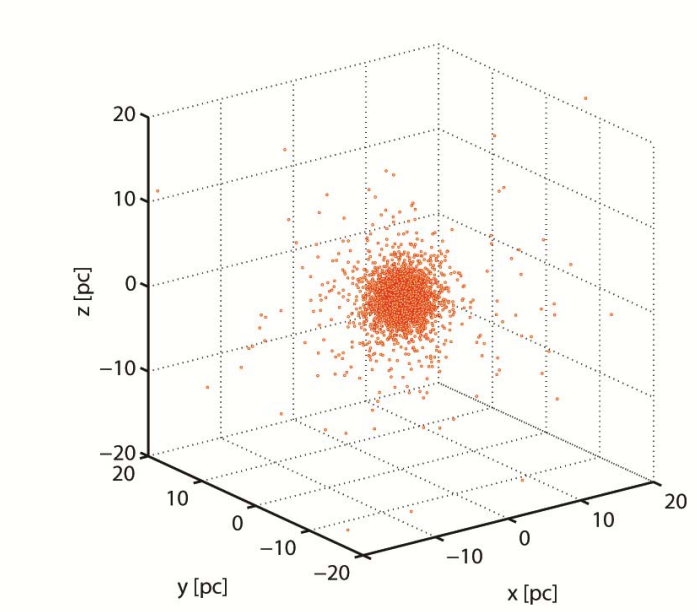

FIGURE 3.2: Spatial distribution of stars according to the Plummer model for a SC of $N = 10^4$ stars and with a scale radius $a = 1\,\mathrm{pc}$.

at different radii. We choose a Plummer model for two reasons: first, it is a very good approximation of star distribution in a SC, and second, this model has an analytical description for the potential (see Eq. 1.31), the density distribution (see Eq. 1.32), and velocity dispersion (see Eq. 1.33).

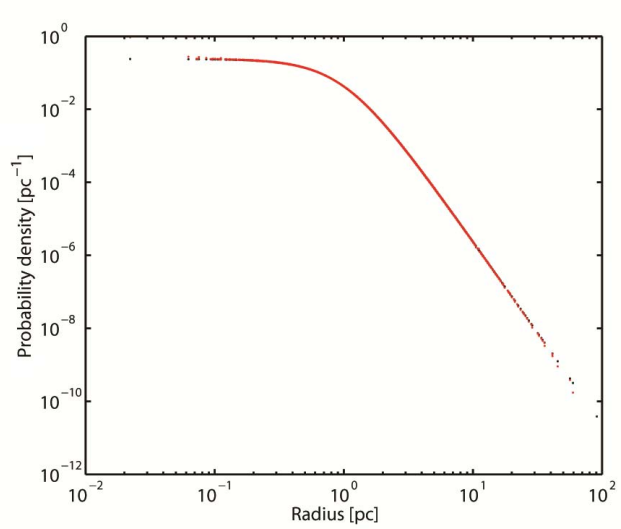

FIGURE 3.3: Radius probability density according to the Plummer model for a SC of $N = 10^4$ stars and with a scale radius $a = 1\,\mathrm{pc}$.

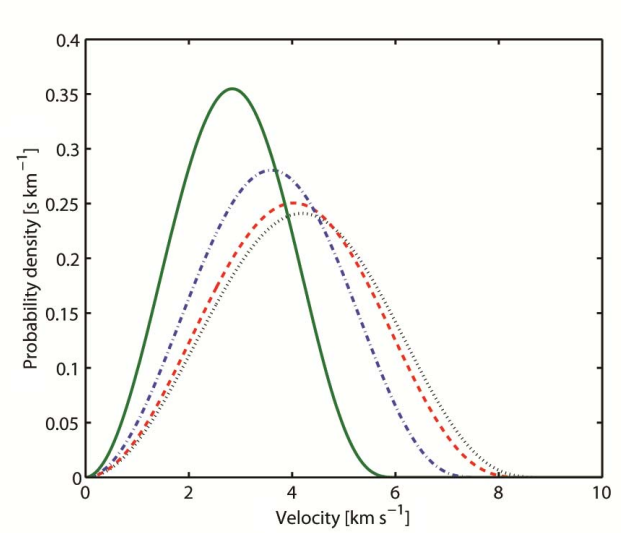

FIGURE 3.4: Velocity probability density at different radii (at 0.25, 0.5 times the scale radius, at scale radius and at two times the scale radius, from left to right, respectively) according to the Plummer model for a SC of $N = 10^4$ stars and with a scale radius $a = 1\,\mathrm{pc}$.

3.2 Initial mass function

We choose a Salpeter IMF [94]

$$f(m) = F_2 m^{-2.35}\ , \tag{3.3}$$

with low limit $m_{\mathrm{min}} = 0.2\,\mathrm{M}_\odot$ and high limit $m_{\mathrm{max}} = 120\,\mathrm{M}_\odot$, and where F_2 is a normalization constant. By generating random numbers, the procedure to obtain the appropriate mass distribution is the same of Sec. 3.1. The mass probability density

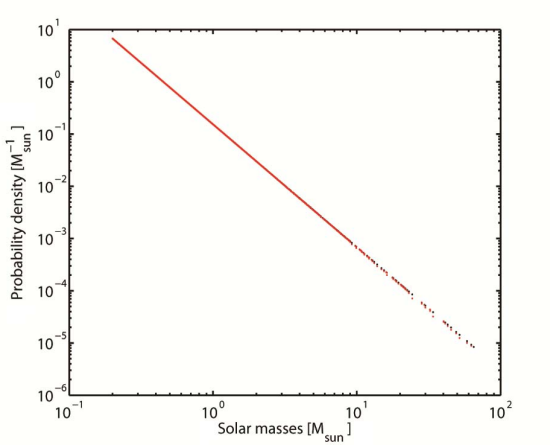

FIGURE 3.5: Mass probability density according to the Salpeter IMF for a SC of $N = 10^4$ stars and with a scale radius $a = 1\,\mathrm{pc}$.

associated to the Salpeter IMF is reported in Fig. 3.5. We choose the Salpeter IMF since it generates a mass distribution very close to the observed one. It is a matter of fact that the Salpeter IMF does not differ so much from other used IMFs, such as the Kroupa IMF [61], except at masses $\lesssim 1\,\mathrm{M}_\odot$, where the Kroupa IMF is flatter (i.e., predicts less low-mass stars) than the Salpeter IMF.

3.3 Primordial binary initial conditions

A binary is completely described by the mass m_1 of the more massive star, the mass m_2 of the less massive star, the semi-major axis a and its eccentricity e. We introduce also the ratio between the lighter and the heavier star $q = m_2/m_1$.

Since we do not know the initial condition of binaries we generate q, a, and e according to distributions functions which are in agreement with observations [82].

Going into more details, we first choose at random a star in the system and we consider it as the more massive star. Then we calculate the value of q to generate the mass of the second star. The mass ratio is generated following the distribution function

$$f(q) = F_3 \frac{1}{(1+q)^2} \ , \tag{3.4}$$

with $q_{\min} = 0.1$ and $q_{\max} = 1$, with F_3 a normalization constant. We do not choose $q_{\min} = 0$ in order to avoid unrealistic values for the mass of the least massive component of the binary. For the same reason, if the star selected at the beginning as the more massive star in the binary has mass $< 0.5\,\mathrm{M}_\odot$, this star is considered to be the lighter one and we take q^{-1} to generate the mass of the heavier star.

The semi major axis is generated following the distribution function

$$f(a) = F_4 \frac{1}{a} \ , \tag{3.5}$$

with F_4 a normalization constant. The upper and lower limits of the semi major axis $a_{\rm min}$ and $a_{\rm max}$ depend on the initial hardness of the binary in the SC. Typical values are $a_{\rm min} = 0.5\,{\rm AU}$ and $a_{\rm max} = 10^3\,{\rm AU}$.

The eccentricity is generated following the distribution function

$$f(e) = F_5 e \ , \tag{3.6}$$

with low limit $e_{\rm min} = 0$ and high limit $e_{\rm max} = 1$, and with F_5 a normalization constant.

By generating random numbers, the procedure to obtain the appropriate mass ratio, semi major axis, and eccentricity distribution is the same as in Secs. 3.1 and 3.2.

Chapter 4

Gas infall into star clusters

In this Chapter we explore the consequences of gas infall inside SCs. In the first section we shortly review the mechanisms for the formation of IMBHs and SMBH seeds, as discussed in the literature. In particular, we focus on the importance of gas infall to help the formation of IMBHs and SMBH seeds inside SCs. In the second section we study the response of the stellar system to a infall of gas, and we compute the increase in the velocity dispersion and in the stellar density. In the third part we study the consequences of gas infall on the dynamics of SCs: in particular, we want to understand if and in which conditions the gas infall is able to destroy primordial binaries and favour the runaway merger of stars/BHs [21].

4.1 State of the art

BHs exist in Nature with a very broad range of masses ($1 - 10^9\,\mathrm{M}_\odot$). BHs with mass between $1\,\mathrm{M}_\odot$ and $100\,\mathrm{M}_\odot$ are the result of the evolution of massive stars. BHs in the mass range $10^5 - 10^9\,\mathrm{M}_\odot$ (SMBHs) are located in the centre of many galaxies. The existence of BHs in the intermediate range of masses $10^3 - 10^5\,\mathrm{M}_\odot$ (IMBHs) is still debated. IMBHs are proposed as an explanation of several observations [19, 35, 36, 71, 108], but their existence is not demonstrated. Beside the speculation about the formation of IMBH at present epochs (redshift $z = 0$), IMBHs are considered as good candidates to be SMBH seeds in the past ($z > 6$).

One of the most likely mechanisms for the formation of IMBHs at the present epoch is that they can form from the collapse of very massive stars produced inside YSCs by the runaway merger of main-sequence stars via direct physical collisions [26, 43, 44, 83, 85]. Such runaway merger is expected to happen in YSCs whose segregation time is smaller

than the stellar evolution time of the most massive stars, a condition necessary to prevent feedback effects due to stellar evolution (for more details on SC evolution see Chapter 1 Sec. 1.3). One or two very massive stars can form in function of the primordial binary fraction [44], while metallicity and possible gas infall can drastically change YSC fate (Chapter 1 Sec. 1.3). This mechanism can be extended in the past to SCs with similar properties as YSCs. In this fashion, this channel can be considered also for the formation of SMBH seeds.

There are two main mechanisms for the formation of IMBHs in the past ($z > 6$) or SMBH seeds ($\sim 10^5\,\mathrm{M}_\odot$), as discussed in the literature, but they suffer some problems: Population III stars [69, 111] definitely existed and were likely more massive than present-day stars, but the mass of the resulting stellar-mass BHs is likely too low ($M_{\mathrm{sbh}} < 300\,\mathrm{M}_\odot$); quasi-stars [10, 66] are much more massive ($\gg 1000\,\mathrm{M}_\odot$), but their existence is very much debated.

An alternative approach is considered in [21]. The main idea is that a massive and dense SC can undergo core collapse, producing a massive central BH through mergers of compact objects. This process is inefficient in SCs with little or no gas [89].

A SC undergoes core collapse due to two-body relaxation, and at the same time segregation of the most massive stars occurs towards the cluster centre. As a result, a very dense core of massive stars forms at the centre – in evolved systems the core is mainly composed of BHs and other collapsed objects. The core is dynamically decoupled from the rest of the cluster. However, the presence of binaries complicates this scenario, as they represent an internal energy source for the cluster. Depending on the fraction of hard binaries, they can prevent the formation of SMBH seeds via stellar-mass BH runaway merger.

If BH binaries are not present at the centre, the BH-main sequence star binaries will quickly undergo exchange interactions that replace the lighter star companion with a heavier BH [97]. As a result the core is almost completely composed by single BHs and BH binaries. Dynamical interactions involving BH binaries and single BHs have a tremendous impact on the fate of the SC core. In fact, in a BH subcluster of a typical SC, interactions involving hard BH binaries will eventually lead to the ejection of the BHs from the subcluster. Recoil and ejections lead to complete evaporation of the BH core on a timescale $\sim 10^9\,\mathrm{yr}$ for typical globular cluster parameters [23, 24, 80]. This process goes on until there are only a few BHs in the subsystem and this latter relaxes.

In addition, the subsystem can experience BH binary mergers because of orbital decay driven by gravitational radiation. In this case, a moderate BH growth can be possible. However, the time scale for merger by gravitational wave emission is usually longer

than the interaction time in the BH cluster. BH binaries interact before they can coalesce. As a result, most BH binaries are ejected. Furthermore, even if coalescence can happen before three-body interaction we must consider the merger recoil speed. In fact, approaching to coalescence, the merger product receive a kick due to the asymmetric emission of gravitational radiation. If the merger recoil speed is higher than the escape speed, the merger product is ejected, and no more BH growth can happen.

We can conclude that a typical SC can hardly experience stellar-mass BH runaway merger to produce a SMBH seed. A suitable cluster for this process to happen should have wide BH binaries (semi major axes $> 0.5\,\mathrm{AU}$, wider than the those typically observed): in this way, they would be unable to heat the cluster core and three-body interactions would not so strong to eject BH binaries from the cluster. Alternatively, the SC should arise with an extremely high single star average kinetic energy at its birth.

While the former condition is quite exotic, the latter can be obtained during SC evolution through gas infall. In fact, [21] suggested that a large gas infall might speed up the process, and lead to the formation of seeds as massive as $10^5\,\mathrm{M}_\odot$ in a short time scale.

It is conjectured that at high redshifts ($z \sim 10$) gas infalls of up to 10 times the mass of the SC are common, because of instabilities arising during galaxy mergers or evolution of the galactic discs [11, 72]. The addition of the gas makes the potential well deeper, and shrinks Lagrangian radii, increasing the central stellar density and the interaction/merger rate. Furthermore, the increase in the average kinetic energies due to the additional mass will make many hard binaries soft, removing much of the energy source that initially prevented/slowed the core collapse and approaching the case of a binary-free core, where (according to [22]) stellar-mass BH runaway mergers should be possible.

In order to be more quantitative, three conditions must be met to allow for the collapse of the BH subcluster into a SMBH seed: (i) BH binaries must be softened to an extent that BH binaries which are soft after the gas infall are destroyed by three-body interaction; (ii) the timescale of gravitational radiation inspiral must be faster than the interaction timescale for binaries which remain hard after gas infall (i.e., binaries merge/are disrupted before they can heat the cluster); (iii) BH-BH merger products must be retained within the SC (i.e. the escape velocity must be high enough). The last two conditions are met if the SC velocity dispersion is $\sim 500\,\mathrm{km/s}$ [21] – however, such a high value is rather extreme.

We focus on gas infall mechanism [21] in order to understand if and in which conditions it can prevent binary heating in a massive SC helping SMBH seed formation via BH runaway merger. We extend also the possibility of gas infall to YSCs in order to inquire

if the gas infall can help the formation of an IMBH via the collapse of a very massive star produced by the runaway merger of main-sequence stars [26, 43, 44, 83, 85].

4.2 Gas infall in the absence of physical interactions

In this section we want to study the infall of gas inside a spherical SC. We model the distribution of stars within the SC using a Plummer density profile [88] (see Chapter 3 Sec. 3.1) with initial scale radius $a_{*,i}$. We suppose that the gas profile (supposed to have a spherical distribution) can be described by a Plummer profile as well: we call $a_{\rm G}$ the gas scale radius. We use a Salpeter IMF [94] (see Chapter 3 Sec. 3.2) for the stellar mass distribution [1]. The potential associated to the stellar distribution reads

$$\phi_{*,i}(r) = -\frac{M_* G}{\sqrt{a_{*,i}^2 + r^2}}, \tag{4.1}$$

where M_* is the total stellar mass, G is the gravitational constant and r is the radial distance from the centre of the cluster. A similar equation can be written to describe the gas potential $\phi_{\rm G}$ by substituting $a_{*,i}$ with $a_{\rm G}$ and M_* with $M_{\rm G,0}$, where $M_{\rm G,0}$ is the total amount of gas falling inside the SC. We define $\phi_{\rm G}$ the gravitational potential associated to the gas. The total initial potential $\phi_i \equiv \phi_{*,i}$ since gas has not fallen inside the SC yet.

Our aim is to provide an analytical estimate of the value of the stellar scale radius after the infall of a mass $M_{\rm G,0}$ of gas settling on a gas scale radius $a_{\rm G}$. We call $a_{*,f}$ the final stellar scale radius and $\sigma_{*,i}$ and $\sigma_{*,f}$ the initial and final velocity dispersion, respectively. We can easily write the final gravitational potential ϕ_f as the sum of the final star potential and of the gas potential

$$\phi_f(r) = -\frac{M_* G}{\sqrt{a_{*,f}^2 + r^2}} - \frac{M_{\rm G,0} G}{\sqrt{a_{\rm G}^2 + r^2}}. \tag{4.2}$$

We start by considering the conservation of the angular momentum of a star which has an initial distance $R_i = a_{*,i}$ from the centre and will have, for consistence, a final distance $R_f = a_{*,f}$ after the gas infall

$$V_{{\rm circ},f}(a_{*,f}) a_{*,f} = V_{{\rm circ},i}(a_{*,i}) a_{*,i}, \tag{4.3}$$

where $V_{{\rm circ},i}$ and $V_{{\rm circ},f}$ are the velocities of the considered star in a circular orbit at radius $a_{*,i}$ and $a_{*,f}$ before and after the gas infall, respectively. In general, the circular

[1] By definition, for the case of absence of physical interactions each result is independent by the choice of the IMF.

velocity $V_{\rm circ}$ of a test particle in a circular orbit at radius r is related to the norm of the gravitational field $||\mathbf{g}||$

$$||\mathbf{g}|| = \frac{V_{\rm circ}^2}{r}. \tag{4.4}$$

Thanks to the spherical symmetry of the system we observe that the gravitational potential ϕ is function only of the radial distance r and can be easily related to the norm of the gravitational field ($||\mathbf{g}|| = d\phi/dr$). So, we obtain the link between the potential ϕ and circular velocity $V_{\rm circ}$

$$V_{\rm circ}^2 = r\frac{d\phi}{dr}. \tag{4.5}$$

By calculating $V_{{\rm circ},i}$ and $V_{{\rm circ},f}$ by using Eq. (4.5), we can exploit the angular momentum conservation of Eq. (4.3) and, in this way, we obtain an implicit expression that links the stellar scale radius $a_{*,f}$ after the gas infall with $a_{*,i}$ (before the infall)

$$a_{*,f}^4(a_{\rm G}, M_{\rm G,0}) = \frac{M_*}{2^{3/2}}\left(\frac{M_*}{2^{3/2}a_{*,f}^3(a_{\rm G}, M_{\rm G,0})} + \frac{M_{\rm G,0}}{(a_{*,f}^2(a_{\rm G}, M_{\rm G,0}) + a_{\rm G}^2)^{3/2}}\right)^{-1} a_{*,i}. \tag{4.6}$$

By defining

$$\alpha_* = \frac{a_{*,f}}{a_{*,i}},\ \ \alpha_{\rm G} = \frac{a_G}{a_{*,i}},\ \ \beta_* = \frac{\sigma_{*,f}}{\sigma_{*,i}},\ \ W_{\rm G} = \frac{M_{\rm G,0}}{M_*}, \tag{4.7}$$

Eq. (4.6) can be rewritten in the dimensionless form

$$\alpha_*^4(\alpha_{\rm G}, W_{\rm G}) = \frac{1}{2^{3/2}}\left(\frac{1}{2^{3/2}\alpha_*^3(\alpha_{\rm G}, W_{\rm G})} + \frac{W_{\rm G}}{(\alpha_*^2(\alpha_{\rm G}, W_{\rm G}) + \alpha_{\rm G}^2)^{3/2}}\right)^{-1}. \tag{4.8}$$

Eq. (4.8) relates the relative reduction of the scale radius α_* (with respect to a generic $a_{*,i}$) with the relative gas scale radius $\alpha_{\rm G}$ (with respect to a generic $a_{*,i}$) as a function of different relative amounts of gas $W_{\rm G}$ (with respect to a generic M_*). For completeness, β_* represents the relative increase of the velocity dispersion (with respect to a generic $\sigma_{*,i}$). In this way, we obtain an expression (4.8) which is valid for a SC of whatever mass M_* and scale radius $a_{*,i}$.

The implicit equation (4.8) can be solved numerically.

We model the gas infall as

$$M_{\rm G}(t) = \frac{M_{\rm G,0}}{2}\left[1 + {\rm erf}\left(\frac{t - t_0}{\sqrt{2}\tau}\right)\right], \tag{4.9}$$

where $M_{\rm G,0}$ is the total amount of gas falling in the SC, t_0 is the time at which the gas infall happens and τ measures the infall duration. We tried several choices for the duration τ (from small fractions of the crossing time to small fractions of the relaxation time) but there is no appreciable difference in the final results.

The analytic treatment allows us to infer $a_{*,f}$, but other information is still missing. For example, we do not know how does the velocity dispersion evolve and how the SC as a whole does contract. In order to obtain this information, we performed several simulations of SCs with the properties mentioned above by using the code `MYSCE` which is based on the Monte Carlo method presented in Chapter 2. We considered SCs of $N = 10^4$ stars with initial scale radius $a_{*,i} = 1\,\mathrm{pc}$. For these simulations we turned off two- and three-body interactions in `MYSCE`. In our simulations we introduced an amount of gas equal, two times, five times, and ten times the total stellar mass of the SC. The left, and the right panel of Fig. 4.1 show the behaviour of the stellar scale radius after the infall of the gas with different choices of the gas scale radius and of the total amount of gas in our analytical estimate and in our performed simulation, respectively. Fig. 4.2 shows the simulated behaviour of the velocity dispersion of the cluster stars once gas infall occurs as a function of the gas scale radius and of the total amount of gas.

We can have a zero-order check of the correctness of the behaviour of β_* thanks to the virial theorem. The SC is in virial equilibrium both before and after the gas infall. As a consequence, by calling $E_{\mathrm{k},i} \sim 0.5 M_* \sigma_{*,i}^2$ and $E_{\mathrm{k},f} \sim 0.5 M_* \beta_*^2 \sigma_{*,i}^2$ the initial and final (after the gas infall) SC kinetic energy and $U_i \sim -GM_*^2/a_{*,i}$ and $U_f \sim -GM_*^2(1 + W_\mathrm{G})/(\alpha_* a_{*,i})$ the initial and final (after the gas infall) SC potential energy, from Eq. (1.8) we infer

$$\beta_*^2 \sigma_{*,i}^2 = G\frac{M_*(1+W_\mathrm{G})}{\alpha_* a_{*,i}}, \;\; \sigma_{*,i}^2 = G\frac{M_*}{a_{*,i}}. \tag{4.10}$$

By dividing the first expression by the second one we get

$$\beta_* = \sqrt{\frac{1+W_\mathrm{G}}{\alpha_*}}. \tag{4.11}$$

This zero-order estimate is in a rather good agreement with Fig. 4.2 for low values of α_G, between 10^{-2} and 10^{-1}. For higher values, Eq. (4.11) becomes progressively less accurate since the gas is less concentrated and W_G becomes a function of α_G. We can explain the right part of Fig. 4.2 by observing that a gas with a very low density (with respect to the SC one) is unable to shrink the system and increase its velocity dispersion. For values of α_G between 10^{-2} and 10^{-1} (where the analytical estimate makes sense) the relative error between data from simulation and analytical estimate reads $|\beta_{*,\mathrm{theor}} - \beta_{*,\mathrm{simul}}|/\beta_{*,\mathrm{theor}} \sim 0.1 - 0.15$.

We conclude this section by considering a measure of the efficiency of the gas infall to shrink the SC and to increase its velocity dispersion. We can relate $a_{*,f}$ with $a_{*,i}$, M_*,

and $M_{\mathrm{G},0}$ and define the contraction parameter according to

$$a_{*,f}(a_{\mathrm{G}}, M_{\mathrm{G}}) = a_{*,i}\left(\frac{M_* + M_{\mathrm{G},0}}{M_*}\right)^{-\xi(a_{\mathrm{G}}, M_{\mathrm{G},0})} . \tag{4.12}$$

The behaviour of the simulated contraction parameter ξ as a function of different values of the gas scale radius and of the total amount of gas is shown in Fig. 4.3. We can also relate $\sigma_{*,f}$ with $\sigma_{*,i}$, M_*, and $M_{\mathrm{G},0}$ and define the velocity gain parameter according to

$$\sigma_{*,f}(a_{\mathrm{G}}, M_{\mathrm{G}}) = \sigma_{*,i}\left(\frac{M_* + M_{\mathrm{G},0}}{M_*}\right)^{\eta(a_{\mathrm{G}}, M_{\mathrm{G},0})} . \tag{4.13}$$

The behaviour of the simulated velocity gain parameter η as a function of different values of the gas scale radius and of the total amount of gas is shown in Fig. 4.4.

In the absence of other physical interactions (two- and three-body interactions), gas infall is able to shrink the SC allowing an increase of its density and velocity dispersion. By taking $a_{\mathrm{G}} = a_{*,i}$, a glance at Fig. 4.1 allows us to infer that a gas infall of $M_{\mathrm{G},0}$ interior to the orbit of a star is unable to shrink the orbit of $M_*/M_{\mathrm{G},0}$ times its initial size (i.e. before the gas infall). In order to obtain a major contraction for the SC, lower values of a_{G} must be considered. A similar conclusion can be inferred for the velocity dispersion $\sigma_{*,f}$: Fig. 4.2 demonstrates that only a large amount of concentrated gas ($a_{\mathrm{G}} < a_{*,i}$) can increase the initial velocity dispersion $\sigma_{*,i}$ more than one order of magnitude. Fig. 4.3 shows that a low gas infall is more efficient in shrinking the SC allowing higher values for the parameter ξ.

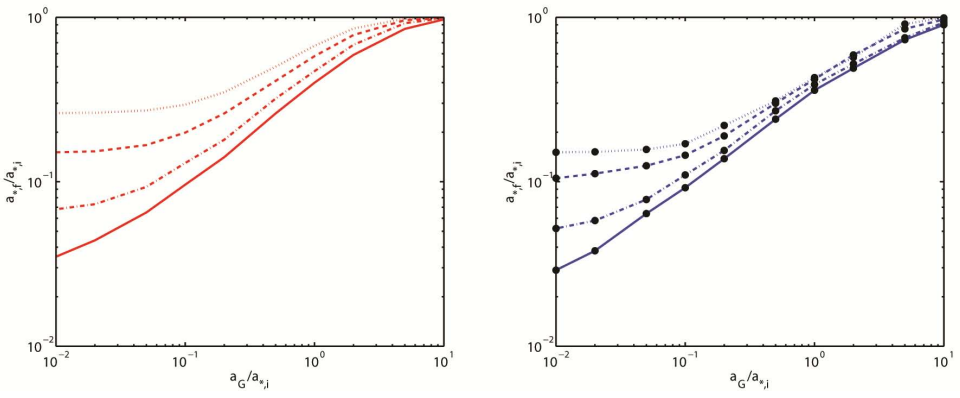

FIGURE 4.1: Theoretical estimate (left panel) and simulation results (right panel) of the final stellar scale radius $a_{*,f}$ after gas infall for different choices of the gas scale radius a_{G}. $a_{*,f}$ and a_{G} are in units of the initial stellar scale radius $a_{*,i}$. From top to bottom curves refer to $M_{\mathrm{G},0} = 1, 2, 5, 10\, M_*$.

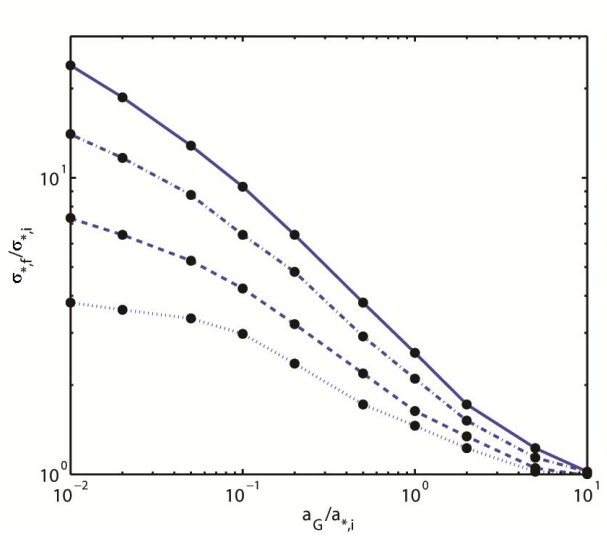

FIGURE 4.2: Final stellar velocity dispersion $\sigma_{*,f}$ after gas infall for different choices of the gas scale radius $a_{\rm G}$, as obtained from the numerical simulations. $\sigma_{*,f}$ is in units of the initial stellar velocity dispersion $\sigma_{*,i}$ and $a_{\rm G}$ is in units of the initial stellar scale radius $a_{*,i}$. From bottom to top curves refer to $M_{\rm G,0} = 1, 2, 5, 10\, M_*$.

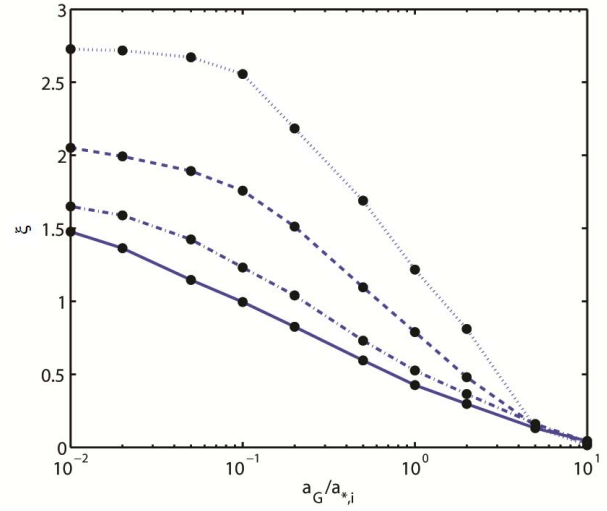

FIGURE 4.3: Contraction parameter ξ after gas infall for different choices of the gas scale radius $a_{\rm G}$, as obtained from the numerical simulations. $a_{\rm G}$ is in units of the initial stellar scale radius $a_{*,i}$. From top to bottom curves refer to $M_{\rm G,0} = 1, 2, 5, 10\, M_*$.

4.3 Gas infall in the presence of physical interactions

In this section we want to inquire the consequences of gas infall on different types of SCs when two- and three-body interactions are considered. In particular, we want to understand if a physically reasonable gas infall is able to increase the SC velocity dispersion to the extent that hard binaries cannot heat the system and slow down the core collapse. If this were the case, conditions for stellar/BH runaway merging [21] would be possible. While in [21] only very massive SCs ($\sim 10^6\,{\rm M}_\odot$) are considered,

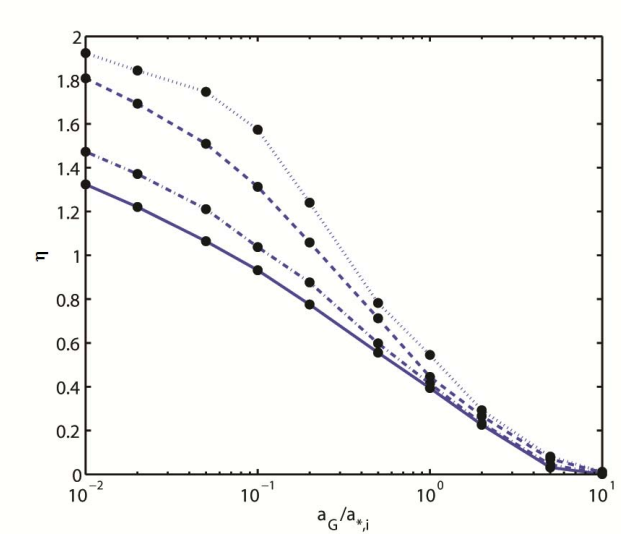

FIGURE 4.4: Velocity gain parameter η after gas infall for different choices of the gas scale radius $a_{\rm G}$, as obtained from the numerical simulations. $a_{\rm G}$ is in units of the initial stellar scale radius $a_{*,i}$. From top to bottom curves refer to $M_{\rm G,0} = 1, 2, 5, 10\, M_*$.

we extend this possibility also to YSCs ($\sim 10^4 - 10^5\,{\rm M}_\odot$). In particular, we want to understand if the mechanism [21] may be used to produce IMBHs inside unevolved YSCs (i.e. before feedback effects due to stellar evolution happen – with characteristic time $t_{\rm se} \sim 3 - 5\,{\rm Myr}$ for the Salpeter IMF upper limit $\sim 120\,{\rm M}_\odot$) – helping the mechanism of runaway merging of main-sequence stars [26, 43, 44, 83, 85] – and/or it may be used to form SMBH seeds ($\sim 10^4 - 10^5\,{\rm M}_\odot$) inside already evolved massive SCs ($\sim 10^6\,{\rm M}_\odot$) via runaway merging of compact objects [21].

We describe all the SCs by a Plummer model. As a first step, we do not consider three-body interactions: in this case, we can estimate the variation of the core collapse time $t_{\rm cc}$ after the gas infall by using the expression of the local relaxation time $t_{\rm rel}$ of Eq. (1.51), recalling that the core collapse time $t_{\rm cc} \simeq 0.15 - 0.2\, t_{\rm rel}$ for multi-mass systems (see Chapter 1 Sec. 1.3.2) and using information about the decrease of the stellar radius and increase of velocity dispersion due to the gas infall (see Figs. 4.1 and 4.2). The results are plotted in Fig. 4.5: we infer that $t_{\rm cc}$ decreases in the presence of gas infall with a mass $M_{\rm G,0}$ in the range $1 - 10\, M_*$ and a gas scale radius $a_{\rm G} = 0.1 - 1\, a_{*,i}$ and in the absence of three-body interactions – three-body encounters could heat the SC and increase the core-collapse time estimated without them. The rate of decrease of $t_{\rm cc}$ slows down as the total mass of the gas falling into the SCs grows.

Let us now consider also three-body interactions by starting from YSCs analyzed at their birth – when more massive stars have not evolved yet.

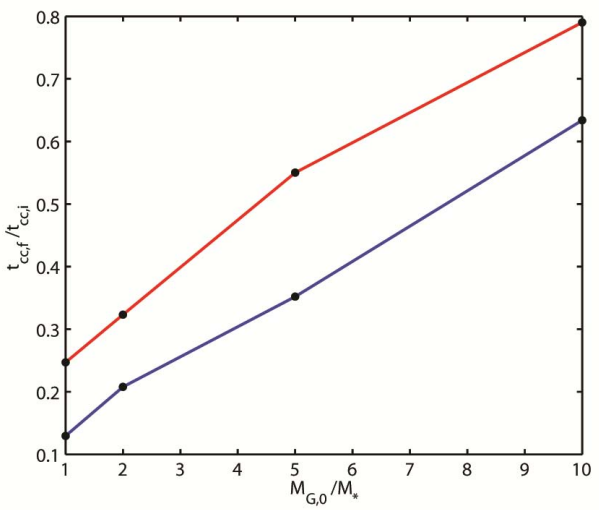

FIGURE 4.5: Core-collapse time (calculated in the absence of three-body interactions) after gas infall as a function of the mass $M_{\rm G,0}$ of the gas and of the gas scale radius $a_{\rm G}$. The final core-collapse time $t_{{\rm cc},f}$ is in units of the initial core-collapse time $t_{{\rm cc},i}$. Lower curve refers to the case $\alpha_{\rm G} = 0.1$, upper curve to the case $\alpha_{\rm G} = 1$

4.3.1 Young star clusters

We consider two YSCs of $N = 10^4$ and $N = 10^5$ stars. Both the YSCs are described by a Plummer profile with initial scale radius $a_{*,i} = 1\,{\rm pc}$, a Salpeter IMF in the mass range $0.2 - 120\,{\rm M}_\odot$, initial velocity dispersion $\sigma_{*,i} \sim 3.5\,{\rm km/s}$ for $N = 10^4$ and $\sigma_{*,i} \sim 10\,{\rm km/s}$ for $N = 10^5$ stars [2] and a ratio of 10% of (primordial) binaries with semi major axis a in the range $0.5 - 10^3\,{\rm AU}$ [3] (for more details about initial conditions see Chapter 3).

We consider the best possible physically consistent case of gas infall: a gas infall of mass $M_{\rm G,0}$ equal to ten times the total stellar mass of the cluster ($M_{\rm G,0} \sim 10^5\,{\rm M}_\odot$ for the YSC of $N = 10^4$ stars and $M_{\rm G,0} \sim 10^6\,{\rm M}_\odot$ for the YSC of $N = 10^5$ stars) and a gas scale radius a_G equal to one tenth of $a_{*,i}$ ($a_{\rm G} = 0.1\,{\rm pc}$). For these values of gas infall we can estimate the reduction of the stellar scale radius and the increase of the stellar velocity dispersion from Figs. 4.1 and 4.2. We have $\alpha_* \sim 0.1$ and $\beta_* \sim 10$ and from Eqs. (4.7) we expect a final stellar scale radius $a_{*,f} \sim 0.1\,{\rm pc}$ and final velocity dispersion $\sigma_{*,f} \sim 35\,{\rm km/s}$ for $N = 10^4$ stars and $\sigma_{*,f} \sim 100\,{\rm km/s}$ for $N = 10^5$ stars after the gas infall. Higher gas masses and/or higher gas concentrations appear to be

[2] These are typical values for YSCs [103].

[3] These are plausible values for semi major axes distribution [21]. Harder primordial binaries (a down to $\sim 0.001\,{\rm AU}$ [25, 60]) are used in the literature. Anyway, the real semi major axis distribution remains rather uncertain. We use a softer initial distribution in order to avoid starting from extreme initial conditions. In fact, if this were instead the case, a physical reasonable gas infall could not destroy hard binaries.

TABLE 4.1: Calculation of the relaxation time $t_{\rm rel}$, core-collapse time $t_{\rm cc}$ and single star-binary interaction time t_{2+1} ($m_1 = 10\,{\rm M}_\odot, m_2 = m_3 = 1\,{\rm M}_\odot$) for the two cases of a YSCs of $N = 10^4$ and 10^5 stars in the presence/absence of gas infall ($M_{\rm G,0} = 10\,M_*$, $a_{\rm G} = 0.1\,a_{*,i}$). a_* and σ_* are the initial scale radius (gas, no) and after gas infall (gas, yes). We consider the two cases: (i) we calculate the hardness ratio x starting from the semi major axis lower limit $a = 0.5\,{\rm AU}$ (initial condition) and (ii) we calculate which is a for the case $x = 1$.

N	a_* [pc]	σ_* [km/s]	$t_{\rm rel}$ [yr]	$t_{\rm cc}$ [yr]	a [AU]	x	t_{2+1} [yr]	gas
10^4	1	3.5	$5\cdot10^7$	$8\cdot10^6$	0.5	1500	10^9	no
10^4	1	3.5	$5\cdot10^7$	$8\cdot10^6$	700	1	$6\cdot10^5$	no
10^4	0.1	35	$3\cdot10^7$	$5\cdot10^6$	0.5	15	10^4	yes
10^4	0.1	35	$3\cdot10^7$	$5\cdot10^6$	7	1	$6\cdot10^2$	yes
10^5	1	10	10^8	$1.5\cdot10^7$	0.5	200	$6\cdot10^8$	no
10^5	1	10	10^8	$1.5\cdot10^7$	100	1	$2\cdot10^6$	no
10^5	0.1	100	$6\cdot10^7$	10^7	0.5	2	$5\cdot10^3$	yes
10^5	0.1	100	$6\cdot10^7$	10^7	1	1	$2\cdot10^3$	yes

physically rather unreasonable at present epoch (redshift $z \sim 0$) [4]. We assume that gas falls in the SC in the first $\sim 3-5\,{\rm Myr}$ so that feedback effects due to stellar evolution (i.e. supernova explosions) have not happened yet. As a result, we can ignore stellar evolution and metallicity effects.

By using Eq. (1.51) we can calculate the relaxation time before, $t_{{\rm rel},i}$, and after, $t_{{\rm rel},f}$, the gas infall and by remembering $t_{\rm cc} \simeq 0.15 - 0.2\,t_{\rm rel}$ for multi-mass systems (see Chapter 1 Sec. 1.3.2) we can evaluate the corresponding core-collapse time (calculated in the absence of three-body interactions) $t_{{\rm cc},i}$ and $t_{{\rm cc},f}$. By using Eq. (1.57) and (1.61) we can evaluate the hardness ratio before, x_i, and after, x_f, the gas infall and the corresponding single star-binary interaction time $t_{2+1,i}$ and $t_{2+1,f}$. For the calculation of the hardness ratio and of the single star-binary interaction time we consider a typical single star of $m_3 = 1\,{\rm M}_\odot$ and relative velocity of the order of the velocity dispersion, and a typical binary with stellar masses $m_1 = 10\,{\rm M}_\odot$ and $m_2 = 1\,{\rm M}_\odot$. In Table 4.1 we report all these quantities before and after gas infall for both the YSCs of $N = 10^4$ and $N = 10^5$ stars. For the SC with $N = 10^4$ stars and for the same choice of m_1, m_2 and m_3 in Fig. 4.6 we plot the interaction time as a function of different relative velocities ($\sim$ velocity dispersion) for the semi major axes lower ($a = 0.5\,{\rm AU}$) and upper ($a = 1000\,{\rm AU}$) limits and for the fixed hardness ratio $x = 1$.

From Table 4.1 and Fig. 4.6 we infer that in the case $N = 10^4$ without gas infall, we

[4] We restrict to the simulations by [72] which suggest that self-gravitating gas is subject to instabilities that drive it to the SC centre with low angular momentum: the bulk of the gas gets as close as 0.2 pc or even closer to the centre. Turbulence prevents the gas from fragmentation into stars. Other authors claim that such possibility is however quite difficult to get [27].

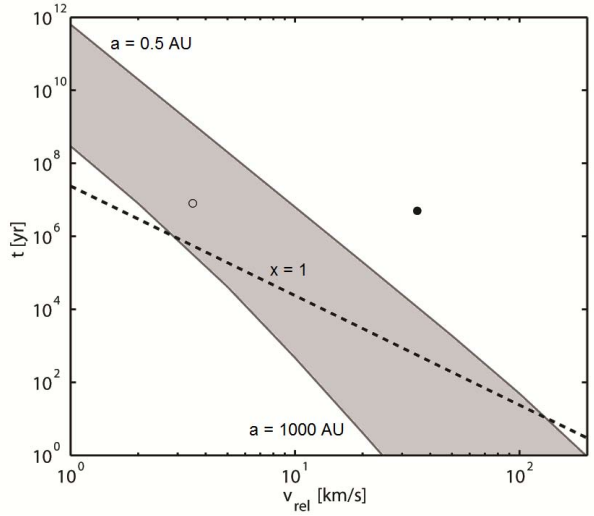

FIGURE 4.6: Interaction time as a function of different relative velocities ($\sim$ velocity dispersion) for the semi major axes lower ($a = 0.5\,\mathrm{AU}$) and upper ($a = 1000\,\mathrm{AU}$) limits and for the fixed hardness ratio $x = 1$, for the SC with $N = 10^4$ stars and for $m_1 = 10\,\mathrm{M}_\odot$, $m_2 = m_3 = 1\,\mathrm{M}_\odot$. Open circle represents the core-collapse time (calculated in the absence of three-body interactions) before gas infall. Filled circle represents the core-collapse time (calculated in the absence of three-body interactions) after gas infall.

expect the system to experience the core collapse at a time $\sim t_{\mathrm{cc},i}$ [5] since the hardest binaries have an extremely long interaction time $t_{2+1,i}$ – they do not interact with single stars before core collapse – and the moderate-hard binaries ($x_i \gtrsim 1$) are only a few because of the initial semi-major axis distribution (see Chapter 3 Sec. 3.3). As a result, binaries cannot heat the system. If we consider gas infall, we reduce the initial core-collapse time $t_{\mathrm{cc},i}$ (calculated in the absence of three-body interaction) and we reduce the binary hardness ratio ($x_f \ll x_i$). However, also the final single star-binary interaction time $t_{2+1,f}$ is smaller than the initial one $t_{2+1,i}$ and also than $t_{\mathrm{cc},f}$ (see Table 4.1 and Fig. 4.6). As a result, all binaries that are still hard ($x_f > 1$) after gas infall now interact with the single stars (see Fig. 4.6) and the core collapse is slowed down.

From this simple scaling we find that gas infall does not help the runaway merger of main sequence stars [26, 43, 44, 83, 85]. In fact, the bulk of stellar collisions and mergers happens when approaching deep core collapse but this latter is slowed down by binaries which heat the system. The resulting core-collapse time grows to an extent that it becomes greater than the most massive star evolution time t_{se} (see Chapter 1 Sec. 1.3.5): if we included metallicity dependence and stellar evolution, feedback effects due

[5] In a SC of $N = 10^4$ stars we expect the most massive stars to have mass $\lesssim 30\,\mathrm{M}_\odot$. Moreover, the number of massive stars ($> 10\,\mathrm{M}_\odot$) is very low because of the Salpeter IMF (see Chapter 3 Sec. 3.2). As a consequence, the actual t_{se} is greater than 10 Myr (the value $t_{\mathrm{se}} \sim 3 - 5\,\mathrm{Myr}$ is calculated for the Salpeter IMF upper limit $\sim 120\,\mathrm{M}_\odot$ – but, so massive stars are not present inside a SC of $N = 10^4$ stars). In conclusion, $t_{\mathrm{cc},i}$ ($\sim 8\,\mathrm{Myr}$, see Table 4.1) is smaller than the actual t_{se} ($> 10\,\mathrm{Myr}$) for a SC of $N = 10^4$ stars.

TABLE 4.2: Same as Table 4.1 but with a gas infall of $M_{\rm G,0} = 5\,M_*$ and $a_{\rm G} = a_{*,i}$.

N	a_* [pc]	σ_* [km/s]	$t_{\rm rel}$ [yr]	$t_{\rm cc}$ [yr]	a [AU]	x	t_{2+1} [yr]	gas
10^4	1	3.5	$5 \cdot 10^7$	$8 \cdot 10^6$	0.5	1500	10^9	no
10^4	1	3.5	$5 \cdot 10^7$	$8 \cdot 10^6$	700	1	$6 \cdot 10^5$	no
10^4	0.4	7	$3 \cdot 10^7$	$4 \cdot 10^6$	0.5	350	$4 \cdot 10^7$	yes
10^4	0.4	7	$3 \cdot 10^7$	$4 \cdot 10^6$	180	1	$7 \cdot 10^4$	yes
10^5	1	10	10^8	$1.5 \cdot 10^7$	0.5	200	$6 \cdot 10^8$	no
10^5	1	10	10^8	$1.5 \cdot 10^7$	100	1	$2 \cdot 10^6$	no
10^5	0.4	20	$5 \cdot 10^7$	$8 \cdot 10^6$	0.5	50	$2 \cdot 10^7$	yes
10^5	0.4	20	$5 \cdot 10^7$	$8 \cdot 10^6$	20	1	$3 \cdot 10^5$	yes

to the most massive stars would prevent the system from reaching a deep core collapse (see Chapter 1 Sec. 1.3.5). As a result, the runaway merger of main sequence stars is excluded.

All conclusions for the system with $N = 10^4$ stars can be applied to the case $N = 10^5$. In addition, in this case, the final core-collapse time $t_{{\rm cc},f}$ (even not considering three-body heating which would slow down the resulting core-collapse time) is longer than the stellar evolution time ($t_{\rm se} \sim 3 - 5\,$Myr), so that it is impossible for the SC to experience a runaway growth of main-sequence stars before feedback effects due to stellar evolution halt the core collapse [26, 43, 44, 83, 85]. In this case, the gas is unable to soften efficiently the binaries but even if this were the case, the core-collapse time would be too long ($t_{{\rm cc},f} > t_{\rm se}$).

We considered also a more conservative case of gas infall ($M_{\rm G,0} = 5\,M_*$, $a_{\rm G} = a_{*,i}$) but our conclusions are the same both for the system of $N = 10^4$ stars and $N = 10^5$ stars (see Table 4.2).

We performed a simulation with our code `MYSCE` in the case $N = 10^4$ and a gas infall of $M_{\rm G,0} = 10\,M_*$ and with $a_{\rm G} = 0.1\,a_{*,i}$ to test our conclusions. The evolution of binary semi major axes is shown in Fig. 4.7 in the absence of gas infall and in Fig. 4.8 in the presence of gas infall. The evolution of SC Lagrangian radii is shown in Fig. 4.9 in the absence of gas infall and in Fig. 4.10 in the presence of gas infall. We observe that our predictions are confirmed: from Figs. 4.9 and 4.10 we observe that the core collapse-time in the absence of gas infall happens at $\sim 8\,$Myr (as calculated in Table 4.1) while the gas infall increases this time to $\sim 30\,$Myr. By comparing Figs. 4.7 and 4.8 we conclude that only a few binaries are destroyed by the gas infall. A larger fraction of them can interact with single stars since the interaction time gets reduced (see Table 4.1). This is why the core-collapse time is increased after gas infall. By comparing Figs. 4.7 and 4.8 we observe that gas infall reduces the number of hard binaries ($x > 1$): in fact, the vertical line ($x = 1$) of Fig. 4.7 moves to the left in Fig. 4.8. In both Figs. 4.7 (in the

absence of gas infall) and 4.8 (in the presence of gas infall) binaries with $x < 1$ (i.e. to the right of the $x = 1$ line) are soft and tend to be destroyed by three-body encounters as the right panels of Figs. 4.7 and 4.8 show. By comparing right panels of Figs. 4.7 and 4.8 we observe that in the presence of gas infall the final number of binaries decreases. The reason for this decrease is that in the presence of gas infall all binaries interact and a higher number is now soft and can be destroyed. Moreover, in our simulation we observe that in the presence of gas infall a greater number of stellar systems (single or binary – both hard and soft) can become unbound and leave the SC (see Chapter 2 Sec. 2.2.7) [6]. As already stressed the remaining hard binaries, now interacting, slow down the core-collapse time.

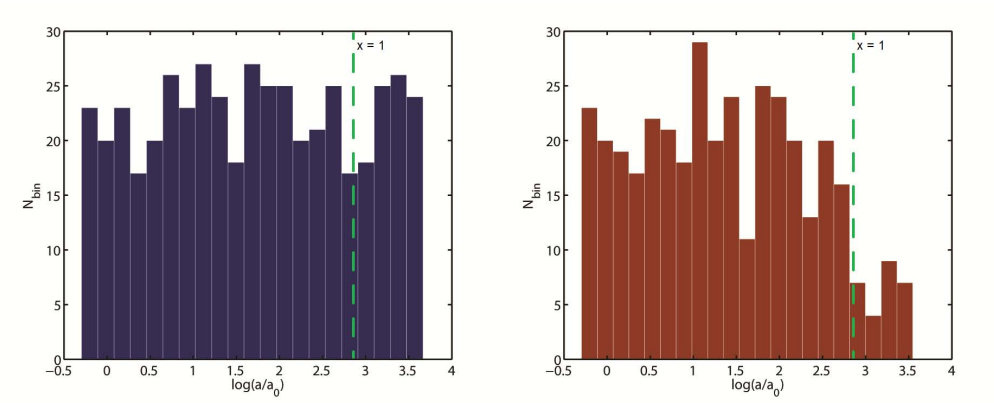

FIGURE 4.7: Evolution of the binary semi major axes a in a YSC of $N = 10^4$ stars, with $a_{*,i} = 1\,\mathrm{pc}$ without gas infall. a is in units of $a_0 = 1\,\mathrm{AU}$. Left panel represents the initial semi major axis distribution, right panel represents the semi major axis distribution at core-collapse time ($\sim 8\,\mathrm{Myr}$, see Fig. 4.9). The vertical dashed line represents the boundary ($x = 1$) between hard ($x > 1$, on the left) and soft ($x < 1$, on the right) binaries.

We can conclude that the mechanism proposed by [21] is not efficient to improve the runaway merger of main-sequence stars [26, 43, 44, 83, 85]. As a result, a gas infall with the properties considered here cannot help in the formation of IMBHs inside YSCs.

4.3.2 Massive star clusters

In this section we study the case of a massive SC of $N = 10^6$ stars (i.e. a very massive GC) with the same strategy used for the YSC case. However, we do not perform a

[6] The reason for this higher evaporation rate could be explained as follows. Even in the absence of gas infall in each time step a very small number of stars can have positive total energy. These stars are removed from the system because they become unbound (for more details see Chapter 2 Sec. 2.2.7). The rate of evaporation is roughly proportional to the number of stars in a system. Therefore, systems with a higher number of stars have a higher number of unbound stars in each step. Gas infall increases velocity dispersion and, in this way, makes the evolution of a system of N stars similar to that of a system with a much higher number of stars. As a result, the system experiences a higher evaporation rate.

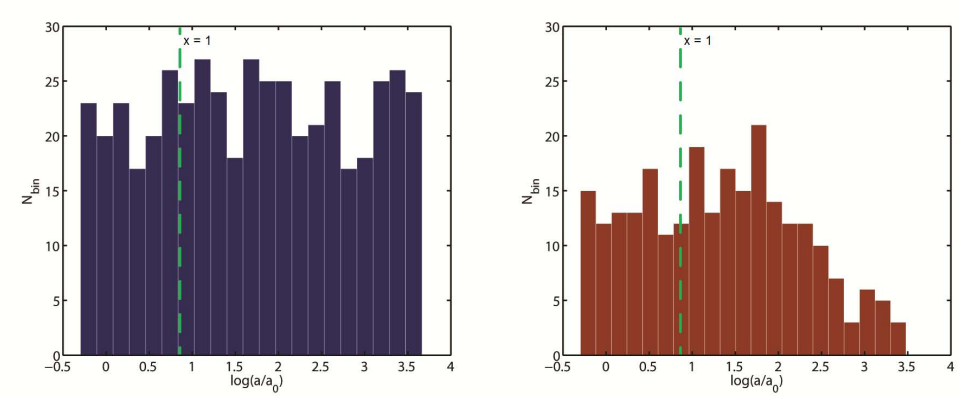

FIGURE 4.8: Same as Fig. 4.7 but now in the presence of a gas infall with $M_{\rm G,0} = 10\,M_*$ and $a_{\rm G} = 0.1\,$pc. In the right panel we plot semi major axis distribution at core-collapse time ($\sim 30\,$Myr, see Fig. 4.10).

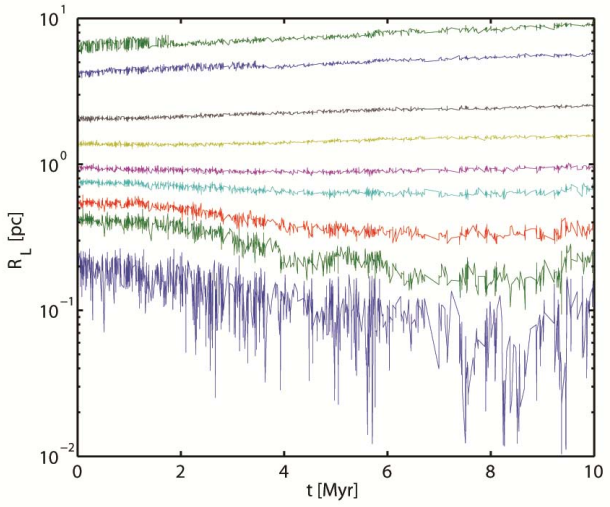

FIGURE 4.9: Evolution of the Lagrangian radii of a YSC of $N = 10^4$ stars, with $a_{*,i} = 1\,$pc without gas infall. From bottom to top, lines represent the Lagrangian radii corresponding to 0.5%, 5%, 10%, 20%, 30%, 50%, 70%, 90%, 95% of the mass of the system, respectively.

simulation for reasons of computational time (more further). We consider this system so as to inquire if it can be a possible environment for the formation of SMBH seeds ($\sim 10^5\,{\rm M}_\odot$). A caveat is necessary: we now consider an evolved system, where the most massive stars have already produced stellar-mass BHs which are located in the centre because of the mass segregation process (see Chapter 1 Sec. 1.3.2). The result is the formation of a subcluster formed by stellar-mass BHs in the centre. The evolution of the most massive stars has another important consequence on SCs: the mass range is greatly reduced. If for young systems stellar masses are distributed between $\sim 0.2 - 120\,{\rm M}_\odot$, now they are in the range $\sim 0.2 - 2\,{\rm M}_\odot$. Instead, the BH subcluster should contain BHs with a mass range $\sim 5 - 20\,{\rm M}_\odot$. The consequence of the reduction of the width of the mass range is an increase of the core-collapse time (calculated in the absence

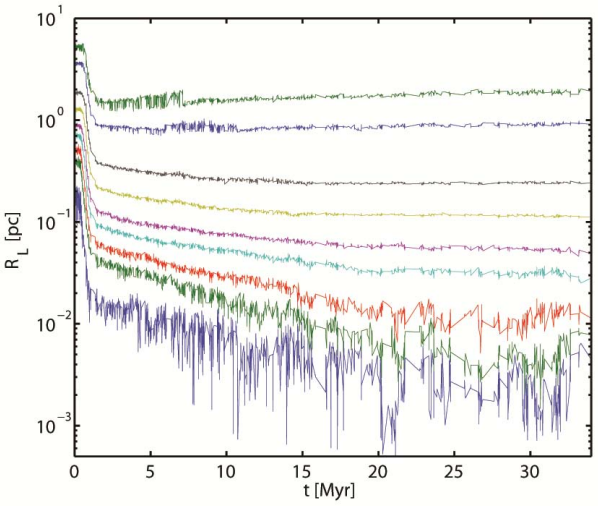

FIGURE 4.10: Same as Fig. 4.9 but now in the presence of a gas infall with $M_{\rm G,0} = 10\,M_*$ and $a_{\rm G} = 0.1\,{\rm pc}$.

of three-body interactions). We must remember that three-body interactions involving hard BH binaries can lead to the ejection of BHs from the subcluster and that this process can lead to complete evaporation of the BH core within $\sim 10^9\,{\rm yr}$ (see Sec. 4.1) [23, 24, 80]. As a result, gas infall must happen at an epoch between the segregation time (so that the BH subcluster has already formed) and the BH subcluster evaporation time (in order to play efficiently its role). Therefore, we consider this massive SC in the past (at redshift $z \sim 6$).

The SC we study is described by a Plummer profile with initial scale radius $a_{*,i} = 1\,{\rm pc}$, initial velocity dispersion $\sigma_{*,i} \sim 30\,{\rm km/s}$ [7]. The subcluster of BHs is very dense (with a scale radius $a_{{\rm BH},i} \sim 0.1\,{\rm pc}$) and formed by $N_{\rm BH} \sim 10^3$ BHs. Its velocity dispersion is $\sigma_{{\rm BH},i} \sim 35\,{\rm km/s}$. For the BH subscuster we consider a mass function constant between $5\,{\rm M}_\odot$ and $20\,{\rm M}_\odot$. We take a ratio of 10% of subcluster BH binaries with semi major axis a in the range $0.1 - 100\,{\rm AU}$ [8]. We concentrate on the evolution of the BH subcluster.

We consider the best possible physically consistent case of gas infall: a gas infall of mass $M_{\rm G,0}$ equal to ten times the total stellar mass of the cluster ($M_{\rm G,0} \sim 10^7\,{\rm M}_\odot$) and a gas scale radius $a_{\rm G}$ equal to two tenths of $a_{*,i}$ ($a_{\rm G} = 0.2\,{\rm pc}$). We want to consider the effects of the gas infall on the BH subcluster: we get $\alpha_* \sim 0.15$ and $\beta_* \sim 6$ (see Figs. 4.1 and 4.2) and from Eqs. (4.7) we get a final BH scale radius $a_{{\rm BH},f} \sim 0.02\,{\rm pc}$ and final velocity dispersion $\sigma_{{\rm BH},f} \sim 200\,{\rm km/s}$. Higher gas masses and/or higher gas concentrations appear to be physically rather unreasonable at epoch $z \sim 6$. In this case, we limit to $a_{\rm G} = 0.2\,{\rm pc}$ since with $M_{\rm G,0} = 10^7\,{\rm M}_\odot$ the gas reaches central densities of

[7] These are plausible values for a very massive SC of $N = 10^6$ stars [103].

[8] These are plausible values for such SCs [21]. Harder BH binaries [23, 24] are also considered in the literature. We use a softer initial distribution for the same reason of Footnote 3.

TABLE 4.3: Same as Table 4.1 but with a gas infall of $M_{\rm G,0} = 10\,M_*$ and $a_{\rm G} = 0.2\,a_{*,i}$). In this case the SC is an evolved system, more massive stars have already gone out of the main-sequence. As a result, several BHs formed: we consider typical BH binaries ($m_1 = m_2 = 10\,{\rm M}_\odot$) in the centre ($a$, x, t_{2+1} are referred to them). We calculate also the BH binary coalescence time for gravitational radiation inspiral $t_{\rm gr}$. In addition, we calculate the segregation time $t_{\rm seg}$ instead of the core-collapse time.

N	a_* [pc]	σ_* [km/s]	$t_{\rm rel}$ [yr]	$t_{\rm seg}$ [yr]	a [AU]	x	t_{2+1} [yr]	$t_{\rm gr}$ [yr]	gas
10^6	1	30	$3\cdot10^8$	$3\cdot10^7$	0.1	100	$4\cdot10^9$	$7\cdot10^7$	no
10^6	1	30	$3\cdot10^8$	$3\cdot10^7$	10	1	$3\cdot10^7$	$7\cdot10^{15}$	no
10^6	0.15	200	$2\cdot10^8$	$2\cdot10^7$	0.1	3	$2\cdot10^5$	$7\cdot10^7$	yes
10^6	0.15	200	$2\cdot10^8$	$2\cdot10^7$	0.3	1	$8\cdot10^4$	$6\cdot10^9$	yes

$\sim 10^9\,{\rm M}_\odot/{\rm pc}^3$ – higher densities look unreasonable [9]. The gas infall duration is about $\sim 3\,{\rm Myr}$. Since we consider evolved SCs we can ignore stellar evolution and metallicity effects in first approximation.

Following the same strategy we used for the YSC case, we can infer the relaxation time, the segregation time (see Eq. (1.55) referred to a BH, we take $\langle m\rangle = 1\,{\rm M}_\odot$ and $m_* = M_{\rm BH} = 10\,{\rm M}_\odot$), the hardness ratio and the single star/BH-BH binary interaction time before and after the gas infall. The SC core collapse may have happened during the mass segregation phase but we are now interested to the BH subcluster. Since we consider BH binaries, we must consider also the binary coalescence time for gravitational radiation inspiral defined by [81] as

$$t_{\rm gr} \simeq \frac{10^{28}}{2}\left(\frac{m_{\rm BH}}{1{\rm M}_\odot}\right)\left(\frac{1{\rm km/s}}{v_{\rm rel}}\right)^8 x^{-4}(1-e^2)^{7/2}, \tag{4.14}$$

where $m_{\rm BH}$ is the BH mass – we take $m_{\rm BH} = 10\,{\rm M}_\odot$ – $v_{\rm rel}$ is the relative velocity which is of the order of the velocity dispersion, and e is the binary eccentricity – we take the median eccentricity $e_{\rm med} = 1/\sqrt{2}$. For the calculation of the hardness ratio and of the single star-binary interaction time we consider a typical single BH of $m_3 = 10\,{\rm M}_\odot$ and relative velocity of the order of the velocity dispersion, and a typical binary with BH masses $m_1 = m_2 = 10\,{\rm M}_\odot$. In Table 4.3 we report all these quantities before and after the gas infall for the BH subcluster. For the same choice of m_1, m_2 and m_3 in Fig. 4.11 we plot the interaction time and the gravitational radiation inspiral time as a function of different relative velocities ($\sim$ velocity dispersion). We consider two values for the semi major axes, i.e. the lower ($a = 0.1\,{\rm AU}$) and upper ($a = 100\,{\rm AU}$) limits of the distribution we adopt; finally, we consider the hardness ratio $x = 1$.

From Table 4.3 and Fig. 4.11 we observe that, in the absence of gas infall, the hardest binaries ($a \sim 0.1\,{\rm AU}$) have a gravitational radiation inspiral time $t_{\rm gr}$ smaller than their

[9] We consider [72], see Footnote 4. In addition such gas infalls are frequent at high redshift [11].

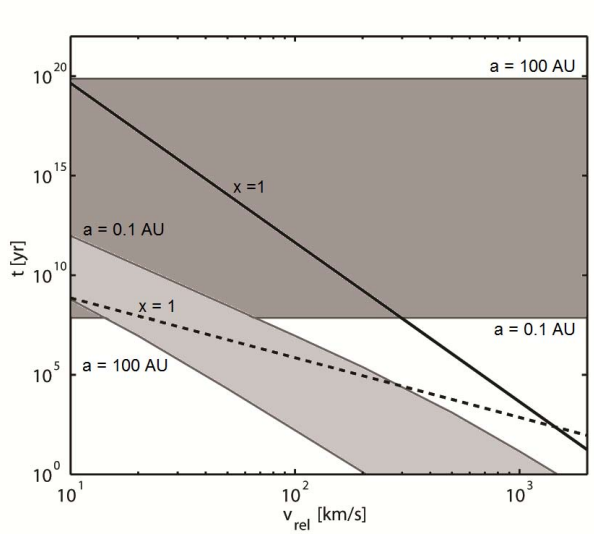

FIGURE 4.11: Interaction time (broken black line and light grey area) and gravitational radiation inspiral time (solid black line and dark grey area) as a function of different relative velocities ($\sim$ velocity dispersion) for the semi major axes lower ($a = 0.1\,\mathrm{AU}$) and upper ($a = 100\,\mathrm{AU}$) limits and for the fixed hardness ratio $x = 1$, for a SC of $N = 10^6$ stars and for $m_1 = m_2 = m_3 = 10\,\mathrm{M}_\odot$.

initial interaction time $t_{2+1,i}$ so that they coalesce before they can heat the SC. However, we expect anyway that, in the absence of gas infall, moderate-hard BH binaries ($x_i \gtrsim 1$) can heat the cluster, and produce BH ejection from the BH subcluster, through three-body interactions. In this way, they prevent the runaway merger of BHs in the dark core since their single star/BH-BH binary interaction time $t_{2+1,i}$ is smaller than $t_{\rm gr}$. In fact, $t_{\rm gr}$ for these moderate-hard binaries is too high to suppose that they coalesce before they can heat the cluster. If we consider gas infall, we observe that the hardness ratio gets reduced ($x_f < x_i$) and that the single star/BH-BH binary interaction time $t_{2+1,f}$ is smaller than the initial one $t_{2+1,i}$ for all binaries. $t_{\rm gr}$ remains constant, as expected and becomes much higher than the final interaction time $t_{2+1,f}$ for all binaries (see Table 4.3 and Fig. 4.11) so that single stars/BHs interact with BH binaries before they coalesce through gravitational radiation inspiral. We can conclude that a non-negligible fraction of hard BH binaries ($x_f > 1$) remains – however, they are not so hard ($x_f \lesssim 3$). In other words, the gas infall can help the BH runaway merger only if it is able to make BH binaries soft enough, otherwise they surely interact with single stars/BHs since $t_{2+1,f} \ll t_{\rm gr}$ for all binaries. If the BH binaries are still hard enough after the gas infall, they prevent the formation of a SMBH seed via BH runaway merger. The question is as to whether these survived hard binaries can heat the subcluster and produce BH ejection from the BH subcluster.

We plan to perform a simulation with our code `MYSCE` to test our conclusions and give a definitive answer to our question. Unfortunately, the computational time of our code

in its serial version is too high to perform such a simulation – the bottle neck consists of the three-body interactions. This is the reason why we are now parallelizing our code.

We must remember that our starting assumption on the hardness of the BH binaries is very conservative – a higher initial hardness ratio is not only possible but also probable [23, 24]. In conclusion, a physical reasonable gas infall may help the runaway merger of BHs [21] only with very particular BH binary initial conditions.

4.3.3 An extreme case

In this section we follow the same strategy of Sec. 4.3.2 by taking an extreme case in order to inquire if with an extreme gas infall it is possible to soften all binaries and to form a SMBH seed via BH runaway merger. In this fashion, we consider a SC of $N = 10^7$ stars with the same properties of the SC in Sec. 4.3.2. This SC is described by a Plummer profile with initial scale radius $a_{*,i} = 1\,\mathrm{pc}$, initial velocity dispersion $\sigma_{*,i} \sim 100\,\mathrm{km/s}$. The subcluster of BHs is very dense (with a scale radius $a_{\mathrm{BH},i} \sim 0.1\,\mathrm{pc}$) and formed by $N_{\mathrm{BH}} \sim 10^4$ BHs. Its velocity dispersion is $\sigma_{\mathrm{BH},i} \sim 110\,\mathrm{km/s}$. For the BH subscuster we consider a mass function constant between $5\,\mathrm{M}_\odot$ and $20\,\mathrm{M}_\odot$. We take a ratio of 10% of subcluster BH binaries with semi major axis a in the range $0.1 - 100\,\mathrm{AU}$. We concentrate on the evolution of the BH subcluster.

We consider an extreme gas infall: a gas infall of mass $M_{\mathrm{G},0}$ equal to ten times the total stellar mass of the cluster ($M_{\mathrm{G},0} \sim 10^8\,\mathrm{M}_\odot$) and a gas scale radius a_{G} equal to one tenth of $a_{*,i}$ ($a_{\mathrm{G}} = 0.1\,\mathrm{pc}$). We want to consider the effects of the gas infall on the BH subcluster: we get $\alpha_* \sim 0.1$ and $\beta_* \sim 10$ (see Figs. 4.1 and 4.2) and from Eqs. (4.7) we get a final BH scale radius $a_{\mathrm{BH},f} \sim 0.01\,\mathrm{pc}$ and final velocity dispersion $\sigma_{\mathrm{BH},f} \sim 1000\,\mathrm{km/s}$.

In Table 4.4 we report the relaxation time, the segregation time, the hardness ratio, the single star/BH-BH binary interaction time and the binary coalescence time for gravitational radiation inspiral before and after the gas infall. We take $\langle m \rangle = 1\,\mathrm{M}_\odot$, $m_* = M_{\mathrm{BH}} = 10\,\mathrm{M}_\odot$, $m_1 = m_2 = m_3 = 10\,\mathrm{M}_\odot$. For the same choice of m_1, m_2 and m_3 in Fig. 4.12 we plot the interaction time and the gravitational radiation inspiral time as a function of different relative velocities ($\sim$ velocity dispersion) for the semi major axes lower ($a = 0.1\,\mathrm{AU}$) and upper ($a = 100\,\mathrm{AU}$) limits and for the fixed hardness ratio $x = 1$.

From Table 4.4 and Fig. 4.12 we observe that, in the absence of gas infall, we get roughly the same conclusions of Sec. 4.3.2. If we consider gas infall, we observe that the hardness

TABLE 4.4: Same as Table 4.3 but for a SC of $N = 10^7$ stars and with a gas infall of $M_{\rm G,0} = 10\,M_*$ and $a_{\rm G} = 0.1\,a_{*,i}$.

N	a_* [pc]	σ_* [km/s]	$t_{\rm rel}$ [yr]	$t_{\rm seg}$ [yr]	a [AU]	x	t_{2+1} [yr]	$t_{\rm gr}$ [yr]	gas
10^7	1	100	$8 \cdot 10^8$	$8 \cdot 10^7$	0.1	10	$9 \cdot 10^8$	$7 \cdot 10^7$	no
10^7	1	100	$8 \cdot 10^8$	$8 \cdot 10^7$	1	1	$6 \cdot 10^7$	$7 \cdot 10^{11}$	no
10^7	0.1	1000	$5 \cdot 10^8$	$5 \cdot 10^7$	0.1	0.1	10^3	$7 \cdot 10^7$	yes
10^7	0.1	1000	$5 \cdot 10^8$	$5 \cdot 10^7$	0.01	1	$6 \cdot 10^4$	$7 \cdot 10^3$	yes

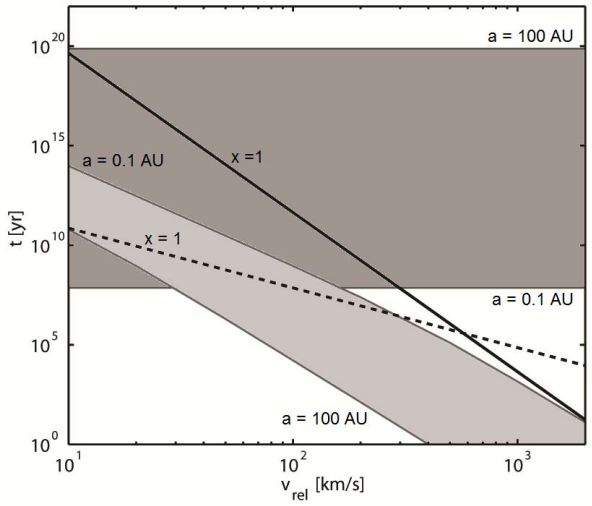

FIGURE 4.12: Same as Fig. 4.11 for a SC of $N = 10^7$ stars.

ratio is reduced ($x_f < x_i$) to an extent that all binaries are soft. The final single star/BH-BH binary interaction time $t_{2+1,f}$ is smaller than the initial interaction time $t_{2+1,i}$ for all binaries. $t_{\rm gr}$ remains constant, becomes much higher than the final interaction time $t_{2+1,f}$ for all binaries (see Table 4.4 and Fig. 4.12) so that single stars/BHs interact with BH binaries before they coalesce through gravitational radiation inspiral. However, in this case, even if all binaries interact, they are all soft, and they are disrupted by three-body interactions so that they cannot prevent the formation of a SMBH seed via BH runaway merger and cannot produce BH ejection from the BH subcluster.

In conclusion, this is a case where gas infall is able to favour the formation of a SMBH seed via BH runaway merger. The gas infall considered here has extreme properties, leading to central densities $\sim 10^{11}\,{\rm M}_\odot/{\rm pc}^3 \simeq 7 \cdot 10^{-12}\,{\rm g/cm}^3$. The question is as to whether a gas with these characteristics could have existed in the past (redshift $z \sim 6$), and could have avoided fragmentation and/or to collapse into stars/quasi-stars: this remains an open question. If this were the case, a massive SC of 10^7 stars with a gas infall like that considered in this section could be the best environment for the formation of a SMBH seed via BH runaway merger.

Conclusions

In the first part of this thesis we studied SCs (for more details see Chapter 1) as favoured environments for the formation of BHs of intermediate mass. In order to achieve this goal we developed a new code called `MYSCE` based on a modified Monte Carlo method.

In Chapter 2 we presented several numerical methods existing in the literature to simulate the SC equilibrium properties and evolution: the N-body method (see e.g. [55]), statistical methods (see e.g. [63]) and the MC approach (see e.g. [49, 99]). We adopted the MC scheme since it inherits some of the advantages of the methods mentioned above, and at the same time it allows to simulate systems with a larger number ($\gtrsim 10^6$) of stars with respect to the N-body method with an accuracy better than a pure statistical approach and similar to a N-body method when dealing with SC global properties (Lagrangian radii, dispersion velocity, etc.).

We presented also our code `MYSCE` which is based on the Hénon MC scheme but with some differences and improvements. We chose the Hénon approach since among the MC methods is the fastest (since it allows to take a time step fraction of the relaxation time instead of a fraction of the crossing time) and the easiest to adapt (since it allows to introduce stellar evolution, stellar merger, etc.). The disadvantage is that it cannot be used to treat violent initial phases in SC evolution (such as, the violent relaxation). We modified the classical scheme in four aspects: (i) we considered each particle as a star (instead of as a superstar) in order to study stellar interactions and stellar evolution effects in detail, (ii) we adopted a smaller time step in order to follow the interaction processes in the core with more accuracy, (iii) we introduced a few-body integrator to study three-body interaction in order to be more precise than the results of a statistical/semi-analytical approach, (iv) we added a mechanism to solve a numerical problem, the spurious relaxation.

In Appendix A we discussed the spurious relaxation problem which is basically a numerical artefact first discovered by [50] that introduces an additional relaxation to the system beyond the physical one.

An important result of the first part of this thesis is that we solved the spurious relaxation problem basically by correcting the mismatch (which forms and accumulates at each time step) among total energy, gravitational potential, and kinetic energy of each star. As a result, we can simulate a system for a much longer time than previously possible and/or consider shorter time steps so that we can be more accurate in simulating processes occurring on short timescales.

In Chapter 4 we applied our code `MYSCE` to the study of SCs with a wide mass range $10^4 - 10^7\,M_\odot$ in order to inquire if they are suitable environments for the formation of BHs of very high mass.

In Chapter 4 we presented several mechanisms for the formation of IMBHs ($10^3 - 10^5\,M_\odot$) and SMBH seeds ($\sim 10^5\,M_\odot$). Then, we quantitatively analyzed if a gas infall similar to the one proposed by [21] can help and accelerate the formation of very-massive stars (which will collapse to form IMBHs) via runaway collision of main-sequence stars in YSCs [26, 43, 44, 83, 85]. We studied also if a gas infall in massive SCs ($\sim 10^6\,M_\odot$) can decrease the BH binary fraction to an extent that a central SMBH seed can form through mergers of compact objects [21].

Our results can be summarized as follows.

Gas infall in YSCs is unable to help the formation of very-massive stars. The reason is that the hardening time is extremely reduced after gas infall for those hard binaries which had a single star-binary interaction time higher than the core-collapse time before gas infall. As a result, binaries can heat the cluster after gas infall and the core collapse time is increased to an extent that it becomes longer than the evolution time of most massive stars. In this way, feedback effects due to stellar evolution prevent the SC from a deep core collapse. As a consequence, the runaway merger of main-sequence stars [26, 43, 44, 83, 85] is prevented (since the bulk of mergers happens during the deep core collapse phase).

The effects of gas infall in massive SCs ($\sim 10^6\,M_\odot$) with regard to the formation of SMBH seeds is more debated. Gas infall can reduce the hardness ratio of the BH binaries, but after gas infall, the hardest BH binaries can interact with the single stars/BHs since gas infall reduces their interaction time (after gas infall all BH binaries interact before they can coalesce through gravitational radiation inspiral). However, their hardness ratio is not so high ($\lesssim 3$). As a result, it is not clear whether they can heat the cluster and, in this way, produce BH ejection from the BH subcluster and prevent the BH runaway merger for the formation of a SMBH seed. We would like to perform a simulation of this SC configuration in order to get a definite answer. In order to obtain this goal we need to parallelize our code since a system of 10^6 stars is currently too computationally

burdensome because of the three-body encounter integration time. However, our starting assumption on the hardness of the BH binaries is very conservative. In fact, it is possible and even likely to have massive SCs with a higher initial hardness ratio [23, 24]. We can conclude that a physical reasonable gas infall may help the runaway merger of BHs [21] only with very particular BH binary initial conditions.

We considered also an extreme case: a very massive SC of 10^7 stars. In this case, gas infall is able to help the formation of a SMBH seed via BH runaway merger. After gas infall, binary interaction time is smaller than the coalescence time for all binaries so that they interact with single stars/BHs before binaries coalesce. However, the hardness ratio is reduced to an extent that all binaries are soft: as a result, they are disrupted by three-body interactions so that they cannot eject BHs from the BH subcluster and the formation of a SMBH seed via BH runaway merger may happen. The open question is as to whether a gas infall with these characteristics could have existed in the past (redshift $z \sim 6$), and could have avoided fragmentation and/or to collapse into stars/quasi-stars.

Future work

In the near future we plan to parallelize our Monte Carlo code `MYSCE`: in this way, we will be able to simulate SCs with a very high number of stars ($> 10^6 - 10^7$). As a result, we will be able to give a definitive answer about the importance of gas infall for the formation of SMBH seeds inside massive SCs [21]. We plan also to explore the parameter space of YSCs by including in our simulation stellar metallicity and evolution in order to test the formation of IMBHs inside YSCs though the collapse of very-massive stars formed via runaway collision of main-sequence stars [26, 43, 44, 83, 85].

Appendix A

Spurious relaxation

One of the problems of Monte Carlo (hereafter MC) simulations of star clusters is the so-called "spurious relaxation" (hereafter, SR): because of a numerical inconsistencies, simulated clusters are found to evolve (e.g. Lagrangian radii change with time) even when close interactions (which are responsible for exchanges of energy and angular momentum among particles) are switched off, i.e. even when the energy and angular momentum of each particle should be conserved. Here we report a modification to the basic algorithm described by [49], that largely reduces the effects of the SR.

A.1 Overview

Many physical mechanisms change the stellar distribution and density within a star cluster. The most important are the two-body and three-body interactions (i.e. interactions between a binary star and an "intruder"). Two-body interactions are responsible for the relaxation of the system, which moves towards the equipartition of kinetic energy: this should cause mass segregation, and other possible processes (such as a core collapse), which can be eventually stopped by feedback effects (e.g. because of stellar evolution). Three-body interactions can reduce the speed of the above-mentioned processes since they can extract the internal energy of binaries, converting it into kinetic energy; therefore, they might be able to prevent the core collapse and/or the relaxation of the system.

In MC codes assuming spherical symmetry, particles are mainly subject to the central force from the cluster potential. Therefore, in the absence of the perturbations representing few-body interactions (i.e., in the absence of non-central forces), the system must remain in a globally stationary state: single stars move along their orbits, but

these do not evolve, and global properties such as gravitational potential, density, velocity dispersion, Lagrangian radii etc. must remain constant. Unfortunately, this is not what happens in the standard MC algorithm. In fact, if non-central interactions are turned off, SR occurs. This numerical artifact was first discovered by [50]: the cluster undergoes a residual numerical relaxation, so that the inner Lagrangian radii tend to shrink, and the outer Lagrangian radii tend to expand (see e.g. Fig. A.1)

The reason for this behaviour lies in the randomness of the MC algorithm: at each time step, the algorithm generates a different realization of an underlying distribution (e.g., of radial distances), and such realizations differ from each other even when the underlying distribution does not evolve. For example, in MC simulations of spherically symmetric objects the gravitational potential is calculated at the beginning of each time step, using the approximation that the mass m_i of the i-th particle is distributed in a zero-thickness spherical shell of radius r_i (where r_i is the distance of the particle from the centre of the system). However, since the values of r_i are the results of a random process (albeit one that takes into account physical constraints), the potential undergoes (small) random fluctuations at each time step. Such fluctuations lead to SR, and the effect becomes more and more dramatic as the core shrinks and high central densities develop.

As pointed out by [50], it is possible to estimate the "SR time scale" $t_{\rm SR}$ over which SR effects become important, as

$$t_{\rm SR} = N\Delta t, \tag{A.1}$$

where N represents the number of particles in the system, and Δt is the average length of the time steps. Such equation can be interpreted in terms of the number of time steps: SR effects become important in simulations where the number of time steps exceeds the number of particles. Alternatively, we can compare $t_{\rm SR}$ to the relaxation time $t_{\rm rel}$ of the system: the effects of the SR are negligible if

$$t_{\rm SR} \gg t_{\rm rel}, \tag{A.2}$$

since in this case the two body relaxation is dominant over the unwanted effect of the SR.

A.2 Spurious relaxation correction

A.2.1 Previous approaches

Several solutions were proposed to deal with SR:

1. Increase the number N of particles in the system, so as to increase $t_{\rm SR}$ [30, 31, 57]. The most important limitation to this approach is that there are many cases where N is essentially fixed by the nature of the problem (e.g., in the case of a stellar clusters we should choose N as the number of stars).

2. Increase the average duration Δt of time steps [43, 106, 107]. However, Δt cannot be longer than the time scale of the fastest physical processes considered in the simulation, which in many cases is $\ll t_{\rm rel}/N$.

3. [50] considered a more fundamental solution, i.e. re-normalize the system after each time step, so as to keep the total energy constant. However, it was immediately understood that this procedure is unable to eliminate SR. In fact, SR effects are stronger near the center, while the renormalization process acts uniformly on the entire system: the result is that the renormalization slows down (but does not eliminate) the contraction of the inner Lagrangian radii, whereas the outer Lagrangian radii artificially contract.

4. Finally, another solution considered by [50] is to recalculate the potential after the displacement of each star. In codes like the one by [49], this approach is quite impractical, because it requires N recalculations of the potential at each time step (rather than 1), so that the MC algorithm would lose its computational edge. However, [30, 31] were able to efficiently implement this strategy by using a binary tree: their tests show that SR is still present, although its level is significantly lower than for other MC codes (see their Fig. D.1).

No one of the above solutions can be considered satisfactory, since there are many cases where the two first suggestions cannot be applied, whereas the third *reduces* but does not eliminate SR, and the fourth is too expensive in its original formulation – and again, *reduces* but does not eliminate SR.

A.2.2 A possible effective correction

In order to understand the correction to the MC algorithm that we propose, we investigate in detail the causes of SR.

In the MC method (applied to a system with spherical symmetry), the sets of radial positions $\{r_i\}$ and of masses $\{m_i\}$ of the particles at the start of the step is used to calculate the cluster gravitational potential $P(r)$. On this basis, the code generates the radial position $\tilde{r}_i$ that each particle will have in the next step. This is done using its radial and tangential velocities ($v_{{\rm R},i}$, and $v_{{\rm T},i}$), as well as $P(r)$: in fact, the particle is

assumed to move on a rosette orbit in the central cluster potential, so that its radial position oscillates between two values $r_{\min,i}$ and $r_{\max,i}$ (periapis and apoapsis), which are the roots of [50]:

$$Q_i(r) = 0, \tag{A.3}$$

where

$$Q_i(r) \equiv 2E_i - 2P(r) - A_i^2/r^2 \tag{A.4}$$

with $E_i \equiv P(r_i) + (v_{\mathrm{R},i}^2 + v_{\mathrm{T},i}^2)/2$ (total energy per unit mass of the particle), and $A_i \equiv r v_{\mathrm{T},i}$ (angular momentum per unit mass). After the new radial position $\tilde{r}_i$ is generated (according to an appropriate distribution keeping into account the amount of time that the particle spends at each radius), the new velocities are calculated as $\tilde{v}_{\mathrm{T},i} = A_i/\tilde{r}_i$, $\tilde{v}_{\mathrm{R},i} = \pm\sqrt{Q_i(\tilde{r}_i)}$ (the sign is assigned randomly).

Because of random fluctuations, the potential $\tilde{P}(r)$ which can be calculated on the basis of the set of the $\{\tilde{r}_i\}$ is slightly different from the potential $P(r)$ which is used throughout the step. This is a problem, because in the next step the energy (per unit mass) of the particles will be $\tilde{E}_i \equiv \tilde{P}(\tilde{r}_i) + (\tilde{v}_{\mathrm{R},i}^2 + \tilde{v}_{\mathrm{T},i}^2)/2 \simeq E_i + \tilde{P}(\tilde{r}_i) - P(\tilde{r}_i)$[1]. The small difference between $\tilde{E}_i$ and E_i is the main cause of SR.

We verified that this is the case by implementing in our MC code `MYSCE` (see Chapter 2) a simple variation of the above algorithm that reduces to 0 the above difference. The basic idea is that after generating the set of the $\{\tilde{r}_i\}$ we calculate the new potential $\tilde{P}(r)$, and estimate $\tilde{v}_{\mathrm{R},i}$ as $\pm\sqrt{\tilde{Q}_i(\tilde{r}_i)}$, where $\tilde{Q}_i(r) \equiv 2E_i - 2\tilde{P}(r) - A_i^2/r^2$. In this way, $\tilde{E}_i$ remains $\simeq E_i$.

The actual procedure is made slightly more complicated by the fact that for a small number of particles the argument of the square root might be negative: in fact, the roots $\tilde{r}_{\min,i}$ and $\tilde{r}_{\max,i}$ of the equation $\tilde{Q}_i(r) = 0$ are slightly different from $r_{\min,i}$ and $r_{\max,i}$, and it is possible that some values of $\tilde{r}_i$ fall outside the new range (by a small amount, since $\tilde{P}(r)$ is close to $P(r)$). Since this happens only for a tiny fraction of the particles, we slightly move these particles to the closest extreme of the $\tilde{r}_{\min,i}$–$\tilde{r}_{\max,i}$ range. After that, we recalculate $\tilde{P}(r)$ on the basis of the modified $\{\tilde{r}_i\}$, and repeat the process until we have that $\tilde{Q}_i(\tilde{r}_i) \geq 0 \ \forall\ i$, i.e. until we can assign radial velocities to all the particles. Such condition is usually achieved in ≤ 2 iterations. Therefore, the computational cost of this process is relatively small: for each step, it requires 1-2 additional recalculations of the potential, and 1-2 assignments of the N radial velocities of the particles.

[1] In the codes of [40, 105] we have instead $\tilde{E}_i \simeq E_i + (1/2)[\tilde{P}(\tilde{r}_i) - P(\tilde{r}_i)] + (1/2)[\tilde{P}(r_i) - P(r_i)]$.

TABLE A.1: Ratio between final and initial Lagrangian radii at 0.5%, 5%, 10%, 20%, 30%, 50%, 70%, 90%, 95% of the total mass of the system when SR correction is neglected after a number of time steps equal to the number of stars.

		NO SR CORRECTION $R_L(T)/R_L(0)$								
stars	steps	0.5%	5%	10%	20%	30%	50%	70%	90%	95%
2000	2000	0.029	0.073	0.15	0.25	0.31	0.70	1.44	4.65	9.94
5000	5000	0.055	0.15	0.22	0.30	0.42	0.76	1.49	3.81	6.42
10000	10000	0.11	0.16	0.19	0.28	0.39	0.61	1.45	3.37	5.19

A.2.3 Tests

The tests consisted in simulating stellar clusters of various sizes with two versions of `MYSCE`. We simulated three stellar clusters with 2000, 5000, and 10000 stars with total mass of about 1400, 3400, and 6700 solar masses, respectively. We chose a Salpeter initial mass function. All clusters are described by a Plummer initial density profile with a scale radius of 1 pc (see Chapter 3). In both versions we switched off all few-body interactions (i.e. all non-central forces), but in one of them we used the "standard" MC algorithm, whereas in the other we corrected the MC algorithm as described above. In the case of the standard MC algorithm the system was simulated for a number of steps equal to the number of stars, whereas in the presence of SR correction we performed a number of steps equal to the number of stars and equal to ten times the number of stars.

The results of tests are given in Table A.1 and in Table A.2, and Figs. A.1 and A.2 show the evolution of Lagrangian radii for a particular cluster in the two cases. It is apparent that in the "corrected" version of `MYSCE` Lagrangian radii are much more stable, and remain constant even after a number of steps which is of the order of N or even greater.

We can also perform a raw comparison with the tests of [30]: looking at their Fig. D.1, we estimate that in 4000 (average) steps, the Lagrangian radius including 0.5% of the mass of a 4000 (super)star cluster reduced by $\sim 15 - 20\%$; whereas the Lagrangian radius including 95% of the mass of the same cluster expands by $\sim 25 - 30\%$. This is a remarkable improvement with respect to the values reported in Table A.1; but Table A.2 shows that the correction we are proposing can achieve even better results: in a similar cluster (5000 particles) these two Lagrangian radii change by less than 7%, even after 50000 steps.

TABLE A.2: Ratio between final and initial Lagrangian radii at 0.5%, 5%, 10%, 20%, 30%, 50%, 70%, 90%, 95% of the total mass of the system when SR correction is considered after a number of time steps equal to the number of stars and equal to ten times the number of stars.

		SR CORRECTION $R_L(T)/R_L(0)$								
stars	steps	0.5%	5%	10%	20%	30%	50%	70%	90%	95%
2000	2000	1.13	0.89	1.10	1.18	1.41	1.21	1.06	0.97	0.97
5000	5000	1.07	1.09	1.08	1.09	0.99	1.05	1.02	0.99	1.02
10000	10000	0.99	0.98	1.02	1.04	1.06	0.95	0.98	0.99	1.00
2000	20000	1.19	1.39	1.29	1.35	1.31	1.12	0.99	1.04	0.97
5000	50000	1.07	1.19	1.24	1.12	1.09	0.98	0.96	0.97	1.01
10000	100000	0.95	0.96	0.90	0.89	0.87	0.94	0.97	0.97	0.99

A.3 Discussion

We have described a new method to minimize the SR problem that affects MC codes. This solution largely removes the problem since at each time step it corrects the mismatch between total energy, gravitational potential, and kinetic energy that is due to the recalculation of the potential. This method allows to simulate a system with a relatively small number of particles (stars) for a much longer time than previously possible (in fact, the number of time steps can be increased by a factor of at least 10–100, as demonstrated by Table A.2), and/or to consider shorter time steps, so as to simulate the evolution of a system for a long time while following processes occurring on short timescales. SR correction is fundamental in order to simulate, for example, a large number of small star clusters.

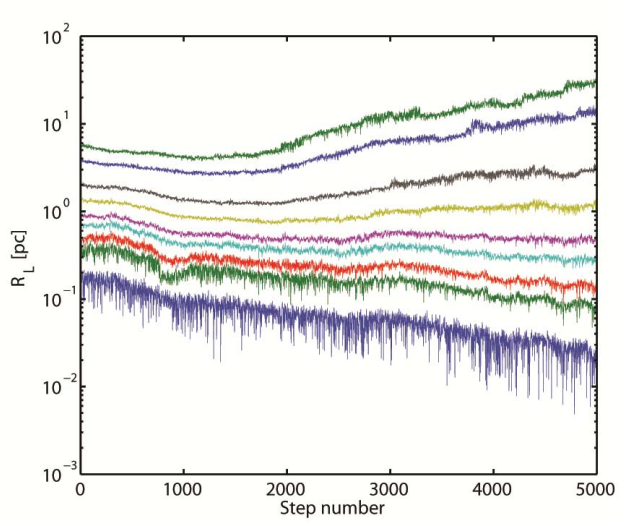

FIGURE A.1: Evolution of the Lagrangian radii within a 5000 particles system, as a function of the number of time steps. The simulations were performed with `MYSCE` in the absence of non-radial forces (e.g. few-body interactions), and in the absence of the proposed SR correction. From bottom to top, lines represent the Lagrangian radii corresponding to 0.5%, 5%, 10%, 20%, 30%, 50%, 70%, 90%, 95% of the mass of the system, respectively.

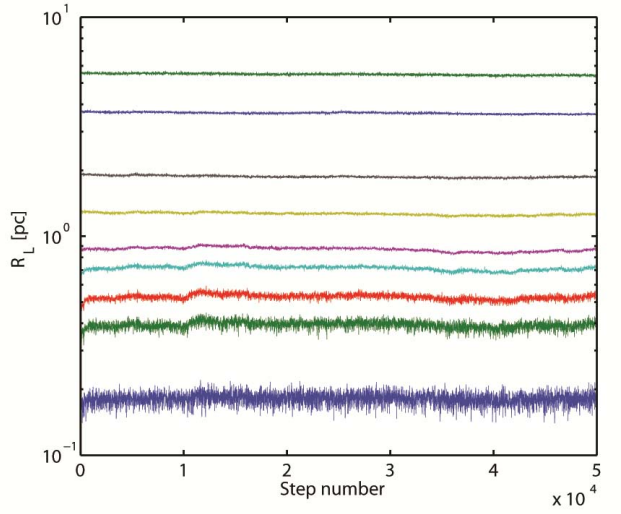

FIGURE A.2: Same as Fig. A.1, but in this case the simulations included the proposed SR correction. For clarity of visualization, data are binned: each point is the average of ten real steps. Note that the scales are different from Fig. A.1, as we plot a much larger number of time steps, over a smaller vertical range.

Bibliography

[1] Aarseth, S. J. 1963, MNRAS, 126, 223

[2] Aarseth, S. J., & Heggie, D. C. 1998, MNRAS, 297, 794

[3] Allison, R. J., Goodwin, S. P., Parker, R. J., et al. 2009, ApJ, 700, L99

[4] Angeletti, L., & Giannone, P. 1977, A&A, 58, 363

[5] Angeletti, L., & Giannone, P. 1980, A&A, 85, 113

[6] Applegate, J. H. 1986, ApJ, 301, 132

[7] Barmby, P., & Huchra, J. P. 2001, AJ, 122, 2458

[8] Barth, A. J., Martini, P., Nelson, C. H., & Ho, L. C. 2003, ApJ, 594, L95

[9] Baumgardt, H., Hut, P., Makino, J., McMillan, S., & Portegies Zwart, S. 2003, ApJ, 582, L21

[10] Begelman, M. C., Volonteri, M., & Rees, M. J. 2006, MNRAS, 370, 289

[11] Bellovary, J. M., Governato, F., Quinn, T., & Volonteri, M. 2011, Bulletin of the American Astronomical Society, 43, #128.01

[12] Binney, J., & Tremaine, S. 1987, Princeton, NJ, Princeton University Press, 1987, 747 p.

[13] Binney, J., Tremaine, S., 2008, Galactic dynamics: Second Edition, Princeton University Press

[14] Bonnell, I. A., & Davies, M. B. 1998, MNRAS, 295, 691

[15] Bressan, A., Marigo, P., Girardi, L., et al. 2012, MNRAS, 427, 127

[16] Chazy, J. 1929, J. Math. Pures Appl., 8, 353

[17] Chernoff, D. F., & Weinberg, M. D. 1990, ApJ, 351, 121

[18] Clark, J. S., Negueruela, I., Crowther, P. A., & Goodwin, S. P. 2005, A&A, 434, 949

[19] Colpi, M., Mapelli, M., & Possenti, A. 2003, ApJ, 599, 1260

[20] Davies, B., Figer, D. F., Law, C. J., et al. 2008, ApJ, 676, 1016

[21] Davies, M. B., Miller, M. C., & Bellovary, J. M. 2011, ApJ, 740, L42

[22] Devecchi, B., & Volonteri, M. 2009, ApJ, 694, 302

[23] Downing, J. M. B., Benacquista, M. J., Giersz, M., & Spurzem, R. 2010, MNRAS, 407, 1946

[24] Downing, J. M. B., Benacquista, M. J., Giersz, M., & Spurzem, R. 2011, MNRAS, 416, 133

[25] Duquennoy, A., & Mayor, M. 1991, A&A, 248, 485

[26] Ebisuzaki, T., Makino, J., Tsuru, T. G., et al. 2001, ApJ, 562, L19

[27] Ferrara, A., Haardt, F., & Salvaterra, R. 2013, MNRAS, 434, 2600

[28] Fregeau, J. M., Joshi, K. J., Portegies Zwart, S. F., & Rasio, F. A. 2002, ApJ, 570, 171

[29] Fregeau, J. M., Gürkan, M. A., Joshi, K. J., & Rasio, F. A. 2003, ApJ, 593, 772

[30] Freitag, M., & Benz, W. 2001, A&A, 375, 711

[31] Freitag, M., & Benz, W. 2002, Stellar Collisions, Mergers and their Consequences, 263, 261

[32] Figer, D. F. 2008, IAU Symposium, 250, 247

[33] Fujii, M. S., & Portegies Zwart, S. 2013, arXiv:1304.1550

[34] Fryer, C. L., Woosley, S. E., & Heger, A. 2001, ApJ, 550, 372

[35] Gebhardt, K., Rich, R. M., & Ho, L. C. 2005, ApJ, 634, 1093

[36] Gerssen, J., van der Marel, R. P., Gebhardt, K., et al. 2002, AJ, 124, 3270

[37] Giersz, M., & Heggie, D. C. 1994, MNRAS, 268, 257

[38] Giersz, M., & Spurzem, R. 1994, MNRAS, 269, 241

[39] Giersz, M., & Heggie, D. C. 1996, MNRAS, 279, 1037

[40] Giersz, M. 1998, MNRAS, 298, 1239

[41] Gouliermis, D., Keller, S. C., Kontizas, M., Kontizas, E., & Bellas-Velidis, I. 2004, A&A, 416, 137

[42] Gültekin, K., Miller, M. C., & Hamilton, D. P. 2004, ApJ, 616, 221

[43] Gürkan, M. A., Freitag, M., & Rasio, F. A. 2004, ApJ, 604, 632

[44] Gürkan, M. A., Fregeau, J. M., & Rasio, F. A. 2006, ApJ, 640, L39

[45] Hammersley, J. M., Handscomb, D. C., & Weiss, G. 1965, Physics Today, 18, 55

[46] Harris, W. E. 1996, VizieR Online Data Catalog, 7195, 0

[47] Heggie, D. C. 1975, MNRAS, 173, 729

[48] Heggie, D. C., Giersz, M., Spurzem, R., & Takahashi, K. 1998, Highlights of Astronomy, 11, 591

[49] Hénon, M. 1971, Ap&SS, 13, 284

[50] Hénon, M. H. 1971, Ap&SS, 14, 151

[51] Hénon, M. 1975, Dynamics of the Solar Systems, 69, 133

[52] Hills, J. G. 1983, AJ, 88, 1269

[53] Hut, P., & Bahcall, J. N. 1983, ApJ, 268, 319

[54] Hut, P., & Makino, J. 1996, Dynamical Evolution of Star Clusters: Confrontation of Theory and Observations, 174,

[55] Hut, P., McMillan, S., Makino, J., & Portegies Zwart, S. 2010, Astrophysics Source Code Library, 10076

[56] Inagaki, S. 1986, PASJ, 38, 853

[57] Joshi, K. J., Rasio, F. A., & Portegies Zwart, S. 2000, ApJ, 540, 969

[58] Kim, C.-H., Chun, M.-S., & Min, K. W. 1992, Ap&SS, 196, 191

[59] King, I. R. 1966, AJ, 71, 64

[60] Kraicheva, Z. T., Popova, E. I., Tutukov, A. V., & Iungelson, L. R. 1978, AZh, 55, 1176

[61] Kroupa, P. 2001, MNRAS, 322, 231

[62] Kulkarni, S. R., Hut, P., & McMillan, S. 1993, Nature, 364, 421

[63] Larson, R. B. 1970, MNRAS, 147, 323

[64] Larson, R. B. 1970, MNRAS, 150, 93

[65] Leitherer, C., Robert, C., & Drissen, L. 1992, ApJ, 401, 596

[66] Lodato, G., & Natarajan, P. 2006, MNRAS, 371, 1813

[67] Louis, P. D., & Spurzem, R. 1991, MNRAS, 251, 408

[68] Lynden-Bell, D., & Eggleton, P. P. 1980, MNRAS, 191, 483

[69] Madau, P., & Rees, M. J. 2001, ApJ, 551, L27

[70] Makino, J. 1996, ApJ, 471, 796

[71] Mapelli, M., Colpi, M., Possenti, A., & Sigurdsson, S. 2005, MNRAS, 364, 1315

[72] Mayer, L., Kazantzidis, S., Escala, A., & Callegari, S. 2010, Nature, 466, 1082

[73] McMillan, S. L. W. 1986, ApJ, 307, 126

[74] McMillan, S. L. W. 1993, Structure and Dynamics of Globular Clusters, 50, 171

[75] Merritt, D. 2001, ApJ, 556, 245

[76] Miller, M. C., & Hamilton, D. P. 2002, MNRAS, 330, 232

[77] Miller, M. C., & Colbert, E. J. M. 2004, International Journal of Modern Physics D, 13, 1

[78] Murphy, B. W., Cohn, H. N., & Hut, P. 1990, MNRAS, 245, 335

[79] Navarro, J. F., Frenk, C. S., & White, S. D. M. 1996, ApJ, 462, 563

[80] O'Leary, R. M., Rasio, F. A., Fregeau, J. M., Ivanova, N., & O'Shaughnessy, R. 2006, ApJ, 637, 937

[81] Peters, P. C. 1964, Physical Review, 136, 1224

[82] Portegies Zwart, S. F., & Verbunt, F. 1996, A&A, 309, 179

[83] Portegies Zwart, S. F., Makino, J., McMillan, S. L. W., & Hut, P. 1999, A&A, 348, 117

[84] Portegies Zwart, S. F., & McMillan, S. L. W. 2000, ApJ, 528, L17

[85] Portegies Zwart, S. F., & McMillan, S. L. W. 2002, ApJ, 576, 899

[86] Portegies Zwart, S. F., & McMillan, S. L. W. 2007, Massive Stars in Interactive Binaries, 367, 597

[87] Portinari, L., Chiosi, C., & Bressan, A. 1998, A&A, 334, 505

[88] Plummer, H. C. 1911, MNRAS, 71, 460

[89] Quinlan, G. D., & Shapiro, S. L. 1989, ApJ, 343, 725

[90] Quinlan, G. D. 1996, New A, 1, 35

[91] Rasio, F. A., Fregeau, J. M., & Joshi, K. J. 2001, The Influence of Binaries on Stellar Population Studies, 264, 387

[92] Roncadelli, M., Aspetti astrofisici della materia oscura, Quaderni di fisica teorica

[93] Rosenbluth, M. N., MacDonald, W. M., & Judd, D. L. 1957, Physical Review, 107, 1

[94] Salpeter, E. E. 1955, ApJ, 121, 161

[95] Shapiro, S. L. 1985, Dynamics of Star Clusters, 113, 373

[96] Sigurdsson, S., & Hernquist, L. 1993, Nature, 364, 423

[97] Sigurdsson, S., & Phinney, E. S. 1993, ApJ, 415, 631

[98] Sirianni, M., Nota, A., De Marchi, G., Leitherer, C., & Clampin, M. 2002, ApJ, 579, 275

[99] Spitzer, L., Jr. 1975, Dynamics of the Solar Systems, 69, 3

[100] Spitzer, L., Jr., & Shull, J. M. 1975, ApJ, 200, 339

[101] Spitzer, L., Jr., & Shull, J. M. 1975, ApJ, 201, 773

[102] Spitzer, L., Jr., & Mathieu, R. D. 1980, ApJ, 241, 618

[103] Spitzer, L., 1987, Dynamical Evolution of Globular Clusters, Princeton University Press

[104] Spurzem, R., & Giersz, M. 1996, MNRAS, 283, 805

[105] Stodolkiewicz, J. S. 1982, Acta Astron., 32, 63

[106] Umbreit, S., Fregeau, J. M., & Rasio, F. A. 2008, IAU Symposium, 246, 351

[107] Umbreit, S., Fregeau, J. M., Chatterjee, S., & Rasio, F. A. 2012, ApJ, 750, 31

[108] van der Marel, R. P., Gerssen, J., Guhathakurta, P., Peterson, R. C., & Gebhardt, K. 2002, AJ, 124, 3255

[109] van der Marel, R. P., & Anderson, J. 2010, ApJ, 710, 1063

[110] Vesperini, E., McMillan, S. L. W., & Portegies Zwart, S. 2009, ApJ, 698, 615

[111] Volonteri, M., Haardt, F., & Madau, P. 2003, ApJ, 582, 559

[112] von Hoerner, S. 1960, ZAp, 50, 184

[113] Willott, C. J., McLure, R. J., & Jarvis, M. J. 2003, ApJ, 587, L15

Part II

Axion-like particles and very-high energy astrophysics

Introduction

The Standard Model (SM) of strong, weak and electromagnetic interactions with three sequential families of quarks and leptons provides a satisfactory description of the experimental results concerning elementary-particle physics at energies up to about the Fermi scale of weak interactions $G_F^{-1/2} \simeq 250\,\mathrm{GeV}$, and the recent discovery of the Higgs boson with the right properties has fully confirmed the correctness of the SM.

Yet, nobody would seriously regard the SM as the ultimate theory of fundamental processes. Apart from more or less aesthetic reasons and some anomalies like the $g-2$ value of the muon and the forward-backward asymmetry of the top quark, such an expectation is made compelling by the observational evidence for non-baryonic dark matter ultimately responsible for the formation of structure in the Universe as well as for dark energy presumably triggering the present accelerated cosmic expansion.

So, the SM is presently viewed as the low-energy manifestation of some more fundamental and complete theory of all elementary-particle interactions including gravity. Every specific approach to extend the SM in such a way is characterized by a set of new particles along with their mass spectrum and their interactions with the standard world.

Although it is presently impossible to tell which proposal out of so many ones has any chance to successfully describe Nature, it looks remarkable that attempts along very different directions such as four-dimensional ordinary and supersymmetric models [1], Kaluza-Klein theories [2, 3] and especially superstring theories [4–6] all suggest the existence of *axion-like particles* (ALPs) (for a review, see [7]). A general argument supporting this conclusion will be given in Chapter 1.

ALPs are very light pseudo-scalar spin-zero bosons denoted by a characterized by a two-photon coupling $a\gamma\gamma$. As the name itself suggests, they are a sort of generalization of the axion, the pseudo-Goldstone boson associated with the Peccei-Quinn symmetry proposed as a natural solution to the strong CP problem [8–11]. But while the axion is constrained by a strict relationship between its mass and the $a\gamma\gamma$ coupling constant, these two parameters are regarded as unrelated for ALPs. In fact, depending on the

actual values of their mass and $a\gamma\gamma$ coupling constant, ALPs can play an important role in cosmology, either as cold dark matter particles [12] or as quintessential dark energy [13].

A remarkable consequence of the $a\gamma\gamma$ coupling is the phenomenon of photon-ALP mixing, which takes place in the presence of an external electromagnetic field and leads to two distinct effects. One is photon-ALP oscillations [14, 15], which is quite similar to the oscillations of massive neutrinos with different flavours. The other consists in the change of the polarization state of photons travelling in a magnetic field [15, 16].

It turns out that ALPs are extremely elusive in high-energy experiments and the only way to look for them in the laboratory requires very careful polarimetric measurements to be carried out on a laser beam [17] or alternatively a photon regeneration experiment to be performed [18]. Successful detection of ALPs in present-day experiments of this kind is possible in either case for a fairly large $a\gamma\gamma$ coupling.

Astrophysical manifestations of ALPs appear the best strategy to discover their existence, since they can give rise to observable effects even for values of the $a\gamma\gamma$ coupling constant much smaller than those tested so far in laboratory experiments. Indeed, it is known since a long time that for values of the $a\gamma\gamma$ coupling constant that look hopelessly small to be probed today in the laboratory the stellar evolution would be dramatically altered [19] and this fact sets a strong upper bound on the coupling in question, which is consistent with the robust negative result of the CAST experiment at CERN [20].

In the last few years it has been realized that photon-ALP oscillations triggered by intervening cosmic magnetic fields along the line of sight can produce detectable effects in observations of bright X-ray and γ-ray sources [21–30, 32]. The effect becomes larger as the distance of the sources increases: blazars, which are Active Galactic Nuclei (AGN) with the beam pointing towards us, constitute the most distant long-lasting gamma-ray sources observed, and are thus the most obvious case study. In order to bring out most simply the relevance of ALPs in the present context, we neglect cosmological effects at this introductory level.

The mean free path of very-high-energy (VHE) photons – namely with energy above 100 GeV – is limited by their interaction with background photons in the Universe through the process $\gamma\gamma \to e^+e^-$. A high energy photon from a distant blazar has a nonnegligible probability to scatter off background photons in the optical/near infrared band permeating the Universe – the so-called *extragalactic background light* (EBL) – thereby disappearing into an e^+e^- pair [33, 34]. The VHE photon mean free path depends on the EBL density. Recently it has become possible to model accurately such density: several parametrizations are available, essentially coincident, and throughout

this thesis we employ the recent EBL model of Franceschini, Rodighiero and Vaccari (FRV) [35]). Fig. 3 shows the pair-production mean free path λ_γ of a VHE photon as a function of its energy E within the FRV model.

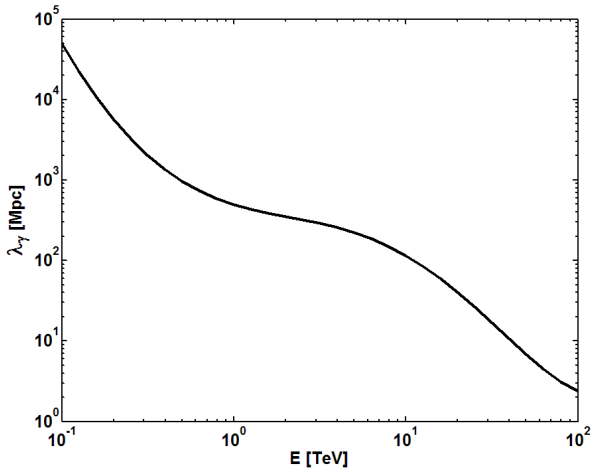

FIGURE 3: The pair-production mean free path λ_γ of a VHE photon is plotted versus its energy E within the EBL model of FRV. Only conventional physics is assumed and in particular the possibility of photon-ALP oscillations is ignored.

The effects of the photon-ALP oscillations on the gamma yield from blazars can be summarized as follows:

- For $E < 100\,\mathrm{GeV}$ we infer from Fig. 3 that $\lambda_\gamma(E)$ is comparable with the Hubble radius, and so EBL absorption is negligible. In such a situation photon-ALP oscillations can only give rise to a source dimming above a certain energy threshold E'. Hence a characteristic *distortion* of the source spectrum around E' is the observable prediction, which can be searched for with the *Fermi*/LAT mission if E' happens to lie in the instrument energy range, namely for $30\,\mathrm{MeV} < E' < 300\,\mathrm{GeV}$ [23].

- For $E > 100\,\mathrm{GeV}$ Fig. 3 shows that EBL effects become important since now $\lambda_\gamma(E)$ quickly decreases as E increases. Once emitted, photons can convert into ALPs and next reconvert back into photons before reaching the Earth. A possibility is that photon-ALP oscillations take place in intergalactic space and the resulting scenario has been called DARMA (acronym for De Angelis, Roncadelli and Mansutti) [24–26]. Alternatively, the $\gamma \to a$ conversion can occur inside the blazar while the $a \to \gamma$ reconversion can happen in the Milky Way [27]. Of course, also both options can be realized [30]. Finally, if the blazar happens to be inside a cluster of galaxies – where a magnetic field of order $1\,\mu$G is invariably present – the $\gamma \to a$ conversion can take place in the cluster whereas the $a \to \gamma$ conversion still happens in the Milky Way [31]. In any case, photons acquire a split identity, travelling for

some time as real photons and for some time as ALPs. However, they suffer EBL absorption *only* when they are real photons, which means that the effective photon mean free path $\lambda_{\gamma,\mathrm{eff}}(E)$ is actually *larger* than $\lambda_\gamma(E)$ as predicted by conventional physics (see Fig. 3). Since the photon survival probability depends exponentially on minus the optical depth – which in turn goes like the source distance divided by $\lambda_{\gamma,\mathrm{eff}}(E)$ – even a slight increase of $\lambda_{\gamma,\mathrm{eff}}(E)$ with respect to $\lambda_\gamma(E)$ produces a *substantial enhancement* of the photon survival probability and so of the observed flux. Note that for a given detector sensitivity a larger photon survival probability just means that a larger distance can be probed, so that the VHE Universe becomes more transparent than generally believed. Actually, since the EBL absorption increases with energy whereas the photon-ALP oscillation probability is energy-independent, the observed flux enhancement gets larger and larger as the energy increases. As a consequence, the observed spectra are harder than currently expected.

Thus – depending on the values of the free parameters – a *hardening* of the observed blazar spectra is the main prediction of photon-ALP oscillations concerning the VHE band between 100 GeV and 100 TeV, which can be probed by Imaging Atmospheric Cherenkov Telescopes (IACTs). More in detail, the presently operating IACTs H.E.S.S., MAGIC and VERITAS can reach up $\sim$ 20 TeV with difficulty, whereas the planned Cherenkov Telescope Array (CTA) and the HAWC water Cherenkov γ-ray observatory will be able to explore the whole VHE band with a much larger sensitivity. We should add that the VHE range can also be analyzed by other available detectors, like the Extensive Air Shower arrays ARGO-YBJ and MILAGRO.

Our aim is to investigate the DARMA scenario in great detail by employing the EBL model of FRV [35], and systematically working out all its implications for VHE blazar observations (Chapters 1-5). Everything is calculated starting from first principles.

More specifically, our primary goal is to evaluate the photon survival probability within the DARMA scenario, which allows in turn to quantify the resulting hardening of VHE blazar spectra and to determine how much the Universe becomes more transparent to VHE photons than usually thought.

We find that these effects can be quite substantial for the free parameters in allowed realistic ranges provided that the ALP mass satisfies the condition $m < 5 \cdot 10^{-10}$ eV. Actually, our prediction can become spectacular above an energy threshold which is well below the upper detection limit of the CTA and the HAWC observatory. Denoting by E_{10} the energy at which the photon survival probability is 10 times larger than that dictated by conventional physics, E_{10} turns out to decrease as the source redshift z increases. In

the most favourable case, we get $E_{10} \simeq 30\,\mathrm{TeV}$ for Mrk 421 at $z = 0.030$, $E_{10} \simeq 8\,\mathrm{TeV}$ for 1ES 0347-121 at $z = 0.188$, $E_{10} \simeq 2\,\mathrm{TeV}$ for 3C 66A at $z = 0.444$ and $E_{10} \simeq 2\,\mathrm{TeV}$ for 3C 279 at $z = 0.536$. In addition, it follows from the above considerations that for energies larger than E_{10} the photon survival probability gets even more enhanced.

In spite of the fact that only future observations can provide a clear-cut check of the DARMA scenario – and so ultimately of the existence of an ALP lighter than $5 \cdot 10^{-10}\,\mathrm{eV}$ – it looks natural to inquire whether available data from IACTs contain some hints in favour of this scenario. As we shall see, the emitted as well as the observed spectra of VHE blazars detected so far have to a good approximation a single power-law behaviour [2], so that they are characterized by their slope, which – up to a minus sign – is the emitted Γ_{em} and observed Γ_{obs} spectral index, respectively. So, we can rephrase the above conclusion by stating that for a fixed value of Γ_{em} pertaining to a given source the DARMA scenario predicts that under suitable conditions Γ_{obs} should be *smaller* than within conventional physics.

In 2006 the H.E.S.S. collaboration reported some evidence that the spectra of the two blazars H 2356-309 and 1ES 1101-232 have Γ_{obs} smaller than expected and this fact was interpreted as strongly suggesting an EBL attenuation lower than currently believed [37]. A similar conclusion emerged in 2007 with the discovery of the blazar 3C 279 by the MAGIC collaboration [38]. Based on preliminary data [39] and a specific EBL model [40], the DARMA model [24] has shown for the first time that the mechanism of photon-ALP oscillations can substantially reduce the EBL attenuation for distant blazars and in particular that it can successfully explain the observed spectrum of 3C 279 for allowed realistic values of the free parameters.

Subsequent developments have demonstrated that realistic EBL models account for VHE blazar observations without the need of any unconventional physics, provided that the large spread in the values of Γ_{obs} is fully traced back to an equally large spread in the values of Γ_{em}. Further, far-away sources – for which EBL absorption is a large effect – turn out to have energy spectra similar to those of some nearby blazars, for which EBL attenuation is negligible. This means that for distant sources Γ_{em} has to be considerably smaller than for nearby ones. Even though a physical explanation for the occurrence of very small values of Γ_{em} has recently been proposed [41–43], one is nevertheless led to the *cosmic opacity problem*, namely to wonder why these physical effects are important for distant blazars *only*. Nevertheless, two hints have been put forward suggesting the existence of photon-ALP oscillation in extragalactic space.

[2] Although the actual spectra exhibit some curvature due to the bump related to Inverse Compton (see later), power-law approximations, both from an observational and theoretical point of view, are good over the energy range used in this thesis, namely 0.2-2 TeV, as emphasized by [36].

One of them concerns the so-called pair-production anomaly. Basically, depending on the distance of the source, the Universe should be opaque to VHE photons above a certain energy. However, indications exist that the Universe is more transparent than previously thought. A recent careful statistical analysis of a large sample of VHE spectra shows that the correction for absorption with current EBL models is too strong for the data points with the highest attenuation [44–47]. The phenomenon of photon-ALP oscillation in extragalactic space would naturally solve this problem.

The other hint has to do with the observed low value of the extragalactic magnetic field as determined from observations of blazars [48]. According to the authors, a possible solution consists in the photon-ALP oscillation mechanism.

We show that within the DARMA scenario the situation is quite different. As a result of the competition between EBL attenuation and photon-ALP oscillations, two important conclusions emerge:

- The values of $\Gamma_{\rm em}$ for far-away VHE blazars are in the same ballpark of nearby ones, so that the cosmic opacity problem is solved.
- The observed large spread in the values of $\Gamma_{\rm obs}$ arises mainly from the wide spread in the source distances while the required scatter in the values of $\Gamma_{\rm em}$ is small.

Subsequently, we move our attention on flat spectrum radio quasars (FSRQs), and in particular on PKS 1222+216 (Chapters 6-7). The recent evidence of VHE emission by FSRQs poses a quite serious challenge. The surrounding of the inner jet in FSRQs is rich of optical/ultraviolet photons emitted by the broad line region (BLR), necessarily implying a huge optical depth for γ rays above 10 – 20 GeV (see e.g. [141, 160]). Therefore, the observation of some FSRQs at TeV energies raised great surprise [38, 161, 162]. Moreover, the detection of an intense VHE emission from PKS 1222+216 at redshift $z = 0.432$ in the energy range 70 – 400 GeV [161] observed by MAGIC to double its flux in only about 10 minutes – thereby flagging the extreme compactness of the emitting region – is very difficult to fit within the standard blazar models [142].

So far, the only possibility to solve the apparent contradiction with conventional expectations arising from both the detection of the intense and relatively hard VHE flux and the rapid variation appears to invoke the existence of very small ($r \sim 10^{14}$ cm) emitting regions (or beams of particles) beyond the BLR ($R \sim 10^{18}$ cm), that is at a large distance from the central engine [142, 151, 163].

An additional question is that PKS 1222+216 has also been simultaneously detected by *Fermi*/LAT in the energy range $0.3 - 3\,\mathrm{GeV}$ [150].

So, one would like not only to understand why the VHE γ rays are actually *emitted* by PKS 1222+216 but also to find a *realistic and physically motivated* spectral energy distribution (SED) that fits *both* the observed *Fermi*/LAT and the MAGIC spectra, which is a logically distinct and more ambitious task.

Our proposal to naturally explain all these observations assumes the validity of a standard blazar model for photon production, but we add the new assumption that photon-ALP oscillations take place inside the source in such a way that a considerable fraction of VHE photons can leave it, indeed much in the same fashion that a sizable amount of VHE photons emitted by blazars largely avoid EBL absorption if extragalactic space is permeated by a large-scale magnetic field in the nG range. More specifically, we envisage that the $\gamma \to a$ conversion occurs before most of the VHE photons reach the BLR. Accordingly, ALPs traverse this region unimpeded and outside it the re-conversion $a \to \gamma$ takes place either in the same magnetic field of the source or in that of the host galaxy. Thus, our proposal differs from any previously considered one. Moreover, we find that for observationally allowed values of the parameters of our model the resulting SED looks quite realistic and nicely fits the *Fermi*/LAT and MAGIC spectra observed at the same time.

Thereafter, we critically analyze a result obtained by D. Wouters and P. Brun (WB) [156] (Chapter 8). The authors claim that an observable effect in the spectra of distant VHE blazars arises as a consequence of oscillations of photons into ALPs in the presence of random extragalactic magnetic fields. WB state that in a pretty small range about the energy $E_{\rm thr} \equiv E_*$ (defined in Chapter 1 Sec. 1.5) that marks the transition from the weak to the strong mixing regime the photon survival probability along every single trajectory that the beam can follow exhibits fluctuations, which are claimed to be an *observable* signature of the existence of photon-ALP oscillations. We show that they consider an initially *polarized* beam, whereas a physically correct treatment demands the beam to be initially *unpolarized*. As a consequence, the result of WB changes substantially (with correct physical treatment of the beam) to an extent that their result can only make bounds at the 3σ level, which cannot rule out the existence of an ALP (in this field a detection should be at the 5σ level).

Finally, we stress that ALPs with the right properties to produce the above effects can be discovered in the near future by the planned upgrade of the photon regeneration experiment ALPS at DESY [49] or with the Cherenkov Telescope Array (CTA). Thus, it looks amazing that the discovery of a new particle – besides very important in its own right – would also provide a sort of glasses that allow us to watch much farther out into the γ-ray Universe.

Plan of the second part of the thesis

The second part of this thesis is organized as follows. In Chapter 1 we review the motivation and the main properties of ALPs. Particular attention is paid to the propagation of a photon/ALP beam in the presence of a homogeneous magnetic field. Also the astrophysical and cosmological constraints on the ALP parameters are considered. In Chapter 2 we carefully evaluate the transparency of the Universe to gamma rays in the energy range $10 - 10^{13}$ GeV using the most recent observational data concerning the EBL and the Radio Background (RB). Chapter 3 addresses in great detail the properties of VHE blazar spectra. Everything in this Chapter is discussed within conventional physics and at this stage ALPs are totally neglected. The cosmic opacity is also addressed. In Chapter 4 the main conclusions drawn in Chapters 1, 2 and 3 are combined together to build up the DARMA scenario which considers photon-ALP oscillations in the presence of EBL absorption as well as for a domain-like configuration typical of large-scale magnetic fields. The photon survival probability is ultimately computed by a numerical code and it arises as an average over 5000 random realizations of the beam propagation from the source to us, each corresponding to randomly chosen directions of the magnetic field inside every domain. Chapter 5 is devoted to the discussion of the implications of the DARMA scenario for VHE blazar observations. We calculate the photon survival probability for some representative values of the free parameters and we offer a new interpretation of the observed VHE blazars, which solves the cosmic opacity problem and traces the large spread in the values of $\Gamma_{\rm obs}$ mainly to the wide spread in the source distances while the required scatter in the values of $\Gamma_{\rm em}$ is small. In Chapter 6 we describe our model for the FSRQ PKS 1222+216 and we show that we naturally solve the problem within standard AGN models with the additional assumption of the existence of photon/ALP oscillations. In Chapter 7 we provide a specific picture which gives rise to the required SED for the FSRQ PKS 1222+216 and we compare our results to others present in the literature. In Chapter 8 we critically analyze a result obtained by D. Wouters and P. Brun about a clamed observable effect in the blazar spectra which is consequence of oscillations of photons into ALPs and we show that a physically correct treatment of the photon/ALP beam substantially changes their result. A convenient method to solve the Schödinger-like equation with constant coefficients describing the photon/ALP beam propagation is presented in Appendix A, whereas an approximate analytic evaluation of the optical depth within the FRV model of the EBL is reported in Appendix B.

The matter described in the second part of this thesis is reported also in the following publications:

- [ax1] De Angelis, A., Galanti, G., & Roncadelli, M., *"Relevance of axionlike particles for very-high-energy astrophysics"*, Phys. Rev. D, **84**, 105030 (2011)
- [ax2] Tavecchio, F., Roncadelli, M., Galanti, G., & Bonnoli, G., *"Evidence for an axion-like particle from PKS 1222+216?"*, Phys. Rev. D, **86**, 085036 (2012)
- [ax3] Galanti, G., & Roncadelli, M., *"Comment on: Irregularity in gamma ray source spectra as a signature of axion-like particles"*, arXiv:1305.2114, submitted to Phys. Rev. D (2013)
- [ax4] De Angelis, A., Galanti, G., & Roncadelli, M., *"Transparency of the Universe to gamma-rays"*, Mon. Not. R. Astron. Soc. **432**, 3245 (2013)

In particular, [ax1] deals with the topics of Chapters 1, 3, 4 and 5, Appendixes A and B; [ax2] treats the matter developed in Chapters 6 and 7; [ax3] discusses the subject of Chapter 2; [ax4] deals with the topic of Chapter 8.

Chapter 1

Axion-like particles (ALPs)

We review the conceptual motivations in favour of ALPs as well as their properties that are most relevant for our further needs. Natural Lorentz-Heaviside units with $\hbar = c = k_{\rm B} = 1$ are employed throughout this thesis unless otherwise stated.

1.1 Motivation

As already stressed, the SM of particle physics is presently regarded as the low-energy manifestation of some more fundamental theory (FT) characterized by a very large energy scale $\Lambda \gg G_F^{-1/2}$, with $G_F^{-1/2} \simeq 250\,\text{GeV}$. We collectively denote by ϕ the SM particles together with possibly new undetected particles with mass smaller than $G_F^{-1/2}$, while all particles much heavier than $G_F^{-1/2}$ that are present in the FT are collectively represented by Φ. Correspondingly, the FT is defined by a Lagrangian of the form $\mathcal{L}_{\rm FT}(\phi, \Phi)$ and the generating functional for the corresponding Green's functions reads

$$Z_{\rm FT}[J,K] = N \int \mathcal{D}\phi \int \mathcal{D}\Phi \, \exp\left(i \int d^4x \left[\mathcal{L}_{\rm FT}(\phi,\Phi) + \phi J + \Phi K \right] \right) \,, \tag{1.1}$$

where J and K are external sources and N is a normalization constant. The resulting low-energy effective theory then emerges by integrating out the heavy particles in $Z_{\rm FT}[J,K]$, and so the low-energy effective Lagrangian $\mathcal{L}_{\rm eff}(\phi)$ is defined by

$$\exp\left(i \int d^4x \, \mathcal{L}_{\rm eff}(\phi) \right) \equiv \int \mathcal{D}\Phi \exp\left(i \int d^4x \, \mathcal{L}_{\rm FT}(\phi,\Phi) \right) \,. \tag{1.2}$$

Evidently, the SM Lagrangian is contained in $\mathcal{L}_{\rm eff}(\phi)$, and – in the absence of any new physics below $G_F^{-1/2}$ – it will differ from $\mathcal{L}_{\rm eff}(\phi)$ only by non-renormalizable terms involving the ϕ particles alone, that are suppressed by inverse powers of Λ.

In any theory with a sufficiently rich gauge structure – which is certainly the case of the FT – some global symmetry $\mathcal{G}$ invariably shows up as an accidental consequence of gauge invariance. Since the Higgs fields which spontaneously break gauge symmetries carry nontrivial global quantum numbers, it follows that the group $\mathcal{G}$ undergoes spontaneous symmetry breaking as well. As a consequence, some Goldstone bosons – which are collectively denoted by a if $\mathcal{G}$ is non-abelian – are expected to appear in the physical spectrum and their interactions are described by the low-energy effective Lagrangian, in spite of the fact that $\mathcal{G}$ is an invariance of the FT. We stress that Goldstone bosons are necessarily pseudo-scalar particles [50].

As far as our main line of development is concerned, the FT is supposed to describe quantum gravitational effects and it is a common lore that they always explicitly break global symmetries [51]. In fact, this point can be understood in an intuitive fashion. Since black holes do not possess any definite global charges, global symmetries are violated in any scattering process involving black holes. So, we end up with the general conclusion that provided that the Lagrangian of the FT possesses some spontaneously broken global symmetry then pseudo-Goldstone bosons with mass much smaller than $G_F^{-1/2}$ are necessarily present in the low-energy effective Lagrangian.

Therefore, by splitting up the set ϕ into the set of SM particles $\phi_{\rm SM}$ plus the pseudo-Goldstone bosons a, the low-energy effective Lagrangian has the structure

$$\mathcal{L}_{\rm eff}(\phi_{\rm SM}, a) = \mathcal{L}_{\rm SM}(\phi_{\rm SM}) + \mathcal{L}_{\rm nonren}(\phi_{\rm SM}) + \mathcal{L}_{\rm ren}(a) + \mathcal{L}_{\rm ren}(\phi_{\rm SM}, a) + \mathcal{L}_{\rm nonren}(\phi_{\rm SM}, a) \ , \tag{1.3}$$

where $\mathcal{L}_{\rm ren}(\phi_{\rm SM}, a)$ stands for renormalizable soft-breaking terms that can be present whenever $\mathcal{G}$ is not an automatic symmetry of the low-energy effective theory [1].

Needless to say, it can well happen that between $G_F^{-1/2}$ and Λ other relevant mass scales Λ_1, Λ_2, ... exists. In such a situation the above scheme remains true, but then $\mathcal{G}$ may be spontaneously broken at such an intermediate scale.

Finally, we would like to stress that a very thoroughly analysis by Arvanitaki *et al.* [6] in the context of superstring theories and by Turok [3] in fundamental theories with compact extra dimensions have made the above conclusion more specific, showing that in either case the pseudo-Goldstone bosons are actually ALPs.

[1] We recall that by automatic symmetry it is meant any global symmetry which is present in the most general renormalizable Lagrangian invariant under the gauge group.

1.2 Axion as a prototype

A characteristic feature of the SM is that non-perturbative effects produce the term $\Delta\mathcal{L}_\theta = \theta g^2 G_a^{\mu\nu}\tilde{G}_{a\mu\nu}/32\pi^2$ in the QCD Lagrangian, where θ is an angle, g and $G_a^{\mu\nu}$ are the gauge coupling constant and the gauge field strength of $SU_c(3)$, respectively, and $\tilde{G}_a^{\mu\nu} \equiv \frac{1}{2}\epsilon^{\mu\nu\rho\sigma}G_{a\rho\sigma}$. All values of θ are allowed and theoretically on the same footing, but nonvanishing θ values produce a P and CP violation in the strong sector of the SM. An additional source of CP violation comes from the chiral transformation needed to bring the quark mass matrix $\mathcal{M}_q$ into diagonal form, and so the total strong CP violation is parametrized by $\bar{\theta} = \theta + \arg\,\mathrm{Det}\,\mathcal{M}_q$. Observationally, a nonvanishing $\bar{\theta}$ would show up in an electric dipole moment d_n for the neutron. Consistency with the experimental upper bound $|d_n| < 3 \cdot 10^{-26}\,\mathrm{e\,cm}$ requires $|\bar{\theta}| < 10^{-9}$ (for a review, see [11]). Thus, the question arises as to why $|\bar{\theta}|$ is so unexpectedly small. A natural way out of this fine-tuning problem – which is the *strong CP problem* – was proposed by Peccei and Quinn [8] over 30 years ago. Basically, the idea is to make the SM Lagrangian invariant under an additional global $U(1)_{\mathrm{PQ}}$ symmetry in such a way that the $\Delta\mathcal{L}_\theta$ term can be rotated away. While this strategy can be successfully implemented, it turns out that the $U(1)_{\mathrm{PQ}}$ is spontaneously broken and then a Goldstone boson is necessarily present in the physical spectrum. Things are slightly more complicated, because $U(1)_{\mathrm{PQ}}$ is also explicitly broken by the same non-perturbative effects which give rise to $\Delta\mathcal{L}_\theta$. Therefore, the would-be Goldstone boson becomes a pseudo-Goldstone boson – the original axion [9] – with nonvanishing mass given by

$$m \simeq 0.6 \left(\frac{10^7\,\mathrm{GeV}}{f_a}\right)\,\mathrm{eV}\ , \tag{1.4}$$

where f_a denotes the scale at which $U(1)_{\mathrm{PQ}}$ is spontaneously broken. Qualitatively, the axion is quite similar to the pion and it possesses Yukawa couplings to quarks which go like the inverse of f_a. Moreover – just like for the pion – a two-photon coupling $a\gamma\gamma$ of the axion a is generated at one-loop via the triangle graph with internal fermion lines, which is described by the effective Lagrangian

$$\mathcal{L}_{a\gamma\gamma} = -\frac{1}{4M}\,F^{\mu\nu}\,\tilde{F}_{\mu\nu}\,a = \frac{1}{M}\,\mathbf{E}\cdot\mathbf{B}\,a\ , \tag{1.5}$$

where $F^{\mu\nu} \equiv (\mathbf{E},\mathbf{B}) \equiv \partial^\mu A^\nu - \partial^\nu A^\mu$ is the usual electromagnetic field strength and $\tilde{F}^{\mu\nu} \equiv \frac{1}{2}\epsilon^{\mu\nu\rho\sigma}F_{\rho\sigma}$. The constant M entering Eq. (1.5) has the dimension of an energy and is given by

$$M = 1.2 \cdot 10^{10}\,k\,\left(\frac{f_a}{10^7\,\mathrm{GeV}}\right)\,\mathrm{GeV}\ , \tag{1.6}$$

with k a model-dependent parameter of order one [52]. Note that $M \propto f_a$ and turns out to be independent of the mass of the fermions running in the loop. Hence, the axion is characterized by a strict relation between its mass and two-photon coupling

$$m = 0.7\, k \left(\frac{10^{10}\,\mathrm{GeV}}{M}\right) \mathrm{eV}\ . \tag{1.7}$$

In the original proposal [8], $U(1)_{\mathrm{PQ}}$ is spontaneously broken by two Higgs doublets which also break $SU_w(2) \times U_y(1)$ spontaneously, so that $f_a \leq G_F^{-1/2}$. Correspondingly, from Eq. (1.4) we get $m \geq 24\,\mathrm{KeV}$. In addition, the axion is rather strongly coupled to quarks and induces observable nuclear de-excitation effects [53]. In fact, it was soon realized that the original axion was experimentally ruled out [54].

A slight change in perspective led shortly thereafter to the resurrection of the axion strategy. Conflict with experiment arises because the original axion is too strongly coupled and too massive. But, given the fact that both m and all axion couplings go like the inverse of f_a the axion becomes weakly coupled and sufficiently light provided that one arranges $f_a \gg G_F^{-1/2}$. This is straightforwardly achieved by performing the spontaneous breakdown of $U(1)_{\mathrm{PQ}}$ with a Higgs field which is a singlet under $SU_w(2) \times U_y(1)$ [10]. Note that we are thereby led to the conclusion that the $U(1)_{\mathrm{PQ}}$ symmetry has nothing to do with the low-energy effective theory to which the axion belongs, but rather it arises within an underlying more fundamental theory.

Thus, we see that the axion strategy provides a particular realization of the general scenario outlined in Sec. 1.1, with $\mathcal{G} = U(1)_{\mathrm{PQ}}$, $\Lambda_1 = f_a$ and $\mathcal{L}_{\mathrm{nonren}}(\phi_{\mathrm{SM}}, a)$ including $\mathcal{L}_{a\gamma\gamma}$ among other terms involving the SM fermions. This fact also entails that new physics should lurk around the scale at which $U(1)_{\mathrm{PQ}}$ is spontaneously broken. The same conclusion is reached from the recognition that the Peccei-Quinn symmetry is dramatically unstable against a tiny perturbation – even at the Planck scale – unless it is protected by some discrete gauge symmetry which can only arise in a more fundamental theory [55].

1.3 Beyond the axion: ALPs

A generic feature of many extensions of the SM along the lines discussed in the Introduction is the prediction of ALPs. Generally speaking, ALPs are a straightforward generalization of the axion but important differences exist between the axion and ALPs mainly because the axion arises in a very specific context while in dealing with ALPs the aim is to bring out their properties in a model-independent fashion as much as possible [7]. This attitude has two main consequences:

- Only ALP-photon interaction terms are taken into account. Therefore, any other possible coupling of ALPs to SM particles is presently discarded and this entails that $\mathcal{L}_{\rm nonren}(\phi_{\rm SM}, a)$ in Eq. (1.3) *only* includes $\mathcal{L}_{a\gamma\gamma}$ as defined by Eq. (1.5). Observe that such an ALP coupling to two photons $a\gamma\gamma$ is just supposed to exist without further worrying about its origin.

- The parameters m and M are to be regarded as *unrelated* for ALPs, and it is merely assumed that $m \ll G_F^{-1/2}$ and $M \gg G_F^{-1/2}$.

As a result, ALPs are described by the Lagrangian

$$\mathcal{L}_{\rm ALP} = \frac{1}{2}\,\partial^\mu a\,\partial_\mu a - \frac{1}{2}\,m^2\,a^2 - \frac{1}{4M}\,F_{\mu\nu}\tilde{F}^{\mu\nu}a = \frac{1}{2}\,\partial^\mu a\,\partial_\mu a - \frac{1}{2}\,m^2\,a^2 + \frac{1}{M}\,\mathbf{E}\cdot\mathbf{B}\;a. \quad (1.8)$$

1.4 Photon-ALP mixing

What ultimately characterizes ALPs is the trilinear $a\gamma\gamma$ vertex in $\mathcal{L}_{\rm ALP}$, which gives rise to photon-ALP mixing in the presence of an *external* magnetic field $\mathbf{B}$. More specifically, what happens can be described as follows.

In such a situation, an off-diagonal element in the mass matrix for the photon-ALP system shows up. Therefore, the interaction eigenstates differ from the propagation eigenstates and the phenomenon of photon-ALP oscillations shows up [14, 15]. This is analogous to what takes place in the case of massive neutrinos with different flavours, apart from an important difference. All neutrinos have equal spin, and so neutrino oscillations can freely occur. Instead, ALPs are supposed to have spin zero whereas the photon has spin one, hence one of them can transform into the other only if the spin mismatch is compensated for by an external magnetic field. Note that the strength of this effect depends on the ratio B/M and not on B and M separately.

We denote by $\mathbf{E}$ the electric field and by $\mathbf{k}$ the wave vector of a propagating photon at a given space-time point. Further, let $\mathbf{B}_L$ and $\mathbf{B}_T$ be the components of the external magnetic field $\mathbf{B}$ along $\mathbf{k}$ and perpendicular to $\mathbf{k}$, respectively. Because $\mathbf{E}$ is orthogonal to $\mathbf{k}$ it follows that only the term $\mathbf{E}\cdot\mathbf{B}_T$ survives in $\mathcal{L}_{\rm ALP}$. We next split up $\mathbf{E}$ into two components, one $\mathbf{E}_\parallel$ in the plane defined by $\mathbf{k}$ and $\mathbf{B}$ and the other $\mathbf{E}_\perp$ perpendicular to that plane. By construction, $\mathbf{E}_\perp$ is orthogonal to $\mathbf{B}_T$, and so the $a\gamma\gamma$ coupling in $\mathcal{L}_{\rm ALP}$ goes like $E_\parallel\,B_T\,a$, which exhibits two characteristic properties of ALPs. First, the photon-ALP mixing depends only on the transverse component $\mathbf{B}_T$ of the external magnetic field; for notational simplicity we will write $\mathbf{B}$ rather than $\mathbf{B}_T$ in the following. Second, only photons linearly polarized along $\mathbf{E}_\parallel$ actually mix with ALPs, whereas photons with polarization $\mathbf{E}_\perp$ do not mix. As a consequence, the $a\gamma\gamma$ coupling acts

like a polarimeter, in the sense that it gives rise to a change of the photon polarization state. This effect can be used to look for ALPs both in high-precision polarimetric measurements performed in the laboratory [17] and in certain astrophysical observations in which the polarization state of the detected photons can be measured [32].

1.5 Photon/ALP beam propagation

We shall be concerned throughout with a monochromatic, unpolarized photon/ALP beam of energy E and wave vector $\mathbf{k}$ propagating in a cold medium which is both magnetized and ionized (from now on E denotes the energy, and since the electric field will never be considered again no confusion arises). We suppose for the moment that the external magnetic field $\mathbf{B}$ is homogeneous and we denote by n_e the electron number density. We employ an orthogonal reference frame with the y-axis along $\mathbf{k}$, while the x and z axes are chosen arbitrarily.

It can be shown that in this case the beam propagation equation following from $\mathcal{L}_{\rm ALP}$ can be written as [15]

$$\left(\frac{d^2}{dy^2} + E^2 + 2E\mathcal{M}_0\right)\psi(y) = 0 \tag{1.9}$$

with

$$\psi(y) \equiv \begin{pmatrix} A_x(y) \\ A_z(y) \\ a(y) \end{pmatrix} , \tag{1.10}$$

where $A_x(y)$ and $A_z(y)$ denote the photon amplitudes with polarization (electric field) along the x- and z-axis, respectively, while $a(y)$ is the amplitude associated with the ALP. It is useful to introduce the basis $\{|\gamma_x\rangle, |\gamma_z\rangle, |a\rangle\}$ defined by

$$|\gamma_x\rangle \equiv \begin{pmatrix} 1 \\ 0 \\ 0 \end{pmatrix} , \tag{1.11}$$

$$|\gamma_z\rangle \equiv \begin{pmatrix} 0 \\ 1 \\ 0 \end{pmatrix} , \tag{1.12}$$

$$|a\rangle \equiv \begin{pmatrix} 0 \\ 0 \\ 1 \end{pmatrix} , \tag{1.13}$$

where $|\gamma_x\rangle$ and $|\gamma_z\rangle$ represent the two photon linear polarization states along the x- and z-axis, respectively, and $|a\rangle$ denotes the ALP state. Accordingly, we can rewrite $\psi(y)$ as

$$\psi(y) = A_x(y)\,|\gamma_x\rangle + A_z(y)\,|\gamma_z\rangle + a(y)\,|a\rangle \ , \tag{1.14}$$

and the real, symmetric photon-ALP mixing matrix $\mathcal{M}_0$ entering Eq. (1.9) has the form

$$\mathcal{M}_0 = \begin{pmatrix} \Delta_{xx} & \Delta_{xz} & \Delta^x_{a\gamma} \\ \Delta_{zx} & \Delta_{zz} & \Delta^z_{a\gamma} \\ \Delta^x_{a\gamma} & \Delta^z_{\mathrm{a}\gamma} & \Delta_{aa} \end{pmatrix} \ , \tag{1.15}$$

where we have set

$$\Delta^x_{a\gamma} \equiv \frac{B_x}{2M} \ , \tag{1.16}$$

$$\Delta^z_{a\gamma} \equiv \frac{B_z}{2M} \ , \tag{1.17}$$

$$\Delta_{aa} \equiv -\frac{m^2}{2E} \ . \tag{1.18}$$

While the terms appearing in the third row and column of $\mathcal{M}_0$ are dictated by $\mathcal{L}_{\mathrm{ALP}}$ and have an evident physical meaning, the other Δ-terms require some explanation. They reflect the properties of the medium – which are not included in $\mathcal{L}_{\mathrm{ALP}}$ – and the off-diagonal Δ-terms directly mix the photon polarization states giving rise to Faraday rotation.

In the present thesis we are interested in the situation where the photon/ALP energy is much larger than the ALP mass, namely $E \gg m$. As a consequence, the short-wavelength approximation can be successfully employed and can be implemented as [15]

$$\left(\frac{d^2}{dy^2} + E^2\right)\psi(y) = \left(i\frac{d}{dy} + E\right)\left(-i\frac{d}{dy} + E\right)\psi(y) = 2E\left(i\frac{d}{dy} + E\right)\psi(y) \ , \tag{1.19}$$

which turns the second-order beam propagation equation (1.9) into the first-order one

$$\left(i\frac{d}{dy} + E + \mathcal{M}_0\right)\psi(y) = 0 \ . \tag{1.20}$$

We see that a remarkable picture emerges, wherein the beam looks formally like a three-state nonrelativistic quantum system. Explicitly, they are the two photon polarization states and the ALP state. The evolution of the *pure* beam states is then described by the three-dimensional wave function $\psi(y)$ – with the y-coordinate replacing time – which obeys the Schödinger-like equation (1.20) with Hamiltonian

$$H_0 \equiv -\left(E + \mathcal{M}_0\right) \ . \tag{1.21}$$

Denoting by $U_0(y, y_0)$ the transfer matrix – namely the solution of Eq. (1.20) with initial condition $U_0(y_0, y_0) = 1$ – the propagation of a generic wave function can be represented as

$$\psi(y) = U_0(y, y_0)\, \psi(y_0) \ . \tag{1.22}$$

Moreover, we have

$$U_0(y, y_0) = e^{iE(y-y_0)}\, \mathcal{U}_0(y, y_0) \ , \tag{1.23}$$

where $\mathcal{U}_0(y, y_0)$ is the transfer matrix associated with the reduced Schödinger-like equation

$$\left(i\frac{d}{dy} + \mathcal{M}_0 \right) \psi(y) = 0 \ . \tag{1.24}$$

Because $\mathbf{B}$ is supposed to be homogeneous, we have the freedom to choose the z-axis along $\mathbf{B}$, so that $B_x = 0$. The diagonal Δ-terms receive in principle two different contributions. One comes from the Heisenberg-Euler-Weisskopf (HEW) effective lagrangian

$$\mathcal{L}_{\rm HEW} = \frac{2\alpha^2}{45 m_e^4} \left[\left(\mathbf{E}^2 - \mathbf{B}^2 \right)^2 + 7 \left(\mathbf{E} \cdot \mathbf{B} \right)^2 \right] \ , \tag{1.25}$$

accounting for the photon one-loop vacuum polarization in the presence of an external magnetic field (α is the fine-structure constant and m_e is the electron mass) [56]. Hence, we can define the two terms

$$\Delta_{xx}^{\rm QED} = \frac{2\alpha E}{45\pi} \Big(\frac{B}{B_{cr}} \Big)^2 \ , \tag{1.26}$$

$$\Delta_{zz}^{\rm QED} = \frac{7\alpha E}{90\pi} \Big(\frac{B}{B_{\rm cr}} \Big)^2 \ , \tag{1.27}$$

where $B_{\rm cr} \simeq 4.41 \cdot 10^{13}\,{\rm G}$ is the critical magnetic field. The other contribution arises from the fact that the beam is supposed to propagate in a cold plasma, where charge screening produces an effective photon mass resulting in the plasma frequency

$$\omega_{\rm pl} = \left(\frac{4\pi\alpha n_e}{m_e} \right)^{1/2} \ , \tag{1.28}$$

which entails

$$\Delta_{\rm pl} = -\frac{\omega_{\rm pl}^2}{2E} \ . \tag{1.29}$$

Finally, the Δ_{xz}, Δ_{zx} terms account for Faraday rotation, but since we are going to take E in the VHE γ-ray band Faraday rotation is negligible. Altogether, the mixing matrix becomes

$$\mathcal{M}_0^{(0)} = \begin{pmatrix} \Delta_{xx}^{\rm QED} + \Delta_{\rm pl} & 0 & 0 \\ 0 & \Delta_{zz}^{\rm QED} + \Delta_{\rm pl} & \Delta_{a\gamma} \\ 0 & \Delta_{a\gamma} & \Delta_{aa} \end{pmatrix} \ , \tag{1.30}$$

with the superscript (0) recalling the present choice of the coordinate system and

$$\Delta_{a\gamma} \equiv \frac{B}{2M} \ . \tag{1.31}$$

We see that A_x decouples away while only A_z mixes with a, showing that in the present approximation plasma effects do not change the qualitative features previously found in vacuo.

Application of the discussion reported in Appendix A with $\mathcal{M} \to \mathcal{M}_0^{(0)}$ yields for the corresponding eigenvalues

$$\lambda_{0,1} = \Delta_{xx}^{\rm QED} + \Delta_{\rm pl} \ , \tag{1.32}$$

$$\lambda_{0,2} = \frac{1}{2}\Big(\Delta_{zz}^{\rm QED} + \Delta_{\rm pl} + \Delta_{aa} - \Delta_{\rm osc}\Big) \ , \tag{1.33}$$

$$\lambda_{0,3} = \frac{1}{2}\Big(\Delta_{zz}^{\rm QED} + \Delta_{\rm pl} + \Delta_{aa} + \Delta_{\rm osc}\Big) \ , \tag{1.34}$$

where we have set

$$\Delta_{\rm osc} \equiv \Big[\big(\Delta_{zz}^{\rm QED} + \Delta_{\rm pl} - \Delta_{\rm aa}\big)^2 + 4\,(\Delta_{a\gamma})^2\Big]^{1/2} = \left[\left(\Delta_{zz} + \frac{m^2}{2E}\right)^2 + \left(\frac{B}{M}\right)^2\right]^{1/2} \ . \tag{1.35}$$

As a consequence, the transfer matrix associated with Eq. (1.24) with mixing matrix $\mathcal{M}_0^{(0)}$ can be written with the help of Eq. (A.16) as

$$\mathcal{U}_0(y, y_0; 0) = e^{i\lambda_1(y-y_0)}\, T_{0,1}(0) + e^{i\lambda_2(y-y_0)}\, T_{0,2}(0) + e^{i\lambda_3(y-y_0)}\, T_{0,3}(0) \ , \tag{1.36}$$

where the matrices $T_{0,1}(0)$, $T_{0,2}(0)$ and $T_{0,3}(0)$ are just those defined by Eqs. (A.17), (A.18) and (A.19) as specialized to the present situation. Actually, a simplification is brought about by introducing the photon-ALP mixing angle

$$\alpha = \frac{1}{2}\,\mathrm{arctg}\left(\frac{2\,\Delta_{a\gamma}}{\Delta_{zz}^{\rm QED} + \Delta_{\rm pl} - \Delta_{aa}}\right) \ , \tag{1.37}$$

since then simple trigonometric manipulations allow us to express the above matrices in the simpler form

$$T_{0,1}(0) \equiv \begin{pmatrix} 1 & 0 & 0 \\ 0 & 0 & 0 \\ 0 & 0 & 0 \end{pmatrix} \ , \tag{1.38}$$

$$T_{0,2}(0) \equiv \begin{pmatrix} 0 & 0 & 0 \\ 0 & \sin^2\alpha & -\sin\alpha\cos\alpha \\ 0 & -\sin\alpha\cos\alpha & \cos^2\alpha \end{pmatrix} \ , \tag{1.39}$$

$$T_{0,3}(0) \equiv \begin{pmatrix} 0 & 0 & 0 \\ 0 & \cos^2\alpha & \sin\alpha\cos\alpha \\ 0 & \sin\alpha\cos\alpha & \sin^2\alpha \end{pmatrix} . \tag{1.40}$$

Now, the probability that a photon polarized along the z-axis oscillates into an ALP after a distance y is evidently

$$P^{(0)}_{0,\gamma_z\to a}(y) = |\langle a|\mathcal{U}_0(y,0;0)|\gamma_z\rangle|^2 \tag{1.41}$$

and in complete analogy with the case of neutrino oscillations [19] it reads

$$P^{(0)}_{0,\gamma_z\to a}(y) = \sin^2 2\alpha\, \sin^2\left(\frac{\Delta_{\rm osc}\, y}{2}\right) , \tag{1.42}$$

which shows that $\Delta_{\rm osc}$ plays the role of oscillation wave number, thereby implying that the oscillation length is $L_{\rm osc} = 2\pi/\Delta_{\rm osc}$. Owing to Eq. (1.37), Eq. (1.42) can be rewritten as

$$P^{(0)}_{0,\gamma_z\to a}(y) = \left(\frac{B}{M\,\Delta_{\rm osc}}\right)^2 \sin^2\left(\frac{\Delta_{\rm osc}\, y}{2}\right) , \tag{1.43}$$

which shows that the photon-ALP oscillation probability becomes both maximal and energy-independent for

$$\Delta_{\rm osc} \simeq \frac{B}{M} , \tag{1.44}$$

and explicitly reads

$$P^{(0)}_{0,\gamma_z\to a}(y) \simeq \sin^2\left(\frac{By}{2M}\right) . \tag{1.45}$$

This is the *strong-mixing regime*, which – from the comparison of Eqs. (1.35) and (1.44) – turns out to be characterized by the condition

$$\left|\Delta_{zz} + \frac{m^2}{2E}\right| \ll \frac{B}{M} , \tag{1.46}$$

and so it takes place in the energy range

$$E_* \ll E \ll E_{**} , \tag{1.47}$$

where

$$E_* \equiv \frac{|m^2 - \omega^2_{\rm pl}|M}{2B} , \tag{1.48}$$

and

$$E_{**} \equiv \frac{90\pi}{7\alpha}\frac{B^2_{\rm cr}}{BM} . \tag{1.49}$$

Outside the range $E_* \ll E \ll E_{**}$ the photon-ALP oscillation probability becomes energy-dependent and vanishingly small.

So far, our discussion was confined to the case in which the beam is in a pure polarization state. This assumption possesses the advantage of making the resulting equations particularly transparent but it has the drawback that it is too restrictive for our analysis. For, photon polarization cannot be measured in the VHE γ-ray band, and so we have to treat the beam as unpolarized. As a consequence, it will be described by a generalized polarization density matrix

$$\rho(y) = \begin{pmatrix} A_x(y) \\ A_z(y) \\ a(y) \end{pmatrix} \otimes \begin{pmatrix} A_x(y) & A_z(y) & a(y) \end{pmatrix}^* \tag{1.50}$$

rather than by a wave function $\psi(y)$. Remarkably, the analogy with non-relativistic quantum mechanics entails that $\rho(y)$ obeys the Von Neumann-like equation

$$i\frac{d\rho}{dy} = [\rho, \mathcal{M}_0] \tag{1.51}$$

associated with Eq. (1.24). Thus, the propagation of a generic $\rho(y)$ is given by

$$\rho(y) = \mathcal{U}_0(y, y_0)\, \rho(y_0)\, \mathcal{U}_0^\dagger(y, y_0) \tag{1.52}$$

and the probability that a photon/ALP beam initially in the state ρ_1 will be found in the state ρ_2 after a distance y is

$$P_{0,\rho_1\to\rho_2}(y) = \mathrm{Tr}\Big(\rho_2\, \mathcal{U}_0(y,0)\, \rho_1\, \mathcal{U}_0^\dagger(y,0)\Big)\ , \tag{1.53}$$

since we are assuming as usual that $\mathrm{Tr}\rho_1 = \mathrm{Tr}\rho_2 = 1$. Observe that in Eqs. (1.51), (1.52) and (1.53) we have dropped the superscript (0) in $\mathcal{M}_0$ and replaced $\mathcal{U}_0(y, y_0; 0)$ by $\mathcal{U}_0(y, y_0)$ because they retain their form for an arbitrary choice of the coordinate system.

In view of our subsequent discussion it proves essential to deal with the general case in which $\mathbf{B}$ is not aligned with the z-axis but forms a nonvanishing angle ψ with it. Correspondingly, the mixing matrix $\mathcal{M}_0$ presently arises from $\mathcal{M}_0^{(0)}$ through the similarity transformation

$$\mathcal{M}_0 = V^\dagger(\psi)\, \mathcal{M}_0^{(0)}\, V(\psi) \tag{1.54}$$

operated by the rotation matrix in the x–z plane, namely

$$V(\psi) = \begin{pmatrix} \cos\psi & -\sin\psi & 0 \\ \sin\psi & \cos\psi & 0 \\ 0 & 0 & 1 \end{pmatrix}\ . \tag{1.55}$$

This leads to [28]

$$\mathcal{M}_0 = \begin{pmatrix} \Delta_{xx}^{\mathrm{QED}} + \Delta_{\mathrm{pl}} & 0 & \Delta_{a\gamma}\,\sin\psi \\ 0 & \Delta_{zz}^{\mathrm{QED}} + \Delta_{\mathrm{pl}} & \Delta_{a\gamma}\,\cos\psi \\ \Delta_{a\gamma}\,\sin\psi & \Delta_{a\gamma}\,\cos\psi & \Delta_{aa} \end{pmatrix} , \tag{1.56}$$

indeed in agreement with Eq. (1.15) within the considered approximation. Therefore the transfer matrix reads

$$\mathcal{U}_0(y, y_0; \psi) = V^\dagger(\psi)\,\mathcal{U}_0(y, y_0; 0)\,V(\psi) \tag{1.57}$$

and its explicit representation turns out to be

$$\mathcal{U}_0(y, y_0; \psi) = e^{i\lambda_1(y-y_0)}\,T_{0,1}(\psi) + e^{i\lambda_2(y-y_0)}\,T_{0,2}(\psi) + e^{i\lambda_3(y-y_0)}\,T_{0,3}(\psi)\ , \tag{1.58}$$

with

$$T_{0,1}(\psi) \equiv \begin{pmatrix} \cos^2\psi & -\sin\psi\cos\psi & 0 \\ -\sin\psi\cos\psi & \sin^2\psi & 0 \\ 0 & 0 & 0 \end{pmatrix} , \tag{1.59}$$

$$T_{0,2}(\psi) \equiv \begin{pmatrix} \sin^2\theta\sin^2\psi & \sin^2\alpha\sin\psi\cos\psi & -\sin\alpha\cos\alpha\sin\psi \\ \sin^2\alpha\sin\psi\cos\psi & \sin^2\alpha\cos^2\psi & -\sin\alpha\cos\alpha\cos\psi \\ -\sin\alpha\cos\alpha\sin\psi & -\sin\alpha\cos\alpha\cos\psi & \cos^2\alpha \end{pmatrix} , \tag{1.60}$$

$$T_{0,3}(\psi) \equiv \begin{pmatrix} \sin^2\psi\cos^2\alpha & \sin\psi\cos\psi\cos^2\alpha & \sin\alpha\cos\alpha\sin\psi \\ \sin\psi\cos\psi\cos^2\alpha & \cos^2\psi\cos^2\alpha & \sin\alpha\cos\alpha\cos\psi \\ \sin\psi\cos\alpha\sin\alpha & \cos\psi\sin\alpha\cos\alpha & \sin^2\alpha \end{pmatrix} . \tag{1.61}$$

1.6 Astrophysical and cosmological constraints

Astrophysics has turned out to be quite effective in setting an upper bound on the $a\gamma\gamma$ vertex in $\mathcal{L}_{\mathrm{ALP}}$, which therefore holds for the axion as well as for ALPs.

In the first place, the failure to detect ALPs emitted by the Sun in the CAST experiment at CERN has led to

$$M > 1.14 \cdot 10^{10}\,\mathrm{GeV} \tag{1.62}$$

for $m < 0.02\,\mathrm{eV}$ [20].

On the theoretical side, the most reliable method concerns ALP photo-production through the Primakoff process, which takes place when an incoming photon scatters on a charged particle and becomes an ALP upon the exchange of a virtual photon.

Hot, dense plasmas in stellar cores are ideal environments wherein the Primakoff process involving thermal photons can occur. Once produced, the ALPs escape because their mean free path is much larger than the stellar radius, thereby carrying off energy. Owing to the virial equilibrium, the stellar core has a negative specific heat. Therefore it reacts to such an energy loss by getting hotter. As a result, the rate of nuclear reactions sharply increases, bringing about a substantial change in the observed properties of stars. Since current models of stellar evolution are in fairly good agreement with observations, M has to be large enough to provide a sufficient suppression of unwanted ALP effects. This argument has been applied systematically in a quantitative fashion to the Sun, to main-sequence stars and to red-giants stars in globular clusters, with the result [19]

$$M > 10^{10}\,\mathrm{GeV}\ . \tag{1.63}$$

A consequence of photon-ALP oscillations is that a lower bound on M stronger than conditions (1.62) and (1.63) – even if much less robust – can be derived for $m < 10^{-10}\,\mathrm{eV}$. In this connections, two methods have been put forward. One is based on the observation of a time-lag between opposite-polarization modes in pulsar radio emission and yields [57]

$$M > 5 \cdot 10^{10}\,\mathrm{GeV}\ . \tag{1.64}$$

The other involves ALPs emitted by the supernova SN1987A, which would convert them into γ-rays in the magnetic field of the Galaxy. Using the absence of these photons in the Solar Maximum Mission Gamma-Ray Detector, the lower bound

$$M > 10^{11}\,\mathrm{GeV} \tag{1.65}$$

has been derived [58]. We stress however that condition (1.65) is affected by large uncertainties, reflecting the lack of precise knowledge of the Galactic magnetic field as well as of the energy dependence of the detector response.

Let us next turn our attention to the cosmological constraints on ALPs. At variance with the previous astrophysical analysis, the case of the axion differs drastically from that of generic ALPs.

We recall that cosmology sets strong constraints on the axion properties because of their coupling to quarks and gluons (indeed necessary in order to solve the strong CP problem). Basically, both thermal and non-thermal mechanisms can produce axions in the early Universe. Since this issue is not directly relevant for our discussion, we cursorily summarize the main results remarking that the situation is in reality much more complex than sketched here. Recalling that f_a denotes the scale at which $U(1)_{\mathrm{PQ}}$

is spontaneously broken, only the range

$$0.6 \cdot 10^7\,\mathrm{GeV} < f_a < 0.6 \cdot 10^{13}\,\mathrm{GeV} \tag{1.66}$$

is cosmologically allowed. Thanks to Eqs. (1.4) and (1.6), this constraint translates into the conditions

$$10^{-6}\,\mathrm{eV} < m < 1\,\mathrm{eV} \tag{1.67}$$

and

$$0.7 \cdot 10^{10}\,\mathrm{GeV} < M < 0.7 \cdot 10^{16}\,\mathrm{GeV}\ , \tag{1.68}$$

respectively (we have taken for simplicity $k = 1$ in Eq. (1.6)). We stress that these bounds should be regarded merely as order-of-magnitude estimates. Moreover, the axion is a very good candidate for dark matter. More specifically, for m close to $10^{-6}\,\mathrm{eV}$ non-thermal production dominates and it behaves as a cold dark matter candidate, whereas for m close to $1\,\mathrm{eV}$ thermal production dominates and it is a hot dark matter particle [12]. Searches for axionic dark matter are currently underway with the ADMX experiment [59]. Finally, it has recently been realized that cold dark matter axions ought to form a Bose-Einstein condensate [60].

Clearly, all these considerations do not apply to ALPs, since they are supposed to interact with the rest of the world through the two-photon coupling only. As a consequence, they can be produced in the early Universe only thermally through the processes $e^{\pm}\,\gamma \to e^{\pm}\,a$ and $e^+\,e^- \to \gamma\,a$. It has been shown that in the case $m \ll 1\,\mathrm{eV}$ – which is the one relevant for us as we shall see later – ALPs are relativistic today and their abundance is anyway smaller than that of CMB photons [61]. Hence, we are led to the conclusion that the ALP considered in this thesis are totally unconstrained by cosmology and play no role for the dark matter problem.

Chapter 2

Transparency of the Universe to γ rays

VHE astrophysics is on the verge to enter its golden age. Planned ground-based detectors like CTA (Cherenkov Telescope Array) [126], HAWC (High Altitude Water Cherenkov Experiment) [127] and HiSCORE (Hundred Square-km Cosmic ORigin Explorer) [128] will probe within the next few years the energy range from 10 GeV up to 10^5 GeV (CTA and HAWC) and even up to 10^9 GeV (HiSCORE) with unprecedented sensitivity.

Unfortunately, a stumbling block along this exciting avenue is the existence of a soft photon background in the Universe which leads to a strong suppression of the observed flux through the $\gamma\gamma \to e^+e^-$ pair-production process. The onset of this process depends both on the observed energy and on the source redshift, as it will become apparent later. Specifically, it is mostly due to the EBL – i.e. to the background in the infrared, visible and ultraviolet region – in the energy range 10 GeV $- 10^5$ GeV, to the Cosmic Microwave Background (CMB) in the range 10^5 GeV $- 10^{10}$ GeV and to the RB in the range 10^{10} GeV $- 10^{13}$ GeV. Moreover, even though the SED of the EBL has remained quite uncertain for a long time, a remarkable agreement among the various EBL models has been reached recently, and also the RB has been measured in 2008 with considerably better precision than before.

All this prompts us to carefully evaluate the optical depth – which quantifies the photon absorption due to the above pair-production process – in the energy range 10 GeV $-$ 10^{13} GeV for a source redshift up to $z_s = 3$. As a particular case, we derive the photon mean free path for $\gamma\gamma \to e^+e^-$ as a function of energy in the local Universe ($z_s \simeq 0$) in order to compare it with that obtained by Coppi and Aharonian (CA) in 1997 [123]. A less detailed but similar result was independently derived at the same time by Phrotheroe and Biermann [129].

2.1 Evaluation of the pair-production cross-section

We start by recalling that the photon survival probability $P_{\gamma\to\gamma}(E_0, z_s)$ is currently parameterized as

$$P_{\gamma\to\gamma}(E_0, z_s) = e^{-\tau_\gamma(E_0, z_s)} \ , \tag{2.1}$$

where E_0 is the observed energy and $\tau_\gamma(E_0, z_s)$ is the optical depth that quantifies the dimming of the source at redshift z_s. Clearly $\tau_\gamma(E_0, z_s)$ increases with z_s, since a greater source distance implies a larger probability for a photon to disappear. Apart from atmospheric effects, one typically has $\tau_\gamma(E_0, z_s) < 1$ for z_s not too large, in which case the Universe is optically thin all the way out to the source. But depending on E_0 it can happen that $\tau_\gamma(E_0, z_s) > 1$, and so at some point the Universe becomes optically thick along the line of sight to the source. The value z_h such that $\tau_\gamma(E_0, z_h) = 1$ defines the *γ-ray horizon* for a given E_0, and sources beyond the horizon (namely with $z_s > z_h$) tend to become progressively invisible as z_s further increases past z_h.

Whenever dust effects can be neglected, photon depletion arises solely when hard photons of energy E scatter off soft background photons of energy ϵ permeating the Universe, which gives rise to hard photon absorption. Let us proceed to quantify this issue.

Regarding E as an independent variable, the process is kinematically allowed for

$$\epsilon > \epsilon_{\rm thr}(E, \varphi) \equiv \frac{2\, m_e^2\, c^4}{E\,(1 - \cos\varphi)} \ , \tag{2.2}$$

where φ denotes the scattering angle and m_e is the electron mass. Note that E and ϵ change along the line of sight in proportion of $1 + z$ because of the cosmic expansion. The corresponding Breit-Wheeler cross-section is [62]

$$\begin{aligned} \sigma_{\gamma\gamma}(E, \epsilon, \varphi) &= \frac{2\pi\alpha^2}{3m_e^2} W(\beta) \\ &\simeq 1.25 \cdot 10^{-25}\, W(\beta)\, {\rm cm}^2 \ , \end{aligned} \tag{2.3}$$

with

$$W(\beta) = \left(1 - \beta^2\right) \left[2\beta\left(\beta^2 - 2\right) + \left(3 - \beta^4\right) \ln\left(\frac{1+\beta}{1-\beta}\right)\right] .$$

The cross-section depends on E, ϵ and φ only through the speed β – in natural units – of the electron and of the positron in the center-of-mass

$$\beta(E, \epsilon, \varphi) \equiv \left[1 - \frac{2\, m_e^2\, c^4}{E\epsilon\,(1 - \cos\varphi)}\right]^{1/2} \ , \tag{2.4}$$

and Eq. (2.2) implies that the process is kinematically allowed for $\beta^2 > 0$. The cross-section $\sigma_{\gamma\gamma}(E, \epsilon, \varphi)$ reaches its maximum $\sigma_{\gamma\gamma}^{\rm max} \simeq 1.70 \cdot 10^{-25}\, {\rm cm}^2$ for $\beta \simeq 0.70$. Assuming

head-on collisions for definiteness ($\varphi = \pi$), it follows that $\sigma_{\gamma\gamma}(E, \epsilon, \pi)$ gets maximized for the background photon energy

$$\epsilon(E) \simeq \left(\frac{500\,\mathrm{GeV}}{E}\right)\,\mathrm{eV}\ , \tag{2.5}$$

where E and ϵ correspond to the same redshift. For an isotropic background of photons, the cross-section is maximized for background photons of energy [133]

$$\epsilon(E) \simeq \left(\frac{900\,\mathrm{GeV}}{E}\right)\,\mathrm{eV}\ . \tag{2.6}$$

Explicitly, the situation can be summarized as follows.

- For $10\,\mathrm{GeV} \leq E < 10^5\,\mathrm{GeV}$ the EBL plays the leading role. In particular, for $E \sim 10\,\mathrm{GeV}$ $\sigma_{\gamma\gamma}(E, \epsilon)$ – integrated over an isotropic distribution of background photons – is maximal for $\epsilon \sim 90\,\mathrm{eV}$, corresponding to far-ultraviolet soft photons, whereas for $E \sim 10^5\,\mathrm{GeV}$ $\sigma_{\gamma\gamma}(E, \epsilon)$ is maximal for $\epsilon \sim 9 \cdot 10^{-3}\,\mathrm{eV}$, corresponding to soft photons in the far-infrared.
- For $10^5\,\mathrm{GeV} \leq E < 10^{10}\,\mathrm{GeV}$ the interaction with the CMB becomes dominant.
- For $E \geq 10^{10}\,\mathrm{GeV}$ the main source of opacity of the Universe is the RB.

2.2 Evaluation of the optical depth

Within the standard ΛCDM cosmological model $\tau_\gamma(E_0, z_s)$ arises by first convolving the spectral number density $n_\gamma(\epsilon(z), z)$ of background photons at a generic redshift z with $\sigma_{\gamma\gamma}(E(z), \epsilon(z), \varphi)$ for fixed values of z, φ and $\epsilon(z)$, and next integrating over all these variables [33]. Hence, we have

$$\begin{aligned}\tau_\gamma(E_0, z_s) = \int_0^{z_s} \mathrm{d}z\ \frac{\mathrm{d}l(z)}{\mathrm{d}z} \int_{-1}^{1} \mathrm{d}(\cos\varphi)\ \frac{1-\cos\varphi}{2}\ \times \\ \times \int_{\epsilon_{\mathrm{thr}}(E(z),\varphi)}^{\infty} \mathrm{d}\epsilon(z)\, n_\gamma(\epsilon(z), z)\, \sigma_{\gamma\gamma}\big(E(z), \epsilon(z), \varphi\big)\ ,\end{aligned} \tag{2.7}$$

where the distance travelled by a photon per unit redshift at redshift z is given by

$$\frac{\mathrm{d}l(z)}{\mathrm{d}z} = \frac{c}{H_0} \frac{1}{(1+z)\left[\Omega_\Lambda + \Omega_M\,(1+z)^3\right]^{1/2}}\ , \tag{2.8}$$

with Hubble constant $H_0 \simeq 70\,\mathrm{km\,s^{-1}\,Mpc^{-1}}$, while $\Omega_\Lambda \simeq 0.7$ and $\Omega_M \simeq 0.3$ represent the average cosmic density of matter and dark energy, respectively, in units of the critical density $\rho_{\rm cr} \simeq 0.97 \cdot 10^{-29}\,\mathrm{g\,cm^{-3}}$.

Once $n_\gamma(\epsilon(z), z)$ is known, $\tau_\gamma(E_0, z)$ can be computed exactly; generally the integration over $\epsilon(z)$ in Eq. (2.7) must be performed numerically.

Finally, in order to get a feeling about the considered physical situation, it looks suitable to discard cosmological effects, which evidently makes sense only for z_s small enough. Accordingly, z_s is best expressed in terms of the source distance $D = cz_s/H_0$, and the optical depth becomes [1]

$$\tau_\gamma = \frac{D}{\lambda_\gamma(E)} \ , \tag{2.9}$$

where $\lambda_\gamma(E) = D/\tau_\gamma(E, DH_0/c)$ is the photon mean free path for $\gamma\gamma \to e^+e^-$ referring to the present cosmic epoch. As a consequence, Eq. (2.1) becomes

$$P_{\gamma\to\gamma}(E, D) = e^{-D/\lambda_\gamma(E)} \ . \tag{2.10}$$

2.3 Soft photon background

Our main goal is at this point the determination of $n_\gamma(\epsilon(z), z)$. For the sake of clarity, we consider separately the EBL, the CMB, and the RB.

The EBL density $n_\gamma(\epsilon(z), z)$ is in principle affected by large uncertainties arising mainly from foreground contamination produced by zodiacal light which is various orders of magnitude larger than the EBL itself [91]. Below, we sketch schematically the different approaches that have been pursued, without any pretension of completeness.

- *Forward evolution* – This is the most ambitious approach, since it starts from first principles, namely from semi-analytic models of galaxy formation in order to predict the time evolution of the galaxy luminosity function [92].
- *Backward evolution* – This begins from observations of the present galaxy population and extrapolates the galaxy luminosity function backward in time. Among others, this strategy has been followed by Stecker, Malkan and Scully [94] – whose result has unfortunately been ruled out by the measurements by *Fermi*/LAT [130] – and by FRV [35].

[1] Since in this case the energy is independent of the source distance, we simply write the observed energy as E instead of E_0.

- *Inferred evolution* – This approach models the EBL by using quantities like the star formation rate, the initial mass function and the dust extinction as inferred from observations [40, 95].

- *Observed evolution* – This method developed by Dominguez and collaborators (D) relies on observations by using a very rich sample of galaxies extending over the redshift range $0 \leq z_s \leq 2$ [97].

- *Compared observations* – This technique has been implemented in two different ways. One consists in comparing observations of the EBL itself with blazar observations with Imaging Atmospheric Cherenkov Telescopes (IACTs) and deducing the EBL level from the VHE photon dimming [98]. The other starts from some γ-ray observations of a given blazar below 100 GeV where EBL absorption is negligible – typically using *Fermi*/LAT data – and infers the EBL level by comparing the IACT observations of the same blazar with the source spectrum as extrapolated from former observations [99] (but see also [131]). In the latter case the main assumption is that the emission mechanism is presumed to be determined with great accuracy. In either case, the crucial unstated assumption is that photon propagation in the VHE band is governed by conventional physics.

- *Empirical determination* – A newer method of determining the EBL, made possible by recent extensive deep galaxy surveys, is to use the observed luminosity densities at different wavelengths together with observational error bars to directly determine the EBL and opacity without the need of any theoretical assumption [132].

- *Minimal EBL model* – Its aim is to provide a strict lower limit on the EBL level. It relies on the same strategy underlying the *inferred evolution*, but with the parameters tuned in such a way to reproduce the EBL measurements from galaxy counts [96].

Quite remarkably, all methods – apart obviously from the last one – yield basically the same results in the redshift range where they overlap, so that at variance with the time when the CA analysis was done (1997) nowadays the SED of the EBL is fixed to a very good extent. We will employ here the FRV model [35] but we shall check our results using the D model [97]. As far as the CMB is concerned we take the standard temperature value $T = 2.73\,\mathrm{K}$; due to the large density of CMB photons, this background corresponds to the minimum mean-free-path [133, 134]. Finally, the most recent available data for the RB are employed [135], with a low-frequency cutoff taken at 2 MHz.

2.4 Results

Taking into account the EBL, the CMB, and the RB, we directly evaluate $\tau_\gamma(E_0, z_s)$ over the energy range $10\,\mathrm{GeV} \leq E_0 \leq 10^{13}\,\mathrm{GeV}$ and within the source redshift interval $10^{-3} \leq z_s \leq 3$, which is the range where the FRV model yields the contribution of the EBL to $\tau_\gamma(E_0, z_s)$ (the D model is restricted to $10^{-2} \leq z_s \leq 2$). We linearly extrapolate $\tau_\gamma(E_0, DH_0/c)$ down to $D \simeq 4\,\mathrm{kpc}$. Such an extrapolation looks quite reliable not only since $\tau_\gamma(E_0, DH_0/c)$ behaves linearly already in the range $4\,\mathrm{Mpc} \leq D \leq 43\,\mathrm{Mpc}$, but mainly because at such low distances Eq. (2.9) indeed implies $\tau_\gamma(E_0, DH_0/c) \propto DH_0/c$. Moreover, we stress that the extrapolation in question does not practically affect our result. As it is evident from Fig. 2.1, for $D < 4\,\mathrm{Mpc}$ the energies E_0 for which $\tau_\gamma(E_0, DH_0/c)$ takes our prescribed values exceed $\sim 10^5\,\mathrm{GeV}$, which means that our result for $D \simeq 4\,\mathrm{Mpc}$ is dominated by the CMB and the RB rather than by the EBL. Although we have computed $\tau_\gamma(E_0, z_s)$ using the FRV model, we have checked that it basically remains unaffected by employing the D model in the redshift range where they overlap. This is our main result, which is plotted in Fig. 2.1, where the solid line corresponds to $\tau_\gamma(E_0, z_s) = 1$, the dot-dashed line corresponds to $\tau_\gamma(E_0, z_s) = 2$, the dashed line corresponds to $\tau_\gamma(E_0, z_s) = 3$ and the dotted line corresponds to $\tau_\gamma(E_0, z_s) = 4.6$, which give rise to an observed flux dimming of about 0.37, 0.14, 0.05 and 0.01, respectively. For $D \leq 8\,\mathrm{kpc}$ it turns out that $\tau_\gamma(E_0, DH_0/c) < 1$ for any value of E_0.

In order to compare our finding with the CA result, we disregard cosmological effects thereby computing the $\gamma\gamma \to e^+e^-$ mean free path $\lambda_\gamma(E)$ in the local Universe ($z_s \simeq 0$) by using Eq. (2.9) with $\tau_\gamma(E_0, z_s)$ evaluated by means of Eq. (2.7) with $D \simeq 4\,\mathrm{Mpc}$ (formally $z_s \simeq 10^{-6}$).

To facilitate the comparison between our and the CA results we have superposed in Fig. 2.2 the behavior of $\lambda_\gamma(E)$ as found with the above procedure – represented by red dot-dashed line – over Fig. 1 of CA, where the black lines represent the similar results derived by them (see captions). There is of course little surprise that at $z_s \simeq 0$ our result is barely in agreement with that of CA at $z_s = 0$. Still, it should be appreciated that the improved behaviour of $\lambda_\gamma(E)$ found here is in disagreement with the one arising from a *single* choice of the EBL model in the CA analysis. In addition, while the CMB contribution is obviously identical in both cases, as far as the RB is concerned our curve – which corresponds to a low-frequency cutoff of 2 MHz – lies between those corresponding to the low-frequency cutoffs of 2 MHz and 1 MHz, respectively, of the CA result.

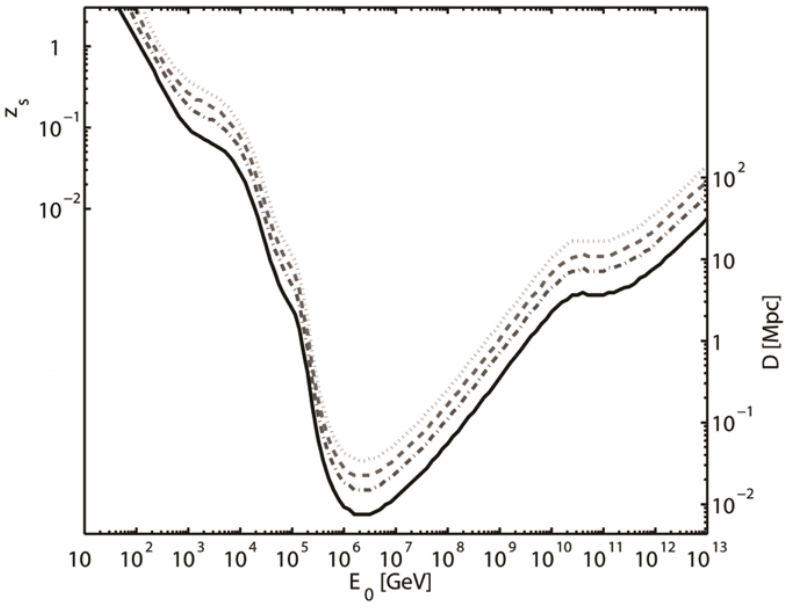

FIGURE 2.1: Source redshifts z_s at which the optical depth takes fixed values as a function of the observed hard photon energy E_0; the y-scale on the right side shows the distance in Mpc for nearby sources. The curves from bottom to top correspond to a photon survival probability of $e^{-1} \simeq 0.37$ (the horizon), $e^{-2} \simeq 0.14$, $e^{-3} \simeq 0.05$ and $e^{-4.6} \simeq 0.01$. For $D \simeq 8$ kpc the photon survival probability is larger than 0.37 for any value of E_0.

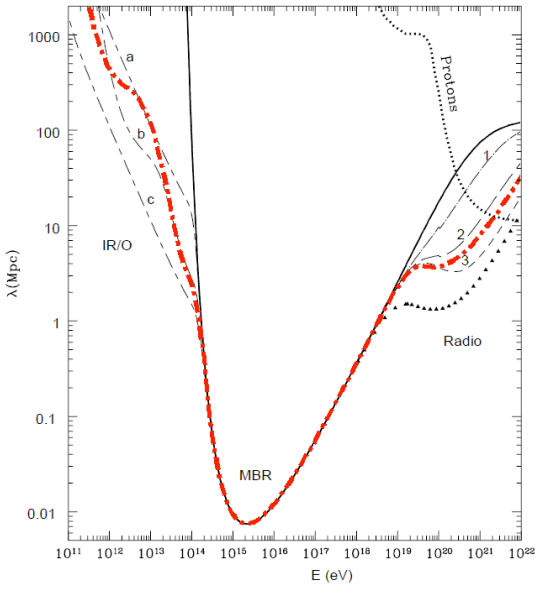

FIGURE 2.2: Comparison of the mean free path λ_γ for $\gamma\gamma \to e^+e^-$ as derived in the text using a low-frequency cutoff at 2 MHz (red dot-dashed line) with the one obtained by CA in the local Universe ($z_s = 0$) as a function of the observed energy E. The CA black lines labelled by a, b, c represent three different EBL models, the black solid line corresponds to the CMB, the black lines labelled by 1, 2, 3 represent a model of the RB with low-frequency cutoff at 5, 2 and 1 MHz, respectively, and the black triangles correspond to the RB under the assumption that it is completely extragalactic.

2.5 Discussion

We have quantified by means of the optical depth the photon absorption caused by the pair-production process in the observed energy range $10\,\mathrm{GeV} \leq E_0 \leq 10^{13}\,\mathrm{GeV}$ and for a source redshift up to $z_s = 3$. We have found that depending on E_0 the absorption can be quite large, and becomes dramatic around $10^6\,\mathrm{GeV}$. However, for a source distance $D \leq 8\,\mathrm{kpc}$ the absorption is irrelevant for any value of E_0.

As it is clear from Fig. 2.1, our conclusion is of great importance for the planned VHE detectors like CTA, HAWC and HiSCORE.

Moreover, we have specialized our analysis to the local Universe ($z_s \simeq 0$) where the optical depth is more conveniently replaced by the mean free path, and we have compared it with the same quantity as evaluated by Coppi and Aharonian in 1997.

It has been realized that the blazars observed so far by IACTs give rise to the *pair-production anomaly*. The H.E.S.S. collaboration [37] first observed that the SED from the blazars H 2356-309 and 1ES 1101-232, at redshifts $z_s = 0.165$ and $z_s = 0.186$, respectively, could be explained by a very low EBL level; subsequently, the MAGIC collaboration [38] have reinforced this evidence with the data from the AGN 3C279 at $z_s = 0.54$. Later, De Angelis et al. [25] have observed this effect in the spectral indices at VHE of a sample of AGN at $z_s > 0.2$. Recently a statistical analysis of the SED from all blazars observed at VHE indicates a level of the EBL lower than that predicted even by the *minimal EBL model*; the indication remains at a confidence level between 2.6 and 4.3 depending on the adopted EBL model [44, 45]. Among many other things, we find it very interesting to see whether this effect persists also at energies much higher than those presently explored by IACTs, and our result looks essential as a benchmark for comparison.

We plan to carry out a similar analysis in the near future taking ALPs into account, since photon-ALP oscillations tend to drastically reduce photon absorption effects of the kind considered here, thereby considerably enlarging the γ-ray horizon at the VHEs that CTA, HAWC and HiSCORE will be able to probe (see Chapters 4 and 5). Moreover, it has very recently been pointed out that such a mechanism would explain the pair-production anomaly in a natural fashion and works for values of the photon-ALP coupling in the reach of the planned upgrade of the ALPS experiment at DESY [46].

Another possible mechanism to explain the apparent reduction of the cosmic gamma-opacity contemplates an additional contribution of secondary gamma rays arising from interactions along the line of sight of high energy cosmic rays produced by the source [136].

Chapter 3

Very-high energy blazar spectra

Among the many achievements of IACTs is the determination of blazar spectra at energies above 100 GeV, and to date this task has been accomplished for about 30 sources with redshift up to $z = 0.536$ for 3C 279. Most of these blazars are listed in Table 3.1.

In view of our later analysis, we carefully address the propagation of a monochromatic photon beam emitted by a blazar at redshift z and detected at energy E_0 within the standard ΛCDM cosmological model, so that the emitted energy is $E_0(1+z)$ owing to the cosmic expansion. Clearly – regardless of the actual physics responsible for photon propagation – the observed and emitted differential photon number fluxes – namely dN/dE – are related by

$$\Phi_{\rm obs}(E_0, z) = P_{\gamma\to\gamma}(E_0, z)\, \Phi_{\rm em}\left(E_0(1+z)\right) \ , \tag{3.1}$$

where $P_{\gamma\to\gamma}(E_0, z)$ is the photon survival probability throughout the whole travel from the source to us. We suppose hereafter that E_0 lies in the VHE γ-ray band, and throughout this Chapter we employ cgs units for clarity.

3.1 Blazars

Blazars are associated with accreting supermassive black holes at the center of active galaxies that host AGN (see Fig. 3.1). They dominate the extragalactic γ-ray sky, both at high energy (> 100 MeV) and at VHE. Their powerful non-thermal emission, spanning the entire electromagnetic spectrum, is produced in a relativistic jet pointing toward the Earth. Their SED shows two well defined "humps". The first one – peaking somewhere between the IR and the X-ray bands – derives from the synchrotron emission

Source	z	Observed energy range	$\Gamma_{\rm obs}$	Reference	$\Gamma_{\rm em}$
3C 66B	0.022	$120\,\mathrm{GeV} < E_0 < 1.8\,\mathrm{TeV}$	3.10 ± 0.37	[63]	3.00
Mrk 421	0.030	$140\,\mathrm{GeV} < E_0 < 6\,\mathrm{TeV}$	2.33 ± 0.22	[64]	2.16
Mrk 501	0.034	$150\,\mathrm{GeV} < E_0 < 6\,\mathrm{TeV}$	2.09 ± 0.20	[65]	1.90
Mrk 501	0.034	$150\,\mathrm{GeV} < E_0 < 3\,\mathrm{TeV}$	2.20 ± 0.20	[65]	2.03
1ES 2344+514	0.044	$180\,\mathrm{GeV} < E_0 < 4\,\mathrm{TeV}$	2.95 ± 0.23	[66]	2.70
Mrk 180	0.045	$180\,\mathrm{GeV} < E_0 < 1.4\,\mathrm{TeV}$	3.30 ± 0.70	[67]	3.07
1ES 1959+650	0.047	$190\,\mathrm{GeV} < E_0 < 6\,\mathrm{TeV}$	2.72 ± 0.24	[68]	2.43
BL Lacertae	0.069	$170\,\mathrm{GeV} < E_0 < 700\,\mathrm{GeV}$	3.60 ± 0.54	[69]	3.27
PKS 0548-322	0.069	$440\,\mathrm{GeV} < E_0 < 2.2\,\mathrm{TeV}$	2.80 ± 0.32	[70]	2.39
PKS 2005-489	0.071	$230\,\mathrm{GeV} < E_0 < 2.3\,\mathrm{TeV}$	4.00 ± 0.41	[71]	3.59
RGB J0152+017	0.080	$320\,\mathrm{GeV} < E_0 < 3\,\mathrm{TeV}$	2.95 ± 0.41	[72]	2.47
W Comae	0.102	$270\,\mathrm{GeV} < E_0 < 1.2\,\mathrm{TeV}$	3.81 ± 0.49	[73]	3.18
PKS 2155-304	0.117	$230\,\mathrm{GeV} < E_0 < 3\,\mathrm{TeV}$	3.37 ± 0.12	[74]	2.67
RGB J0710+591	0.125	?	2.80 ± 0.30	[75]	?
H 1426+428	0.129	$800\,\mathrm{GeV} < E_0 < 10\,\mathrm{TeV}$	2.60 ± 0.61	[76]	0.85
1ES 0806+524	0.138	$320\,\mathrm{GeV} < E_0 < 630\,\mathrm{GeV}$	3.60 ± 1.04	[77]	2.70
1ES 0229+200	0.140	$580\,\mathrm{GeV} < E_0 < 12\,\mathrm{TeV}$	2.50 ± 0.21	[78]	0.41
H 2356-309	0.165	$220\,\mathrm{GeV} < E_0 < 900\,\mathrm{GeV}$	3.09 ± 0.26	[79]	2.06
1ES 1218+304	0.182	$180\,\mathrm{GeV} < E_0 < 1.5\,\mathrm{TeV}$	3.08 ± 0.39	[80]	2.00
1ES 1101-232	0.186	$280\,\mathrm{GeV} < E_0 < 3.2\,\mathrm{TeV}$	2.94 ± 0.20	[81]	1.72
1ES 0347-121	0.188	$300\,\mathrm{GeV} < E_0 < 3.0\,\mathrm{TeV}$	3.10 ± 0.25	[82]	1.87
1ES 1011+496	0.212	$160\,\mathrm{GeV} < E_0 < 600\,\mathrm{GeV}$	4.00 ± 0.54	[83]	2.90
S5 0716+714	0.31	$180\,\mathrm{GeV} < E_0 < 680\,\mathrm{GeV}$	3.45 ± 0.58	[84]	1.60
PG 1553+113	0.40	$95\,\mathrm{GeV} < E_0 < 620\,\mathrm{GeV}$	4.27 ± 0.14	[85]	2.48
PKS 1222+216	0.432	$80\,\mathrm{GeV} < E_0 < 360\,\mathrm{GeV}$	3.75 ± 0.34	[86]	2.47
3C 66A	0.444	$230\,\mathrm{GeV} < E_0 < 470\,\mathrm{GeV}$	4.10 ± 0.72	[87]	1.28
PKS 1424+240	0.5	$140\,\mathrm{GeV} < E_0 < 500\,\mathrm{GeV}$	3.80 ± 0.58	[88]	1.16
3C 279	0.536	$80\,\mathrm{GeV} < E_0 < 480\,\mathrm{GeV}$	4.10 ± 0.73	[89]	2.05
$\Delta\Gamma_{\rm em}$					3.18
$\langle\Gamma_{\rm em}\rangle$					2.22

TABLE 3.1: Blazars observed so far with the IACTs with known redshift z, measured energy range, measured spectral index $\Gamma_{\rm obs}$, and unfolded spectral index at emission $\Gamma_{\rm em}$ using the FRV model of the EBL. Statistical and systematic errors are added in quadrature to produce the total error reported on the measured spectral index. When only statistical errors are quoted, systematic errors are taken to be 0.1 for H.E.S.S. and 0.2 for MAGIC. The last two rows show the spread $\Delta\Gamma_{\rm em}$ of the values of $\Gamma_{\rm em}$ discarding errors and the average value $\langle\Gamma_{\rm em}\rangle$ including errors, respectively.

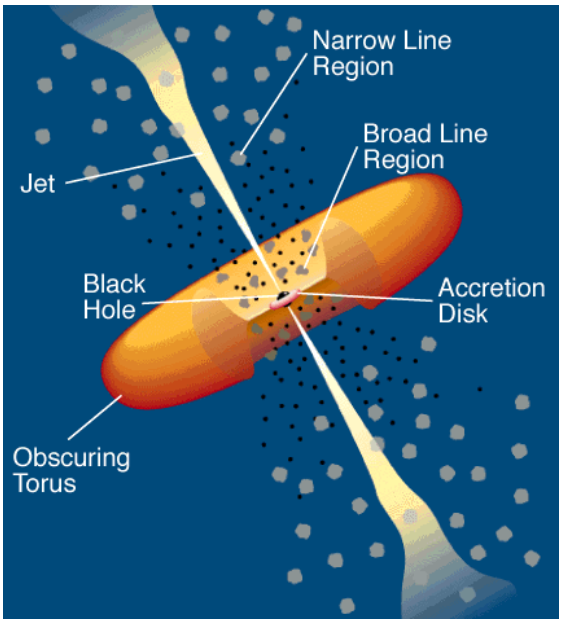

FIGURE 3.1: Schematic structure of an AGN.

of relativistic electrons (or, more generally, e^+e^- pairs) in the jet. The origin of the second component which exhibits a maximum at γ-ray energies is more debated. Leptonic models with the *synchro-self-Compton* (SSC) mechanism [137] attribute it to the inverse Compton emission of the same electrons responsible for the lower energy bump (with the possible additional contribution from external photons). Hadronic models with the *hadronic pion production* (HPP) mechanism (for a review, see [34]), instead, assume that the γ rays are the leftover of reactions involving relativistic hadrons.

Blazars are further divided into two broad groups, BL Lac objects and FSRQs [138]. BL Lacs are defined by the weakness (or even absence) of thermal features (most notably broad emission lines) in their optical spectra. This evidence leads to the common belief that the nuclear region of BL Lacs, where the jet forms and accelerates, is rather poor of soft photons. On the contrary, FSRQs display luminous broad ($v > 1000$ km s^{-1}) emission lines, indicating the existence of photo-ionized clouds rapidly rotating around the central black hole and organized in the so-called broad line region (BLR) (see e.g. [147]).

Besides their importance for the study of the structure and functioning of relativistic jets, growing interest for blazars is motivated by the use of their intense γ-ray beam as a probe of the EBL (see e.g. [37]) and of the large-scale magnetic fields (see e.g. [139]), and even more fundamentally for the study of new physical phenomena beyond the SM – like indeed ALPs – along with quite radical departures from conventional physics such as violation of Lorentz invariance (for a review, see [140]).

3.2 Conventional photon propagation

Within conventional physics the photon survival probability $P^{\rm CP}_{\gamma\to\gamma}(E_0, z)$ is usually parametrized as

$$P^{\rm CP}_{\gamma\to\gamma}(E_0, z) = e^{-\tau_\gamma(E_0,z)} \ , \tag{3.2}$$

where $\tau_\gamma(E_0, z)$ is the optical depth, defined in Chapter 2, Sec. 2.1 and Sec. 2.2. Owing to Eq. (3.2), Eq. (3.1) becomes

$$\Phi_{\rm obs}(E_0, z) = e^{-\tau_\gamma(E_0,z)}\, \Phi_{\rm em}\left(E_0(1+z)\right) \ . \tag{3.3}$$

When cosmological effects (which evidently makes sense for z small enough) can be neglected, z is best expressed in terms of the source distance $D = cz/H_0$ and the optical depth and $P^{\rm CP}_{\gamma\to\gamma}(E_0, z)$ are expressed by Eq. (2.9) and by Eq. (2.10), respectively. Hence, Eq. (3.3) reduces to

$$\Phi_{\rm obs}(E, D) = e^{-D/\lambda_\gamma(E)}\ \Phi_{\rm em}(E) \ . \tag{3.4}$$

Note that we have dropped the subscript 0 for simplicity.

Blazars detected or detectable in the near future with IACTs lie in the VHE range $100\,{\rm GeV} < E_0 < 100\,{\rm TeV}$, and so from Eq. (2.5) it follows that the resulting dimming is expected to be maximal for a background photon energy in the range $0.005\,{\rm eV} < \epsilon_0 < 5\,{\rm eV}$ (corresponding to the frequency range $1.21\cdot 10^3\,{\rm GHz} < \nu_0 < 1.21\cdot 10^5\,{\rm GHz}$ and to the wavelength range $2.48\,\mu{\rm m} < \lambda_0 < 2.48\cdot 10^2\,\mu{\rm m}$), extending from the ultraviolet to the far-infrared. This is just the EBL. We stress that at variance with the case of the CMB, the EBL has nothing to do with the Big Bang. It is instead produced by stars in galaxies during the whole history of the Universe and possibly by a first generation of stars formed before galaxies were assembled. Therefore, a lower limit to the EBL level can be derived from integrated galaxy counts [90].

We sketch schematically the different approaches that have been pursued to describe the EBL spectral number density $n_\gamma(\epsilon(z), z)$, without any pretension of completeness, in Chapter 2, Sec. 2.3.

Throughout this thesis, we adopt the FRV model mainly because it supplies a very detailed numerical evaluation of the optical depth based on Eq. (2.7), which will henceforth be denoted by $\tau^{\rm FRV}_\gamma(E_0, z)$ [1]). Regretfully, the errors affecting $\tau^{\rm FRV}_\gamma(E_0, z)$ are unknown.

[1] These tables can be found on the WEB site [101]

3.3 Understanding observed VHE blazar spectra

As a preliminary step to find out the potential relevance of the DARMA scenario for available observations of VHE blazars, we consider in some detail the energy range $0.2\,\mathrm{TeV} < E_0 < 2\,\mathrm{TeV}$ where most of the blazars in question have been detected. It follows from Eq. (2.5) that the EBL energy band where $\sigma_{\gamma\gamma}(E_0, \epsilon_0, \pi)$ becomes maximal is $0.25\,\mathrm{eV} < \epsilon_0 < 2.5\,\mathrm{eV}$ (corresponding to $6.07 \cdot 10^4\,\mathrm{GHz} < \nu_0 < 6.07 \cdot 10^5\,\mathrm{GHz}$ and $0.50\,\mu\mathrm{m} < \lambda_0 < 4.94\,\mu\mathrm{m}$).

The two models – leptonic and hadronic (see Sec 3.1) – proposed to give rise to the emission of VHE photons lead to emission spectra which are so far observationally indistinguishable, and in particular within the energy range $0.2\,\mathrm{TeV} < E < 2\,\mathrm{TeV}$ they both predict a single power-law behaviour for blazar emitted spectra

$$\Phi_{\mathrm{em}}(E) = K\,E^{-\Gamma_{\mathrm{em}}}\ , \tag{3.5}$$

where K is a suitable constant.

We next turn our attention to the observed energy spectra. It follows directly from observations that blazar spectra are successfully fitted by a single power law [2]

$$\Phi_{\mathrm{obs}}(E_0, z) = K\,E_0^{-\Gamma_{\mathrm{obs}}(z)}\ . \tag{3.6}$$

As a consequence, the observed spectra of all blazars detected so far are characterized by the observed spectral index Γ_{obs}, which is reported in Table 3.1 for every source. It is also very useful to plot Γ_{obs} versus the source redshift z for all detected VHE blazars in Fig. 3.2 (blobs with error bars).

Let us first try to understand what Fig. 3.2 is telling us leaving aside any theoretical prejudice. A striking feature is that the horizontal strip $3.5 < \Gamma_{\mathrm{obs}} < 4.5$ is almost uniformly populated for all considered redshifts, which would suggest that Γ_{obs} is independent of z. However, things are different for the lower strip $2.5 < \Gamma_{\mathrm{obs}} < 3.5$. Because it is populated only up to $z \simeq 0.2$ (with the exception of a single source close to $z \simeq 0.3$), the above interpretations is ruled out and we are forced to conclude that Γ_{obs} *correlates* with z. Actually, when looking at Fig. 3.2 from this viewpoint a simple trend is easily recognized: Γ_{obs} increases linearly from 2.5 – 3 at $0.1 < z < 0.2$ to roughly 3.5 – 4 at $0.3 < z < 0.6$. Similarly, also for $\Gamma_{\mathrm{obs}} > 3$ a linear increase is found – even if with a different slope – but the number of sources with $\Gamma_{\mathrm{obs}} > 3$ following this behaviour decreases as z increases until it vanishes for $z > 0.25$.

[2] Because Eq. (3.5) has to reduce to Eq. (3.6) in the limit $z \to 0$, the constant K is the same in both equations.

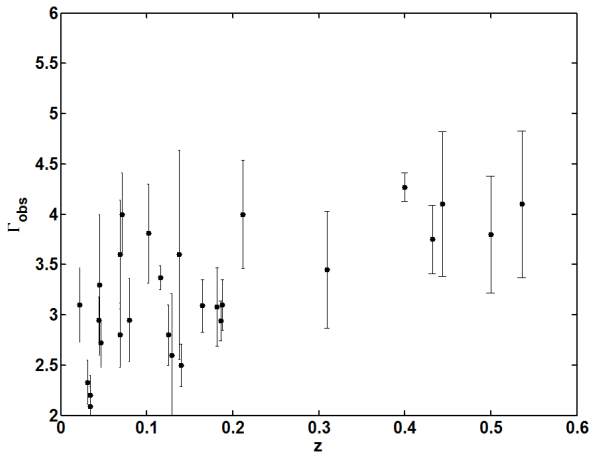

FIGURE 3.2: The observed values of the observed spectral index $\Gamma_{\rm obs}$ versus the source redshift for all blazars detected so far in the VHE band are represented by dots and corresponding error bars.

A qualitative understanding of this situation emerges naturally by taking the EBL attenuation into account. We stress in the first place that rather nearby blazars – such as those at $z < 0.05$ – do not practically suffer EBL absorption at the energies probed so far, thereby implying that the shape of their observed VHE spectra should be the same as that of the emitted spectra, namely $\Gamma_{\rm obs} \simeq \Gamma_{\rm em}$. This is an important fact, since it allows us to see directly the blazar spectra at emission. In addition, we show in Appendix B that an approximate analytic expression for the optical depth within the FRV model is given by

$$\tau_\gamma^{\rm app}(E_0, z) \simeq 2.25\,\alpha \left(\frac{E_0}{500\,{\rm GeV}}\right)^{0.85} I(z)\ , \tag{3.7}$$

with $0.9 \leq \alpha \leq 3.6$ and roughly $I(z) \sim z$. Hence, by combining Eqs. (3.3), (3.5) and (3.7) the expected observed flux is

$$\Phi_{\rm obs}^{\rm app}(E_0, z) = K \exp\left\{-\,2.25\,\alpha \left(\frac{E_0}{500\,{\rm GeV}}\right)^{0.85} I(z)\right\} E_0^{-\Gamma_{\rm em}}\ (1+z)^{-\Gamma_{\rm em}}\ . \tag{3.8}$$

Now, Eq. (3.8) possesses to two conceptually distinct implications:

- $\Phi_{\rm obs}^{\rm app}(E_0, z)$ is exponentially damped as the energy increases, thereby entailing that it gets much softer than the emitted flux.
- $\Phi_{\rm obs}^{\rm app}(E_0, z)$ is exponentially suppressed as the distance increases, so that sufficiently far-away sources tend to become invisible.

Although Eq. (3.8) holds up to 2 TeV only, one can check that these conclusions remain true under the replacement $\tau_\gamma^{\rm app}(E_0,z) \to \tau_\gamma^{\rm FRV}(E_0,z)$ up to 100 TeV.

We can relate the expected observed spectral index $\Gamma_{\rm obs}^{\rm exp}(z)$ to $\Gamma_{\rm em}$ and z by best-fitting the l.h.s. of Eq. (3.8) to the power-law expression (3.6) over the energy range where the considered source is observed, which is reported in Table 3.1.

Because $I(z)$ is independent of E_0, it is unaffected by the considered best-fitting procedure, and so we have $\Gamma_{\rm obs}^{\rm exp}(z) \sim I(z) \sim z$ up to logarithmic corrections. This indeed explains in a qualitative fashion both why nearby sources with $2.5 < \Gamma_{\rm obs} < 3$ get replaced by sources with $3.5 < \Gamma_{\rm obs} < 4$ at larger redshift according to a linear trend and why nearby sources with $\Gamma_{\rm obs} > 3$ follow a similar linear behaviour up to a point where $\Gamma_{\rm obs}$ would be so large that the source becomes invisible at sufficiently large distances, thereby disappearing from Fig. 3.2 for z large enough.

An intrinsic correlation – due to an observational bias – between the spectral index and the distance, however, cannot be excluded on the basis of the experimental data. In addition, given the blazar sequence [102], the fact that the Inverse Compton bump moves according to luminosity might give a bias related to the fact that for the same energy range we are actually sampling different regions of the spectral energy distribution. Finally, the fact that the upper limit of the energy sampled decreases with energy might introduce in itself a bias. However, a direct search for spectral index hardening associated with blazar variability gave no evidence [103]. Attempts are presently done (see for example [104]) to analyze individually blazars and derive their spectral energy distribution from multi-wavelength data. We hope that in a near future this work will be made more precise. However, the models have presently a large uncertainty, since, in order to have reasonably constrained fits, one must assume a purely leptonic emission and a 1-zone SSC emission mechanism, while we have indications that the situation can be more complicated for most blazars we know in detail.

In order to derive the exact value of $\Gamma_{\rm em}$ for the various blazars from observations the use of Eq. (3.8) with $\Phi_{\rm obs}^{\rm app}(E_0,z) \to \Phi_{\rm obs}(E_0,z)$ combined with Eq. (3.6) would be unsuited because of its approximate character. A better strategy consists in first de-absorbing $\Gamma_{\rm obs}$ for every source by employing Eq. (3.3) with $\tau_\gamma(E_0,z) \to \tau_\gamma^{\rm FRV}(E_0,z)$ combined with Eq. (3.6), and next inferring $\Gamma_{\rm em}$ by best-fitting the resulting $\Phi_{\rm em}(E)$ to the power-law expression (3.5) over the energy range where the considered source is observed (see Table 3.1). Observe that since $\Gamma_{\rm em}$ depends linearly on $\Gamma_{\rm obs}$, the derived values of $\Gamma_{\rm em}$ have the *same* error bars of $\Gamma_{\rm obs}$ as reported in Table 3.1 to the extent that errors in $\tau_\gamma^{\rm FRV}(E_0,z)$ are neglected (they are actually unknown because they are not quoted by the authors). We are of course well aware that the correct procedure would be to first de-absorb each point of the observed spectrum of a given source and next

best-fit these points to a power-law. Unfortunately, the observed energy points with related error bars are not available from published papers, and this explains why we have simply de-absorbed $\Gamma_{\rm obs}$ – hence $\Gamma_{\rm em}$ has to be understood as the average emitted spectral index for the source in question – but we want to remark that for our purposes this simplified approach is adequate. The same strategy has been used for a different model of the EBL [93]. Our results are listed in Table 3.1, along with the spread $\Delta\Gamma_{\rm em}$ of the value of $\Gamma_{\rm em}$ discarding errors and the average value $\langle\Gamma_{\rm em}\rangle$ including errors.

3.4 The cosmic opacity problem

It is evident from Table 3.1 that the values of $\Gamma_{\rm em}$ for some far-away sources are considerably smaller than those for nearby blazars, with the exception of the two sources H 1426+428 and 1ES 0229+200.

As a consequence, the cosmic opacity problem arises concerning the physical mechanism responsible for such a behaviour involving $\Gamma_{\rm em}$ and z.

Certainly cosmology does not help, because no important evolutionary effect is expected to take place for redshifts up to $z \simeq 0.54$ at which the most distant blazar has been detected.

Alternatively, one might guess that it is due to a volume selection effect, since intrinsically brighter sources are the exception rather than the rule. However, the emitted flux depends not only on the slope but also on the normalization factor, which varies by three orders of magnitude over the sample of considered sources. Actually, the existence of the two rather nearby blazars H 1426+428 and 1ES 0229+200 with the hardest emitted spectrum explicitly shows that small $\Gamma_{\rm em}$ does not mean large z. So, also this attempt is unsatisfactory.

Yet another possible explanation consists in assuming that far-away blazars are intrinsically different from nearby ones, but to the best of our knowledge no convincing explanation of this circumstance has been put forward so far.

One might also argue that a solution could come from the fact that some observed blazars are in a quiescent state whereas others are flaring. In fact, because of EBL absorption we might be seeing progressively more distant blazars only during stronger flares (but not all distant blazars are flaring, like e.g. PG 1553+113 which has been observed to have nearly the same luminosity for five years). As a consequence – working within the SSC mechanism for definiteness – we could run the risk to compare $\Gamma_{\rm em}$ for different sources at different positions on the Compton peak, since flaring causes this

peak which normally lies below 100 GeV to slightly shift towards higher energies [105]. Clearly, the slope near the bottom of the pick is steeper than close to the tip, and this circumstance would produce a harder emission spectrum for flaring sources. However, such a possibility seems to us quite unlikely. For, the observed energy range of flaring sources is generally considerably wider that the width of the peak [105] and observations above 100 GeV invariably show that a *single* power law behaviour provides an excellent fit to the data. Hence, we see that we are inferring the spectral index well below the pick whether or not a flare takes place.

In conclusion, no satisfactory explanation for the considered behaviour involving $\Gamma_{\rm em}$ and z seems to emerge.

As a matter of fact, shifting from the astronomical to the physical point of view makes the issue more clear-cut. It is known since a long time that $\Gamma_{\rm em} = 1.5$ arises from the first-order Fermi acceleration mechanism with newtonian shocks for an electron injection spectrum equal to 2 [106]. For this reason, when the cosmic opacity problem was first perceived in 2006 it was thought that the inferred values of $\Gamma_{\rm em}$ were too small to agree with conventional physics assuming current EBL models [37], and indeed values $\Gamma_{\rm em} < 1.5$ were considered unphysical e.g. by the H.E.S.S. collaboration. However, it has recently been shown that the required low values of $\Gamma_{\rm em}$ can be achieved in the presence of strong relativistic shocks [41], because of photon self-absorption inside the source [42] or by the inverse Compton scattering of CMB photons by shock-accelerated electrons in the jet [43].

While these results are gratifying, one still wonders why this kind of physical effects are important for distant blazars *only*. Just as before, an answer seems hardly in sight.

So, either way it is argued no simple solution to the cosmic opacity problem emerges within conventional physics.

Now, what the discussion in Sec. 3.3 has shown is that the origin of this cosmic opacity problem is not qualitative – the z-dependence of $\Gamma_{\rm obs}(z)$ comes out right – but purely numerical, namely because the EBL level predicted by conventional physics is too high. Were the EBL level somewhat smaller, the cosmic opacity problem would automatically disappear.

A way out of the cosmic opacity problem appears therefore to call for some sort of *unconventional* photon propagation which ultimately reduces the cosmic opacity arising from the EBL, thereby bringing the values of $\Gamma_{\rm em}$ for distant blazars in the same ballpark of those for close ones.

Various attempts at reducing the cosmic opacity along these lines have been proposed and they are schematically summarized below:

- A revolutionary option contemplates a breakdown of Lorentz invariance [107].
- An alternative possibility concerns the emission of cosmic rays from blazars – rather than photons – with energy smaller than 50 EeV. These cosmic rays can travel unimpeded over cosmological distances and they can interact with the EBL well before reaching our galaxy. In such an interaction secondary photons are produced, that are ultimately detected by the IACTs [108].
- A different proposal relies upon photon-ALP oscillations, which requires the presence of magnetic fields somewhere along the line of sight. As already pointed out, two concrete realizations of this idea have been investigated. One of them – the DARMA scenario [24–26] – assumes that photon-ALP oscillations take place during propagation in intergalactic space, where large-scale magnetic fields in the nano-Gauss range are supposed to exist. Large-scale magnetic fields of this strength are consistent with current upper bounds and even with the results of the AUGER observatory (more about this, later). The other is in a sense complementary, because it presupposes a $\gamma \to a$ conversion inside the blazar and a $a \to \gamma$ conversion in the Milky way [27]. Although the properties of the Galactic magnetic field are rather well known, those of the magnetic field in the blazar are not, and so it is not clear whether the first step of this mechanism actually takes place and if so how large is its efficiency [29].

Chapter 4

DARMA scenario

Our aim is to offer a detailed description of the structure of the DARMA scenario, and in particular to show how the photon survival probability $P_{\gamma\to\gamma}^{\mathrm{DARMA}}(E_0, z)$ can be computed in terms of the properties of the intergalactic medium in which the photon/ALP beam propagates.

4.1 An intuitive insight

We find it instructive to restate in a slightly different fashion the reason why the mechanism of photon-ALP oscillations allows to substantially reduce the EBL absorption. We neglect here cosmological effects for simplicity.

We suppose that VHE photons are both emitted and detected as usual, but that along their way to us they convert into ALPs and back into photons. Accordingly, the number N_c of either $\gamma \to a$ or $a \to \gamma$ conversions must necessarily be even, and we may schematically regard the beam propagation in large-scale magnetic fields as a succession of such conversions. Assuming ideally that each conversion occurs suddenly at some space point, the source distance D gets divided into a number $N_c + 1$ of steps of equal length L, over which a beam particle behaves either as a real photon or as an ALP. Hence, a beam particle exhibits an overall behaviour as a real photon over a total length equal to

$$D_\gamma = \frac{N_c + 2}{2\,(N_c + 1)}\,D = \left(1 - \frac{N_c}{2N_c + 2}\right) D\ . \tag{4.1}$$

We intuitively expect N_c to increase with the photon-ALP oscillation probability – and so with B/M – which leads in turn to a slight decrease of D_γ starting from D. Correspondingly, since ALPs do not suffer EBL absorption Eq. (2.10) gets presently

replaced by

$$P_{\gamma\to\gamma}^{\rm DARMA}(E,D)=e^{-D_\gamma/\lambda_\gamma(E)}=e^{-\left(1-\frac{N_c}{2N_c+2}\right)D/\lambda_\gamma(E)}\ , \tag{4.2}$$

and thanks to its exponential dependence on $D_\gamma/\lambda_\gamma(E)$ even a small decrease of D_γ starting from D produces a large enhancement of $P_{\gamma\to\gamma}^{\rm DARMA}(E,D)$ as compared to $P_{\gamma\to\gamma}^{\rm CP}(E,D)$ referring to conventional physics and given by Eq. (2.10) [1].

4.2 General strategy

Our ultimate goal consists in the evaluation of the photon survival probability $P_{\gamma\to\gamma}^{\rm DARMA}(E_0,z)$ from a blazar at redshift z to us when allowance is made for photon-ALP oscillations as well as for EBL photon absorption. It is indeed clear that the considerations developed in Chapter 3 can be extended to account for photon-ALP oscillations by the replacement $P_{\gamma\to\gamma}^{\rm CP}(E_0,z)\to P_{\gamma\to\gamma}^{\rm DARMA}(E_0,z)$.

An exact treatment would however be impossible because of the large uncertainty affecting the configuration of the magnetic field ultimately responsible for photon-ALP oscillations.

As a matter of fact, the line of sight to a distant blazar is expected to traverse magnetic fields extending over a variety of scales. A magnetic field is certainly present inside the source [109]. Furthermore, the Milky Way magnetic field can give a nontrivial contribution to the effect under consideration [110], and the same is true if the line of sight happens to cross a cluster of galaxies because intracluster magnetic fields are known to exist with a strength similar to that of the Galactic field [111]. Finally, large-scale magnetic fields can play a key role [112, 113]. Here, our attention will be restricted to magnetic fields of the latter sort.

Unfortunately, almost nothing is known about the morphology of large-scale magnetic fields, which reflects both their origin and the evolutionary history of baryonic matter. While it is evident that their coherence length cannot be arbitrarily large, no reliable estimate of its value is presently available. As far as our analysis is concerned, this means that we cannot suppose that large-scale magnetic fields are homogeneous over the whole distance to the source, but their spatial dependence is largely unknown. The usual way out of this difficulty amounts to suppose that large-scale magnetic fields $\mathbf{B}$ have a *domain-like structure*. That is, $\mathbf{B}$ is assumed to be homogeneous over a domain of size $L_{\rm dom}$ equal to its coherence length, with $\mathbf{B}$ randomly changing its direction from one domain to another but keeping approximately the same strength [112, 113].

[1] We will see later that the situation is more involved, but at this stage we can safely ignore additional complications.

Thus, the whole propagation process of the considered photon/ALP beam can be recovered by iterating the propagation over a single domain as many times as the number of domains crossed by the beam, taking each time a random value for the angle ψ between $\mathbf{B}$ and a fixed fiducial direction equal for all domains. In this way, we are effectively led to the much easier problem of photon-ALP oscillations in a *homogeneous* magnetic field (solved exactly in Chapter 1 Sec. 1.5).

What still remains to be done at this point is to take photon absorption into account. This is easy because photon absorption is *independent* of the properties of the photon-ALP oscillation mechanism and vice-versa.

So, our strategy can be implemented through the following steps [21]:

- We work within the *strong-mixing regime* so as to ensure that the photon-ALP oscillation probability is both maximal and energy-independent. We have seen that such a condition requires $E_* < E < E_{**}$, with the energy thresholds E_* and E_{**} defined by Eqs. (1.48) and (1.49), respectively. But demanding the strong-mixing regime to take place for $E > 100\,\mathrm{GeV}$ evidently requires $E_* < 100\,\mathrm{GeV}$, which sets an upper bound on the ALP mass. The upper bound E_{**} is at energies well above the ones considered for the photon/ALP beam propagation in the intergalactic medium since cosmic magnetic fields are very weak. As a result, for the propagation in the intergalactic medium the QED vacuum polarization terms $\Delta_{xx}^{\mathrm{QED}}$ and $\Delta_{zz}^{\mathrm{QED}}$ of Eqs. (1.26) and (1.27) are totally negligible. But this is not true in general: in fact in Chapters 6 and 7 we will find a situation where the QED vacuum polarization terms cannot be discarded.

- We evaluate the transfer matrix across the generic n-th domain $\mathcal{U}_n(E_0, \psi_n)$, where ψ_n accounts for the random orientation of $\mathbf{B}$ in the domain in question. Note that $\mathcal{U}_n(E_0, \psi_n)$ depends on E_0 only because of the energy-dependence of EBL absorption.

- Iteration of the latter result over the total number N_d of domains crossed by the beam from the blazar to us yields the total transfer matrix $\mathcal{U}(E_0, z; \psi_1, ..., \psi_{N_d})$, from which the photon survival probability $P_{\gamma\to\gamma}(E_0, z; \psi_1, ..., \psi_{N_d})$ can be computed for fixed values of the angles $\psi_1, ..., \psi_{N_d}$ in every domain.

- Finally, $P_{\gamma\to\gamma}^{\mathrm{DARMA}}(E_0, z)$ emerges by averaging $P_{\gamma\to\gamma}(E_0, z; \psi_1, ..., \psi_{N_d})$ over all angles $\psi_1, ..., \psi_{N_d}$.

Our discussion is framed within the ΛCDM cosmological setting, and so the redshift z is the obvious parameter to express distances. Because the proper length per unit

redshift at redshift z is still given by Eq. (2.8), a generic proper length extending over the redshift interval $[z_a, z_b]$ ($z_a < z_b$) is

$$L(z_a, z_b) = \int_{z_a}^{z_b} dz \; \frac{dl(z)}{dz} \simeq 4.29 \cdot 10^3 \int_{z_a}^{z_b} \frac{dz}{(1+z)\left[0.7 + 0.3\,(1+z)^3\right]^{1/2}} \text{ Mpc} \; , \quad (4.3)$$

which approximately reads

$$L(z_a, z_b) \simeq 2.96 \cdot 10^3 \ln\left(\frac{1 + 1.45\, z_b}{1 + 1.45\, z_a}\right) \text{ Mpc} \; . \quad (4.4)$$

This result will be applied in particular to evaluate the size of the magnetic domains.

4.3 Photon absorption

We proceed to extend the discussion in Chapter 1 Sec. 1.5) so as to take EBL absorption into account. This task is greatly facilitated by the fact that the latter effect is independent of the photon-ALP conversion mechanism.

We have seen that the propagation of a monochromatic photon/ALP beam is formally described as a three-level non-relativistic quantum system with Hamiltonian H_0 given by Eq. (1.21) and expressed in terms of the mixing matrix $\mathcal{M}_0$. Taking advantage from this fact, the inclusion of EBL absorption amounts to suppose that the photon/ALP beam is actually analogous to an *unstable* quantum system with decay probability

$$P_{\text{decay}} = e^{-y/\lambda_\gamma(E)} \; , \quad (4.5)$$

where $\lambda_\gamma(E)$ denotes the photon mean free path. As is well known, such a decay probability arises from the inclusion of an absorbitive term $-\Delta_{\text{abs}}$ into the Hamiltonian, with

$$\Delta_{\text{abs}} \equiv \frac{i}{2\,\lambda_\gamma(E)} \; . \quad (4.6)$$

More specifically, since photons undergo absorption but ALPs do not, $\mathcal{M}_0^{(0)}$ in Eq. (1.30) becomes

$$\mathcal{M}^{(0)} = \begin{pmatrix} \Delta_{xx}^{\text{QED}} + \Delta_{\text{pl}} + \Delta_{\text{abs}} & 0 & 0 \\ 0 & \Delta_{zz}^{\text{QED}} + \Delta_{\text{pl}} + \Delta_{\text{abs}} & \Delta_{a\gamma} \\ 0 & \Delta_{a\gamma} & \Delta_{aa} \end{pmatrix} \; , \quad (4.7)$$

where – in parallel with the treatment of Chapter 1 Sec. 1.5) – we are first supposing that $\mathbf{B}$ lies along the z-axis.

As we said, we work throughout within the strong-mixing regime and therefore condition (1.46) has to be met. Recalling the explicit expression for the various Δ-terms entering Eq. (4.7) and defined in Chapter 1 Sec. 1.5), $\mathcal{M}^{(0)}$ takes the simpler form

$$\mathcal{M}^{(0)} = \begin{pmatrix} \Delta_{\rm abs} & 0 & 0 \\ 0 & \Delta_{\rm abs} & \Delta_{a\gamma} \\ 0 & \Delta_{a\gamma} & 0 \end{pmatrix} , \tag{4.8}$$

which is denoted by the same symbol for notational simplicity (only Eq. (4.8) will be used hereafter). Note that m and $\omega_{\rm pl}$ presently drop out of $\mathcal{M}^{(0)}$. Just as before, use of the results contained in Appendix A with $\mathcal{M} \to \mathcal{M}^{(0)}$ directly gives the corresponding eigenvalues

$$\lambda_1 = \frac{i}{2\,\lambda_\gamma(E)} , \tag{4.9}$$

$$\lambda_2 = \frac{i}{4\,\lambda_\gamma(E)} \left(1 - \sqrt{1 - 4\,\delta^2}\right) , \tag{4.10}$$

$$\lambda_3 = \frac{i}{4\,\lambda_\gamma(E)} \left(1 + \sqrt{1 - 4\,\delta^2}\right) , \tag{4.11}$$

where we have set

$$\delta \equiv \frac{B\,\lambda_\gamma(E)}{M} , \tag{4.12}$$

roughly measuring the ratio of the photon mean free path to the photon-ALP oscillation length. Hence, the transfer matrix associated with the reduced Schödinger-like equation (1.24) with $\mathcal{M}_0 \to \mathcal{M}^{(0)}$ reads

$$\mathcal{U}(y, y_0; 0) = e^{i\lambda_1 (y - y_0)}\, T_1(0) + e^{i\lambda_2 (y - y_0)}\, T_2(0) + e^{i\lambda_3 (y - y_0)}\, T_3(0) , \tag{4.13}$$

with the matrices $T_1(0)$, $T_2(0)$ and $T_3(0)$ dictated by Eqs. (A.17), (A.18) and (A.19) as specialized to the present case. Explicitly

$$T_1(0) \equiv \begin{pmatrix} 1 & 0 & 0 \\ 0 & 0 & 0 \\ 0 & 0 & 0 \end{pmatrix} , \tag{4.14}$$

$$T_2(0) \equiv \begin{pmatrix} 0 & 0 & 0 \\ 0 & \frac{-1+\sqrt{1-4\delta^2}}{2\sqrt{1-4\delta^2}} & \frac{i\delta}{\sqrt{1-4\delta^2}} \\ 0 & \frac{i\delta}{\sqrt{1-4\delta^2}} & \frac{1+\sqrt{1-4\delta^2}}{2\sqrt{1-4\delta^2}} \end{pmatrix} , \tag{4.15}$$

$$T_3(0) \equiv \begin{pmatrix} 0 & 0 & 0 \\ 0 & \frac{1+\sqrt{1-4\delta^2}}{2\sqrt{1-4\delta^2}} & -\frac{i\delta}{\sqrt{1-4\delta^2}} \\ 0 & -\frac{i\delta}{\sqrt{1-4\delta^2}} & \frac{-1+\sqrt{1-4\delta^2}}{2\sqrt{1-4\delta^2}} \end{pmatrix} . \tag{4.16}$$

Clearly, we will need the generalization of this result to the case in which **B** forms an arbitrary angle ψ with the z-axis. Proceeding exactly like in Chapter 1 Sec. 1.5), we find

$$\mathcal{M} = V^{\dagger}(\psi)\, \mathcal{M}^{(0)}\, V(\psi) \ , \tag{4.17}$$

where the matrix $V(\psi)$ is given by Eq. (1.55). This yields

$$\mathcal{M} = \begin{pmatrix} \Delta_{\rm abs} & 0 & \Delta_{a\gamma}\, \sin\psi \\ 0 & \Delta_{\rm abs} & \Delta_{a\gamma}\, \cos\psi \\ \Delta_{a\gamma}\, \sin\psi & \Delta_{a\gamma}\, \cos\psi & 0 \end{pmatrix} \ , \tag{4.18}$$

and now the resulting transfer matrix evidently reads

$$\mathcal{U}(y, y_0; \psi) = V^{\dagger}(\psi) \mathcal{U}(y, y_0; 0)\, V(\psi) \ , \tag{4.19}$$

whose explicit form arises by inserting Eq. (4.13) into Eq. (4.19). We obtain

$$\mathcal{U}(y, y_0; \psi) = e^{i\lambda_1 (y-y_0)}\, T_1(\psi) + e^{i\lambda_2 (y-y_0)}\, T_2(\psi) + e^{i\lambda_3 (y-y_0)}\, T_3(\psi) \ , \tag{4.20}$$

with

$$T_1(\psi) \equiv \begin{pmatrix} \cos^2\psi & -\sin\psi\cos\psi & 0 \\ -\sin\psi\cos\psi & \sin^2\psi & 0 \\ 0 & 0 & 0 \end{pmatrix} \ , \tag{4.21}$$

$$T_2(\psi) \equiv \begin{pmatrix} \frac{-1+\sqrt{1-4\delta^2}}{2\sqrt{1-4\delta^2}}\, \sin^2\psi & \frac{-1+\sqrt{1-4\delta^2}}{2\sqrt{1-4\delta^2}}\, \sin\psi\cos\psi & \frac{i\delta}{\sqrt{1-4\delta^2}}\, \sin\psi \\ \frac{-1+\sqrt{1-4\delta^2}}{2\sqrt{1-4\delta^2}}\, \sin\psi\cos\psi & \frac{-1+\sqrt{1-4\delta^2}}{2\sqrt{1-4\delta^2}}\, \cos^2\psi & \frac{i\delta}{\sqrt{1-4\delta^2}}\, \cos\psi \\ \frac{i\delta}{\sqrt{1-4\delta^2}}\, \sin\psi & \frac{i\delta}{\sqrt{1-4\delta^2}}\, \cos\psi & \frac{1+\sqrt{1-4\delta^2}}{2\sqrt{1-4\delta^2}} \end{pmatrix} \ , \tag{4.22}$$

$$T_3(\psi) \equiv \begin{pmatrix} \frac{1+\sqrt{1-4\delta^2}}{2\sqrt{1-4\delta^2}}\, \sin^2\psi & \frac{1+\sqrt{1-4\delta^2}}{2\sqrt{1-4\delta^2}}\, \sin\psi\cos\psi & \frac{-i\delta}{\sqrt{1-4\delta^2}}\, \sin\psi \\ \frac{1+\sqrt{1-4\delta^2}}{2\sqrt{1-4\delta^2}}\, \sin\psi\cos\psi & \frac{1+\sqrt{1-4\delta^2}}{2\sqrt{1-4\delta^2}}\, \cos^2\psi & \frac{-i\delta}{\sqrt{1-4\delta^2}}\, \cos\psi \\ \frac{-i\delta}{\sqrt{1-4\delta^2}}\, \sin\psi & \frac{-i\delta}{\sqrt{1-4\delta^2}}\, \cos\psi & \frac{-1+\sqrt{1-4\delta^2}}{2\sqrt{1-4\delta^2}} \end{pmatrix} \ . \tag{4.23}$$

We stress that due to the imaginary nature of $\Delta_{\rm abs}$ the mixing matrix $\mathcal{M}$ is not self-adjoint, and so the transfer matrix $\mathcal{U}(y, y_0; \psi)$ fails to be unitary. In addition, the Von Neumann-like equation (1.51) becomes

$$i\frac{d\rho}{dy} = \rho\, \mathcal{M}^{\dagger} - \mathcal{M}\rho \ . \tag{4.24}$$

Still, it is straightforward to check that Eq. (1.52) remains valid with $\mathcal{U}_0(y, y_0) \to \mathcal{U}(y, y_0; \psi)$ in spite of the fact that $\mathcal{M}^{\dagger} \neq \mathcal{M}$. Since we now have $\rho(y)^{\dagger} \neq \rho(y)$, it follows that in general ${\rm Tr}\rho(y) \neq 1$, and so the probability that a photon/ALP beam initially in

the state ρ_1 will be found in the state ρ_2 after a distance y is presently given by

$$P_{\rho_1\to\rho_2}(y) = \mathrm{Tr}\left(\rho_2\,\mathcal{U}(y,0;\psi)\,\rho_1\,\mathcal{U}^\dagger(y,0;\psi)\right)\,, \tag{4.25}$$

where we assume $\mathrm{Tr}\rho_1 = \mathrm{Tr}\rho_2 = 1$ as before.

4.4 Intergalactic medium (IGM)

As is well known, the absence of the Gunn-Peterson effect [114] is generally regarded as evidence that the IGM is ionized, and from the resulting high electrical conductivity it follows that the electron number density $n_e(z)$ traces the cosmic mass distribution. Because of this fact, we have

$$n_e(z) = \bar{n}_{e,0}(1+\delta(z))(1+z)^3\,, \tag{4.26}$$

where $\delta(z) \equiv (\rho(z) - \bar{\rho}(z))/\bar{\rho}(z)$ is the mass density contrast and $\bar{n}_{e,0}$ is the average electron number density. As a consequence, Eq. (1.28) entails for the plasma frequency

$$\omega_{\mathrm{pl}}(z) = \bar{\omega}_{\mathrm{pl},0}(1+\delta(z))^{1/2}\,(1+z)^{3/2}\,, \tag{4.27}$$

with $\bar{\omega}_{\mathrm{pl},0}$ obviously corresponding to $\bar{n}_{e,0}$.

Observations of the primordial abundance of the light elements yields $\bar{n}_{e,0} \simeq 1.8\cdot 10^{-7}\,\mathrm{cm}^{-3}$, but it has been argued that in the $z < 1$ Universe which is relevant for us $n_e(z)$ ought to be smaller than $\bar{n}_{e,0}$ by a factor 15 [115]. Correspondingly, from Eqs. (1.28) and (4.27) we get

$$\omega_{\mathrm{pl}}(z) \simeq 4.04\cdot 10^{-15}\,(1+z)^{3/2}\ \mathrm{eV}\,, \tag{4.28}$$

where the $(1+\delta(z))^{1/2}$ factor has been dropped because irrelevant.

A crucial issue concerns the large-scale magnetic fields traversed by the beam, whose origin and structure is still unknown to a large extent. A possibility is that very small magnetic fields present in the early Universe were subsequently amplified by the process of structure formation [116]. An alternative option is that the considered magnetic fields have been generated in the low-redshift Universe by energetic quasar outflows [117]. Finally, it has been suggested that large-scale magnetic fields originated from the so-called Biermann battery effect [118], namely from electric currents driven by merger shocks during the structure formation processes. Presumably, all these mechanisms can

take place, even if it is presently impossible to assess their relative importance [112, 113]. At any rate, we suppose that magnetic fields already exist out to the redshift $z = 1$.

Owing to the high conductivity of the IGM, the magnetic flux lines can be thought as frozen inside the IGM. Therefore, flux conservation during the cosmic expansion entails that B scales like the volume to the power 2/3, thereby implying the magnetic field strength in a domain at redshift z is [113]

$$B = B_0 \, (1+z)^2 \ . \tag{4.29}$$

In 2007 the AUGER collaboration reported positive evidence for a correlation between charged cosmic rays and candidate sites for emission [119]. More in detail, the AUGER collaboration found that 20 out of the 27 recorded events with energy larger than 57 EeV are located within 3.1° of an AGN closer than 75 Mpc from Earth. The conclusion drown from the AUGER collaboration is that such a result is inconsistent with the hypothesis of an isotropic distribution of these cosmic rays with at least a 99 % confidence level from a prescribed a-priori test. As explained elsewhere, this fact supports the existence of large-scale magnetic fields with coherence length $L_{\rm dom}$ in the range $1 - 10$ Mpc and strength B_0 in the range $0.1 - 1$ nG at $z = 0$ [120]. However, such a correlation has become considerably weaker when a larger data set (69 events, including the events on which the previous publication was based) has been recorded and analyzed by the AUGER collaboration [121]. The fraction of events correlated to a nearby AGN is in the most recent publication of 38 % – to be compared with an expected value of 21 % in the case of no correlation – and no a-priori probability estimate is provided in the new paper. The present situation appears to us unclear, even though the conclusions obtained from the first AUGER results are still statistically consistent with the more recent ones.

For this reason, we prefer to avoid committing ourselves with any conclusion relying upon the AUGER data and we consider only well-established upper bounds. They depend on the size of their domain-like structure $L_{\rm dom}$ and within the current cosmological setting they take the form [122]

$$B_0 < 3.8 \, {\rm nG} \quad \text{for} \quad L_{\rm dom} = 50 \, {\rm Mpc} \ , \tag{4.30}$$

$$B_0 < 6.3 \, {\rm nG} \quad \text{for} \quad L_{\rm dom} = 1 \, {\rm Mpc} \ . \tag{4.31}$$

It is usually supposed that $1\,\mathrm{Mpc} \leq L_{\mathrm{dom}} \leq 10\,\mathrm{Mpc}$, and so we will assume throughout

$$B_0 < 6\,\mathrm{nG}\ . \tag{4.32}$$

Within the cosmological context, the overall structure of the cellular configuration of large-scale magnetic fields is naturally described by a *uniform* mesh in redshift space with elementary step Δz, which can be constructed as follows. The magnetic domain closest to us and labelled by $n = 1$ extends from 0 to Δz. Hence, its size $L_{\mathrm{dom}}^{(1)}$ can also be written as

$$L_{\mathrm{dom}}^{(1)} = L(0, \Delta z) = \left(\frac{L_{\mathrm{dom}}^{(1)}}{5\,\mathrm{Mpc}}\right) 5\,\mathrm{Mpc}\ , \tag{4.33}$$

where $L(0, \Delta z)$ is the domain's proper size and the second equality stresses our preferred choice for $L_{\mathrm{dom}}^{(1)}$. By combining Eqs. (4.4) and (4.33) we infer

$$\Delta z \simeq 1.17 \cdot 10^{-3} \left(\frac{L_{\mathrm{dom}}^{(1)}}{5\,\mathrm{Mpc}}\right)\ , \tag{4.34}$$

indeed in agreement with the linear Hubble law. Because our mesh in redshift space is uniform, Δz sets the redshift size of *all* magnetic domains. Therefore for a source at redshift z the total number N_d of magnetic domains crossed by the beam can be estimated as

$$N_d \simeq \frac{z}{\Delta z} \simeq 0.85 \cdot 10^3 \left(\frac{5\,\mathrm{Mpc}}{L_{\mathrm{dom}}^{(1)}}\right) z \tag{4.35}$$

and since we are assuming $z < 0.54$ we have $N_d \leq 0.46 \cdot 10^3 (5\,\mathrm{Mpc}/L_{\mathrm{dom}}^{(1)})$. Furthermore, the n-th domain extends from $z = (n-1)\Delta z$ to $z = n\Delta z$ and its proper size can be written as $L_{\mathrm{dom}}^{(n)} = L((n-1)\Delta z, n\Delta z)$. Thanks again to Eq. (4.4), it reads

$$\begin{aligned} L_{\mathrm{dom}}^{(n)} &\simeq 2.96 \cdot 10^3 \ln\left(1 + \frac{1.45\,\Delta z}{1 + 1.45\,(n-1)\Delta z}\right) \mathrm{Mpc} \simeq \\ &\simeq \frac{4.29 \cdot 10^3 \Delta z}{1 + 1.45\,(n-1)\Delta z}\,\mathrm{Mpc}\ , \end{aligned} \tag{4.36}$$

where the last equality is justified by the fact that our analysis is confined to $z < 0.54$ in conjunction with Eq. (4.35).

4.5 Propagation over a single domain

We are now in position to describe the propagation of the considered photon/ALP beam across the n-th magnetic domain.

The transfer matrix is directly supplied by Eq. (4.20), which for notational convenience we rewrite as

$$\mathcal{U}_n(E_n,\psi_n) \equiv e^{i\left(\lambda_1^{(n)}\, L_{\rm dom}^{(n)}\right)}\, T_1(\psi_n) + e^{i\left(\lambda_2^{(n)}\, L_{\rm dom}^{(n)}\right)}\, T_2(\psi_n) + e^{i\left(\lambda_3^{(n)}\, L_{\rm dom}^{(n)}\right)}\, T_3(\psi_n)\ , \quad (4.37)$$

with

$$T_1(\psi_n) \equiv \begin{pmatrix} \cos^2\psi_n & -\sin\psi_n\cos\psi_n & 0 \\ -\sin\psi_n\cos\psi_n & \sin^2\psi_n & 0 \\ 0 & 0 & 0 \end{pmatrix}\ , \quad (4.38)$$

$$T_2(\psi_n) \equiv \begin{pmatrix} \frac{-1+\sqrt{1-4\delta_n^2}}{2\sqrt{1-4\delta_n^2}}\sin^2\psi_n & \frac{-1+\sqrt{1-4\delta_n^2}}{2\sqrt{1-4\delta_n^2}}\sin\psi_n\cos\psi_n & \frac{i\delta_n}{\sqrt{1-4\delta_n^2}}\sin\psi_n \\ \frac{-1+\sqrt{1-4\delta_n^2}}{2\sqrt{1-4\delta_n^2}}\sin\psi_n\cos\psi_n & \frac{-1+\sqrt{1-4\delta_n^2}}{2\sqrt{1-4\delta_n^2}}\cos^2\psi_n & \frac{i\delta_n}{\sqrt{1-4\delta_n^2}}\cos\psi_n \\ \frac{i\delta_n}{\sqrt{1-4\delta_n^2}}\sin\psi_n & \frac{i\delta_n}{\sqrt{1-4{\delta_n}^2}}\cos\psi_n & \frac{1+\sqrt{1-4\delta_n^2}}{2\sqrt{1-4\delta_n^2}} \end{pmatrix}\ , \quad (4.39)$$

$$T_3(\psi_n) \equiv \begin{pmatrix} \frac{1+\sqrt{1-4\delta_n^2}}{2\sqrt{1-4\delta_n^2}}\sin^2\psi_n & \frac{1+\sqrt{1-4\delta_n^2}}{2\sqrt{1-4\delta_n^2}}\sin\psi_n\cos\psi_n & \frac{-i\delta_n}{\sqrt{1-4\delta_n^2}}\sin\psi_n \\ \frac{1+\sqrt{1-4\delta_n^2}}{2\sqrt{1-4\delta_n^2}}\sin\psi_n\cos\psi_n & \frac{1+\sqrt{1-4\delta_n^2}}{2\sqrt{1-4\delta_n^2}}\cos^2\psi_n & \frac{-i\delta_n}{\sqrt{1-4\delta_n^2}}\cos\psi_n \\ \frac{-i\delta_n}{\sqrt{1-4\delta_n^2}}\sin\psi_n & \frac{-i\delta_n}{\sqrt{1-4\delta_n^2}}\cos\psi_n & \frac{-1+\sqrt{1-4\delta_n^2}}{2\sqrt{1-4\delta_n^2}} \end{pmatrix}\ , \quad (4.40)$$

where ψ_n denotes the angle between $\mathbf{B}_n$ and the z-axis, which is fixed for all domains. Moreover, we have set

$$\lambda_1^{(n)} \equiv \frac{i}{2\,\lambda_\gamma^{(n)}(E_0)}\ , \quad (4.41)$$

$$\lambda_2^{(n)} \equiv \frac{i}{4\,\lambda_\gamma^{(n)}}\left(1-\sqrt{1-4\,\delta_n^2}\right)\ , \quad (4.42)$$

$$\lambda_3^{(n)} \equiv \frac{i}{4\,\lambda_\gamma^{(n)}}\left(1+\sqrt{1-4\,\delta_n^2}\right)\ , \quad (4.43)$$

with

$$E_n \equiv E_0\left[1+(n-1)\,\Delta z)\right]\ , \quad (4.44)$$

$$\delta_n \equiv \frac{B_n\,\lambda_\gamma^{(n)}(E_0)}{M} \quad (4.45)$$

and we have introduced the shorthand

$$\lambda_\gamma^{(n)}(E_0) \equiv \lambda_\gamma\left(E_n\right)\ . \quad (4.46)$$

In addition, Eq. (4.29) implies

$$B_n = B_0\left[1+(n-1)\,\Delta z)\right]^2\ . \quad (4.47)$$

What remains to be done in to evaluate the photon mean free path $\lambda_\gamma^{(n)}(E_0)$. A convenient procedure is as follows. Let us suppose to observe two hypothetical sources located at both edges of the n-th domain. Then we apply Eq. (3.3) to either source. With the notational simplifications $\Phi_{\rm obs}(E_0, z) \to \Phi(E_0)$ and $\Phi_{\rm em}\left(E_0(1+z)\right) \to \Phi\left(E_0(1+z)\right)$, we have

$$\Phi(E_0) = e^{-\tau_\gamma(E_0,(n-1)\Delta z)}\, \Phi\left(E_n\right) \ , \tag{4.48}$$

$$\Phi(E_0) = e^{-\tau_\gamma(E_0,n\Delta z)}\, \Phi\left(E_{n+1}\right) \ , \tag{4.49}$$

and so the flux change across the considered domain is

$$\Phi\left(E_n\right) = e^{-[\tau_\gamma(E_0,n\,\Delta z)-\tau_\gamma(E_0,(n-1)\Delta z)]}\, \Phi\left(E_{n+1}\right) \ . \tag{4.50}$$

Now, since $\Delta z \sim 10^{-3}$ evolutionary effects can be neglected inside a single domain and only accounted for when jumping from one domain to the next. As a consequence – owing to Eq. (3.4) – Eq. (4.50) reduces to

$$\Phi\left(E_n\right) = e^{-L_{\rm dom}^{(n)}/\lambda_\gamma^{(n)}(E_0)}\, \Phi\left(E_{n+1}\right) \ , \tag{4.51}$$

and the comparison of Eqs. (4.50) and (4.51) yields

$$\lambda_\gamma^{(n)}(E_0) = \frac{L_{\rm dom}^{(n)}}{\tau_\gamma\left(E_0, n\,\Delta z\right) - \tau_\gamma\left(E_0, (n-1)\Delta z\right)} \ . \tag{4.52}$$

Further, by inserting Eq. (4.36) into Eq. (4.52), we get the desired photon mean free path

$$\lambda_\gamma^{(n)}(E_0) = \left(\frac{4.29\cdot 10^3}{1+1.45\,(n-1)\Delta z}\right)\left(\frac{\Delta z}{\tau_\gamma\left(E_0, n\,\Delta z\right) - \tau_\gamma\left(E_0, (n-1)\Delta z\right)}\right) \text{Mpc} \ . \tag{4.53}$$

4.6 Propagation over many domains

We are finally ready to carry the strategy outlined in Sec. 4.2 to completion, namely to evaluate the photon survival probability $P_{\gamma\to\gamma}^{\rm DARMA}(E_0, z)$ for a monochromatic beam emitted by a blazar at redshift z and detected at energy E_0.

This task can be accomplished by first noticing that for a considered blazar at redshift z the overall behaviour of the photon/ALP beam is described by the following transfer matrix

$$\mathcal{U}\left(E_0, z; \psi_1, ..., \psi_{N_d}\right) = \prod_{n=1}^{N_d} \mathcal{U}_n\left(E_n, \psi_n\right) \ . \tag{4.54}$$

According to Eq. (4.25), the probability that a photon/ALP beam emitted by a blazar at z in the state ρ_1 will be detected in the state ρ_2 for fixed orientations $\psi_1, ..., \psi_{N_d}$ of $\mathbf{B}$ in every domain is

$$P_{\rho_1 \to \rho_2}\left(E_0, z; \psi_1, ..., \psi_{N_d}\right) = \mathrm{Tr}\left(\rho_2 \mathcal{U}\left(E_0, z; \psi_1, ..., \psi_{N_d}\right) \rho_1 \mathcal{U}^{\dagger}\left(E_0, z; \psi_1, ..., \psi_{N_d}\right)\right) , \tag{4.55}$$

where it is assumed that $\mathrm{Tr}\rho_1 = \mathrm{Tr}\rho_2 = 1$. As a consequence, the actual detection probability for the beam in question emerges by averaging the above expression over all angles, namely

$$P_{\rho_1 \to \rho_2}\left(E_0, z\right) = \left\langle P_{\rho_1 \to \rho_2}\left(E_0, z; \psi_1, ..., \psi_{N_d}\right) \right\rangle_{\psi_1, ..., \psi_{N_d}} . \tag{4.56}$$

Because of the fact that the photon polarization cannot be measured at the energies considered here we have to sum this result over the two final polarization states

$$\rho_x = \begin{pmatrix} 1 & 0 & 0 \\ 0 & 0 & 0 \\ 0 & 0 & 0 \end{pmatrix} , \tag{4.57}$$

$$\rho_z = \begin{pmatrix} 0 & 0 & 0 \\ 0 & 1 & 0 \\ 0 & 0 & 0 \end{pmatrix} . \tag{4.58}$$

Moreover, we suppose for simplicity that the emitted beam consists 100 % of unpolarized photons, so that the initial beam state is described by

$$\rho_{\mathrm{unpol}} = \frac{1}{2} \begin{pmatrix} 1 & 0 & 0 \\ 0 & 1 & 0 \\ 0 & 0 & 0 \end{pmatrix} . \tag{4.59}$$

Hence, we ultimately have

$$\begin{aligned} P^{\mathrm{DARMA}}_{\gamma \to \gamma}\left(E_0, z\right) = &\left\langle P_{\rho_{\mathrm{unpol}} \to \rho_x}\left(E_0, z; \psi_1, ..., \psi_{N_d}\right) \right\rangle_{\psi_1, ..., \psi_{N_d}} + \\ &+ \left\langle P_{\rho_{\mathrm{unpol}} \to \rho_z}\left(E_0, z; \psi_1, ..., \psi_{N_d}\right) \right\rangle_{\psi_1, ..., \psi_{N_d}} . \end{aligned} \tag{4.60}$$

We implement this procedure as follows. In the first place, we arbitrarily choose the angle ψ_n in the n-th domain and we evaluate the corresponding transfer matrix $\mathcal{U}_n\left(E_n, \psi_n\right)$ for a given value of E_0, keeping Eq. (4.44) in mind. Next, the application of Eqs. (4.54) and (4.55) yields the corresponding photon survival probabilities entering Eq. (4.60) for a single realization of the propagation process. We repeat these steps 5000 times, by

randomly varying all angles ψ_n each time, thereby generating 5000 random realizations of the propagation process. Finally, we average the resulting photon survival probabilities over all these realizations of the propagation process, thereby accomplishing the average process in Eq. (4.60). We find in this way the physical photon survival probability $P_{\gamma\to\gamma}^{\mathrm{DARMA}}(E_0, z)$.

Chapter 5

ALP consequences on blazar spectra

Let us proceed to investigate the implications of the DARMA scenario for VHE blazars observations.

We begin by stressing that all its physical predictions depend solely on B/M and not on B and M separately (this was true for photon-ALP oscillations and it remains true in general, because absorption does not depend on these quantities). For this reason, it is quite useful to introduce the dimensionless parameter

$$\xi \equiv \left(\frac{B_0}{\mathrm{nG}}\right)\left(\frac{10^{11}\,\mathrm{GeV}}{M}\right) \ . \tag{5.1}$$

Owing to conditions (1.65) and (4.32), it will be assumed

$$\xi < 6 \tag{5.2}$$

throughout our discussion. Specifically, we will focus our attention on the representative cases $\xi = 5.0$, $\xi = 1.0$, $\xi = 0.5$, $\xi = 0.1$, taking both $L_{\mathrm{dom}} = 4\,\mathrm{Mpc}$ and $L_{\mathrm{dom}} = 10\,\mathrm{Mpc}$ at $z = 0$. Nevertheless, it is important to keep under control which values of B_0 and M are allowed in each case. From the constraints (1.65) and (4.32) we find the allowed ranges reported in Table 5.1.

Next, we have to make sure that we stay within the strong-coupling regime all the way up to the source for $E_0 > 100\,\mathrm{GeV}$. Therefore, by combining Eq. (1.48) with the requirement $E_* < 100\,\mathrm{GeV}$ the resulting upper bound on m can be expressed as

$$|m^2 - \omega_{\mathrm{pl}}^2|^{1/2} < 1.97 \cdot 10^{-10} \left(\frac{B}{\mathrm{nG}}\right)^{1/2} \left(\frac{10^{11}\,\mathrm{GeV}}{M}\right)^{1/2} \mathrm{eV} \ , \tag{5.3}$$

ξ	$M/(10^{11}\,\mathrm{GeV})$	B_0/nG
0.1	1 – 60	0.1 – 6
0.5	1 – 12	0.5 – 6
1.0	1 – 6.0	1 – 6
5.0	1 – 1.2	5 – 6

TABLE 5.1: Allowed values of M and B_0 in the considered cases.

Upper bound on m	Value of the ξ parameter
$4.40 \cdot 10^{-10}\,\mathrm{eV}$	$\xi = 5.0$
$1.97 \cdot 10^{-10}\,\mathrm{eV}$	$\xi = 1.0$
$1.39 \cdot 10^{-10}\,\mathrm{eV}$	$\xi = 0.5$
$0.62 \cdot 10^{-10}\,\mathrm{eV}$	$\xi = 0.1$

TABLE 5.2: Upper bounds on the ALP mass in the considered cases.

which – on account of Eqs. (4.28) and (5.1) – can be more suitably rewritten in the form

$$\left| \left(\frac{m}{10^{-10}\,\mathrm{eV}} \right)^2 - \left(1.14 \cdot 10^{-4} \right)^2 \right|^{1/2} < 1.97\,\xi^{1/2} \tag{5.4}$$

valid for all sources considered here [1]. Thanks to condition (5.2), we see that within the DARMA scenario ALPs have to be very light, with mass never exceeding $5 \cdot 10^{-10}\,\mathrm{eV}$. In particular, the axion needed to solve the strong CP problem is therefore ruled out by several orders of magnitude. Observe that for $m < 1.14 \cdot 10^{-14}\,\mathrm{eV}$ the plasma frequency dominates, so that even massless ALPs behave as if their mass where equal to the plasma frequency. The upper bounds on m corresponding to the cases under consideration are reported in Table 5.2.

As far as EBL absorption is concerned, we will take for the optical depth entering Eq. (4.53) the exact expression $\tau_\gamma^{\mathrm{FRV}}(E_0, z)$ provided by the FRV model [101].

A general expectation is that – because in the absence of EBL absorption photon-ALP oscillations only produce a dimming [23] – an enhancement of the photon survival probability with respect to the case of conventional physics shows up only at sufficiently high energy, where EBL absorption becomes substantial. Therefore, close enough to 100 GeV a dimming rather than an enhancement should occur.

[1] Because ω_{pl} increases with z, we have evaluated it at $z = 1$ to be conservative. Similarly, since also B increases with z, we have conservatively taken B_0 rather than B in the r.h.s. of condition (5.4).

5.1 Predictions for future observations

The best way to figure out the relevance of the DARMA scenario for future observations to be performed with the CTA and with the HAWC water Cherenkov γ-ray observatory is to compare the photon survival probability $P_{\gamma\to\gamma}^{\rm DARMA}(E_0, z)$ with the one predicted by conventional physics $P_{\gamma\to\gamma}^{\rm CP}(E_0, z)$, with the EBL described in either case by the FRV model.

We do that for a sample of different redshifts, like $z = 0.031$, $z = 0.188$, $z = 0.444$ and $z = 0.536$. We remark that the case of $z = 0.031$ may look somewhat academic, since its location inside the Local Group is likely to make the morphology of the magnetic field crossed by its line of sight more complicated than assumed in this thesis. Nevertheless, we include $z = 0.031$ in the present analysis in order to see what happens for a very nearby blazar even if a drastic simplifying assumption is made.

The results are displayed in Figs. 5.1. For each of the selected sources, we consider the above choices for ξ, which are represented by a solid black line ($\xi = 5.0$), a dotted-dashed line ($\xi = 1.0$), a dashed line ($\xi = 0.5$) and a dotted line ($\xi = 0.1$), while the solid grey line corresponds to conventional physics. We take both $L_{\rm dom} = 4\,{\rm Mpc}$ and $L_{\rm dom} = 10\,{\rm Mpc}$ for the domain size at $z = 0$.

All plots show one common trend. At energies only slightly in excess of 100 GeV, $P_{\gamma\to\gamma}^{\rm CP}(E_0, z)$ is *larger* than $P_{\gamma\to\gamma}^{\rm DARMA}(E_0, z)$, indeed in agreement with expectations. As the energy further increases, the situation reverses and $P_{\gamma\to\gamma}^{\rm DARMA}(E_0, z)$ gets progressively larger and larger than $P_{\gamma\to\gamma}^{\rm CP}(E_0, z)$ until the value 100 TeV is attained which is the highest energy value considered in the present analysis.

A somewhat surprising result emerges at large enough energies. Indeed, since ξ sets the strength of the photon-ALP oscillation mechanism, it would be natural to expect $P_{\gamma\to\gamma}^{\rm DARMA}(E_0, z)$ to monotonically increase with ξ. However, this is not the case. More specifically, for $\xi = 5.0$ the behaviour of $P_{\gamma\to\gamma}^{\rm DARMA}(E_0, z)$ as a function of E_0 resembles closely that of $P_{\gamma\to\gamma}^{\rm CP}(E_0, z)$ – apart from an overall shift towards higher energies – and it is practically independent of $L_{\rm dom}$ apart from the case of $z = 0.031$ which exhibits a mild $L_{\rm dom}$-dependence. Moreover, at sufficiently high energies the values of $P_{\gamma\to\gamma}^{\rm DARMA}(E_0, z)$ corresponding to $\xi = 5.0$ are the *lowest* predicted by the DARMA scenario for all sources. The case $\xi = 1.0$ is different, since the resulting values of $P_{\gamma\to\gamma}^{\rm DARMA}(E_0, z)$ are among the highest predicted at low redshift but become among the lowest at high redshift even though they always exceed those corresponding to $\xi = 5.0$. In addition – with the exception of $z = 0.031$ – $P_{\gamma\to\gamma}^{\rm DARMA}(E_0, z)$ strongly increases as $L_{\rm dom}$ decreases. As ξ decreases the trend exhibits a radical modification. Actually, the case $\xi = 0.5$ shows a mild $L_{\rm dom}$-dependence for all considered sources, and with the exception of $z = 0.031$

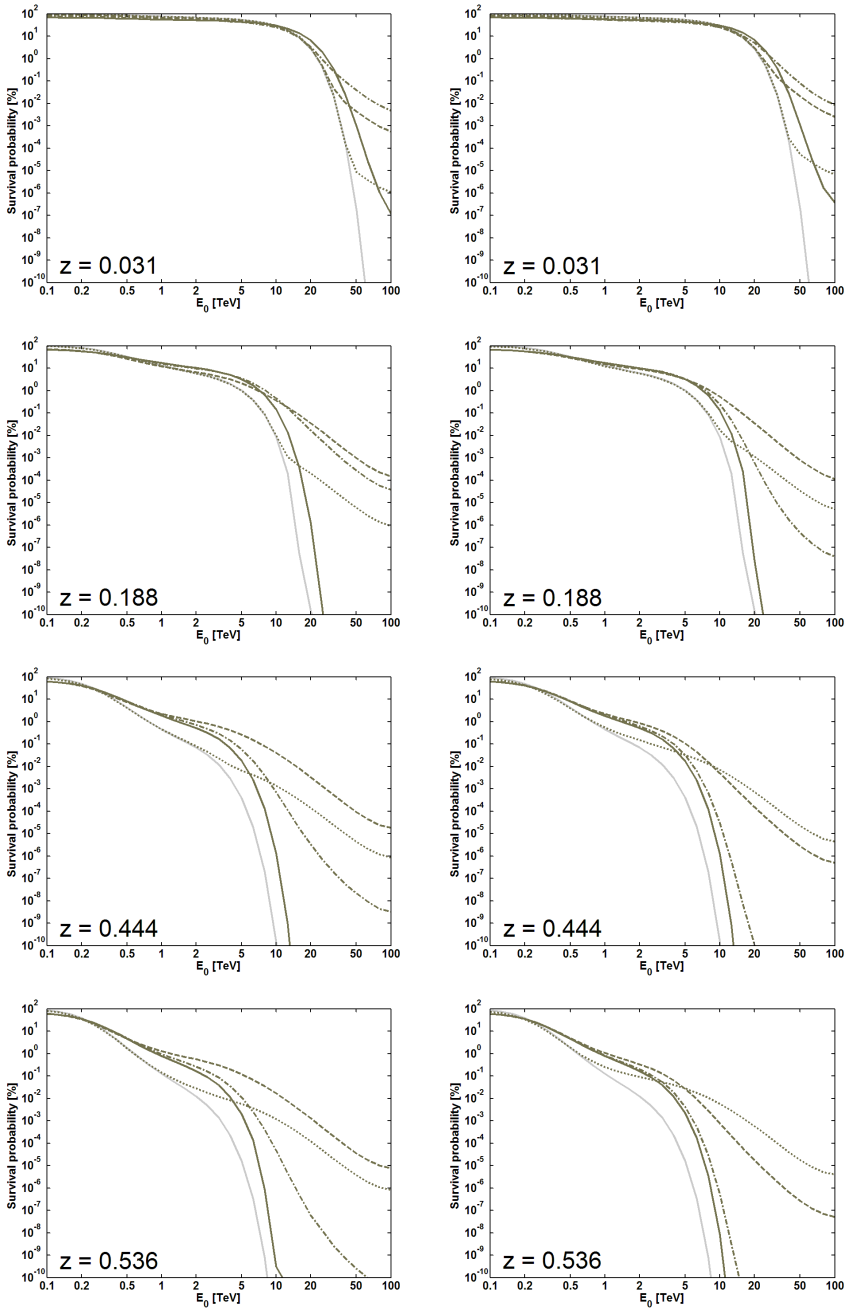

FIGURE 5.1: Behaviour of $P_{\gamma\to\gamma}^{\mathrm{DARMA}}$ versus the observed energy E_0 for: $z = 0.031$ (top row), $z = 0.188$ (second row), $z = 0.444$ (third row), $z = 0.536$ (bottom row). The solid black line corresponds to $\xi = 5.0$, the dotted-dashed line to $\xi = 1.0$, the dashed line to $\xi = 0.5$, the dotted line to $\xi = 0.1$ and the solid grey line to conventional physics. We have taken $L_{\mathrm{dom}} = 4\,\mathrm{Mpc}$ (left column) and $L_{\mathrm{dom}} = 10\,\mathrm{Mpc}$ (right column).

it leads to the largest values of $P_{\gamma\to\gamma}^{\rm DARMA}(E_0, z)$ for $L_{\rm dom} = 4\,{\rm Mpc}$. Finally, the case $\xi = 0.1$ depends more strongly on $L_{\rm dom}$ and – again with the exception of $z = 0.031$ – for some energy values it can make $P_{\gamma\to\gamma}^{\rm DARMA}(E_0, z)$ larger than in the case $\xi = 0.5$ for $L_{\rm dom} = 10\,{\rm Mpc}$, but this never occurs for $L_{\rm dom} = 4\,{\rm Mpc}$. We observe that the different situation found for $z = 0.031$ as compared to the other blazars should not come as a surprise, owing to the above remarks.

What is the reason for such a behaviour?

Owing to the random structure of the considered magnetic field, coherence is maintained only within one domain and so $P_{\gamma\to\gamma}^{\rm DARMA}(E_0, z)$ is ultimately controlled by two quantities: the photon-ALP conversion probability over a single domain $P_{\gamma\to a}(L_{\rm dom})$ and the photon absorption probability in Eq. (4.5). In order to clarify this issue in an intuitive fashion, we argue as follows, discarding cosmological effects for simplicity.

As far as $P_{\gamma\to a}(L_{\rm dom})$ is concerned, we have seen that it is given by Eq. (1.45) in the case of photons linearly polarized in the direction parallel to $\mathbf{B}$. This is not true in the present situation where the beam photons are assumed to be unpolarized, but for the sake of an order-of-magnitude estimate we can still suppose that $P_{\gamma\to a}(L_{\rm dom})$ has the form (1.45) and therefore we write it as

$$P_{\gamma\to a}(L_{\rm dom}) \simeq \sin^2\left[1.6\cdot 10^{-2}\,\xi\left(\frac{L_{\rm dom}}{\rm Mpc}\right)\right]\ . \tag{5.5}$$

We distinguish two cases and we discuss them in turn:

- As long as $\xi \ll 60\,({\rm Mpc}/L_{\rm dom})$, Eq. (5.5) yields $P_{\gamma\to a}(L_{\rm dom}) \ll 1$ which entails that the fraction of ALPs produced over a single domain is very small. Since we are supposing the beam to be initially fully made of photons, it takes a length much larger than $L_{\rm dom}$ before a sizeable fraction of the beam consists of ALPs. In the same fashion, once such a situation is realized, a similar long length is needed in order for the beam to contain a sizeable amount of photons. Moreover, it follows from Eq. (5.5) that presently $P_{\gamma\to a}(L_{\rm dom})$ becomes a quadratic function of ξ which therefore increases monotonically with ξ. Accordingly, the picture outlined in Chapter 4 Sec. 4.1 is expected to emerge straightforwardly and this is confirmed by a numerical simulation in which ξ takes the above values but we assume $L_{\rm dom} = 0.05\,{\rm Mpc}$, which yields the behaviour shown in the plots reported in Figs. 5.2.

- When condition $\xi \ll 60\,({\rm Mpc}/L_{\rm dom})$ is not fulfilled the situation becomes considerably more complicated. In the first place, $P_{\gamma\to a}(L_{\rm dom})$ fails to be a monotonically

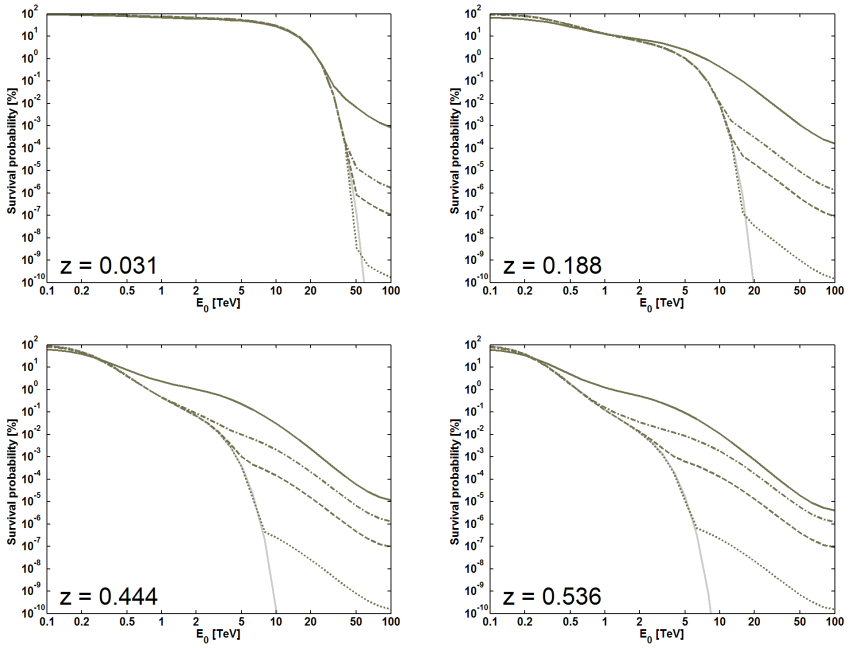

FIGURE 5.2: Behaviour of $P_{\gamma\to\gamma}^{\mathrm{DARMA}}$ versus the observed energy E_0 for: $z = 0.031$ (top row left), $z = 0.188$ (top row right), $z = 0.444$ (bottom row left), $z = 0.536$ (bottom row right) for $L_{\mathrm{dom}} = 0.05\,\mathrm{Mpc}$. The solid black line corresponds to $\xi = 5.0$, the dotted-dashed line to $\xi = 1.0$, the dashed line to $\xi = 0.5$, the dotted line to $\xi = 0.1$ and the solid grey line to conventional physics.

increasing function of ξ and it becomes oscillatory. So, depending on the actual value of L_{dom} it follows that $P_{\gamma\to a}(L_{\mathrm{dom}})$ can decrease as ξ increases. As stressed above, Eq. (5.5) can be taken at most to provide an order-of-magnitude estimate but it is clear that condition $\xi \ll 60\,(\mathrm{Mpc}/L_{\mathrm{dom}})$ fails to be met for $L_{\mathrm{dom}} = 4\,\mathrm{Mpc}$ and $L_{\mathrm{dom}} = 10\,\mathrm{Mpc}$ along with the considered values of ξ. Hence, for a fixed source distance the behaviour exhibited in the plots in Figs. 5.1 can arise. Still, this is not the end of the story, since in the present situation even after the domain closest to the source a relevant fraction of the beam consists of ALPs. In other words, a large enough number of $\gamma \to a$ and $a \to \gamma$ transitions take place inside a single domain. So, the overall effect is to have a larger number of photons per unit length between the source and us as compared to the previous case. As a consequence, EBL absorption is now more effective thereby giving rise to a *smaller* observed photon flux. Moreover, this dimming evidently increases with the source distance, which explains why $P_{\gamma\to\gamma}^{\mathrm{DARMA}}(E_0, z)$ tends to decrease as z increases at fixed energy and eventually it behaves like $P_{\gamma\to\gamma}^{\mathrm{CP}}(E_0, z)$, which indeed occurs for $\xi = 5.0$.

In conclusion, it is evident from Figs. 5.1 that in the most favourable case a boost factor of 10 in $P_{\gamma\to\gamma}^{\mathrm{DARMA}}(E_0, z)$ occurs at progressively lower energies as the source distance

increases. Explicitly, for $z = 0.031$, $z = 0.188$, $z = 0.444$, $z = 0.536$ it takes place at $E_{10} \simeq 30\,\mathrm{TeV}, 8\,\mathrm{TeV}, 2\,\mathrm{TeV}, 1.2\,\mathrm{TeV}$, respectively. Above E_{10} the boost factor can be much larger.

5.2 A new interpretation of observed VHE blazars

Observed VHE blazars provide a great deal of information which can challenge the DARMA scenario. Within conventional physics the values of $\Gamma_{\rm em}$ have to be tuned for every source in such a way to reproduce the corresponding values of $\Gamma_{\rm obs}$. No rational lies behind this procedure and a large spread in the values of $\Gamma_{\rm em}$ is demanded in order to account for the equally large spread in the values of $\Gamma_{\rm obs}$. While this procedure does not pose any technical problem, such a systematic fine-tuning lacks any conceptual appeal and moreover leads to the cosmic opacity problem.

Thus, it looks natural to inquire whether the DARMA scenario sheds some light on this issue.

The most straightforward way to investigate this question is to proceed somehow in parallel with the treatment followed in Chapter 3 Sec. 3.3, namely to de-absorb the values of $\Gamma_{\rm obs}$ within the present context.

Our starting point is the general relation between the observed and emitted fluxes expressed by Eq. (3.1), which presently reads

$$\Phi_{\rm obs}(E_0, z) = P^{\rm DARMA}_{\gamma\to\gamma}(E_0, z)\, \Phi_{\rm em}\left(E_0(1+z)\right) \ . \tag{5.6}$$

Thanks to Eq. (3.6), we first rewrite Eq. (5.6) as

$$K\, E_0^{-\Gamma_{\rm obs}(z)} = P^{\rm DARMA}_{\gamma\to\gamma}(E_0, z)\, \Phi_{\rm em}\left(E_0(1+z)\right) \ , \tag{5.7}$$

from which we get $\Phi_{\rm em}\left(E_0(1+z)\right)$ for every detected VHE blazar. We next best-fit this function to the power-law expression (3.5), namely

$$\Phi_{\rm em}\left(E_0(1+z)\right) = K\left[E_0(1+z)\right]^{-\Gamma^{\rm DARMA}_{\rm em}} \tag{5.8}$$

over the energy range where the considered source is observed (see Table 3.1). We obtain in this way the values of $\Gamma^{\rm DARMA}_{\rm em}$.

We stress that for a given choice of ξ and $L_{\rm dom}$ the photon survival probability $P^{\rm DARMA}_{\gamma\to\gamma}(E_0, z)$ is uniquely fixed, apart from errors affecting $\tau^{\rm FRV}_{\gamma}(E_0, z)$ which are unknown and therefore again ignored. Since $\Gamma^{\rm DARMA}_{\rm em}$ is linearly related to $\Gamma_{\rm obs}$, the associated error bars

are the *same* even in the present context (see Table 3.1) and so they will not be explicitly exhibited.

We implement the considered procedure by taking for the free parameters ξ and $L_{\rm dom}$ the same representative values chosen above. The resulting numerical values of $\Gamma_{\rm em}^{\rm DARMA}$ for the various cases are reported in Tables 5.3 and 5.4, together with the corresponding spread $\Delta\Gamma_{\rm em}^{\rm DARMA}$ of the value of $\Gamma_{\rm em}$ neglecting errors and the average value $\langle\Gamma_{\rm em}^{\rm DARMA}\rangle$ including errors.

Let us consider first what happens as ξ increases from $\xi = 0.1$ to $\xi = 5.0$ assuming $L_{\rm dom} = 4\,{\rm Mpc}$. As long as $\xi = 0.1$ the difference between the DARMA scenario and conventional physics strictly vanishes up to $z = 0.138$ and becomes negligible at larger redshifts. However, as soon as the regime $\xi = 0.5$ is attained the DARMA scenario starts to differ drastically from conventional physics. As ξ increases from 0.5 to 5.0 it is found that $\langle\Gamma_{\rm em}^{\rm DARMA}\rangle$ monotonically increases, even if at a rate that slows down for increasing ξ, which entails that no improvement is to be expected for $\xi > 5.0$ regardless of any other consideration. On the other hand, $\Delta\Gamma_{\rm em}^{\rm DARMA}$ decreases for $\xi = 0.1 \to \xi = 1.0$ but next increases for $\xi = 1.0 \to \xi = 5.0$.

A somewhat similar pattern is found for $L_{\rm dom} = 10\,{\rm Mpc}$. Again for $\xi = 0.1$ the difference between the DARMA scenario and conventional physics strictly vanishes up to $z = 0.116$ and remains negligible at larger redshifts. A big difference shows up around $\xi = 0.5$. As before, $\langle\Gamma_{\rm em}^{\rm DARMA}\rangle$ increases monotonically, but its rate slows down for increasing ξ and just vanishes in the step $\xi = 1.0 \to \xi = 5.0$. Here $\Delta\Gamma_{\rm em}^{\rm DARMA}$ still decreases for $\xi = 0.1 \to \xi = 0.5$ but then increases for $\xi = 0.5 \to \xi = 5.0$.

Let us next find out what happens in the change $L_{\rm dom} = 4\,{\rm Mpc} \to L_{\rm dom} = 10\,{\rm Mpc}$ at fixed ξ. As far as $\Delta\Gamma_{\rm em}^{\rm DARMA}$ is concerned, it decreases for $\xi = 0.1$ and $\xi = 0.5$ but it increases for $\xi = 1.0$ while it remains practically unchanged for $\xi = 5.0$. The behaviour of $\langle\Gamma_{\rm em}^{\rm DARMA}\rangle$ is slightly different, since only in the case $\xi = 0.5$ it shows a slight variation.

Physically, all this means that for $\xi = 0.1$ DARMA effects are negligible, but they suddenly become important shortly before $\xi = 0.5$ is reached and they remain more or less unchanged up to $\xi = 5.0$. This conclusion is in remarkable agreement with our previous results concerning the behaviour of $P_{\gamma\to\gamma}^{\rm DARMA}(E_0, z)$. In this connection, two points should be stressed. It follows from Eqs. (5.7) and (5.8) that at fixed z $\Gamma_{\rm em}^{\rm DARMA}$ depends logarithmically on $P_{\gamma\to\gamma}^{\rm DARMA}(E_0, z)$, which makes its dependence on ξ, E_0 and $L_{\rm dom}$ much shallower than that of $P_{\gamma\to\gamma}^{\rm DARMA}(E_0, z)$ itself. Consequently, the sharp differences found in Sec. 5.1 among the cases with different ξ get smoothed out here, apart from one thing: since in the case $\xi = 0.1$ the photon survival probability is nearly the same in conventional physics and within the DARMA scenario over the

Source	$\Gamma_{\rm em}^{\rm CP}$	$\Gamma_{\rm em}^{\rm DARMA}$ $\xi = 0.1$	$\Gamma_{\rm em}^{\rm DARMA}$ $\xi = 0.5$	$\Gamma_{\rm em}^{\rm DARMA}$ $\xi = 1.0$	$\Gamma_{\rm em}^{\rm DARMA}$ $\xi = 5.0$
3C 66B	3.00	3.00	3.00	3.00	3.03
Mrk 421	2.16	2.16	2.16	2.17	2.21
Mrk 501	1.90	1.90	1.90	1.91	1.96
Mrk 501	2.03	2.03	2.03	2.04	2.08
1ES 2344+514	2.70	2.70	2.71	2.73	2.78
Mrk 180	3.07	3.07	3.07	3.09	3.14
1ES 1959+650	2.43	2.43	2.44	2.46	2.53
BL Lacertae	3.27	3.27	3.28	3.32	3.38
PKS 0548-322	2.39	2.39	2.40	2.45	2.52
PKS 2005-489	3.59	3.59	3.60	3.66	3.73
RGB J0152+017	2.47	2.47	2.48	2.56	2.63
W Comae	3.18	3.18	3.21	3.32	3.39
PKS 2155-304	2.67	2.67	2.72	2.85	2.90
RGB J0710+591	?	?	?	?	?
H 1426+428	0.85	0.85	1.28	1.57	1.44
1ES 0806+524	2.70	2.70	2.77	2.93	3.00
1ES 0229+200	0.41	0.42	1.15	1.37	1.13
H 2356-309	2.06	2.06	2.17	2.35	2.40
1ES 1218+304	2.00	2.00	2.15	2.32	2.36
1ES 1101-232	1.72	1.73	1.96	2.13	2.13
1ES 0347-121	1.87	1.87	2.11	2.28	2.28
1ES 1011+496	2.90	2.90	3.06	3.22	3.26
S5 0716+714	1.60	1.61	2.07	2.22	2.22
PG 1553+113	2.48	2.49	3.00	3.08	3.08
PKS 1222+216	2.47	2.47	2.80	2.88	2.90
3C 66A	1.28	1.30	2.19	2.25	2.22
PKS 1424+240	1.16	1.18	2.03	2.06	2.04
3C 279	2.05	2.06	2.71	2.74	2.73
$\Delta\Gamma_{\rm em}$	3.18	3.17	2.45	2.29	2.60
$\langle\Gamma_{\rm em}\rangle$	2.22	2.23	2.41	2.51	2.52

TABLE 5.3: We have inferred the emitted spectral index $\Gamma_{\rm em}$ by de-absorbing within the DARMA scenario the observed value of $\Gamma_{\rm obs}$ for every source neglecting errors. This procedure has been carried out for the choice of parameters $\xi = 0.1$, $\xi = 0.5$, $\xi = 1.0$ and $\xi = 5.0$. In all cases, we have taken $L_{\rm dom} = 4\,{\rm Mpc}$. The similar values obtained in Chapter 3 Sec. 3.3 within conventional physics have been quoted for comparison and are denoted by $\Gamma_{\rm em}^{\rm CP}$. The last two lines report the spread $\Delta\Gamma_{\rm em}$ of the value of $\Gamma_{\rm em}$ discarding errors and the average value $\langle\Gamma_{\rm em}\rangle$ including errors, respectively, for the various cases.

energy range $0.2\,{\rm TeV} < E_0 < 2\,{\rm TeV}$ where most blazars are observed, the same is evidently true for the values of $\Gamma_{\rm em}$. In addition, the marked difference among the cases $\xi = 0.1, 0.5, 1.0, 5.0$ discovered in Sec. 5.1 takes place at energies considerably larger than those in the presently considered range, which explains why the cases $\xi = 0.5, 1.0, 5.0$ exhibit a fairly similar behaviour for the observed blazars.

Source	$\Gamma_{\rm em}^{\rm CP}$	$\Gamma_{\rm em}^{\rm DARMA}$ $\xi = 0.1$	$\Gamma_{\rm em}^{\rm DARMA}$ $\xi = 0.5$	$\Gamma_{\rm em}^{\rm DARMA}$ $\xi = 1.0$	$\Gamma_{\rm em}^{\rm DARMA}$ $\xi = 5.0$
3C 66B	3.00	3.00	3.03	3.01	3.03
Mrk 421	2.16	2.16	2.16	2.18	2.21
Mrk 501	1.90	1.90	1.90	1.93	1.96
Mrk 501	2.03	2.03	2.03	2.06	2.08
1ES 2344+514	2.70	2.70	2.72	2.76	2.79
Mrk 180	3.07	3.07	3.08	3.11	3.14
1ES 1959+650	2.43	2.43	2.45	2.50	2.53
BL Lacertae	3.27	3.27	3.30	3.36	3.38
PKS 0548-322	2.39	2.39	2.43	2.50	2.52
PKS 2005-489	3.59	3.59	3.63	3.70	3.73
RGB J0152+017	2.47	2.47	2.53	2.61	2.63
W Comae	3.18	3.18	3.28	3.37	3.39
PKS 2155-304	2.67	2.67	2.81	2.89	2.90
RGB J0710+591	?	?	?	?	?
H 1426+428	0.85	0.86	1.53	1.53	1.44
1ES 0806+524	2.70	2.71	2.88	2.98	3.00
1ES 0229+200	0.41	0.48	1.36	1.27	1.12
H 2356-309	2.06	2.06	2.31	2.39	2.40
1ES 1218+304	2.00	2.00	2.29	2.35	2.36
1ES 1101-232	1.72	1.73	2.10	2.14	2.13
1ES 0347-121	1.87	1.88	2.26	2.29	2.28
1ES 1011+496	2.90	2.90	3.19	3.25	3.26
S5 0716+714	1.60	1.62	2.20	2.22	2.22
PG 1553+113	2.48	2.52	3.07	3.08	3.08
PKS 1222+216	2.47	2.49	2.87	2.89	2.90
3C 66A	1.28	1.36	2.25	2.23	2.22
PKS 1424+240	1.16	1.26	2.07	2.05	2.04
3C 279	2.05	2.13	2.74	2.74	2.73
$\Delta\Gamma_{\rm em}$	3.18	3.11	2.27	2.43	2.61
$\langle\Gamma_{\rm em}\rangle$	2.22	2.24	2.49	2.52	2.52

TABLE 5.4: Same as Table 5.3 but with $L_{\rm dom} = 10\,{\rm Mpc}$.

5.2.1 Solution of the cosmic opacity problem

A glance at Tables 5.3 and 5.4 shows that the values of $\Gamma_{\rm em}^{\rm DARMA}$ for *all* VHE blazars happen to be in the same ballpark, thereby implying that within the DARMA scenario the observations can be explained with the same physical mechanism operating in all blazars – as a consequence, there is no cosmic opacity problem.

5.2.2 Fitting individual sources

The foregoing analysis has shown that the gist of the DARMA scenario for the observed VHE blazars is to drastically reduce the spread in the values of $\Gamma_{\rm em}$ as compared with

what happens in conventional physics, thereby tracing the large spread in the values of $\Gamma_{\rm obs}$ to the wide spread in the blazar distances.

It seems therefore worthwhile to investigate this point in a quantitative fashion according the following strategy:

- As a zero-order approximation, we suppose that all blazars have the *same* value of $\Gamma_{\rm em}^{\rm DARMA}$, which for definiteness is taken to be the average value over all observed sources $\langle\Gamma_{\rm em}^{\rm DARMA}\rangle$ for a given choice of ξ and $L_{\rm dom}$.
- As a first-order correction – which is meant to improve on the above idealized situation – we allow for a small spread around $\langle\Gamma_{\rm em}^{\rm DARMA}\rangle$, which we tentatively take to be $\pm\,0.2$.

In order to keep the situation under control, we focus our attention on the single case $\xi = 1.0$ and $L_{\rm dom} = 4\,{\rm Mpc}$ which we regard as the most favourable one not only because $\Delta\Gamma_{\rm em}^{\rm DARMA}$ is very small – the case $\xi = 0.5$ and $L_{\rm dom} = 10\,{\rm Mpc}$ would be even better in this respect – but also because we feel that $L_{\rm dom} = 4\,{\rm Mpc}$ is more realistic than $L_{\rm dom} = 10\,{\rm Mpc}$. This amounts to take $\langle\Gamma_{\rm em}^{\rm DARMA}\rangle = 2.51$, which entails in turn $2.31 < \Gamma_{\rm em}^{\rm DARMA} < 2.71$ for all observed VHE blazars. The value 2.51 is close to the value 2.40 that we used in a previous discussion of the DARMA scenario [25], as well as to 2.47 which is the average value for the observed VHE blazars with $z < 0.05$ that undergo a negligible EBL attenuation.

Next, we evaluate for every source the *expected* observed spectral index $\Gamma_{\rm obs}^{\rm exp}(z)$. Basically, this amounts to run backwards the same procedure whereby we have got the values of $\Gamma_{\rm em}^{\rm DARMA}$ reported in Table 5.3 for $\xi = 1.0$. Explicitly, by combining Eqs. (5.6) and (5.8) we can write

$$\Phi_{\rm obs}^{\rm exp}(E_0, z) = P_{\gamma\to\gamma}^{\rm DARMA}(E_0, z)\, K \left[E_0(1+z)\right]^{-2.51} . \tag{5.9}$$

Since $P_{\gamma\to\gamma}^{\rm DARMA}(E_0, z)$ is known, $\Phi_{\rm obs}^{\rm exp}(E_0, z)$ can be computed exactly. Then we best-fit this function to the power-law expression (3.6), namely

$$\Phi_{\rm obs}^{\rm exp}(E_0, z) = K\, E_0^{-\Gamma_{\rm obs}^{\rm exp}(z)} \tag{5.10}$$

over the energy range where each source is observed. We find in this way the values of $\Gamma_{\rm obs}^{\rm exp}(z)$ for every source. As repeatedly stressed, the observed and emitted spectral indices are linearly related, and so they have the same error bars.

We are now ready to check this view by performing a fit to all observed VHE blazars. This is shown in Figs. 5.3 to 5.7, where the solid black line corresponds to $\Gamma_{\rm obs}^{\rm exp}(z)$ while

the grey strip represents the range $\Gamma_{\rm obs}^{\rm exp}(z) \pm 0.2$. We stress that $\Gamma_{\rm obs}^{\rm exp}(z)$ is different for different sources, owing to the different observed energy range.

A look at those Figures shows that by assuming that *all* VHE blazars have $\Gamma_{\rm em}$ in a range of 2.51 ± 0.2 allows to fit observations of 19 sources out of a total of 27 ones. The role of photon-ALP oscillations is to partially offset EBL absorption, and thus the DARMA scenario departs from conventional physics only to the extent that EBL attenuation becomes important; for $z \geq 0.1$ 12 sources out of a total of 16 ones are successfully fitted, and for $z \geq 0.138$ the fit is successful for 10 blazars out of a total of 11.

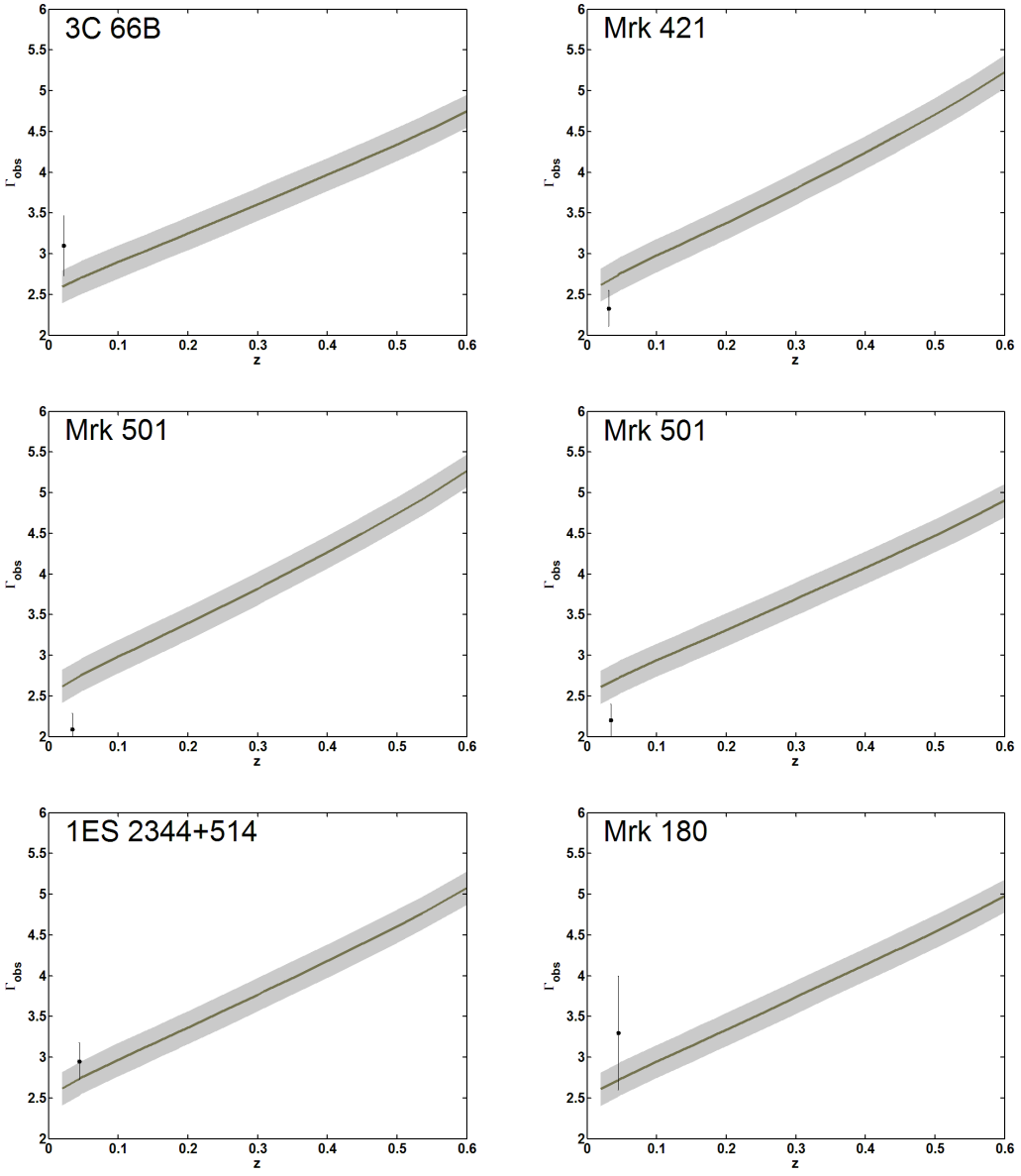

FIGURE 5.3: Behaviour of $\Gamma_{\rm obs}^{\rm DARMA}$ for the blazars 3C 66B, Mrk 421, Mrk 501 (with the two measurements of $\Gamma_{\rm obs}$ in the literature), 1ES 2344+514 and Mrk 180. The solid black line corresponds to $\Gamma_{\rm em}^{\rm DARMA} = 2.51$ and the grey strip represents the range $2.31 < \Gamma_{\rm em}^{\rm DARMA} < 2.71$.

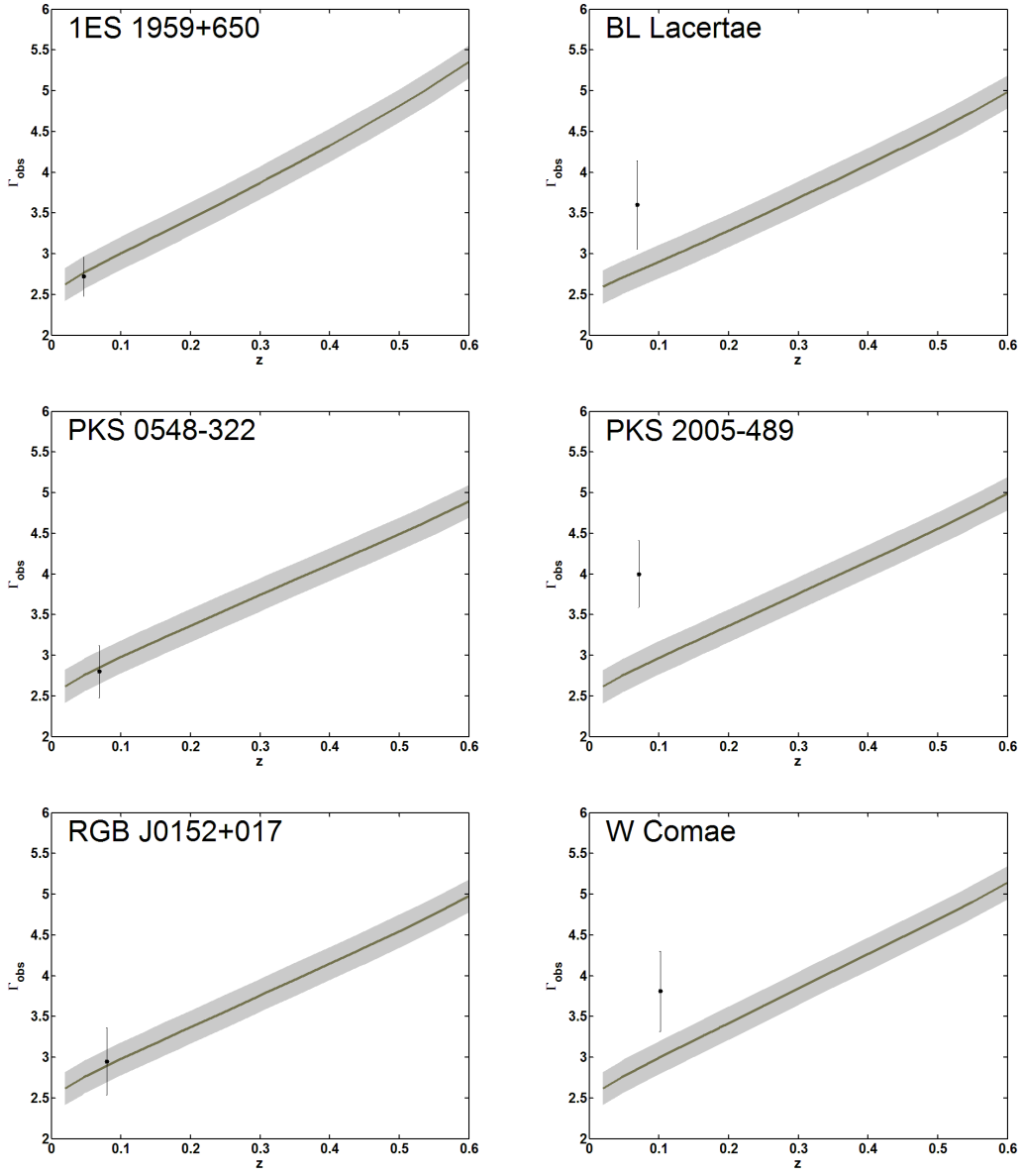

FIGURE 5.4: Behaviour of $\Gamma_{\rm obs}^{\rm DARMA}$ for the blazars 1ES 1959+650, BL Lacertae, PKS 0548-322, PKS 2005-489, RGB J0152+017 and W Comae. The solid black line corresponds to $\Gamma_{\rm em}^{\rm DARMA} = 2.51$ and the grey strip represents the range $2.31 < \Gamma_{\rm em}^{\rm DARMA} < 2.71$.

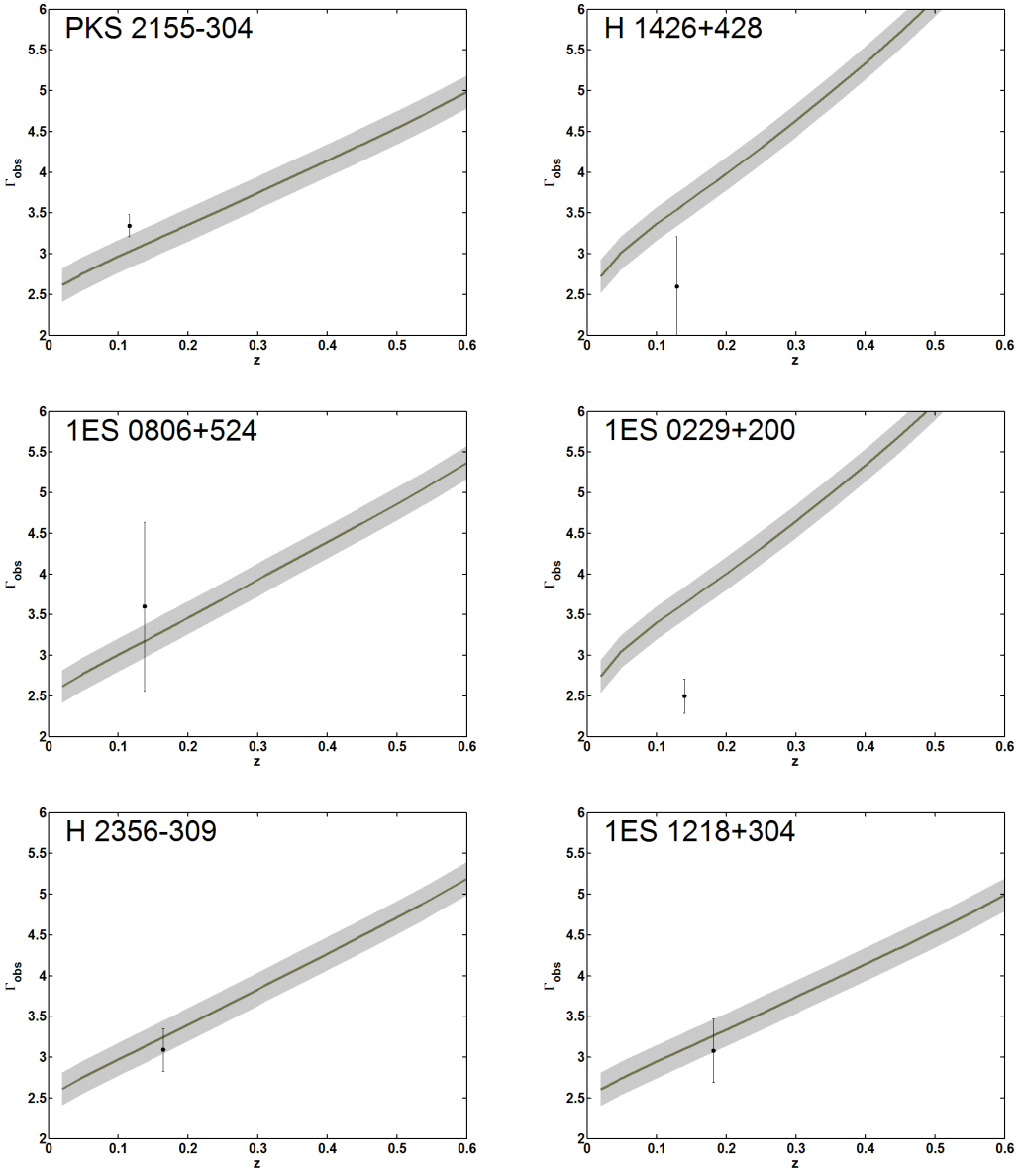

FIGURE 5.5: Behaviour of $\Gamma_{\rm obs}^{\rm DARMA}$ for the blazars PKS 2155-304, H 1426+428, 1ES 0806+524, 1ES 0229+200, H 2356-309 and 1ES 1218+304. The solid black line corresponds to $\Gamma_{\rm em}^{\rm DARMA} = 2.51$ and the grey strip represents the range $2.31 < \Gamma_{\rm em}^{\rm DARMA} < 2.71$.

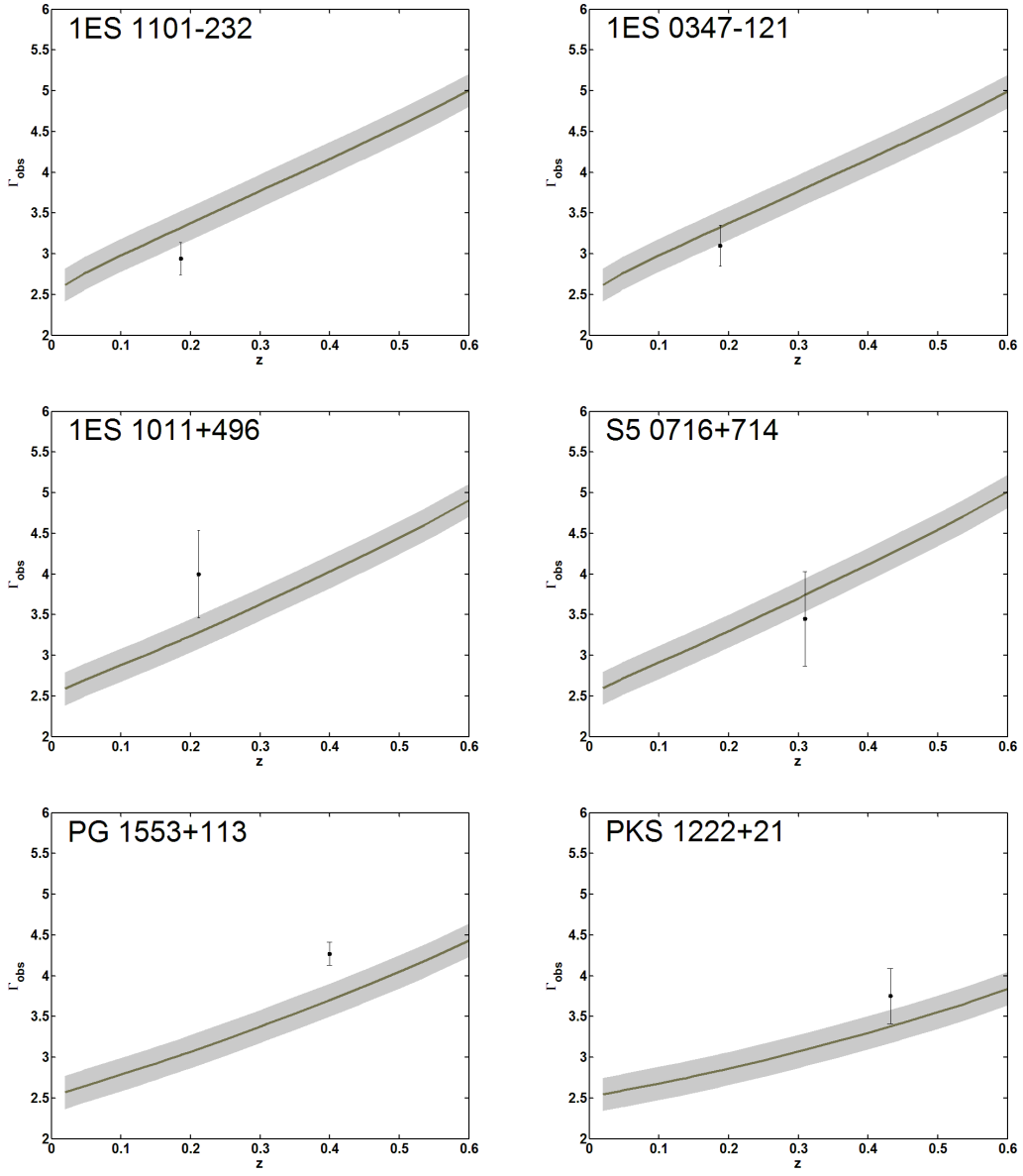

FIGURE 5.6: Behaviour of $\Gamma_{\rm obs}^{\rm DARMA}$ for the blazars 1ES 1101-232, 1ES 0347-121, 1ES 1011+496, S5 0716+714, PG 1553+113 and PKS 1222+216. The solid black line corresponds to $\Gamma_{\rm em}^{\rm DARMA} = 2.51$ and the grey strip represents the range $2.31 < \Gamma_{\rm em}^{\rm DARMA} < 2.71$.

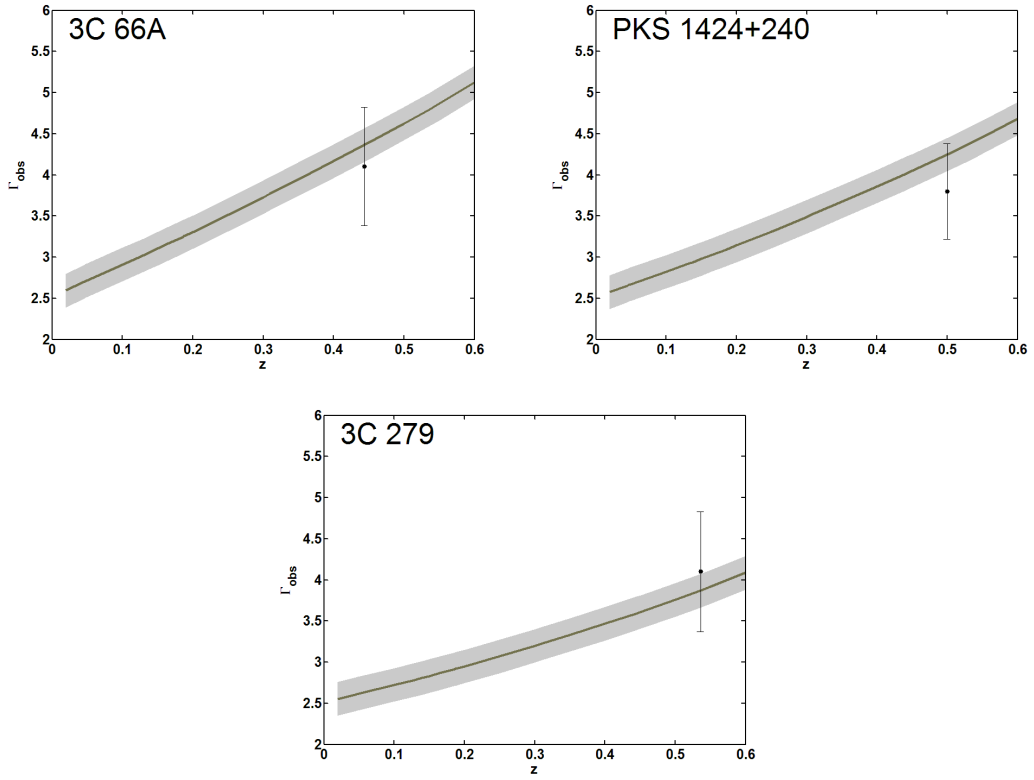

FIGURE 5.7: Behaviour of $\Gamma_{\rm obs}^{\rm DARMA}$ for the blazars 3C 66A, PKS 1424+240 and 3C 279. The solid black line corresponds to $\Gamma_{\rm em}^{\rm DARMA} = 2.51$ and the grey strip represents the range $2.31 < \Gamma_{\rm em}^{\rm DARMA} < 2.71$.

Chapter 6

A model for the FSRQ PKS 1222+216

In this Chapter we proceed to build up our model for PKS 1222+216. We start by explicitly showing why it should not be observed by MAGIC according to conventional physics. We next proceed to discuss photon-ALP conversions in the beam propagation from the central region of PKS 1222+216 to the Earth. Basically, four different regions crossed by the beam are identified, and in each of them we evaluate the relevant transfer matrix. All these pieces of information will be put together in Chapter 7 in order to find out the resulting physical effect.

We stress that in this investigation we will make some rather rough assumptions even because of the lack of knowledge of a few properties of the source (we defer a more detailed modelling to a future publication).

6.1 Observations and setup

In the first place we need to know the relevant physical parameters. We assume a disk luminosity $L_{\rm D} \simeq 1.5 \cdot 10^{46}$ erg s^{-1}, a radius of the BLR $R_{\rm BLR} \simeq 0.23\,$pc, and standard values for cloud number density $n_c \simeq 10^{10}\,{\rm cm}^{-3}$ and temperature $T_c \simeq 10^4\,$K of the BLR (see e.g. [141]). The adopted disk luminosity (a factor of ~ 3 less than that derived in [142] by the observed optical-UV continuum interpreted as the direct emission from the disk) is calculated – following the method outlined in e.g. [143] – from the luminosity of the broad emission lines (Hα, Hβ, MgII) recently obtained in [144] using several optical spectra taken in the period 2008-2011. The adopted value of $R_{\rm BLR}$ is derived from the measured line width and the black hole mass again in [144].

Since the filling factor of the clouds is small, the average electron number density n_e relevant for the beam propagation is much smaller than n_c. Models attributing the confinement of the clouds to a hot $T_e \simeq 10^{7-8}$ K external medium in pressure equilibrium with the clouds yield $n_e \simeq 10^{6-7}\,\mathrm{cm}^{-3}$ (see e.g. [145]). However, the presence of such a hot confining medium is disfavored by the lack of the necessarily expected bright X-ray emission. So, an extra contribution to the pressure confining the BLR clouds is expected and the most likely one is due to a magnetic field with strength $B \sim 1\,\mathrm{G}$ [146] (for a review, see [147]). As a consequence, n_e gets considerably reduced, perhaps to values as low as $n_e \simeq 10^4\,\mathrm{cm}^{-3}$.

In order to bring out quite explicitly the problem posed by the VHE observation of PKS 1222+216, we compute the optical depth $\tau(E)$ of the beam photons in the BLR according to conventional physics, which amounts to consider only the process $\gamma\gamma \to e^+e^-$. We follow the same procedure developed in [141], to which the reader is referred for a full description. The optical depth is given by (Eq. 2.7) but now n_γ is the spectral number density of the BLR. n_γ is calculated using the standard photo-ionization code CLOUDY as in [148] using the input parameters listed above.

The result is plotted as the blue long-dashed line in Fig. 6.1, which shows that PKS 1222+216 should indeed be totally invisible in the energy range $70 - 400\,\mathrm{GeV}$ where it has instead been detected by MAGIC.

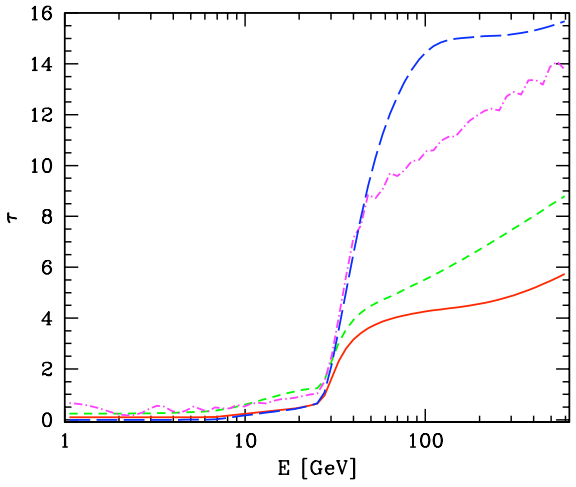

FIGURE 6.1: Effective optical depth plotted as a function of rest-frame energy for VHE photons propagating in the BLR of PKS 1222+216. The blue long-dashed line corresponds to the process $\gamma\gamma \to e^+e^-$. The other three lines pertain to our model containing ALPs. Specifically, the violet dashed-dotted line corresponds to $(B = 2\,\mathrm{G}, M = 4 \cdot 10^{11}\,\mathrm{GeV})$, the green short-dashed line to $(B = 0.4\,\mathrm{G}, M = 1.5 \cdot 10^{11}\,\mathrm{GeV})$ and the red solid line to $(B = 0.2\,\mathrm{G}, M = 7 \cdot 10^{10}\,\mathrm{GeV})$ (more about this, later and in Chapter 7 Sec. 7.1).

The derived $\tau(E)$ is affected by some degree of uncertainty, which is a direct consequence of the uncertainty associated with some of the input parameters, in particular the luminosity of the disk and the radius of the BLR. For instance, a disk luminosity smaller by a factor of ~ 3 was derived in [150] based on the luminosity of the broad Hβ line measured from an old optical spectrum. Moreover, an uncertainty in $L_{\rm D}$ also affects the value of the radius of the BLR, since it is customarily estimated by assuming the empirical relation $R_{\rm BLR} \propto L_{\rm D}^{1/2}$ (see e.g. [149] and references therein). We can roughly summarize the effect of the error associated with $L_{\rm D}$ and $R_{\rm BLR}$ on the optical depth by the following chain involving only the relevant quantities: $\tau \propto R_{\rm BLR}\, n_{\rm ph} \propto R_{\rm BLR}\, L_{\rm BLR}/R_{\rm BLR}^2 \propto L_{\rm D}^{1/2}$, which indeed leads to $\tau \propto L_{\rm D}^{1/2}$. Therefore, the final impact of these uncertainties is moderate. In fact, assuming $L_{\rm D} \simeq 5 \cdot 10^{45}$ erg s^{-1} as in [150], an optical depth comparable to our result is obtained in [151].

A possible complication is the presence within the BLR of disk photons scattered by the high-temperature gas assumed to fill the region between the clouds. The total scattering optical depth associated with such a gas with the density $n_e \simeq 10^4\,{\rm cm}^{-3}$ assumed above is $\tau_{\rm sc} = \sigma_{\rm T} R_{\rm BLR} n_e \simeq 2.5 \cdot 10^{-3}$. A detailed calculation of the optical depth of γ rays associated with the scattered disk photons has been made in [151], where it is found that the maximum absorption caused by this component is localized at ~ 200 GeV, with a corresponding optical depth $\tau \sim 70\,\tau_{\rm sc}$. Clearly $\tau_{\rm sc} = 2.5 \cdot 10^{-3}$ entails $\tau \simeq 0.2$, thus showing that this contribution to the total $\tau(E)$ can be safely neglected.

As pointed out in the Introduction, our proposal to avoid the problem of the huge optical depth is framed within the standard blazar model for photon production, but in addition we assume the existence of ALPs a with parameters allowing for efficient conversions $\gamma \to a$ and $a \to \gamma$. Basically, we envisage that a large fraction of VHE photons produced as usual near the central engine become ALPs before reaching the BLR, thereby crossing it totally unimpeded. Outside the BLR most of the ALPs are supposed to become VHE photons again in the large scale jet and in the host galaxy. Because the beam traverses the extragalactic space, the possibility of photon-ALP oscillations in this region has also to be taken into account. Finally, we recall that the external magnetic field is the crucial quantity that triggers photon-ALP conversions.

As a preliminary step, we find it very useful to rewrite Eqs. (1.48) and (1.49) in the following more convenient form

$$E_* \simeq 25 \left| \left(\frac{m}{10^{-10}\,{\rm eV}}\right)^2 - 0.13 \left(\frac{n_e}{{\rm cm}^{-3}}\right) \right| \left(\frac{G}{B_T}\right) \left(\frac{M}{10^{11}\,{\rm GeV}}\right) {\rm eV} \tag{6.1}$$

and

$$E_{**} \simeq 2.1 \left(\frac{G}{B_T}\right) \left(\frac{10^{11}\,{\rm GeV}}{M}\right) {\rm GeV}\ , \tag{6.2}$$

so that we can very easily find out when the strong-mixing regime occurs. Moreover, we observe that in the mixing matrix the plasma contribution is negligible with respect to the QED one-loop contribution for

$$n_e \ll 7.8 \cdot 10^{11} \left(\frac{E}{100\,\mathrm{GeV}}\right)^2 \left(\frac{B_T}{\mathrm{G}}\right)^2 \mathrm{cm}^{-3}\,, \tag{6.3}$$

thanks to Eqs. (1.27), (1.28), and (1.29). Of course, condition (6.3) is relevant outside the strong-mixing regime.

Below, we will address photon-ALP conversions in the various regions crossed by the beam.

6.2 Oscillations in the inhomogeneous magnetic field

As we will see, in the present model of PKS 1222+216 the beam crosses four regions with very different properties before being detected, and only in the first one **B** can be taken as homogeneous in first approximation. In the second region, **B** has a smooth y-dependence and in this case the beam propagation equation can be solved exactly owing to a drastic simplification of the Δ terms entering the mixing matrix (we find it more natural to address this issue in Sec. 6.4 where the properties of the region in question are discussed, which in turn dictate the form of the Δ terms). In the third region **B** possesses a turbulent structure which is currently modeled as random domain-like network, and this may or may not be the case in the fourth region (more about this, later).

Specifically, in the simplest situation all domains have the same size set by the coherence length of the magnetic field and the strength of **B** is the same in every domain, but the orientation of **B** changes randomly from one domain to the next (however a more general situation has to be considered in the cosmological context, but these complications will be discussed later). Therefore, inside the n-th generic domain ($1 \leq n \leq N$) the mixing matrix in Eq. (1.20) takes the form

$$\mathcal{M}_n(E,\psi_n) \equiv \begin{pmatrix} \Delta_{xx}(E,\psi_n) & \Delta_{xz}(E,\psi_n) & \Delta_{a\gamma}\sin\psi_n \\ \Delta_{zx}(E,\psi_n) & \Delta_{zz}(E,\psi_n) & \Delta_{a\gamma}\cos\psi_n \\ \Delta_{a\gamma}\sin\psi_n & \Delta_{a\gamma}\cos\psi_n & \Delta_{aa}(E) \end{pmatrix}\,, \tag{6.4}$$

where the various $\Delta(E,\psi_n)$ quantities are described in Chapter 1, Sec. 1.5. Manifestly ψ_n is the angle between $\mathbf{B}_T^{(n)}$ and the a fiducial z axis taken to be the same for all domains. Denoting by $\mathcal{U}_n\,(E;\psi_n)$ the transfer matrix in the n-th domain – which is

derived through the same steps as in Chapter 4 Sec. 4.5 – its explicit form just follows from Eq. (1.57) with $y - y_0$ denoting the domain size.

Moreover, according to quantum mechanics the transfer matrix for the whole network of N domains is

$$\mathcal{U}_{\text{random}}\left(E;\psi_1,...,\psi_N\right) = \prod_{n=1}^{N} \mathcal{U}_n\left(E;\psi_n\right) \ . \tag{6.5}$$

Further, it proves convenient to denote by $\mathcal{U}_{\text{smooth}}(E)$ the transfer matrix corresponding to the first two regions. Hence, the overall beam propagation is described by $\mathcal{U}_{\text{random}}\left(E;\psi_1,...,\psi_N\right)\mathcal{U}_{\text{smooth}}(E)$. As a consequence, the probability that the beam emitted in the state ρ_{in} at y_0 will be detected in the state ρ_{fin} at y for *fixed* orientations $\psi_1,...,\psi_N$ of $\mathbf{B}$ in every domain is

$$\begin{aligned} &P_{\rho_{\text{in}}\to\rho_{\text{fin}}}(y,y_0;E;\psi_1,...,\psi_N) = \\ &= \text{Tr}\Big(\rho_{\text{fin}}\,\mathcal{U}_{\text{random}}\left(E;\psi_1,...,\psi_N\right)\mathcal{U}_{\text{smooth}}(E)\,\rho_{\text{in}}\,\mathcal{U}^{\dagger}_{\text{smooth}}(E)\,\mathcal{U}^{\dagger}_{\text{random}}\left(E;\psi_1,...,\psi_N\right)\Big) \ , \end{aligned} \tag{6.6}$$

where it is assumed again that $\text{Tr}\,\rho_{\text{in}} = \text{Tr}\,\rho_{\text{fin}} = 1$.

Now, owing to the turbulent nature of the magnetic field in question the angles ψ_n ($1 \leq n \leq N$) are to be regarded as independent random variables in the range $1 \leq \psi_n \leq 2\pi$. As a consequence, the physical detection probability for the considered beam arises by averaging the last equation over all angles, namely we have

$$P_{\rho_{\text{in}}\to\rho_{\text{fin}}}(y,y_0;E) = \Big\langle P_{\rho_{\text{in}}\to\rho_{\text{fin}}}(y,y_0;E;\psi_1,...,\psi_N)\Big\rangle_{\psi_1,...,\psi_N} \ . \tag{6.7}$$

More specifically, since the photon polarization cannot be measured at the considered energies, we have to sum Eq. (6.7) over the two final polarization states ρ_x and ρ_z given by Eqs. (4.57) and (4.58). In addition, we suppose for simplicity that the emitted beam consists 100 % of unpolarized photons, so that the initial beam state is described by Eq. (4.59). Therefore Eq. (6.7) ultimately takes the form

$$\begin{aligned} P_{\gamma\to\gamma}(y,y_0;E) = &\Big\langle P_{\rho_{\text{unpol}}\to\rho_x}\left(y,y_0;E;\psi_1,...,\psi_N\right)\Big\rangle_{\psi_1,...,\psi_N} + \\ &+ \Big\langle P_{\rho_{\text{unpol}}\to\rho_z}\left(y,y_0;E;\psi_1,...,\psi_N\right)\Big\rangle_{\psi_1,...,\psi_N} \ , \end{aligned} \tag{6.8}$$

which gives the photon survival probability.

The actual evaluation of $P_{\gamma\to\gamma}\left(E\right)$ goes as follows. In the first place we have to know $\mathcal{U}_{\text{smooth}}(E)$. Next, we arbitrarily choose ψ_n in each domain and so we can evaluate $\mathcal{U}_n\left(\psi_n,E\right)$ for a given energy E. Thanks to Eq. (6.5) and the next one, we find the photon survival probability for a single realization of the propagation process. We

repeat these steps 5000 times, by randomly varying all angles ψ_n each time, thereby generating 5000 random realizations of the propagation process. Finally, we average the resulting photon survival probabilities over all these realizations of the propagation process, thereby accomplishing the average process in the last equation. We find in this way the physical photon survival probability $P_{\gamma\to\gamma}^{\rm ALP}(E)$ when ALP effects are included.

6.3 Photon-ALP oscillations before the BLR

We start by considering the inner part of the blazar, namely the region extending from the centre to $R_{\rm BLR} \simeq 0.23\,{\rm pc}$, to be referred to as region 1.

The magnetic field profile along the jet is well known to decrease outwards but unfortunately the presence of strong shocks and relativistic winds makes a precise estimate of the strength profile of $\mathbf{B}$ for distances smaller than $R_{\rm BLR}$ practically impossible. An analysis based on a highly idealized description relying on a one-zone, homogeneous leptonic model with external photons yields for the strength of $\mathbf{B}$ at the base of the jet $B \simeq 2.2\,{\rm G}$ [152]. Therefore, we feel it realistic in this investigation to assume its strength to be constant and equal to its average value from the centre to the BLR, which we take for definiteness $B \simeq 0.2\,{\rm G}$. Moreover, owing to the complicated morphology of $\mathbf{B}$, we similarly suppose that its average direction from the centre to the BLR is nonvanishing and we assume it to be the same everywhere in the considered region (equal to its average direction), so that we are dealing with a *homogeneous* $\mathbf{B}$ having an unknown direction. Because the photon-ALP conversions vanish if $\mathbf{B}$ is just along the beam while it is maximal for $\mathbf{B}$ transverse to the beam, we suppose in line with our heuristic attitude that $\mathbf{B}$ is on average at an angle of 45° with the beam direction. Therefore we have $B_T \simeq 0.14\,{\rm G}$.

A natural question is to find out the energy range $E_* < E < E_{**}$ in which the strong-mixing regime takes place. As a working hypothesis we assume $m < \omega_{\rm pl}$, so that E_* becomes independent of m, and in addition it follows that we are dealing with a *very light* ALP just like in previous work [23–27, 30] (see also Chapters 4 and 5) (more about this, later). Hence from Eq. (6.1) we find $E_* \simeq 0.23\,{\rm MeV}$ for $n_e \simeq 10^4\,{\rm cm}^{-3}$ while $E_* \simeq 0.23\,{\rm GeV}$ for $n_e \simeq 10^7\,{\rm cm}^{-3}$. Further, thanks to Eq. (6.2) the robust CAST bound entails $E_{**} < 136\,{\rm GeV}$ and the controversial SN 1987A bound implies $E_{**} < 15\,{\rm GeV}$. Thus, we end up with the conclusion that for *Fermi*/LAT observations we are in the strong-mixing regime but for MAGIC observations we are *not*. Yet, we will see that the latter fact does not undermine the relevance of photon-ALP oscillations well above E_{**}. Below, we put ourselves in the general case where the strong-mixing regime does not take place in order to have a uniform treatment for both the *Fermi*/LAT and MAGIC

observations: Of course, the simplifications characteristic of the strong-mixing regime automatically show up whenever it takes place.

An additional issue concerns the relevance of the QED one-loop effect. We know that it is negligible in the strong-mixing regime, but otherwise it can be important. Since photon absorption is independent of **B** it can presently be discarded, so that the relevant **B**-dependent quantity governing the photon-ALP conversion probability is the oscillation wavenumber $\Delta_{\rm osc}(E)$. Then a look at Eq. (1.35) immediately shows that the QED one-loop is unimportant with respect to the standard magnetic contribution at energies $E < E_{**}$, namely for

$$E < 15 \left(\frac{10^{11}\,{\rm GeV}}{M}\right) {\rm GeV} \ , \tag{6.9}$$

as expected. So, for M rather close to $10^{11}\,{\rm GeV}$ – which we will see to be indeed our case – the QED one-loop effect is negligible for *Fermi*/LAT observations ($0.3 - 3\,{\rm GeV}$) but of paramount importance for MAGIC observations ($70 - 400\,{\rm GeV}$).

Now, owing to Eq. (1.28) $n_e \simeq 10^4\,{\rm cm}^{-3}$ gives $\omega_{\rm pl} \simeq 3.69 \cdot 10^{-9}\,{\rm eV}$ whereas $n_e \simeq 10^7\,{\rm cm}^{-3}$ yields $\omega_{\rm pl} \simeq 1.17 \cdot 10^{-7}\,{\rm eV}$, which correspondingly imply $m < 3.69 \cdot 10^{-9}\,{\rm eV}$ and $m < 1.17 \cdot 10^{-7}\,{\rm eV}$. Furthermore, for our choice $B_T \simeq 0.14\,{\rm G}$ condition (6.3) implies that the plasma contribution is always negligible with respect to the QED one-loop contribution both for *Fermi/LAT* and for MAGIC observations (of course in the former case the plasma contribution is *a fortiori* negligible with respect to the standard magnetic contribution). Hence in the mixing matrix the plasma effect can be discarded. Manifestly, within the strong-mixing regime the ALP mass term in the mixing matrix has to be neglected, but it is easy to check that for the above choice of the parameters the same situation is true to leading order even at higher energies where the strong-mixing regime does not occur.

Finally, we have

$$\lambda_\gamma(E) = \frac{R_{\rm BLR}}{\tau(E)} \ , \tag{6.10}$$

where $\tau(E)$ is the optical depth for $\gamma\gamma \to e^+e^-$ plotted by the blue long-dashed line in Fig. 6.1 and evaluated as in [141].

Thus, on account of Eqs. (1.16), (1.17), (1.18), (1.26), (1.27), (1.29), (4.6) and (6.10) we find that to leading order the elements of the mixing matrix (4.7) (see also Eq. (1.15) for matrix element definition) are

$$\Delta_{xx}(E) = \frac{2\alpha E}{45\pi}\left(\frac{B_T}{B_{\rm cr}}\right)^2 + \frac{i\,\tau(E)}{2\,R_{\rm BLR}} \simeq 10^{-24}\left[\left(\frac{E}{\rm GeV}\right) + 13.9\,i\,\tau(E)\right] {\rm eV} \ , \tag{6.11}$$

$$\Delta_{zz}(E) = \frac{3.5\alpha E}{45\pi}\left(\frac{B_T}{B_{\rm cr}}\right)^2 + \frac{i\,\tau(E)}{2\,R_{\rm BLR}} \simeq 10^{-24}\left[1.75\left(\frac{E}{\rm GeV}\right) + 13.9\,i\,\tau(E)\right] {\rm eV} \ , \tag{6.12}$$

$$\Delta_{a\gamma} = \frac{B_T}{2M} \simeq 1.37 \cdot 10^{-23} \left(\frac{10^{11}\,\mathrm{GeV}}{M}\right) \mathrm{eV}\ , \tag{6.13}$$

$$\Delta_{aa}(E) = 0\ . \tag{6.14}$$

It is now a matter of simple algebra to evaluate the corresponding eigenvalues $\lambda_1(E)$, $\lambda_2(E)$ and $\lambda_3(E)$ as well as the matrices $T_1(E,0)$, $T_2(E,0)$ and $T_3(E,0)$ entering Eq. (4.13), so that we ultimately get the transfer matrix $\mathcal{U}_1(R_{\rm BLR},0;E)$.

6.4 Photon-ALP oscillations in the large scale jet

Let us next focus our attention on the region surrounding the BLR along the line of sight – to be referred to as region 2 – namely on the jet beyond the parsec scale or more precisely beyond $R_{\rm BLR}$. The main question concerns the behavior of $\mathbf{B}$. At variance with the inner region, shocks and winds are expected to be here less relevant so that we can attempt to figure out the y-dependence of $\mathbf{B}$. As is well known, a poloidal field behaves as $B(y) \propto y^{-2}$ whereas a toroidal field goes like $B(y) \propto y^{-1}$ [153]. Clearly, since we are at a sufficiently large distance from the centre the toroidal field dominates, and so it seems more plausible to assume $B(y) \propto y^{-1}$ (see also [154]). As a consequence, in the region 2 we adopt the profile

$$B_T(y) \simeq 0.14 \left(\frac{R_{\rm BLR}}{y}\right) \mathrm{G} \simeq 3.22 \cdot 10^{-2} \left(\frac{\mathrm{pc}}{y}\right) \mathrm{G}\ . \tag{6.15}$$

However, we have checked that even by taking $B(y) \propto y^{-2}$ the corresponding change is small, thereby showing that the choice of the exact profile of $\mathbf{B}$ has a minor impact on the final result.

What is the actual size of the region 2? As we shall see, the typical strength of the turbulent magnetic field in the host elliptical galaxy is about $5\,\mu$G, and so it looks natural to define the outer edge R_* of region 2 as the galactocentric distance where $B_T(y)$ in Eq. (6.15) reaches the value of $5\,\mu$G. Accordingly, we get $R_* \simeq 6.7\,\mathrm{kpc}$.

A relevant question is whether the strong-mixing regime takes place throughout the whole energy range – namely for $0.3\,\mathrm{GeV} < E < 400\,\mathrm{GeV}$ – over region 2. For this to be the case, we must have both $E_* < 0.3\,\mathrm{GeV}$ and $E_{**} > 400\,\mathrm{GeV}$. Explicitly, by combining Eqs. (6.1) and (6.2) with Eq. (6.15) we obtain

$$y < 3 \cdot 10^3 \left(\frac{\mathrm{cm}^{-3}}{n_e}\right) \left(\frac{10^{11}\,\mathrm{GeV}}{M}\right) \mathrm{kpc} \tag{6.16}$$

and

$$y > 6.1 \left(\frac{M}{10^{11}\,\mathrm{GeV}}\right) \mathrm{pc}\ . \tag{6.17}$$

So, we see that even by taking the average electron density as large as $n_e \simeq 10^2\,\mathrm{cm}^{-3}$ we reach the conclusion that the strong-mixing regime takes place over more than 99 % of region 2 for M rather close to 10^{11} GeV. Thus, it will be assumed *tout court*. Consequently, the plasma contribution, the ALP mass term and the QED one-loop contribution should be dropped.

Since in region 2 absorption effects are negligible, owing to the above conclusions from Eqs. (1.16), (1.17), (1.18), (1.26), (1.27), (1.29) and (4.6) we ultimately obtain

$$\Delta_{xx}(E) = 0 \ , \tag{6.18}$$

$$\Delta_{zz}(E) = 0 \ , \tag{6.19}$$

$$\Delta_{a\gamma} = \frac{B_T}{2M} \simeq 3.1 \cdot 10^{-24} \left(\frac{\mathrm{pc}}{y}\right) \left(\frac{10^{11}\,\mathrm{GeV}}{M}\right) \mathrm{eV} \ , \tag{6.20}$$

$$\Delta_{aa}(E) = 0 \ . \tag{6.21}$$

In this case, the transfer matrix can be directly obtaining by explicitly solving the beam propagation equation and reads

$$\mathcal{U}_2(R_*, R_{\mathrm{BLR}}; E) = \begin{pmatrix} 1 & 0 & 0 \\ 0 & \cos\left(\frac{B_T(R_{\mathrm{BLR}})\,R_{\mathrm{BLR}}}{2M} \ln\frac{R_*}{R_{\mathrm{BLR}}}\right) & i\sin\left(\frac{B_T(R_{\mathrm{BLR}})\,R_{\mathrm{BLR}}}{2M} \ln\frac{R_*}{R_{\mathrm{BLR}}}\right) \\ 0 & i\sin\left(\frac{B_T(R_{\mathrm{BLR}})\,R_{\mathrm{BLR}}}{2M} \ln\frac{R_*}{R_{\mathrm{BLR}}}\right) & \cos\left(\frac{B_T(R_{\mathrm{BLR}})\,R_{\mathrm{BLR}}}{2M} \ln\frac{R_*}{R_{\mathrm{BLR}}}\right) \end{pmatrix} , \tag{6.22}$$

where of course $B_T(R_{\mathrm{BLR}})$ is supplied by Eq. (6.15).

6.5 Photon-ALP oscillations in the host galaxy

FSRQs are hosted by elliptical galaxies, whose **B** is very poorly known. Nevertheless, it has been argued [155] that supernova explosions and stellar motion give rise to a turbulent **B** which can be modeled by a domain-like structure, with average strength $5\,\mu$G and domain size equal to 150 pc. We stress that these two quantities are the same for all domains. Correspondingly, we define region 3 as the spherical section with inner radius $R_* \simeq 6.7\,\mathrm{kpc}$ and outer radius R_{host}.

Because absorption is presently irrelevant, the transfer matrix $\mathcal{U}_3\left(R_{\mathrm{host}}, R_*; E; \phi_1, ..., \phi_{N_3}\right)$ just follows from the discussion in Sec. 6.2 with $\psi_n \to \phi_n$ and $N \to N_3$. Furthermore, it is trivial to check that in region 3 the strong-mixing regime takes place and so the plasma contribution, the ALP mass term and the QED one-loop contribution are totally irrelevant. Hence, from Eqs. (1.16), (1.17), (1.18), (1.26), (1.27), (1.29) and (4.6) in

every domain we have

$$\Delta_{xx}(E) = 0 \ , \tag{6.23}$$

$$\Delta_{zz}(E) = 0 \ , \tag{6.24}$$

$$\Delta_{a\gamma} = \frac{B_T}{2M} \simeq 3.4 \cdot 10^{-28} \left(\frac{10^{11}\,\mathrm{GeV}}{M} \right) \mathrm{eV} \ , \tag{6.25}$$

$$\Delta_{aa}(E) = 0 \ , \tag{6.26}$$

and so in the n-th generic domain ($1 \leq n \leq N_3$) the mixing matrix (6.4) takes the explicit form

$$\mathcal{M}_n(E, \phi_n) = \begin{pmatrix} 0 & 0 & (B_T/2M)\sin\phi_n \\ 0 & 0 & (B_T/2M)\cos\phi_n \\ (B_T/2M)\sin\phi_n & (B_T/2M)\cos\phi_n & 0 \end{pmatrix} \ . \tag{6.27}$$

Denoting as in Sec. 6.2 by $\mathcal{U}_n(E, \phi_n)$ the associated transfer matrix with $y - y_0 = 150\,\mathrm{pc}$, the transfer matrix describing the beam propagation over region 3 just follows from Eq. (6.5), namely

$$\mathcal{U}_3\left(R_{\mathrm{host}}, R_*; E; \phi_1, ..., \phi_{N_3}\right) = \prod_{n=1}^{N_3} \mathcal{U}_n(E; \phi_n) \ . \tag{6.28}$$

We should however remark that such an effect plays a very minor role, and even ignoring it the final result is practically unaffected. This means that the back conversions $a \to \gamma$ effectively take place in region 2.

6.6 Photon-ALP oscillations in extragalactic space

What remains to be done is to address the beam propagation in extragalactic space, which is referred to as our region 4.

The propagation of the beam in region 4 is described by the DARMA scenario which is presented in Chapter 4, to which we address the reader for a full treatment – we report here only the final results for completeness.

The discussion is similar to the one treated in Sec. 6.2 with $\psi_n \to \varphi_n$ and $N \to N_4$, but in the cosmological setting: the overall domain-like network of the large-scale magnetic field is described by a uniform mesh in redshift space rather than in ordinary space and the magnetic field B is not exactly the same in all domains (see Chapter 4 for more details).

The DARMA scenario assumes that this is indeed the case for $E_* \simeq 100\,\mathrm{GeV}$, but we can just as well require $E_* \simeq 70\,\mathrm{GeV}$ (the QED one-loop effect is here ridiculously small). Correspondingly, recalling Eq. (6.1) the following constraint has to be met

$$\left|\left(\frac{m}{10^{-10}\,\mathrm{eV}}\right)^2 - 0.13\left(\frac{n_e}{\mathrm{cm}^{-3}}\right)\right|\left(\frac{nG}{B_T}\right)\left(\frac{M}{10^{11}\,\mathrm{GeV}}\right) < 2.8\ . \tag{6.29}$$

Under such an assumption, the plasma contribution and the ALP mass term should be dropped and from Eqs. (1.16), (1.17), (1.18), (1.26), (1.27), (1.29) and (4.6) we find for the Δ terms the following expressions

$$\Delta_{xx}^{(n)}(E_0) = \frac{i}{2\,\lambda_\gamma^{(n)}(E_0)}\ , \tag{6.30}$$

$$\Delta_{zz}^{(n)}(E_0) = \frac{i}{2\,\lambda_\gamma^{(n)}(E_0)}\ , \tag{6.31}$$

$$\Delta_{a\gamma}^{(n)} = \frac{B_T^{(n)}}{2M}\ , \tag{6.32}$$

$$\Delta_{aa}^{(n)}(E_0) = 0\ , \tag{6.33}$$

thereby implying that in the n-th generic domain ($1 \leq n \leq N_4$) the mixing matrix (6.4) takes the explicit form

$$\mathcal{M}_n(E_0,\varphi_n) = \begin{pmatrix} \frac{i}{2\,\lambda_\gamma^{(n)}(E_0)} & 0 & \frac{B_T^{(n)}}{2M}\sin\varphi_n \\ 0 & \frac{i}{2\,\lambda_\gamma^{(n)}(E_0)} & \frac{B_T^{(n)}}{2M}\cos\varphi_n \\ \frac{B_T^{(n)}}{2M}\sin\varphi_n & \frac{B_T^{(n)}}{2M}\cos\varphi_n & 0 \end{pmatrix}\ . \tag{6.34}$$

After some tedious algebra, following the discussion in Chapter 4 the transfer matrix associated with the n-th domain is found to be

$$\mathcal{U}_n(E_0,\varphi_n) = e^{i\left(\lambda_1^{(n)}\,L_{\mathrm{dom}}^{(n)}\right)}\,T_1(\varphi_n) + e^{i\left(\lambda_2^{(n)}\,L_{\mathrm{dom}}^{(n)}\right)}\,T_2(\varphi_n) + e^{i\left(\lambda_3^{(n)}\,L_{\mathrm{dom}}^{(n)}\right)}\,T_3(\varphi_n)\ , \tag{6.35}$$

with $T_1(\varphi_n)$, $T_2(\varphi_n)$ and $T_3(\varphi_n)$ given by Eqs. (4.38), (4.39) and (4.40). The transfer matrix describing the beam propagation over region 4 just follows from Eq. (6.5), namely

$$\mathcal{U}_4\left(D, R_{\mathrm{host}}; E_0; \varphi_1, ..., \varphi_{N_4}\right) = \prod_{n=1}^{N_4}\mathcal{U}_n(E_0,\varphi_n)\ , \tag{6.36}$$

where D denotes the distance of PKS 1222+216.

Chapter 7

Spectral energy distribution of PKS 1222+216

Let us now focus our attention on the overall effect of ALPs on the beam propagation from the central region of PKS 1222+216 to the Earth. This amounts to compute the photon survival probability $P_{\gamma\to\gamma}^{\rm ALP}(E)$, which allows us in turn to figure out how the intrinsic VHE blazar emitted spectrum looks like. We will consider separately the cases in which photon-ALP occur or not in extragalactic space.

7.1 No oscillations in extragalactic space

We first suppose that for whatever reason (too small large-scale magnetic fields, too large ALP mass, an so on) the effect of photon-ALP oscillations in extragalactic space is negligible or even absent altogether. In this way, we can concentrate ourselves on the relevance of $\gamma \to a$ and $a \to \gamma$ conversions inside the source and around it.

Now, in the first place we EBL-deabsorb the observed flux $F_{\rm obs}(E_0, z)$ obtained by MAGIC as usual, so as to get the flux at the edge of the host galaxy. Owing to Eqs. (3.1), (3.2) and (3.3) (we substitute $\Phi \to F$ in order not to confound the flux with the angle), we find

$$F_{\rm R_{host}}(E) = \frac{F_{\rm obs}(E_0, z)}{P_{\gamma\to\gamma}^{\rm CP}(E_0, z)} = e^{\tau_\gamma(E_0,z)}\, F_{\rm obs}(E_0, z)\ , \tag{7.1}$$

with $E = E_0(1+z)$, where E_0 denotes the observed energy and $z = 0.432$ for PKS 1222+216. Manifestly, $F_{\rm R_{host}}(E)$ would be the intrinsic emitted flux $F_{\rm em}(E)$ in the absence of BLR absorption. We exhibit $F_{\rm R_{host}}(E)$ in Fig. 7.1 together with the observed *Fermi*/LAT spectrum.

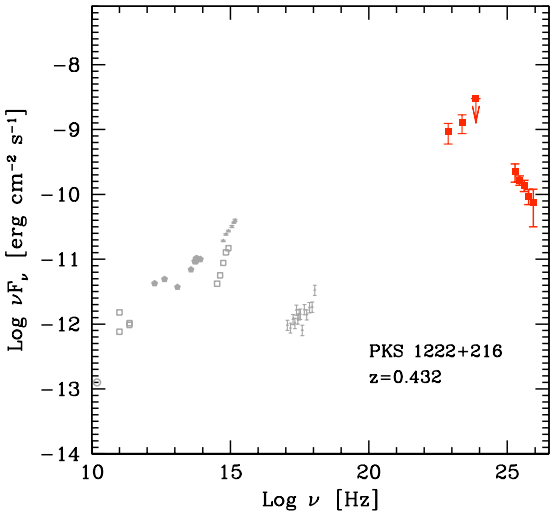

FIGURE 7.1: Red points at high and VHE are the spectrum of PKS 1222+216 recorded by *Fermi*/LAT and the one detected by MAGIC but EBL-deabsorbed according to conventional physics using Eq. (7.1).

Since we know the transfer matrices $\mathcal{U}_1(R_{\rm BLR},0;E)$, $\mathcal{U}_2(R_*,R_{\rm BLR};E)$ and $\mathcal{U}_3\left(R_{\rm host},R_*;E;\phi_1,...,\phi_{N_3}\right)$, we can apply the results of our general discussion presented in Chapter 6.

Recalling the definitions of $\mathcal{U}_{\rm smooth}(E)$ and $\mathcal{U}_{\rm random}\left(E;\psi_1,...,\psi_N\right)$ just after Eq. (6.5), we presently have

$$\mathcal{U}_{\rm smooth}(E)=\mathcal{U}_2(R_*,R_{\rm BLR};E)\,\mathcal{U}_1(R_{\rm BLR},0;E)\ , \tag{7.2}$$

$$\mathcal{U}_{\rm random}\left(E;\phi_1,...,\phi_{N_3}\right)=\mathcal{U}_3\left(R_{\rm host},R_*;E;\phi_1,...,\phi_{N_3}\right)\ , \tag{7.3}$$

in terms of which we can use Eq. (6.6) to get the explicit expression of Eq. (6.7) and ultimately of Eq. (6.8), namely

$$\begin{aligned}P^{\rm ALP}_{\gamma\to\gamma}(R_{\rm host},0;E)=&\left\langle P_{\rho_{\rm unpol}\to\rho_x}\left(R_{\rm host},0;E;\phi_1,...,\phi_{N_3}\right)\right\rangle_{\phi_1,...,\phi_{N_3}}+\\&+\left\langle P_{\rho_{\rm unpol}\to\rho_z}\left(R_{\rm host},0;E;\phi_1,...,\phi_{N_3}\right)\right\rangle_{\phi_1,...,\phi_{N_3}}\ .\end{aligned} \tag{7.4}$$

Therefore, in terms of $F_{\rm R_{host}}(E)$ as dictated by Eq. (7.1), according to our model $F_{\rm em}(E)$ is given by

$$F_{\rm em}(E)=\frac{F_{\rm R_{host}}(E)}{P^{\rm ALP}_{\gamma\to\gamma}\left(R_{\rm host},0;E\right)}\ . \tag{7.5}$$

Manifestly, what we have to do at this stage is to make a choice for M (consistent with the bound $M>1.14\cdot10^{10}$ GeV set by CAST), and even though we have fixed the magnetic field inside the source before the BLR at $B=0.2$ G this value is uncertain to some extent.

Since the principal motivation of the present analysis is to explain why a substantial fraction of VHE photons escape from the BLR, we feel that a deeper insight into the suitable values of M and B can be gained by addressing the effective optical depth $\tau_{\rm eff}(E)$ concerning the photon propagation from the central region to the edge of the host galaxy, which is defined in terms of $P^{\rm ALP}_{\gamma\to\gamma}\left(R_{\rm host}, 0; E\right)$ as

$$P^{\rm ALP}_{\gamma\to\gamma}\left(R_{\rm host}, 0; E\right) = e^{-\tau_{\rm eff}(E)} \ . \tag{7.6}$$

After some attempts, we have been led to select for definiteness three benchmark cases: $(B = 0.2\,{\rm G}, M = 7\cdot 10^{10}\,{\rm GeV})$, $(B = 0.4\,{\rm G}, M = 1.5\cdot 10^{11}\,{\rm GeV})$ and $(B = 2\,{\rm G}, M = 4\cdot 10^{11}\,{\rm GeV})$. We report the corresponding curves for $\tau_{\rm eff}(E)$ in Fig. 6.1, where the red solid line corresponds to $(B = 0.2\,{\rm G}, M = 7\cdot 10^{10}\,{\rm GeV})$, the green short-dashed line to $(B = 0.4\,{\rm G}, M = 1.5\cdot 10^{11}\,{\rm GeV})$ and the violet dashed-dotted line to $(B = 2\,{\rm G}, M = 4\cdot 10^{11}\,{\rm GeV})$, while the blue long-dashed line corresponds to conventional physics (as in [141]). The effect of the photon-ALP oscillations on the beam propagation can readily be appreciated. Indeed, photon-ALP oscillations lead to a drastic reduction of the optical depth in the optically thick range. Our best case in this respect is $(B = 0.2\,{\rm G}, M = 7\cdot 10^{10}\,{\rm GeV})$, where in the MAGIC band the effective optical depth is almost constant at about $\tau_{\rm eff} \simeq 4$, corresponding to a survival probability of about 2%. On the contrary, in the optically thin region below $\sim 30\,{\rm GeV}$ the optical depth in the presence of photon-ALP oscillations is *larger* than the standard one, which instead goes rapidly to zero below 10 GeV. This behaviour can be simply understood: A fraction around 10% of the γ rays originally emitted by the source and converted into ALPs do not reconvert back to photons, therefore leading to a reduction of the observed photon flux.

Still, our goal is not merely to explain why MAGIC has observed PKS 1222+216 but also to find a realistic and physically motivated SED that fits both *Fermi*/LAT and MAGIC spectra. So, it is not enough that photon-ALP oscillations allow for a large photon fraction to avoid the BLR absorption but they also have to give rise to a SED with the above features. In order to settle this issue we find it illuminating to proceed as follows. As we said, our source has been observed by *Fermi*/LAT in the energy range $0.3 - 3\,{\rm GeV}$ and by MAGIC in the band $70 - 400\,{\rm GeV}$. Therefore we focus our attention on the energies $E = 1\,{\rm GeV}$ and $E = 300\,{\rm GeV}$ as representative of the two kinds of measurements. Hence it is useful to define the ratio

$$\Pi \equiv \log\left(\frac{P^{\rm ALP}_{\gamma\to\gamma}\left(R_{\rm host}, 0; 1\,{\rm GeV}\right)}{P^{\rm ALP}_{\gamma\to\gamma}\left(R_{\rm host}, 0; 300\,{\rm GeV}\right)}\right) \ . \tag{7.7}$$

A glance to Fig. 7.1 shows that in order to have an acceptable shape for the emitted VHE component of the SED we need to have Π as low as possible. Moreover, since the photon-ALP conversion is in any case small in the *Fermi*/LAT energy range, a small

Π would imply a huge correction of the flux in the MAGIC spectrum. Therefore, Π allows us to have an effective control of the effects of the photon-ALP oscillations on the corrected SED. We show in Fig. 7.2 Π as a function of B and M in order to find out how strongly Π depends on these two parameters. Incidentally, the oscillatory behavior displayed by Π in Fig. 7.2 arises from $P_{\gamma\to\gamma}(1\,\mathrm{GeV})$ which is in the strong-mixing and absorption-free regime, even though outside R_{BLR} **B** first decreases and then has a random domain-like structure. The oscillatory behavior makes the derived probability a rather complex function of the two parameters. As a general trend, low values of Π are associated with low B and M values (lower left corner). On the contrary, large B and M (upper right corner) result in large Π. Our three benchmark cases are represented by the three white blobs in Fig. 7.2.

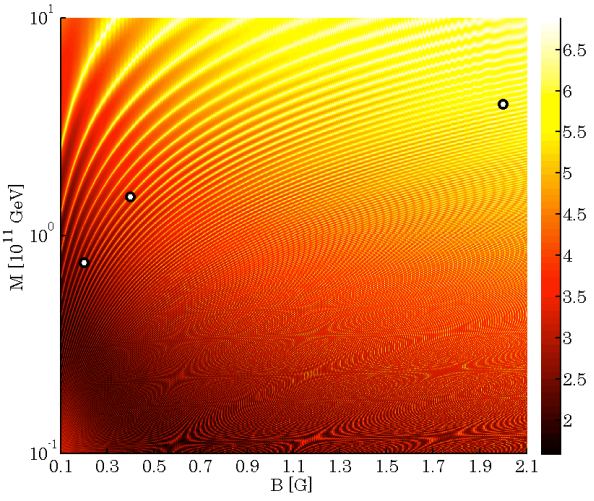

FIGURE 7.2: The quantity Π as a function of B and M. The three white blobs correspond to our benchmark cases.

Quite remarkably, we see that the trend found in Fig. 6.1 is reproduced in Fig. 7.2, in the sense to a progressively increasing $\tau(E)$ there correspond higher values of Π. Thus, we are led to the conclusion that the case ($B = 0.2\,\mathrm{G}, M = 7\cdot10^{10}\,\mathrm{GeV}$) is expected to have also a most realistic SED. Besides, also the cases ($B = 0.4\,\mathrm{G}, M = 1.5\cdot10^{11}\,\mathrm{GeV}$ and $B = 2\,\mathrm{G}, M = 4\cdot10^{11}\,\mathrm{GeV}$ look promising as far as the shape of the SED is concerned even if the corresponding behavior of $\tau_{\mathrm{eff}}(E)$ looks rather high especially at the highest energies, thereby implying a rather hard intrinsic spectrum. We shall come back to a thorough discussion of the SED in Sec. 7.3.

Let us next explicitly address the impact of our model for the emitted spectrum of PKS 1222+216, which is shown in Figs. 7.3 and 7.4 for the cases ($B = 0.2\,\mathrm{G}, M = 7\cdot10^{10}\,\mathrm{GeV}$) and ($B = 0.4\,\mathrm{G}, M = 1.5\cdot10^{11}\,\mathrm{GeV}$), respectively, where the EBL-deabsorbed MAGIC points according to Eq. (7.1) and the observed *Fermi*/LAT points are reported in red whereas the black points are correspondingly obtained by means of Eq. (7.5). We do

not report the Figure pertaining to the case ($B = 2\,\mathrm{G}, M = 4 \cdot 10^{11}\,\mathrm{GeV}$) because the γ-ray peak would give an unacceptably large value for νF_ν.

7.2 Oscillations in extragalactic space

We now consider the possibility that photon-ALP oscillations efficiently occur also in extragalactic space, which is possible only within the strong-mixing regime so that condition (6.29) has to be met. Let us consider first the case ($B = 0.2\,\mathrm{G}, M = 7 \cdot 10^{10}\,\mathrm{GeV}$), assuming a domain-like large-scale magnetic field with strength $B = 0.7\,\mathrm{nG}$ and coherence length $L_{\mathrm{dom}} = 4\,\mathrm{Mpc}$, a situation corresponding to the most favorable case considered within the DARMA scenario (see Chapters 4 and 5).

Accordingly, condition (6.29) is satisfied for $m < 1.7 \cdot 10^{-10}\,\mathrm{eV}$, which is consistent with the upper bound found above.

The form of $\mathcal{U}_{\mathrm{smooth}}(E)$ as given by Eq. (7.2) remains unchanged, but that of $\mathcal{U}_{\mathrm{random}}\,(E; \psi_1, ..., \psi_N)$ now becomes

$$\mathcal{U}_{\mathrm{random}}\,(E; \phi_1, ..., \phi_{N_3}; \varphi_1, ..., \varphi_{N_4}) = \mathcal{U}_4\,(D, R_{\mathrm{host}}; E_0; \varphi_1, ..., \varphi_{N_4})\;\mathcal{U}_3\,(R_{\mathrm{host}}, R_*; E; \phi_1, ..., \phi_{N_3})\;, \tag{7.8}$$

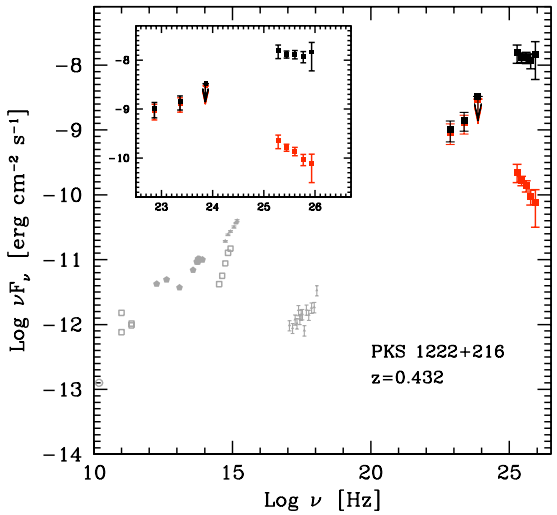

FIGURE 7.3: Red points at high energy and VHE are the spectrum of PKS 1222+216 recorded by *Fermi*/LAT and the one detected by MAGIC but EBL-deabsorbed according to conventional physics using Eq. (7.1). The black points represent the same data once further corrected for the photon-ALP oscillation effect employing Eq. (7.5) in the case ($B = 0.2\,\mathrm{G}, M = 7 \cdot 10^{10}\,\mathrm{GeV}$). The gray data points below $10^{20}\,\mathrm{Hz}$ are irrelevant for the present discussion (details can be found in [142].

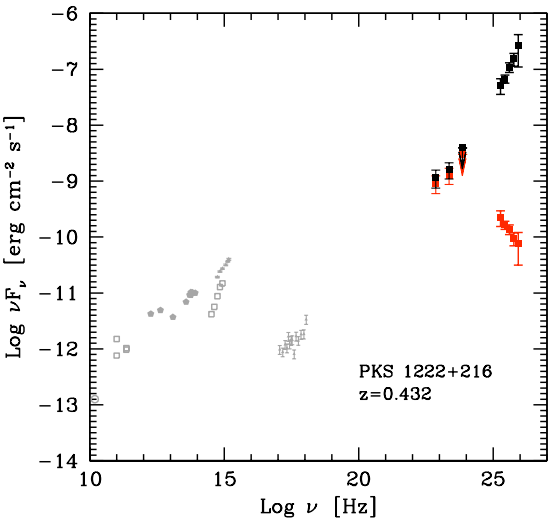

FIGURE 7.4: Red points at high energy and VHE are the spectrum of PKS 1222+216 recorded by *Fermi*/LAT and the one detected by MAGIC but EBL-deabsorbed according to conventional physics using Eq. (7.1). The black points represent the same data once further corrected for the photon-ALP oscillation effect employing Eq. (7.5) in the case ($B = 0.4\,\mathrm{G}, M = 1.5 \cdot 10^{11}\,\mathrm{GeV}$). The gray data points below $10^{20}\,\mathrm{Hz}$ are irrelevant for the present discussion (details can be found in [142].

with $E = E_0(1+z)$. Just as before, we use these equations to find the explicit expression of Eq. (6.7) and finally of Eq. (6.8), which presently reads

$$P^{\mathrm{ALP}}_{\gamma\to\gamma}(D,0;E) = \left\langle P_{\rho_{\mathrm{unpol}}\to\rho_x}\left(D,0;E;\phi_1,...,\phi_{N_3};\varphi_1,...,\varphi_{N_4}\right)\right\rangle_{\phi_1,...,\phi_{N_3};\varphi_1,...,\varphi_{N_4}} + \quad (7.9)$$
$$+ \left\langle P_{\rho_{\mathrm{unpol}}\to\rho_z}\left(D,0;E;\phi_1,...,\phi_{N_3};\varphi_1,...,\varphi_{N_4}\right)\right\rangle_{\phi_1,...,\phi_{N_3};\varphi_1,...,\varphi_{N_4}} .$$

However, at variance with the previous treatment, the intrinsic flux emitted by the source – which is represented in Fig. 7.5 by black dots – is obtained directly from the one *observed* by MAGIC and represented in Fig. 7.5 by open red squares through the relation

$$F_{\mathrm{em}}(E) = \frac{F_{\mathrm{obs}}(E_0,z)}{P^{\mathrm{ALP}}_{\gamma\to\gamma}(D,0;E)} . \quad (7.10)$$

The comparison of Figs. 7.3 and 7.5 reveals that the inclusion of the photon-ALP oscillations in extragalactic space does not lead to a dramatic effect. Although the derived intrinsic spectrum is softer, the peak energy and the luminosity of the high energy peak are roughly the same in either case.

A very similar situation concerns the cases ($B = 0.4\,\mathrm{G}, M = 1.5 \cdot 10^{11}\,\mathrm{GeV}$) and ($B = 2\,\mathrm{G}, M = 4 \cdot 10^{11}\,\mathrm{GeV}$), and so we do not find it useful to report also these results in a Figure (in particular photon-ALP oscillations in extragalactic space do not save the case ($B = 2\,\mathrm{G}, M = 4 \cdot 10^{11}\,\mathrm{GeV}$) so that it remains ruled out).

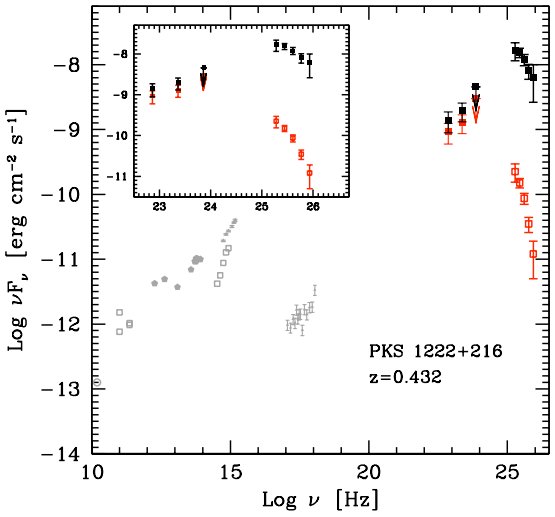

FIGURE 7.5: Red points at high energy and open red squares at VHE are the spectrum of PKS 1222+216 recorded by *Fermi*/LAT and the one *observed* by MAGIC and not EBL-deabsorbed. The black points represent the same data once further corrected for the photon-ALP oscillation effect in the case ($B = 0.2\,\mathrm{G}, M = 7 \cdot 10^{10}\,\mathrm{GeV}$) including also photon-ALP oscillations in extragalactic space, where a magnetic field with strength $B = 0.7$ nG is supposed to exist. So, they are obtained from the red points and the open red squares by means of Eq. (7.10). The gray data points below 10^{20} Hz are irrelevant for the present discussion (details can be found in [142]).

We conclude that in the context of our model for PKS 1222+216 photon-ALP oscillations in the extragalactic space are allowed but not compelling.

7.3 Spectral energy distribution (SED)

Our final step consists in showing that the emitted spectra in the whole γ-ray band obtained in Secs. 7.1 and 7.2 indeed lie on the SED of a realistic and physically motivated blazar model, thereby closing the circle. We stress that this problem does not have a unique solution, in the sense that it is quite conceivable that various leptonic and even hadronic models can work. Nevertheless, from a methodological point of view the present work would be incomplete without the presentation of an explicit emission model.

As already remarked, in an attempt to explain the observed MAGIC emission of PKS 1222+216 within conventional physics a particular model has been put forward [142], which consists in a larger blob located *inside* the source responsible for the emission from IR to X-rays and a much smaller very compact blob accounting for the rapidly varying γ-ray emission detected by MAGIC. In order to avoid the BLR photon absorption, the smaller blob has been located *well outside* the BLR, namely at a large distance from the centre (we refer to the original paper [142] for a full discussion of the problems

and a detailed description of this model). Hence it looks natural to inquire whether a similar two-blob model can produce the SED needed in the present context – namely to fit the black points in Figs. 7.3, 7.4 and 7.5 – with the key difference that now the smaller blob *lies close to the central engine*. Remarkably, this scenario works provided that the following parameters are chosen. Briefly, each region is specified by its size r, magnetic field B, bulk Lorentz factor Γ, electron normalization K, minimum, break and maximum Lorentz factors $\gamma_{\rm min}$, $\gamma_{\rm b}$, $\gamma_{\rm max}$ and slopes n_1, n_2. The electrons radiate through synchrotron and inverse Compton processes (considering both the internally produced synchrotron radiation and the external radiation of the BLR). For the larger region we use the same parameters of the original model while for the compact γ-ray blob region we have:

- Case ($B = 0.2\,{\rm G}, M = 7{\cdot}10^{10}\,{\rm GeV}$) without photon-ALP oscillations in extragalactic space (see Fig. 7.6) : $r = 2.2 \cdot 10^{14}$ cm, $B = 0.008\,{\rm G}$, $\Gamma = 17.5$, $K = 6.2 \cdot 10^{9}$, $\gamma_{\rm min} = 4 \cdot 10^{3}$, $\gamma_{\rm b} = 2.5 \cdot 10^{5}$, $\gamma_{\rm max} = 4.9 \cdot 10^{5}$ and slopes $n_1 = 2.1$, $n_2 = 3.5$;
- Case ($B = 0.4\,{\rm G}, M = 1.5 \cdot 10^{11}\,{\rm GeV}$) without photon-ALP oscillations in extragalactic space (see Fig. 7.7): $r = 2.2{\cdot}10^{14}\,{\rm cm}$, $B = 0.0004\,{\rm G}$, $\Gamma = 17.5$, $K = 2{\cdot}10^{11}$, $\gamma_{\rm min} = 5 \cdot 10^{4}$, $\gamma_{\rm b} = 2.5 \cdot 10^{6}$, $\gamma_{\rm max} = 4.9 \cdot 10^{6}$ and slopes $n_1 = 2.1$, $n_2 = 3.2$.
- Case ($B = 0.2\,{\rm G}, M = 7 \cdot 10^{10}\,{\rm GeV}$) with photon-ALP oscillations in extragalactic space (see Fig. 7.8): $r = 2.2 \cdot 10^{14}$ cm, $B = 0.008\,{\rm G}$, $\Gamma = 17.5$, $K = 6.7 \cdot 10^{9}$, $\gamma_{\rm min} = 3 \cdot 10^{3}$, $\gamma_{\rm b} = 1.2 \cdot 10^{5}$, $\gamma_{\rm max} = 4.9 \cdot 10^{5}$ and slopes $n_1 = 2.1$, $n_2 = 3.5$.

Also here the relative position of the two regions is not relevant for the emission properties.

The resulting SED is exhibited in Figs. 7.6, 7.7 for the cases ($B = 0.2\,{\rm G}, M = 7 \cdot 10^{10}\,{\rm GeV}$) and ($B = 0.4\,{\rm G}, M = 1.5 \cdot 10^{11}\,{\rm GeV}$) without photon-ALP oscillations in extragalactic space, respectively, and in Fig. 7.8 for the case ($B = 0.2\,{\rm G}, M = 7 \cdot 10^{10}\,{\rm GeV}$) with photon-ALP oscillations in extragalactic space.

We find that an optimal choice to explain both *Fermi*/LAT and MAGIC observations corresponds to the case ($B = 0.2\,{\rm G}, M = 7 \cdot 10^{10}\,{\rm GeV}$) without photon-ALP oscillations in extragalactic space, for which we obtain through Eq. (7.5) the black points shown in Fig. 7.6. This result looks completely satisfactory, with the *Fermi*/LAT and MAGIC data well described by a high-energy bump peaking around 50 GeV and a height $\nu F_\nu \simeq 10^{-8}\,{\rm erg\,cm^{-2}\,s^{-1}}$ corresponding to a luminosity $L_\gamma = 6 \cdot 10^{48}\,{\rm erg\,s^{-1}}$. On the other end, the case ($B = 0.4\,{\rm G}, M = 1.5 \cdot 10^{11}\,{\rm GeV}$) looks satisfactory as far as the shape of the SED is concerned with the high-energy peak close to 500 GeV as it can be seen from Fig. 7.7, but the implied luminosity of the γ-ray emission approaches $L_\gamma = 10^{51}$ erg s^{-1}

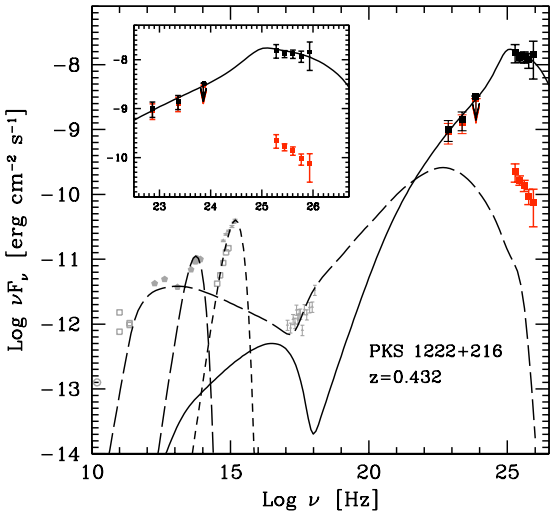

FIGURE 7.6: Same as Fig. 7.3 for the case ($B = 0.2\,\mathrm{G}, M = 7 \cdot 10^{10}\,\mathrm{GeV}$) without photon-ALP oscillations in extragalactic space, but in addition the dashed and solid curves show the SED resulting from the considered two blobs which account for the γ-ray emission at high energy and VHE, respectively.

which appears unrealistic, since it is about 100 times larger than that of the most γ-ray bright blazars (see e.g. [164]). So, this result is unsatisfactory. We recall that the case ($B = 2\,\mathrm{G}, M = 4 \cdot 10^{11}\,\mathrm{GeV}$) has already been ruled out due to the by far too high γ-ray peak. Finally, the inclusion of photon-ALP oscillations in extragalactic space makes the emitted spectrum slightly softer as it is evident from Fig. 7.8, but the situation still remains completely satisfactory.

In conclusion, we find it a highly nontrivial circumstance that the benchmark case ($B = 0.2\,\mathrm{G}$ and $M = 7 \cdot 10^{10}\,\mathrm{GeV}$) turns out to be the best one concerning both the efficiency for VHE photons to escape from the BLR and the SED of the particular two-blob model that we have adopted. Thus, it turns out to be by far our best option.

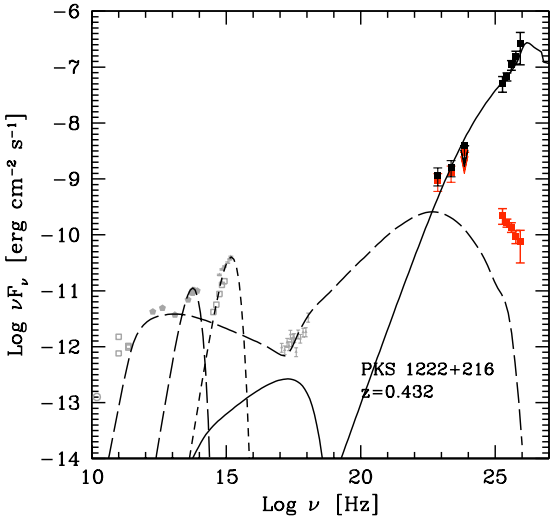

FIGURE 7.7: Same as Fig. 7.4 for the case ($B = 0.4\,\mathrm{G}, M = 1.5 \cdot 10^{11}\,\mathrm{GeV}$) without photon-ALP oscillations in extragalactic space, but in addition the dashed and solid curves show the SED resulting from the considered two blobs which account for the γ-ray emission at high energy and VHE, respectively.

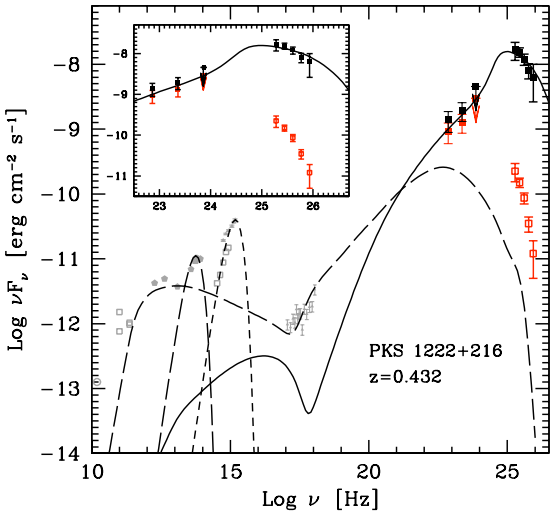

FIGURE 7.8: Same as Fig. 7.5 for the case ($B = 0.2\,\mathrm{G}, M = 7 \cdot 10^{10}\,\mathrm{GeV}$) with photon-ALP oscillations in extragalactic space, but in addition the dashed and solid curves show the SED resulting from the considered two blobs which account for the γ-ray emission at high energy and VHE, respectively.

Chapter 8

ALPs from irregularities in γ ray source spectra?

Recently, Wouters and Brun (WB) [156] proposed a method to detect photon-ALP oscillations taking place in random extragalactic magnetic fields when VHE observations of blazars are performed. Actually, such a method is not new, even though it was introduced in a slightly different context [157].

As discussed in Chapter 4 Sec. 4.2, the extra-galactic magnetic field $\mathbf{B}$ is supposed to have a domain-like structure, with its direction randomly changing from one domain to the next and strength either equal in all domains or with a Kolmogorov spectrum. For simplicity, we shall restrict our attention throughout this thesis to the first option. Manifestly, in such a situation the propagation process of the photon/ALP beam from the source to us becomes a stochastic process. While it is obvious that the beam follows a single trajectory at once joining the source to us, the exact behaviour of the beam cannot be predicted but only its mean properties can be evaluated, and this requires an average over a very large number of possible trajectories followed by the beam (realizations of the stochastic process in question). Among these properties, the simplest ones are the average photon survival probability [24, 25] (see also Chapters 4 and 5) and its variance [26].

The main point made by WB is that in a pretty small range about the energy $E_{\rm thr}$ (E_* with our definition, see Chapter 1 Sec. 1.5) that marks the transition from the weak to the strong mixing regime the photon survival probability along every single trajectory that the beam can follow exhibits fluctuations, which show up in the observed energy spectrum and are claimed to be an *observable* signature of the existence of photon-ALP oscillations.

WB do not state explicitly their assumptions, neither they provide any information about the way they evaluate the photon survival probability along a single trajectory. Do they consider a polarized beam or an unpolarized one? As we will see below, this point is of crucial importance because it changes drastically the result, but nothing is said about that by WB.

We explicitly show that they consider an initially *polarized* beam, whereas a physically correct treatment would demand the beam to be initially *unpolarized*. As a consequence, the result of WB changes *substantially*.

In the following sections we recall some equations of Chapters 1 and 4 and we rewrite them since we uniform to WB conventions and for the convenience of the reader – we send the reader to the above-mentioned Chapters for a complete discussion.

8.1 Setting the stage

Specifically, writing the photon-ALP Lagrangian as

$$\mathcal{L}_{a\gamma} = -\frac{1}{4}\, g\, F_{\mu\nu}\tilde{F}^{\mu\nu} a = g\, \mathbf{E}\cdot\mathbf{B}\, a \ , \tag{8.1}$$

the definition of $E_{\rm thr}$ is

$$E_{\rm thr} \equiv \frac{|m_a^2 - \omega_{\rm pl}^2|}{2g\, B_T} \ , \tag{8.2}$$

where m_a is the ALP mass, $\omega_{\rm pl}$ is the plasma frequency and $\mathbf{B}_T$ is the component of the magnetic field transverse to the beam (WB write $B\sin\theta$ in place of B_T), which is supposed to be monochromatic of energy E.

A very remarkable fact is that under the assumption $E \gg m_a$ the beam propagation equation in a generic magnetic domain n takes a Schrödinger-like form in the variable z along the beam [15], to wit

$$\left(i\frac{d}{dz} + E + \mathcal{M}(\phi_n)\right)\psi_n(z) = 0 \tag{8.3}$$

with the wave function of the form

$$\psi_n(z) \equiv \begin{pmatrix} A_{1,n}(z) \\ A_{2,n}(z) \\ a_n(z) \end{pmatrix} \ , \tag{8.4}$$

where $A_{1,n}(z)$ and $A_{2,n}(z)$ denote the photon amplitudes with polarization (electric field) along the x- and y-axis, respectively, while $a_n(z)$ is the amplitude associated with the

ALP in the n-th domain. Further, we let ϕ_n be the angle between $\mathbf{B}_T$ and the fixed $\hat{\mathbf{x}}$ direction – equal for all domains – in the n-th domain. In the general case in which the EBL is important a fraction of photons gets absorbed through the process $\gamma\gamma \to e^+e^-$ and the mixing matrix $\mathcal{M}(\phi_n)$ reads

$$\mathcal{M}(\phi_n) = \begin{pmatrix} \Delta_{11} + i\,\Delta_{\rm abs} & 0 & \Delta_B \cos\phi_n \\ 0 & \Delta_{22} + i\,\Delta_{\rm abs} & \Delta_B \sin\phi_n \\ \Delta_B \cos\phi_n & \Delta_B \sin\phi_n & \Delta_a \end{pmatrix} . \tag{8.5}$$

The various delta terms are defined as follows: $\Delta_{11} = \Delta_{22} \equiv -\,\omega_{\rm pl}^2/2E$, $\Delta_a \equiv -\,m_a^2/2E$, $\Delta_B \equiv g\,B_T/2$ and $\Delta_{\rm abs} \equiv 1/2\lambda$ with λ being the photon means free path for $\gamma\gamma \to e^+e^-$ scattering [21].

Hence, we see that inside every domain the considered beam is formally described as a three-level unstable non-relativistic quantum system.

In the simplest case of a single domain with $\mathbf{B}$ homogeneous, $\omega_{\rm pl} = 0$, $\lambda = \infty$ and $\phi_n = \pi/2$ the $\gamma \to a$ conversion probability is

$$P_{\gamma\to a} = \frac{\alpha\Delta_B^2}{\Delta_{\rm osc}^2} \sin^2\left(\frac{\Delta_{\rm osc}\, z}{2}\right) , \tag{8.6}$$

having set $\Delta_{\rm osc}^2 \equiv \Delta_a^2 + 4\Delta_B^2$. For a photon beam linearly polarized along $\mathbf{B}_T$ we have $\alpha = 4$, for a linear polarization perpendicular to $\mathbf{B}_T$ we get $\alpha = 0$, whereas for an unpolarized beam it turns out that $\alpha = 2$. Moreover, Eq. (8.6) shows that for E sufficiently larger than $E_{\rm thr}$ $P_{\gamma\to a}$ becomes maximal and energy-independent, which is indeed the strong mixing regime.

So, we see that the question whether the beam is polarized or not is of crucial importance because it *changes* drastically the conclusion.

8.2 Probabilities for polarized and unpolarized beams

Our main criticism indeed concerns the beam polarization. We want to emphasize that the beam polarization is *unknown*. A reason is that it is not clear whether the emission mechanism is leptonic or hadronic, and for instance in the pure synchro-self-Compton model (without external electrons) the polarization of the emitted photons decreases both with the electron energy and the viewing angle, so that it is vanishingly small for the TeV BL Lacs [158]. Another reason is that the polarization cannot be measured in the γ-ray band. So, in the lack of any information about the beam polarization the only sensible option is to suppose that the beam is initially *unpolarized*.

Hence, according to quantum mechanics in the n-th domain the beam *must* be described by a polarization density matrix, namely

$$\rho_n(z) = \begin{pmatrix} A_{n,1}(z) \\ A_{n,2}(z) \\ a_n(z) \end{pmatrix} \otimes \begin{pmatrix} A_{n,1}(z) & A_{n,2}(z) & a_n(z) \end{pmatrix}^* \tag{8.7}$$

rather than by a wave function $\psi_n(z)$ like the one in Eq. (8.4). Moreover, the analogy with non-relativistic quantum mechanics entails that $\rho_n(z)$ obeys the Von Neumann-like equation

$$i\frac{d\rho_n}{dz} = \rho_n\,\mathcal{M}^\dagger(\phi_n) - \mathcal{M}(\phi_n)\,\rho_n \ . \tag{8.8}$$

associated with Eq. (8.3) (see Chapters 4 and 5). Observe that even though the hamiltonian is not self-adjoint, we nevertheless have

$$\rho_n(z) = \mathcal{U}_n(z,0)\,\rho_n(0)\,\mathcal{U}_n^\dagger(z,0) \ , \tag{8.9}$$

where $\mathcal{U}_n(z,0)$ is the transfer matrix, namely the solution of Eq. (8.3) subject to the initial condition $\mathcal{U}_n(0,0) = 1$. Assuming that the number of domains is N, the transfer matrix describing the whole propagation process is

$$\mathcal{U}(z,0) = \prod_{n=1}^{N} \mathcal{U}_n(z_n, z_{n-1}) \tag{8.10}$$

with $z_0 = 0$ and $z_N = z$, and the photon survival probability along a *single* realization of the *unpolarized* beam corresponding to $\phi_1, \phi_2, ..., \phi_N$ is given by (see Chapters 4 and 5)

$$P_{\gamma\to\gamma}^{\rm unpolarized}(z,0;\phi_1,\phi_2,...,\phi_N) = \sum_{i=1,2} {\rm Tr}\Big(\rho_i\,\mathcal{U}(z,0)\,\rho_{\rm unpol}\,\mathcal{U}^\dagger(z,0)\Big) \ , \tag{8.11}$$

while the analogous probability in the case of a *polarized* beam along the x-axis reads [1]

$$P_{\gamma\to\gamma}^{\rm polarized}(z,0;\phi_1,\phi_2,...,\phi_N) = \sum_{i=1,2} {\rm Tr}\Big(\rho_i\,\mathcal{U}(z,0)\,\rho_1\,\mathcal{U}^\dagger(z,0)\Big) \ , \tag{8.12}$$

where

$$\rho_1 = \begin{pmatrix} 1 & 0 & 0 \\ 0 & 0 & 0 \\ 0 & 0 & 0 \end{pmatrix} \ , \quad \rho_2 = \begin{pmatrix} 0 & 0 & 0 \\ 0 & 1 & 0 \\ 0 & 0 & 0 \end{pmatrix} \ , \quad \rho_{\rm unpol} = \frac{1}{2}\begin{pmatrix} 1 & 0 & 0 \\ 0 & 1 & 0 \\ 0 & 0 & 0 \end{pmatrix} \ . \tag{8.13}$$

[1] Needless to say, a similar result arises for a polarized beam along the y direction.

8.3 A particular case

Let us consider first the case in which EBL absorption is absent, so that the hamiltonian is self-adjoint and the transfer matrix must be unitary. Since we cannot know the specific trajectory followed by the beam during its propagation, this has to be true for *any* trajectory. Now, by inserting Eqs. (8.13) into Eq. (8.11) and working out the resulting expression we find

$$P_{\gamma\to\gamma}(z,0;\phi_1,\phi_2,...,\phi_N)=\frac{1}{2}\Big(|u_{11}|^2+|u_{12}|^2+|u_{21}|^2+|u_{22}|^2\Big)\ . \tag{8.14}$$

But owing to the unitarity of $\mathcal{U}$, the condition $\mathcal{U}\,\mathcal{U}^\dagger=1$ implies

$$|u_{11}|^2+|u_{12}|^2+|u_{13}|^2=1\ ,\ \ |u_{21}|^2+|u_{22}|^2+|u_{23}|^2=1\ ,\ \ |u_{31}|^2+|u_{32}|^2+|u_{33}|^2=1\ , \tag{8.15}$$

whereas the condition $\mathcal{U}^\dagger\mathcal{U}=1$ entails

$$|u_{11}|^2+|u_{21}|^2+|u_{31}|^2=1\ ,\ \ |u_{12}|^2+|u_{22}|^2+|u_{32}|^2=1\ ,\ \ |u_{13}|^2+|u_{23}|^2+|u_{33}|^2=1\ , \tag{8.16}$$

which upon insertion into Eq. (8.14) yield

$$P_{\gamma\to\gamma}(z,0;\phi_1,\phi_2,...,\phi_N)=\frac{1}{2}+\frac{1}{2}\,|u_{33}|^2\geq\frac{1}{2}\ . \tag{8.17}$$

This conclusion is in blatant contradiction with the result of WB reported in the upper panel of their Fig. 2, and so we infer that WB consider an initially *polarized* beam.

8.4 Photon survival probability

From now on we address the case in which the EBL absorption is present.

As a benchmark for comparison, we start by dealing with the photon survival probability along a single randomly chosen trajectory of the considered stochastic process in the case of an initially *polarized* beam. For the sake of comparison with WB, we take the same values of the parameters adopted by them, namely a source at redshift $z_s=0.1$ (not to be confused with the coordinate along the beam), the magnetic field strength $B=1\,\mathrm{nG}$, the size of a magnetic domain equal to $1\,\mathrm{Mpc}$, the photo-ALP coupling $g=8\cdot10^{-11}\,\mathrm{GeV}^{-1}$ and the ALP mass $m_a=2\,\mathrm{neV}$. Using Eq. (8.12), we find the result plotted in the upper panel of Fig. 8.1. Manifestly the upper panel of Fig. 8.1 is qualitatively identical to the lower panel of Fig. 2 of WB. This circumstance confirms that WB indeed consider an initially *polarized* beam.

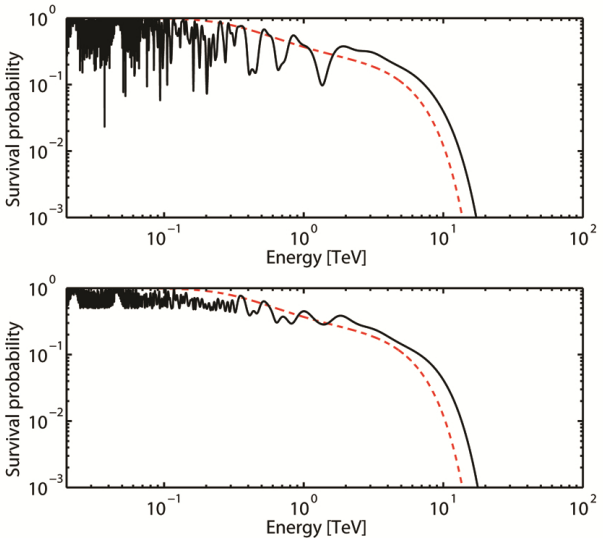

FIGURE 8.1: The upper panel corresponds to the case of an initially *polarized* beam, while the lower panel corresponds to the case of an initially *unpolarized* beam. The solid black line represents the photon survival probability along a single randomly chosen trajectory followed by the beam in the presence of ALPs for a source at $z_s = 0.1$, using $B = 1\,\mathrm{nG}$, the size of a magnetic domain equal to $1\,\mathrm{Mpc}$, $g = 8 \cdot 10^{-11}\,\mathrm{GeV}^{-1}$ and $m_a = 2\,\mathrm{neV}$. The dashed red line represents the same quantity with ALPs discarded (conventional physics).

Let us next address the analogous probability – for the same values of the parameters – in the case of an initially *unpolarized* beam, which is the physically correct case. Employing now Eq. (8.11), the corresponding result is exhibited in the lower panel of Fig. 8.1.

Evidently the size of the fluctuations is *drastically reduced* in the unpolarized case with respect to the polarized one.

8.5 Observed flux

As a further step, we follow as closely as possible the same lines of Sec. III of WB. Explicitly, as a first step we generate photons by a Monte Carlo method according to a log-parabola probability distribution – shape of the initial spectrum – with an integrated flux in the TeV band at the Crab level. We simulate an observation of 50 h with an effective area of $10^5\,\mathrm{m}^2$, which amounts to about 100000 photons. We suppose that 10 observations of 5 h each are performed, so that everyone collects about 10000 photons. Assuming that the observations are performed in the energy band $5 \cdot 10^2\,\mathrm{GeV} - 7\,\mathrm{TeV}$, we divide this range into 33 energy bins. At this point, we bin the 10 observations, computing both the mean and the variance pertaining to the 10 observations for each of the 33 energy bins. Next, we perform a log-log best fit of the binned points and we

evaluate the fit residuals. Finally, we compute the variance of the fit residuals. All this is obtained by averaging over 5000 realizations, as in the case of WB.

We proceed in parallel with the discussion in Sec. 8.4, which amounts to implement such a strategy first in the case of an initially *polarized* beam and next in the case of an initially *unpolarized* one. We show in the upper panel of Fig. 8.2 the unbinned and binned spectra in the case of a *polarized* beam when EBL absorption and photon-ALP oscillations are considered. The model parameters are the same as before. The lower panel of Fig. 8.2 represents the case of an *unpolarized* beam. In either case, the solid black line represents the unbinned spectrum and the red lines the binned spectrum in the situation of photon-ALP oscillations. The dashed black line corresponds to the best fit to the bins (regardless of the underlying physics).

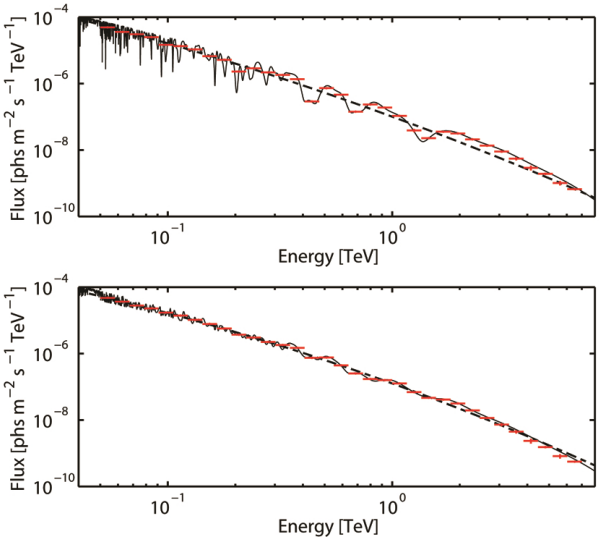

FIGURE 8.2: The upper panel corresponds to the case of a *polarized* beam, while the lower panel corresponds to the case of an *unpolarized* beam. The solid black line represents the unbinned spectrum and the broken red line the binned spectrum, both in the case of photon-ALP oscillations. The dashed black line corresponds to the best fit to the bins (regardless of the underlying physics).

As before, the difference between the upper panel and the lower panel of Fig. 8.2 is great: while in the polarized case the amplitude of the oscillations is large, in the unpolarized one their size gets drastically reduced. The actual physical difference between the two cases is confirmed by the distribution of the residuals – displayed in Fig. 8.3 – where red blobs and green stars represent the cases of a polarized and unpolarized beam, respectively in the presence of photon-ALP oscillations. For comparison, the blue triangles correspond to the situation of conventional physics.

Finally, we report in Table 8.1 the predicted values of the variance of the fit residuals for the above choice of the model parameters.

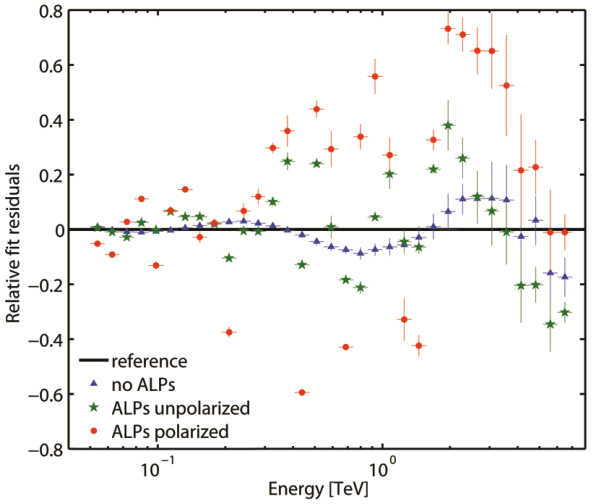

FIGURE 8.3: Distribution of the residuals in three cases. Polarized beam with ALP effects: red blobs. Unpolarized beam with ALP effects: green stars. Conventional physics: blue triangles.

Model	Variance of the fit residuals
No ALPs	0.03 ± 0.01
Unpolarized ALPs	0.09 ± 0.03
Polarized ALPs	0.21 ± 0.06

TABLE 8.1: Values of the variance to the fit residuals for the various cases considered in the text.

8.6 Discussion

We have critically analyzed the claim put forward by WB [156] that an observable effect in the spectra of distant VHE blazars arises as a consequence of oscillations of photons into ALPs in the presence of random extragalactic magnetic fields. In practice, we have redone the same analysis of WB in order to understand whether their result concerning potentially observable fluctuations in the spectra of blazars in the presence of photon-ALP oscillations are derived for a polarized or unpolarized photon/ALP beam, since this point is absolutely unclear from their paper. We have reproduced all their results in the case of an initially *polarized* beam, which however looks physically irrelevant to current observations. But we have shown that for the physically relevant case of an initially *unpolarized* beam the claimed effect is drastically reduced.

As a matter of fact, WB themselves point out that from Table 8.1 our result is at 3σ level [159]. This is precisely the crucial point. For, in the community of very-high-energy astrophysics a result is considered *reliable* only if it is at 5σ level (neglecting systematic errors, which lead to an additional smearing but are very difficult to estimate,

thereby explaining such a requirement). In other words, the difference between the case of conventional physics and that of an unpolarized photon beam with ALPs *is not sufficiently robust to be believable*. We propose instead to turn the argument around, in the sense that if such an effect is seen and cannot be explained by conventional astrophysics, then it should be interpreted as evidence for ALPs.

Conclusions

Very light ALPs are a generic prediction of many attempts to extend the Standard Model along different directions towards a more satisfactory fundamental theory of all elementary-particle interactions including gravity. In this thesis we have studied ALPs properties, their interaction with photons giving rise to photon-ALP oscillations and their consequences on VHE astrophysics.

In particular, in Chapters 1-6 we have systematically investigated the DARMA scenario in which the mechanism of photon-ALP oscillations triggered by large-scale magnetic fields is regarded as a means to effectively reduce the EBL attenuation affecting blazar observations above 100 GeV. Our assumptions can be summarized as follows:

- Large-scale magnetic fields exist with a cellular morphology characterized by a coherence lenth in the $1-10\,\mathrm{Mpc}$ range and a strength not much smaller than the available upper bound $B_0 < 6\,\mathrm{nG}$.
- ALPs have to be very light in order to ensure that the strong-mixing regime is realized. The upper bound on their mass depends on the adopted value of the $a\gamma\gamma$ coupling constant B_0/M – see Table 5.2 – but in any case the condition $m < 5 \cdot 10^{-10}\,\mathrm{eV}$ has to be met. This prevents the axion needed to solve the strong CP problem from playing any role in the present context.
- The parameter M is consistent but fairly close to the strongest upper bound $M > 10^{11}\,\mathrm{GeV}$ coming from observations of supernova SN1987a. We remark that this bound is however affected by a large uncertainty and exceeds by one order of magnitude the robust bound $M > 10^{10}\,\mathrm{GeV}$ coming both from theoretical considerations of star cooling and from the negative result of the CAST collaboration.

We predict that a boost factor of 10 in the photon survival probability with respect to conventional physics takes place for all VHE blazars observed so far well below the upper detection threshold of the planned CTA and HAWC water Cherenkov γ-ray observatory. Moreover, the energy E_{10} at which such a boost factor occurs decreases as the source

distance increases and becomes e.g. as low as 2 TeV for the blazar 3C 279 at $z = 0.536$. Hence, our prediction can certainly be tested with the above planned detectors and possibly also with currently operating IACTs H.E.S.S., MAGIC, VERITAS as well as with the Extensive Air Shower arrays ARGO-YBJ and MILAGRO.

We find it a remarkable fact that the DARMA scenario also offers a new interpretation of the observed VHE blazars, according to which the values of $\Gamma_{\rm em}$ for far-away VHE blazars are in the same ballpark of nearby ones and the large spread in the values of $\Gamma_{\rm obs}$ is mainly traced to the wide spread in the source distances.

Our predicted lower-than-expected transparency of the Universe in the VHE band is supported by an independent result [125] which rests upon a new statistical analysis of all VHE blazars based on a Kolmogorov-Smirnov test in conjunction with the minimal EBL model [96].

In Chapter 2 we have evaluated the transparency of the Universe to gamma rays in the energy range $10{\rm GeV} - 10^{13}{\rm GeV}$ using the most recent observational data concerning the EBL and the RB. The present calculation is of paramount relevance for the planned ground-based detectors like CTA, HAWC and HiSCORE.

In Chapters 6-7 we have focused on the FSRQ PKS 1222+216. We have shown that the surprising γ-ray detection of PKS 1222+216 by MAGIC can be explained – consistently with the simultaneous results by *Fermi*/LAT – within a standard blazar model by adding the new assumption that inside the source photons can oscillate into ALPs. Our explanation assumes an average magnetic field with strength $B \simeq 0.2\,{\rm G}$ in the jet up to the BLR and a value $M = 7 \cdot 10^{10}\,{\rm GeV}$ for the inverse coupling $\gamma\gamma a$. We remark that the emission model presented here is merely an example, and different and possibly more realistic scenarios can be constructed along similar lines. The main point we want to make is that with the photon-ALP oscillation mechanism at work the emission can well originate inside the BLR just like in conventional BL Lac models. As far as photon-ALP oscillations are concerned, their crucial role takes place in the source region before and just after the BLR.

Needless to say, our scenario naturally applies also to the other FSRQs detected at VHE like 3C279 and PKS 1510-089 [38, 162, 165], although these cases appear less problematic for the external emission scenario due to the absence of evident rapid ($t < 1$ day) variability.

As already mentioned some alternative scenarios accounting for the puzzling features of PKS 1222+216 have been recently appeared in the literature. For instance, in [163] it is proposed that the VHE emission arises in the parsec-scale jet through the production of collimated beams of high-energy electrons by fast relativistic magnetic reconnection (see

also [166]). Alternatively, in [151, 167] it is assumed the existence of collimated beams of neutral particles produced in the inner jet through photo-meson reactions of ultra-high energy protons. Neutral particles can freely propagate to distances larger than the BLR and then produce ultra-relativistic leptons interacting with the IR radiation of the dusty torus. In turn, the collimated leptons would produce highly beamed synchrotron emission. If the magnetic field at pc scale is small enough, not exceeding 1 mG, the VHE synchrotron radiation preserves the rapid variability of the inner engine at the pc scale (but in this case the confinement of the clouds of the BLR looks problematic).

It appears to us remarkable that our proposed model lends itself to an observational test. Because photon-ALP oscillations can mitigate – but not completely avoid – the γ-ray absorption inside the BLR, a natural prediction is that at the optically-thin/optically thick transition around 30 GeV (in the source frame) the spectrum should display a feature. So, the absence of such a feature would be hard to explain in our model but would directly support scenarios in which the emission occurs outside the BLR as those discussed above.

We find it quite tantalizing that precisely the most favourable value $M = 7 \cdot 10^{10}\,\mathrm{GeV}$ for the effect considered in the study of the source PKS 1222+216 corresponds to the most favourable case for a large-scale magnetic field of $B = 0.7\,\mathrm{nG}$ in the DARMA scenario that enlarges the "γ-ray horizon" and provides a natural solution to the cosmic opacity problem (see Chapters 4 and 5) (the DARMA scenario requires for the ALP mass $m < 1.7 \cdot 10^{-10}\,\mathrm{eV}$ which is consistent with the present model).

In Chapter 8 we have critically analyzed a result obtained by D. Wouters and P. Brun [156]. They claim potentially observable fluctuations in the spectra of blazars in the presence of photon-ALP oscillations. What is unclear in their paper is if their results are derived for a polarized or unpolarized photon/ALP beam. We have demonstrated that they use a polarized photon/ALP beam while the correct treatment of the problem should imply the use of an unpolarized one. We have reproduced all their results both in the case of an initially polarized beam – which however looks physically irrelevant to current observations – and in the case of an initially unpolarized one – which should be the correct approach to the problem. As a result, in the case of an initially unpolarized beam the claimed effect is drastically reduced to an extent that their result can only make bounds at the 3σ level, which cannot rule out the existence of ALPs.

As is well known, weakly interacting massive particles (WIMPs) can be detected either indirectly through astrophysical effects or directly at the Large Hadron Collider (LHC). The situation of ALPs characteristic of the DARMA scenario is in a sense similar. Besides being detectable indirectly through the astrophysical effects discussed in this thesis, they lend themselves to a direct detection in the near future with the planned

upgrade of the photon regeneration experiment ALPS at DESY [49] and with the next generation of solar axion detectors like IAXO [168], or with the Cherenkov Telescope Array (CTA).

We want also to point out that it has recently been shown that ALPs with precisely the properties needed in our model naturally emerge in the Large Volume Scenario of IIB string compactifications [169]. In addition, a very light ALP of the kind considered here is a viable candidate for the quintessential dark energy [13].

Future work

In the future, we plan to study from a theoretical point of view the photon-ALP mixing taking into account all the terms in the mixing matrix including the absorption term in order to complete the theoretical background and to give an analytical description of the photon/ALP conversion probability and to understand the different mixing regimes (in the presence of absorption). We want also to study in greater detail the parameter space of the DARMA scenario in order to clarify completely the effects of a change of the values of the magnetic field, of the magnetic field domain length, and of the coupling constant. Then, we want to calculate the transparency of the Universe to gamma rays when photon-ALP mixing is considered. We would also like to analyze deeper the cosmic opacity problem and consider the possibility of correlations between blazar spectral indexes and blazar redshift.

Appendix A

Schödinger-like equation with constant coefficients

We solve here the mathematical problem of finding the transfer matrix $\mathcal{U}(y, y_0; 0)$ associated with the reduced Schödinger-like equation

$$\left(i\frac{d}{dy} + \mathcal{M} \right) \psi(y) = 0 \ , \tag{A.1}$$

with

$$\psi(y) \equiv \begin{pmatrix} A_x(y) \\ A_z(y) \\ a(y) \end{pmatrix} \tag{A.2}$$

as in the text, and mixing matrix of the form

$$\mathcal{M} = \begin{pmatrix} s & 0 & 0 \\ 0 & t & v \\ 0 & v & u \end{pmatrix} \ , \tag{A.3}$$

where the coefficients s, t, u and v are supposed to be complex numbers.

We start by diagonalizing $\mathcal{M}$. Its eigenvalues are

$$\lambda_1 = s \ , \tag{A.4}$$

$$\lambda_2 = \frac{1}{2}\left(t + u - \sqrt{(t-u)^2 + 4\,v^2} \right) \ , \tag{A.5}$$

$$\lambda_3 = \frac{1}{2}\left(t + u + \sqrt{(t-u)^2 + 4\,v^2} \right) \ , \tag{A.6}$$

and it is straightforward to check that the corresponding eigenvectors can be taken to be

$$X_1 = \begin{pmatrix} 1 \\ 0 \\ 0 \end{pmatrix} , \tag{A.7}$$

$$X_2 = \begin{pmatrix} 0 \\ v \\ \lambda_2 - t \end{pmatrix} , \tag{A.8}$$

$$X_3 = \begin{pmatrix} 0 \\ v \\ \lambda_3 - t \end{pmatrix} . \tag{A.9}$$

Correspondingly, any solution of Eq. (A.1) can be represented in the form

$$\psi(y) = c_1\, X_1\, e^{i\lambda_1\,(y-y_0)} + c_2\, X_2\, e^{i\lambda_2\,(y-y_0)} + c_3\, X_3\, e^{i\lambda_3\,(y-y_0)} , \tag{A.10}$$

where c_1, c_2, c_3 and y_0 are arbitrary constants. As a consequence, the solution with initial condition

$$\psi(y_0) \equiv \begin{pmatrix} A_x(y_0) \\ A_z(y_0) \\ a(y_0) \end{pmatrix} \tag{A.11}$$

emerges from Eq. (A.10) for

$$c_1 = A_x(y_0) , \tag{A.12}$$

$$c_2 = \frac{\lambda_3 - t}{v(\lambda_3 - \lambda_2)}\, A_z(y_0) - \frac{1}{\lambda_3 - \lambda_2}\, a(y_0) , \tag{A.13}$$

$$c_3 = -\frac{\lambda_2 - t}{v(\lambda_3 - \lambda_2)}\, A_z(y_0) + \frac{1}{\lambda_3 - \lambda_2}\, a(y_0) . \tag{A.14}$$

It is a simple exercise to recast the considered solution into the form

$$\psi(y) = \mathcal{U}(y, y_0; 0)\, \psi(y_0) \tag{A.15}$$

with

$$\mathcal{U}(y, y_0; 0) = e^{i\lambda_1(y-y_0)}\, T_1(0) + e^{i\lambda_2(y-y_0)}\, T_2(0) + e^{i\lambda_3(y-y_0)}\, T_3(0) , \tag{A.16}$$

where we have set

$$T_1(0) \equiv \begin{pmatrix} 1 & 0 & 0 \\ 0 & 0 & 0 \\ 0 & 0 & 0 \end{pmatrix} , \tag{A.17}$$

$$T_2(0) \equiv \begin{pmatrix} 0 & 0 & 0 \\ 0 & \frac{\lambda_3 - t}{\lambda_3 - \lambda_2} & -\frac{v}{\lambda_3 - \lambda_2} \\ 0 & \frac{(\lambda_2 - t)(\lambda_3 - t)}{v(\lambda_3 - \lambda_2)} & -\frac{\lambda_2 - t}{\lambda_3 - \lambda_2} \end{pmatrix} , \tag{A.18}$$

$$T_3(0) \equiv \begin{pmatrix} 0 & 0 & 0 \\ 0 & -\frac{\lambda_2 - t}{\lambda_3 - \lambda_2} & \frac{v}{\lambda_3 - \lambda_2} \\ 0 & -\frac{(\lambda_2 - t)(\lambda_3 - t)}{v(\lambda_3 - \lambda_2)} & \frac{\lambda_3 - t}{\lambda_3 - \lambda_2} \end{pmatrix} , \tag{A.19}$$

from which it follows that the desired transfer matrix is just $\mathcal{U}(y, y_0; 0)$ as given by Eq. (A.16).

Appendix B

Approximate EBL behaviour

It proves very useful for illustrative purposes to have the approximate behaviour of $\tau_\gamma(E_0, z)$ in an analytic form. This goal can be achieved by taking advantage from the fact that $\sigma_{\gamma\gamma}(E, \epsilon, \varphi)$ is maximized when condition (2.5) is met (we restrict ourselves to head-on collisions for simplicity).

Accordingly, the crudest attempt to estimate the dominant contribution to the optical depth would be to approximate the $\epsilon(z)$ integration by the product of $\sigma_{\gamma\gamma}^{\max}$ times $n_\gamma(\epsilon(z), z)$ as evaluated for that particular value of $\epsilon(z)$ selected by condition (2.5) for fixed E. This amounts to insert the Dirac delta $\delta(\epsilon(z')/\mathrm{eV} - 500\,\mathrm{GeV}/E(z'))$ into the r.h.s. of Eq. (2.7), which leads to

$$\tau_\gamma(E_0, z) \simeq 2.25 \cdot 10^3 \int_0^z \mathrm{d}z \, \frac{n_\gamma\left(\epsilon(z), z\right)}{(1+z)\left[0.7 + 0.3\,(1+z)^3\right]^{1/2}} \, \mathrm{cm}^3\,\mathrm{eV} \;, \tag{B.1}$$

with

$$\epsilon(z) \simeq \frac{1}{1+z}\left(\frac{500\,\mathrm{GeV}}{E_0}\right)\mathrm{eV} \;. \tag{B.2}$$

Unfortunately, experience with this problem shows that the resulting E_0-dependence of $\tau_\gamma(E_0, z)$ is too steep, and since $P^{\mathrm{CP}}_{\gamma\to\gamma}(E_0, z)$ depends exponentially on $\tau_\gamma(E_0, z)$ this approximation is doomed to failure.

A more satisfactory conclusion emerges by exploiting a popular approximation [123] which amounts to replace the $\epsilon(z)$ integration in Eq. (2.7) by the product of $\sigma_{\gamma\gamma}^{\max}$ times $\epsilon(z)\, n_\gamma(\epsilon(z), z)$ at the particular value of $\epsilon(z)$ dictated by condition (2.5) for fixed E.

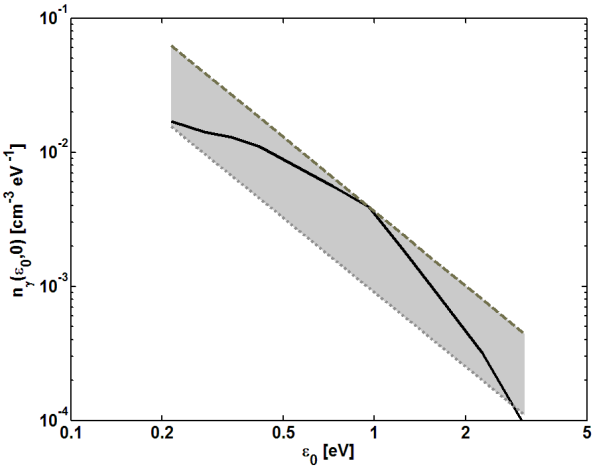

FIGURE B.1: The spectral photon number density in the present Universe $n_\gamma(\cdot, 0)$ is plotted versus the energy ϵ_0 in the energy range $0.25 - 2.5\,\mathrm{eV}$. The solid line represents the result of the FRV model. The dotted and dashed lines correspond to the lower ($\alpha = 0.9$) and upper ($\alpha = 3.6$) limit, respectively, of our power-law approximation defined in Eq. (B.4).

We find in this way

$$\tau_\gamma(E_0, z) \simeq 2.25 \cdot 10^3 \left(\frac{500\,\mathrm{GeV}}{E_0}\right) \int_0^z \frac{\mathrm{d}z}{(1+z)^2 \left[0.7 + 0.3\,(1+z)^3\right]^{1/2}} \times \\ \times\, n_\gamma \left(\frac{(500\,\mathrm{GeV}/E_0)\,\mathrm{eV}}{1+z}, z\right) \mathrm{cm}^3\,\mathrm{eV}\ , \tag{B.3}$$

where Eq. (B.2) has been used.

Owing to Eq. (B.3), the derivation of an approximate analytic behaviour of the optical depth requires an approximate analytic expression for $n_\gamma(\epsilon(z), z)$. Unfortunately, the FRV model does not give an analytic form for $n_\gamma(\epsilon_0, 0)$ but provides a plot of $\epsilon_0\, n_\gamma(\epsilon_0, 0)$ versus ϵ_0 (see their Fig. 4). The corresponding plot of $n_\gamma(\epsilon_0, 0)$ as a function of ϵ_0 is reproduced by the solid line in Fig. B.1 for the EBL energy range relevant for the observed blazas, namely $0.25\,\mathrm{eV} < \epsilon_0 < 2.5\,\mathrm{eV}$. A look at Fig. B.1 shows that within the considered energy range the SED of the EBL departs from a power-law behaviour, owing to the emission bump resulting from the integrated emission of the low-mass stellar population that remained close to the main-sequence over cosmological times. For this reason, we approximate the FRV result for $n_\gamma(\epsilon_0, 0)$ with the shadowed linear strip shown in Fig. B.1 enveloping the exact behaviour, which is expressed by the following power-law representation

$$n_\gamma^{\mathrm{app}}(\epsilon_0, 0) \simeq 10^{-3}\,\alpha \left(\frac{\mathrm{eV}}{\epsilon_0}\right)^{1.85} \mathrm{cm}^{-3}\,\mathrm{eV}^{-1}\ , \tag{B.4}$$

with the constant α in the range $0.9 \leq \alpha \leq 3.6$ so as to enclose the FRV curve.

Evolutionary effects in the EBL SED can be taken into account as follows. Besides redshifting all energies in proportion of $1+z$, the cosmic expansion dilutes the EBL by a factor $(1+z)^3$ similarly to what happens for the CMB. But in addition the EBL spectral photon number density changes because of the intrinsic evolution of the galactic population over cosmic times. A quantitative analysis [124] shows that the EBL photon number density acquires an extra factor $(1+z)^{-1.2}$ as long as $z<1$, which is appropriate to our case. On the whole, the spectral photon number density $n_\gamma^{\rm app}(\epsilon(z),z)$ of the EBL at redshift z is related to $n_\gamma^{\rm app}(\epsilon_0,0)$ by

$$n_\gamma^{\rm app}(\epsilon(z),z)\,{\rm d}\epsilon(z) \simeq (1+z)^{1.8}\; n_\gamma^{\rm app}(\epsilon_0,0)\,{\rm d}\epsilon_0 \;, \tag{B.5}$$

which yields

$$n_\gamma^{\rm app}(\epsilon(z),z) \simeq (1+z)^{0.8}\; n_\gamma^{\rm app}\left(\frac{\epsilon(z)}{1+z},0\right) \;, \tag{B.6}$$

namely

$$n_\gamma^{\rm app}\left(\frac{(500\,{\rm GeV}/E_0)\,{\rm eV}}{1+z},z\right) \simeq (1+z)^{0.8}\; n_\gamma^{\rm app}\left(\frac{(500\,{\rm GeV}/E_0)\,{\rm eV}}{(1+z)^2},0\right) \;, \tag{B.7}$$

thanks to Eq. (B.2). In particular, Eq. (B.4) leads to

$$n_\gamma^{\rm app}\left(\frac{(500\,{\rm GeV}/E_0)\,{\rm eV}}{1+z},z\right) \simeq 10^{-3}\,\alpha\left(\frac{E_0}{500\,{\rm GeV}}\right)^{1.85}(1+z)^{4.5}\;{\rm cm}^{-3}\,{\rm eV}^{-1} \;. \tag{B.8}$$

The approximate evaluation of the optical depth $\tau_\gamma^{\rm app}(E_0,z)$ amounts to insert Eq. (B.8) into Eq. (B.3). Correspondingly, we get

$$\tau_\gamma^{\rm app}(E_0,z) \simeq 2.25\,\alpha\left(\frac{E_0}{500\,{\rm GeV}}\right)^{0.85} I(z) \;, \tag{B.9}$$

where we have set

$$I(z) \equiv \int_0^z {\rm d}z'\;\frac{(1+z')^{2.5}}{\left[0.7+0.3\,(1+z')^3\right]^{1/2}} \;. \tag{B.10}$$

This integral has been evaluated numerically and its behaviour is depicted in Fig. B.2, which shows that up to $z\simeq 0.1$ it goes linearly with z but it increases more rapidly for larger redshifts.

Before leaving this issue it is worthwhile to show how Eq. (2.9) is recovered in the limit of small z where cosmological effects become irrelevant. In such a situation the source distance is $D=cz/H_0$, which allows us to write the optical depth as

$$\tau_\gamma^{\rm app}(E,D) = 5.25\cdot 10^{-4}\,\alpha\left(\frac{E}{500\,{\rm GeV}}\right)^{0.85}\left(\frac{D}{\rm Mpc}\right) \;, \tag{B.11}$$

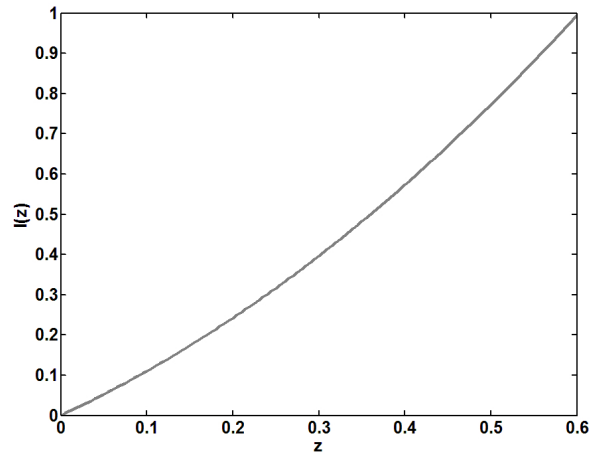

FIGURE B.2: Plot of the behaviour of $I(z)$.

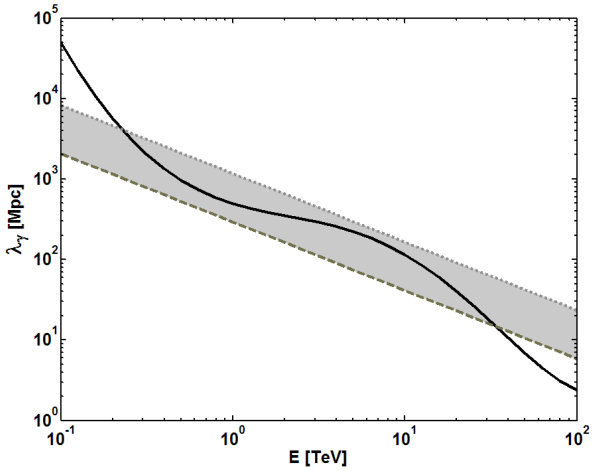

FIGURE B.3: The approximate pair-production mean free path $\lambda_\gamma^{\rm app}$ of a VHE photon is plotted versus its energy E and it is represented by the shadowed area as the parameter α varies in the range 0.9 – 3.6. The dotted and dashed lines correspond to $\alpha = 0.9$ and $\alpha = 3.6$, respectively. Superimposed is the exact result obtained within the FRV model and shown in Fig. 3.

with the replacement $E_0 \to E$. So, we see that $\tau_\gamma^{\rm app}(E, D) \propto D$ in agreement with Eq. (2.9), which entails that in the present approximation the mean free path for $\gamma\gamma \to e^+e^-$ is given by

$$\lambda_\gamma^{\rm app}(E) = 1.90 \cdot 10^3 \, \alpha^{-1} \left(\frac{500\,\mathrm{GeV}}{E} \right)^{0.85} \mathrm{Mpc} \; . \tag{B.12}$$

This quantity is plotted in Fig. B.3 as a function of E, where it is represented by the shadowed region between the dotted line corresponding to $\alpha = 0.9$ and the dashed line corresponding to $\alpha = 3.6$. The solid curve yields $\lambda_\gamma(E)$ as evaluated exactly within the FRV model and exhibited in Fig. 3. We see that the present approximation is indeed consistent with the result of the FRV model for $0.2\,\mathrm{TeV} < E < 2\,\mathrm{TeV}$.

Bibliography

[1] C. Corianò and N. Irges, Phys. Lett. B **651**, 298 (2007); C. Corianò, N. Irges and S. Morelli, JHEP **0708**, 008 (2007); H. Baer, S. Krami, S. Sekmen and H. Summy, JHEP **0803**, 056 (2008); H. Baer and H. Summy, Phys. Lett. B **666**, 5 (2008); H. Baer *et al.*, JCAP **0902**, 002 (2009).

[2] S. Chang, S. Tazawa and M. Yamaguchi, Phys. Rev. D **61**, 084005 (2000); K. R.Dienes, E. Dudas and T. Gherghetta, Phys. Rev. D **62**, 105023 (2000).

[3] N. Turok, Phys. Rev. Lett. **76**, 1015 (1996).

[4] P. Svrcek, E. Witten, JHEP **0606** 051 (2006).

[5] A. Ringwald, Proceedings of *4th Patras Workshop on Axions, WIMPs and WISPs* (DESY Verlag 2008), arXiv:0810.3106 [hep-th].

[6] A. Arvanitaki, S. Dimopoulos, S. Dubovsky, N. Kaloper and J. March-Russell, Phys. Rev. D **81**, 123530 (2010).

[7] E. Masso, Lect. Notes Phys. **741**, 83 (2008); J. Jaeckel and A. Ringwald, Ann. Rev. Nucl. Part. Sci. **60**, 405 (2010).

[8] R. D. Peccei and H. R. Quinn, Phys. Rev. Lett. **38**, 1440 (1977); R. D. Peccei and H. R. Quinn, Phys. Rev. D **16**, 1791 (1977).

[9] S. Weinberg, Phys. Rev. Lett. **40**, 223 (1978); F. Wiczek, Phys. Rev. Lett. **40**, 279 (1978).

[10] J. Kim, Phys. Rev. Lett. **43**, 103 (1979); M. A. Shifman, A. I. Vainshtein and V. I. Zakharov, Nucl. Phys. **B166**, 493 (1980); A. R. Zhitnitsky, Sov. J. Nucl. Phys. **31**, 260 (1980); M. Dine, W. Fischler and M. Srednicki, Phys. Lett. B **104**, 199 (1981); M. B. Wise, H. Georgi and S. L. Glashow, Phys. Rev. Lett. **47**, 402 (1981).

[11] J. H. Kim, Phys. Rep. **150**, 1 (1987); H. Y. Cheng, Phys. Rep. **158**, 1 (1988); J. E. Kim and G. Carosi, Rev. Mod. Phys. **82**, 557 (2010).

[12] E. W. Kolb and M. S. Turner, *The Early Universe* (Addison-Wesley, New York, 1990); M. Turner, Phys. Rep. **197**, 67 (1990); P. Sikivie, *Lect. Notes Phys.* **741**, 19 (2008).

[13] S. M. Carroll, Phys. Rev. Lett. **81**, 3067 (1998).

[14] P. Sikivie, Phys. Rev. Lett. **51**, 1415 (1983); (E) ibid. **52**, 695 (1984).

[15] G. G. Raffelt and L. Stodolsky, Phys. Rev. D **37**, 1237 (1988).

[16] L. Maiani, R. Petronzio and E. Zavattini, Phys. Lett. B **175**, 359 (1986).

[17] E. Zavattini *et al.*, Phys. Rev. D 77, 032006 (2008).

[18] C. Robilliard *et al.*, Phys. Rev. Lett. 99, 190403 (2007); K. Ehret *et al.*, Phys. Lett. B **689**, 149 (2010).

[19] G. G. Raffelt, Phys. Rep. **198**, 1 (1990); G. G. Raffelt, *Stars as Laboratories for Fundamental Physics* (University of Chicago Press, Chicago, 1996).

[20] K. Zioutas *et al.* (CAST Collaboration), Phys. Rev. Lett. **94**, 121301 (2005); S. Andriamonje *et al.* (CAST Collaboration), JCAP **0704**, 010 (2007).

[21] C. Csáki, N. Kaloper, M. Peloso and J. Terning, JCAP **05** 005 (2003).

[22] M. Christensson and M. Fairbairn, Phys. Lett. B **565**, 10 (2003); D. Chelouche, R.Rabadan, S. S. Pavolv and F. Castejon, Astrophys. J. Suppl. **180**, 1 (2009); D. Chelouche and E. Guendelman, Astrophys. J. **699**, L5 (2009); C. Burrage, A.-C. Davis and D. J. Shaw, Phys. Rev. D **79**, 044028 (2009).

[23] D. Hooper and P. D. Serpico, Phys. Rev. Lett. **99**, 231102 (2007); K. A. Hochmuth and G. Sigl, Phys. Rev. D **76**, 123011 (2007); A. De Angelis, O. Mansutti and M. Roncadelli, Phys. Lett. B **659**, 847 (2008).

[24] A. De Angelis, M. Roncadelli and O. Mansutti, Phys. Rev. D **76**, 121301 (2007).

[25] A. De Angelis, O. Mansutti, M. Persic and M. Roncadelli, Mon. Not. R. Astron. Soc. **394**, L21 (2009).

[26] A. Mirizzi and D. Montanino, JCAP **12** 004 (2009).

[27] M. Simet, D. Hooper and P. D. Serpico, Phys. Rev. D **77**, 063001 (2008).

[28] A. Mirizzi, G. G. Raffelt and P. D. Serpico *Lect. Notes Phys.* **741**, 115 (2008).

[29] N. Bassan and M. Roncadelli, arxiv:0905.3752.

[30] M. A. Sánchez-Conde *et al.*, Phys. Rev. D **79**, 123511 (2009).

[31] Horns, D., Maccione, L., Meyer, M., et al. 2012, Phys. Rev. D, 86, 075024

[32] N. Bassan, A. Mirizzi and M. Roncadelli, JCAP **05** 010 (2010); O. Mena, S. Razzaque and F. Villaescusa-Navarro, JCAP **02** 030 (201f1).

[33] A. Nikishov, Sov. Phys. JETP **14**, 393 (1962); R. J. Gould and G. P. Schreder, Phys. Rev. **155**, 1404 (1967); G. G. Fazio and F. W. Stecker, Nature **226**, 135 (1970).

[34] F. Aharonian, *Very High Energy Cosmic Gamma Radiation* (World Scientific, Singapore, 2004).

[35] A. Franceschini, G. Rodighiero and M. Vaccari, Astron. Astrophys. **487**, 837 (2008).

[36] F. W. Stecker and S. V. Scully, J. Phys. **60**, 131 (2007).

[37] F. Aharonian *et al.* (H.E.S.S. Collaboration), Nature **440**, 1018 (2006).

[38] J. Albert *et al.* (MAGIC Collaboration), Science **320**, 1752 (2008).

[39] M. Teshima *et al.* (MAGIC Collaboration), arXiv:0709.1475; A. De Angelis *et al.* (MAGIC Collaboration), arXiv:0708.3571.

[40] T. M. Kneiske, T. Bretz, K. Mannheim and D. H. Hartmann, Astron. Astrophys. **413**, 807 (2004).

[41] F. W. Stecker, M. G. Baring and E. J. Summerlin, Astrophys. J. **667**, L29 (2007).

[42] K. Katarzynski *et al.*, Mon. Not. R. Astron. Soc. **368**, L52 (2006); F. A. Aharonian, D. Khangulyan and L. Costamante, Mon. Not. R. Astron. Soc. **387**, 1206 (2008).

[43] M. Böttcher, C. D. Dermer and J. D. Finke, Astrophys. J. **679**, L9 (2008).

[44] Horns D., Meyer M., 2012, JCAP, 2, 33

[45] Meyer M., Horns D., Raue M., 2012, arXiv, arXiv:1211.6405

[46] Meyer, M., Horns, D., & Raue, M. 2013, Phys. Rev. D, 87, 035027

[47] Horns, D., & Meyer, M. 2013, arXiv:1309.3846

[48] Finke, J., Reyes, L., & Georganopoulos, M. 2013, arXiv:1303.5093

[49] K. Ehret (The ALPS Collaboration), Proceedings of *4th Patras Workshop on Axions, WIMPs and WISPs* (DESY Verlag 2008), arXiv:0812.3495 [hep-ex]. P. Arias, J. Jaeckel, J. Redondo and A. Ringwald, Phys. Rev. D **82**, 115018 (2010).

[50] G. B. Gelmini, S. Nussinov, T. Yanagida, Nucl. Phys. B **219**, 31 (1983).

[51] R. Kallosh, A. D. Linde, D. A. Linde and L. Susskind, Phys. Rev. D **52**, 912 (1995).

[52] S. L. Cheng, C. Q. Geng, W. T. Ni, Phys. Rev. D **94**, 3132 (1995).

[53] T. W. Donnely *et al.*, Phys. Rev. D **18**, 1607 (1978).

[54] A. Zehnder, K. Gabathuler and J. L. Vuilleumier, Phys. Lett. B **110**, 419 (1982).

[55] R. Holman *et al.*, Phys. Lett. B **282**, 132 (1992); M. Kamionkowski and J. March-Russell, Phys. Lett. B **282**, 137 (1992); S. Ghigna, M. Lusignoli and M. Roncadelli, Phys. Lett. B **283**, 278 (1992); S. M. Barr and D. Seckel, Phys. Rev. D **46**, 539 (1992).

[56] W. Heisenberg and H. Euler, Z. Phys. **98**, 714 (1936); V. S. Weisskopf, K. Dan. Vidensk. Selsk. Mat. Fys. Medd. **14**, 6 (1936); J. Schwinger, Phys. Rev. **82**, 664 (1951).

[57] S. Mohanty, S. N. Nayak, Phys. Rev. Lett. **70**, 4038 (1993); (E) ibid. **71**, 1117 (1993).

[58] J. W. Brockway, E. D. Carlson, G. G. Raffelt, Phys. Lett. B **383**, 439 (1996); J. A. Grifols, E. Masso, R. Toldra, Phys. Rev. Lett. **77**, 2372 (1996).

[59] S. J. Asztalos et *al.*, Phys. Rev. Lett. **104**, 041301 (2010).

[60] P. Sikivie and Q. Yang, Phys. Rev. Lett. **103**, 111301 (2009).

[61] E. Masso and R. Toldra, Phys. Rev. D **52**, 1755 (1995); E. Masso and R. Toldra, Phys. Rev. D **55**, 7967 (1997).

[62] G. Breit, J. A. Wheeler, Phys. Rev. **46**, 1087 (1934); W. Heitler, *The Quantum Theory of Radiation* (Oxford University Press, Oxford, 1960).

[63] E. Aliu *et al.*, Astrophys. J. **692**, L29 (2009).

[64] J. Albert *et al.*, Astrophys. J. **663**, 125 (2007).

[65] J. Albert *et al.*, Astrophys. J. **669**, 862 (2007).

[66] J. Albert *et al.*, Astrophys. J. **662**, 892 (2007).

[67] J. Albert *et al.*, Astrophys. J. **648**, L105 (2006).

[68] J. Albert *et al.*, Astrophys. J. **639**, 761 (2006).

[69] J. Albert *et al.*, Astrophys. J. **666**, L17 (2007).

[70] G. Superina *et al.*, Proc. 30th International Cosmic Ray Conference, vol. 3, 913 (2008).

[71] F. Aharonian *et al.*, Astron. Astrophys. **436**, L17 (2005).

[72] F. Aharonian *et al.*, Astron. Astrophys. **481**, L103 (2008).

[73] V. A. Acciari *et al.*, Astrophys. J. **684**, L73 (2008).

[74] F. Aharonian *et al.*, Astron. Astrophys. **448**, L19 (2006).

[75] V. A. Acciari *et al.*, Astrophys. J. **715**, L49 (2010).

[76] F. Aharonian *et al.*, Astron. Astrophys. **384**, L23 (2002).

[77] V. A. Acciari *et al.*, Astrophys. J. **690**, L126 (2009).

[78] F. Aharonian *et al.*, Astron. Astrophys. **475**, L9 (2007).

[79] F. Aharonian *et al.*, Astron. Astrophys. **455**, 461 (2006).

[80] V. A. Acciari *et al.*, Astrophys. J. **695**, 1370 (2009).

[81] F. Aharonian *et al.*, Astron. Astrophys. **470**, 475 (2007).

[82] F. Aharonian *et al.*, Astron. Astrophys. **473**, L25 (2007).

[83] J. Albert *et al.*, Astrophys. J. **667**, L21 (2007).

[84] H. Anderhub *et al.*, Astrophys. J. **704**, L129 (2009).

[85] J. Aleksić *et al.*, arXiv:1101.2764.

[86] J. Aleksić *et al.*, arXiv:1101.4645.

[87] V. A. Acciari *et al.*, Astrophys. J. **693**, L104 (2009); (E) Astrophys. J. **721**, L203 (2010).

[88] V. A. Acciari *et al.*, Astrophys. J. **708**, L100 (2010).

[89] J. Albert *et al.* (MAGIC collaboration), Science **320**, 1752 (2008).

[90] P. Madau and L. Pozzetti, Mon. Not. R. Astron. Soc. **312**, L9 (2000).

[91] M. G. Hauser and E. Dwek, Ann. Rev. Astron. Astrophys. **39**, 249 (2001).

[92] J. R. Primack, R. S. Sommerville, J. S. Bullock and J. E. G. Devriendt, AIP Conference Series **558** 463 (2001); J. R. Primack, J. S. Bullock, R. S. Sommerville, AIP Conference Conference Series, **745** 23 (2005); Gilmore R. C., Madau P., Primack J. R., Somerville R. S., Haardt F., 2009, MNRAS, 399, 1694; Gilmore R. C., Somerville R. S., Primack J. R., Domínguez A., 2012, MNRAS, 422, 3189.

[93] R. C. Gilmore, R. S. Sommerville, J. R. Primack and A. Dominguez, arXiv:1104.0671.

[94] F. W. Stecker, M. A. Malkan and S.T. Scully, Astrophys. J. **648**, 774 (2006).

[95] T. M. Kneiske, K. Mannheim and D. H. Hartmann, Astron. Astrophys. **386**, 1 (2002); J. D. Finke, S. Razzaque and C. D. Dermer, Astrophys. J. **712**, 238 (2010).

[96] T. M. Kneiske and H. Dole, Astron. Astrophys. **515**, 19 (2010).

[97] Domínguez A., et al., 2011, MNRAS, 410, 2556; http://side.iaa.es/EBL/.

[98] M. Schrödter, Astrophys. J. **628**, 617 (2005); F. Aharonian *et al.*, Astron. Astrophys. **448**, L19 (2006); D. Mazin and M. Raue, Astron. Astrophys. **471**, 439 (2007); D. Mazin and F. Goebel, Astrophys. J. **655**, L13 (2007); J. D. Finke and S. Razzaque, Astrophys. J. **698**, 1716 (2009).

[99] Orr M. R., Krennrich F., Dwek E., 2011, ApJ, 733, 77.

[100] Abdo *et al.* arXiv:1005.0996.

[101] http://www.astro.unipd.it/background.

[102] G. Fossati, L. Maraschi, A. Celotti, A. Comastri and G. Ghisellini, Mon. Not. R. Astron. Soc. **299**, 433 (1998).

[103] T. M. Venters and V. Pavlidou, Astrophys. J. **666**, 128 (2007).

[104] G. Ghisellini *et al.*, Astron. Astrophys. **348**, 63 (1999); F. Tavecchio *et al.*, Astrophys. J. **575**, 137 (2002); N. Mankuzhiyil, S. Ansoldi, M. Persic and F. Tavecchio, Astrophys. J. **733**, 14 (2011).

[105] G. Ghisellini, A. Celotti, G. Fossati, L. Maraschi and A. Comastri, Mon. Not. R. Astron. Soc. **301**, 451 (1998).

[106] A. R. Bell, Mon. Not. R. Astron. Soc. **182**, 147 (1978).

[107] T. Kifune, Astrophys. J. **518**, L31 (1999); U. Jacob and T. Piran, Phys. Rev. D **78**, 124010 (2008); L.Shao and B. Ma, Mod. Phys. Lett. A **25**, 3251 (2010).

[108] W. Essey and A. Kusenko, Astropart. Phys. **33**, 81 (2010).

[109] F. Tavecchio *et al.*, Mon. Not. R. Astron. Soc. **401**, 1570 (2010); G. Ghisellini *et al.*, Mon. Not. R. Astron. Soc. **402**, 497 (2010).

[110] R. Jannson, G. R. Farrar, A. H. Waelkens and T. A. Enslin, JCAP **09** 021 (2009); C. V. Eyk *et al.*, Astrophys. J. **728**, 97 (2011).

[111] C. L. Carilli and G. B. Taylor, Ann. Rev. Astron. Astrophys. **40**, 319 (2002); A. Bonafede *et al.*, arXiv:1103.0277.

[112] P. P. Kronberg, Rept. Prog. Phys. **57**, 325 (1994).

[113] D. Grasso and H. Rubinstein, Phys. Rep. **348**, 163 (2001).

[114] J. E. Gunn and B. A. Peterson, Astrophys. J. **142**, 1633 (1965).

[115] C. Csáki, N. Kaloper and J. Terning, Phys. Lett. B **535**, 33 (2002).

[116] G. Sigl, F. Miniati and T. A. Ensslin, Phys. Rev. D **70**, 043007 (2004); K. Dolag, D. Grasso, V. Springel and I. Tkachev, JCAP **05**, 009 (2005).

[117] M. J. Rees and G. Setti, Nature **219**, 127 (1968); S. R. Furlanetto and A. Loeb, Astrophys. J. **556**, 619 (2001).

[118] R. M. Kulsrud, R. Cen, J. P. Ostriker and D. Ryu, Astrophys. J. **480**, 481 (1997).

[119] D. Harari *et al.* (The Pierre Auger collaboration), Science **318**, 938 (2007).

[120] A. De Angelis, M. Persic and M. Roncadelli, Mod. Phys. Lett. A **23**, 315 (2008).

[121] P. Abreu *et al.* (The Pierre Auger Collaboration), Astropart. Phys. **34**, 314 (2010).

[122] P. Blasi, S. Burles and A. V. Olinto, Astrophys. J. **514**, L79 (1999).

[123] P. Coppi and F. Aharonian, Astrophys. J. **487**, L9 (1997).

[124] M. Raue and D. Mazin, Int. J. Mod. Phys. D **17**, 1515 (2008).

[125] M. Meyer and D. Horns, Proceedings of *Cosmic Radiation Fields: Sources in the early Universe*, http://pos.sissa.it/ PoS (CRF 2010) 011.

[126] Actis M., et al., 2011, ExA, 32, 193

[127] Sinnis G., 2005, AIPC, 745, 234

[128] Tluczykont M., Hampf D., Horns D., Kneiske T., Eichler R., Nachtigall R., Rowell G., 2011, AdSpR, 48, 1935

[129] Protheroe R. J., Biermann P. L., 1997, APh, 7, 181

[130] Abdo A. A., et al., 2010, ApJ, 723, 1082

[131] Costamante L., 2012, arXiv, arXiv:1208.0810

[132] Stecker F. W., Malkan M. A., Scully S. T., 2012, ApJ, 761, 128

[133] R. J. Gould and G. P. Schreder, Phys. Rev. **155**, 1404 (1967).

[134] Stecker F. W., 1971, NASSP, 249.

[135] Gervasi M., Tartari A., Zannoni M., Boella G., Sironi G., 2008, ApJ, 682, 223

[136] Essey W., Kalashev O., Kusenko A., Beacom J. F., 2011, ApJ, 731, 51

[137] L. Maraschi, G. Ghisellini and A. Celotti, Astrophys. J. **397**, L5 (1992); C. Dermer and R. Schleickeiser, Astrophys. J. **416**, 458 (1993); M. Sikora, M. Begelman and M. J. Rees, Astrophys. J. **421**, 153 (1994).

[138] C.M. Urry and P. Padovani, Pub. of Astron. Soc. of Pacific **107**, 803 (1995).

[139] A. Neronov and I. Vovk, Science **328**, 73 (2010); F. Tavecchio, G. Ghisellini, L. Foschini, G. Bonnoli, G. Ghirlanda and P. Coppi, Mon. Not. R. Astron. Soc. **406**, L70 (2010).

[140] S. Liberati and L. Maccione, Ann. Rev. Nucl. Part. Sci. **59**, 245 (2009).

[141] F. Tavecchio and D. Mazin, Mon. Not. R. Astron. Soc. **392**, L40 (2009).

[142] F. Tavecchio, J. Becerra-Gonzalez, G. Ghisellini, A. Stamerra, G. Bonnoli, L. Foschini and L. Maraschi, Astron. Astrophys. **534**, A86 (2011).

[143] A. Celotti, P. Padovani and G. Ghisellini, Mon. Not. R. Astron. Soc., **286**, 415, (1997).

[144] E. P. Farina , R. Decarli, R. Falomo, A. Treves, C. M. Raiteri , Mon. Not. R. Astron. Soc. **424**, 393, (2012).

[145] J. H. Krolik, C. F. McKee and C. B. Tarter, Astrophys. J. **249**, (1981).

[146] M. J. Rees, Mon. Not. R. Astron. Soc. **228**, 47P (1987).

[147] H. Netzer, New Astron. Review **52**, 257 (2008).

[148] F. Tavecchio and G. Ghisellini, Mon. Not. R. Astron. Soc. **386**, 945 (2008).

[149] G. Ghisellini and F. Tavecchio, Mon. Not. R. Astron. Soc. **387**, 1669 (2008).

[150] Y. T. Tanaka *et al*, Astrophys. J. **733**, 19 (2011).

[151] C. Dermer, K. Murase and H. Takami, Astrophys. J. **755**, 147 (2012).

[152] A. Celotti and G. Ghisellini, Mon. Not. R. Astron. Soc. **385**, 283 (2008).

[153] M. C. Begelman, R. D. Blandford and M. J. Rees, Rev. Mod. Phys. **56**, 255 (1984).

[154] S. P. O'Sullivan and D. C. Gabuzda, Mon. Not. R. Astron. Soc. **400**, 26 (2009).

[155] D. Moss and A. Shukurov, Mon. Not. R. Astron. Soc. **279**, 229 (1996).

[156] D. Wouters and P. Brun, Phys. Rev. D **86**, 043005 (2012).

[157] L. Östman and E. Mörtsell, J. Cosmol. Astropart. Phys. 0502 (2005) 005.

[158] Private communication from F. Tavecchio.

[159] D. Wouters and P. Brun (private communication through the Editor).

[160] T. H. Liu and J. M. Bai, Astrophys. J. **653**, 1089 (2006); J. Poutanen and B. Stern, Astrophys. J. **717**, L118 (2010).

[161] J. Aleksić *et al.*, Astrophys. J. **730**, L8 (2011).

[162] S. Wagner and B. Behera, 10th HEAD Meeting, Hawaii, BAAS **42**, 07.05 (2010).

[163] K. Nalewajko *et al.*, Mon. Not. R. Astron. Soc. **425**, 2519 (2012).

[164] G. Ghisellini, L. Maraschi and F. Tavecchio, Mon. Not. R. Astron. Soc. **396**, L105 (2009).

[165] J. Aleksić *et al.*, Astron. Astrophys. **530**, A4 (2011).

[166] B. Cerutti *et al.* Astrophys. J. **754**, L33 (2012).

[167] K. Murase, Astrophys. J. **761**, L16 (2012).

[168] I. G. Irastorze et al., JACP 1106, 013 (2011).

[169] M. Cicoli, M. Goodsell and A. Ringwald, arXiv:1206.0819 [hep-th].